Universidade de Aveiro Departamento de Engenharia Mecânica
2015

Tiago Jordão Grilo

Desenvolvimento de modelos computacionais anisotrópicos baseados em hipoelasticidade e hiperelasticidade incluindo endurecimento cinemático não-linear

Development of computational anisotropic hypoelastic- and hyperelastic-based models including nonlinear kinematic hardening

Universidade de Aveiro Departamento de Engenharia Mecânica
2015

Tiago Jordão Grilo

Desenvolvimento de modelos computacionais anisotrópicos baseados em hipoelasticidade e hiperelasticidade incluindo endurecimento cinemático não-linear

Development of computational anisotropic hypoelastic- and hyperelastic-based models including nonlinear kinematic hardening

Dissertação apresentada à Universidade de Aveiro para cumprimento dos requisitos necessários à obtenção do grau de Doutoramento em Engenharia Mecânica, realizada sob orientação científica de Robertt Ângelo Fontes Valente, Professor Auxiliar do Departamento de Engenharia Mecânica da Universidade de Aveiro, e de Stefanie Reese, Professora Catedrática do *Institute of Applied Mechanics*, *RWTH Aachen University*, Alemanha.

Apoio financeiro da FCT e do FSE no âmbito do III Quadro Comunitário de Apoio

o júri

presidente

Doutor João Manuel da Costa e Araújo Pereira Coutinho
professor catedrático da Universidade de Aveiro

Doutora Marta Cristina Cardoso de Oliveira
professora auxiliar da Faculdade de Ciências e Tecnologia da Universidade de Coimbra

Doutor Francisco Manuel Andrade Pires
professor auxiliar da Faculdade de Engenharia da Universidade do Porto

Doutor Luís Filipe Menezes
professor catedrático da Faculdade de Ciências e Tecnologia da Universidade de Coimbra

Doutor António Gil d'Orey Andrade Campos
professor auxiliar da Universidade de Aveiro

Doutor Ricardo José Alves de Sousa
professor auxiliar da Universidade de Aveiro

Doutora Stefanie Reese
professora catedrática do *Institute of Applied Mechanics, RWTH Aachen University*, Alemanha (co-orientadora)

Doutor Robertt Ângelo Fontes Valente
professor auxiliar da Universidade de Aveiro (orientador)

Agradecimentos / Acknowledgements

Ao Professor Doutor Robertt Valente, orientador principal, pelo constante apoio, orientação, disponibilidade, encorajamento, amizade e otimismo demonstrados ao longo destes anos. Fico-lhe também agradecido por me ter possibilitado a realização deste trabalho.

To Professor Stefanie Reese, co-supervisor, my appreciation for the opportunity of developing part of my research at the Institute of Applied Mechanics at RWTH Aachen University. Also, for the fruitful discussions regarding the development of the hyperelastic-based model.

To Doctor Ivaylo Vladimirov, for his constant availability and support during my stay in Aachen. The hours of discussion to identify and solve issues regarding the hyperelastic-based model are much appreciated.

To all IFAM members, for the welcoming spirit and sympathy. In particular, to Reza Kebriaei, Marek Fassin, and Tim Brepols for their friendship and support, softening my adaptation to Aachen. Also, the assistance provided by Tim Brepols about some technical and scientific matters is acknowledged.

Ao Nelson Souto, pela ajuda e coloboração no desenvolvimento do procedimento de identificação de parâmetros constitutivos.

À Fundação para a Ciência e Tecnologia (FCT), pelo apoio financeiro concedido através da bolsa de doutoramento SFRH/BD/82286/2011.

A todos os elementos do GRIDS, pelo seu espírito de grupo e dinamismo.

A todos os meus amigos, quer pelo apoio demonstrado e palavras de encorajamento, quer pelos momentos de descontração proporcionados ao longo desta jornada.

À minha família, pelo apoio incondicional ao longo de toda a minha vida. Em particular, ao meu pai e à minha mãe, pelo apoio basilar em todas as etapas da minha vida, incluindo a jornada académica, os meus profundos agradecimentos.

À Marisa. Sem o seu apoio, carinho, e amizade, demonstrados de forma desmedida e ininterrupta ao longo dos últimos anos, a conclusão desta etapa adivinhar-se-ia muito difícil. Por tudo, e pela plenitude da sua personalidade, a minha eterna gratidão.

Palavras-chave

Anisotropia plástica; Fenómenos de endurecimento cíclico; Grandes deformações; Modelos constitutivos; Algoritmos de integração; Método dos Elementos Finitos

Resumo

No presente trabalho, são desenvolvidas formulações constitutivas elastoplásticas para grandes deformações, adequadas a materiais metálicos avançados. Os principais objectivos deste estudo consistem na correcta descrição do comportamento elastoplástico, incluindo anisotropia plástica acentuada e fenómenos de endurecimento cíclico, no regime de grandes deformações, bem como o desenvolvimento de procedimentos algorítmicos eficientes para a implementação numérica dos modelos constitutivos em códigos de simulação numérica pelo Método dos Elementos Finitos. São usadas duas metodologias diferentes na derivação das formulações constitutivas de grandes deformações, nomeadamente, hipoelasticidade e hiperelasticidade.

Por um lado, relativamente ao modelo baseado em hipoelasticidade, é dada particular atenção ao desenvolvimento de algoritmos eficientes do ponto de vista computacional, considerando técnicas particulares. Por outro lado, em relação ao modelo baseado em hiperelasticidade, a possibilidade de usar qualquer critério de cedência (quadrático ou não-quadrático) e a apresentação de um procedimento inovador, que garante a correcta descrição da anisotropia na presença de grandes deformações, são destacadas. Além disso, as relações constitutivas são expressas unicamente na configuração de referência, resultando no uso de apenas variáveis simétricas de segunda ordem. Esta simetria e o uso de um algoritmo que a preserva são cruciais no que diz respeito à eficiência numérica da implementação do modelo, uma vez que reduz significativamente o espaço de armazenamento e o custo computacional de cálculo, relativamente aos modelos hiperelásticos convencionais.

Os modelos, e respectivos algoritmos de integração, são posteriormente alargados ao uso de múltiplos tensores das tensões inversas de modo a permitir uma melhor descrição dos fenómenos de endurecimento cíclico. Para tal, foi considerado um modelo reológico modificado de endurecimento cinemático e usadas variáveis de estado adicionais.

O desempenho dos modelos desenvolvidos na reprodução precisa de anisotropia plástica e fenómenos de endurecimento cíclico é avaliado através da sua implementação no código comercial Abaqus usando subrotinas de utilizador. A precisão e eficiência computacional dos modelos e algoritmos desenvolvidos são comparados entre si através de simulações de *benchmarks*. Estes *benchmarks* permitem a avaliação dos modelos na descrição de, por exemplo, defeitos na conformação de chapas metálicas, tais como a formação de orelhas e o retorno elástico, bem como a comparação da estabilidade e precisão dos algoritmos numéricos.

Keywords Plastic anisotropy; Cyclic hardening phenomena; Finite strains; Constitutive models; Integration algorithms; Finite Element Method

Abstract

In the present work, finite strain elastoplastic constitutive formulations suitable for advanced metallic materials are developed. The main goals are the correct description of the elastoplastic behaviour, including strong plastic anisotropy and cyclic hardening phenomena, in the large strain regime, as well as the development of numerically efficient algorithmic procedures for numerical implementation of the constitutive models into codes of numerical simulation by the Finite Element Method. Two different approaches are used in the derivation of the finite strain constitutive formulations, namely, hypoelasticity and hyperelasticity.

On the one hand, regarding the hypoelastic-based model, particular attention is given to the development of computationally efficient forward- and backward-Euler algorithms considering distinct techniques. On the other hand, concerning the hyperelastic-based model, the focus is on the possibility of using any (quadratic or nonquadratic) yield criteria and on a new procedure that ensures that the anisotropy is correctly described in the finite strain regime. Moreover, the constitutive relations are solely expressed in the reference configuration, hence yielding symmetric tensor-valued quantities only. This symmetry, allied to an algorithm that preserves it, is crucial for the computational efficiency of the model's implementation since it reduces the storage effort and the required solver capacities when compared to the model's standard counterparts.

For a better description of cyclic hardening phenomena, the developed models and corresponding algorithms, are extended to include several back stresses. This extension is carried out by considering a modified rheological model of nonlinear kinematic hardening and using additional state variables.

The capabilities of the developed models for accurate reproduction of the plastic anisotropy and cyclic hardening phenomena are assessed by means of their implementation into material user subroutines of the commercial code Abaqus. The accuracy and computational efficiency of the models and numerical algorithms are compared by means of simulations of benchmarks. These benchmarks allow the models' assessment in the description of, e.g., metal forming defects such as earing and springback, as well as the comparison of the stability and precision of the numerical algorithms.

Contents

List of Tables

List of Figures

List of Symbols

	Listed in order of appearance in the text
$\mathfrak{B}$	Material body
Ω	Region within $\mathbb{E}^3$ occupied by $\mathfrak{B}$ at t_0
$\boldsymbol{x}$	Position vector of a general point P
$\boldsymbol{e}_i$	Set of global Cartesian basis ($i = 1 \dots 3$)
φ	Deformation map
$\boldsymbol{X}$	Position vector of a general point P at t_0
$\boldsymbol{u}$	Displacement vector
$\boldsymbol{v}$	Spatial velocity vector
$\mathbf{F}$	Deformation gradient tensor
$\mathbf{I}$	Second-order identity tensor
$\mathbf{U}$	Right stretch tensor
$\mathbf{V}$	Left stretch tensor
$\mathbf{R}$	Rotation tensor
$\mathbf{C}$	Right Cauchy-Green tensor
$\mathbf{B}$	Left Cauchy-Green tensor
λ_A	Principal stretches ($A = 1 \dots 3$)
$\boldsymbol{c}_A$	Eigenvectors of $\mathbf{C}$ ($A = 1 \dots 3$)
$\boldsymbol{b}_A$	Eigenvectors of $\mathbf{B}$ ($A = 1 \dots 3$)
$\mathbf{l}$	Spatial velocity gradient tensor
$\mathbf{\Phi}^{\mathrm{GMN}}$	Spin tensor of the Green-McInnis-Naghdi rate
$\mathbf{d}$	Spatial rate of deformation tensor
$\mathbf{w}$	Continuum spin tensor
$\mathbf{\Phi}^{\mathrm{ZJ}}$	Spin tensor of the Zaremba-Jaumann rate
$\mathrm{d}v_0$	Infinitesimal volume in the reference configuration
$\mathrm{d}v$	Infinitesimal volume in the current configuration
J	Determinant of the deformation gradient
$\mathbf{E}^{(m)}$	Lagrangian strain tensor
$\boldsymbol{\varepsilon}^{(m)}$	Eulerian strain tensor
$\mathbf{E}^{(2)}$	Green-Lagrange strain tensor

$\boldsymbol{\sigma}$	Cauchy stress tensor
$\boldsymbol{t}$	Surface force vector per unit area
$\boldsymbol{n}$	Vector normal to a surface defined in the current configuration
$\mathbf{S}$	Second Piola-Kirchhoff stress tensor
$\mathfrak{B}_\mathrm{p}$	Subdomain of the body $\mathfrak{B}$
Ω_p	Region within $\mathbb{E}^3$ occupied by $\mathfrak{B}_\mathrm{p}$ at t_0
ρ	Density of mass
$\mathbf{A}_i$	Tensor-valued internal variables ($i = 1 \dots N$)
$\boldsymbol{a}$	Vector given by scalar-valued internal variables and/or constitutive parameters
σ_y	Yield stress
Φ	Yield potential
$\bar{\sigma}$	Effective stress
σ_i	Principal stresses ($i = 1 \dots 3$)
J_i	Invariants of the deviatoric stress tensor ($i = 1 \dots 3$)
$\mathbf{s}$	Deviatoric stress tensor
$\mathbb{P}$	Operator that maps second-order tensor-valued quantities into their deviatoric part
δ_{ij}	Kronecker's delta
a	Material parameter related to its crystallographic structure
r_θ	Directional Lankford r-value
r_b	Biaxial Lankford r-value
$\mathbb{A}$	Anisotropic tensor, that acts on the Cauchy stress tensor, of Hill's criterion
$\tilde{\mathbf{s}}$, $\tilde{\mathbf{s}}^{(k)}$	Isotropic plasticity equivalent deviatoric stress tensors
$\mathbb{L}$, $\mathbb{L}^{(k)}$	Anisotropic tensors, that act on the Cauchy stress tensor, of *Yld91* and *Yld2004-18p* criteria, respectively ($k = 1 \dots 2$)
c_i, $c_{ij}^{(k)}$	Anisotropic parameters of *Yld91* and *Yld2004-18p* criteria, respectively ($i, j = 1 \dots 6$ and $k = 1 \dots 2$)
$\bar{\varepsilon}_\mathrm{p}$	Accumulated plastic strain
$\boldsymbol{\alpha}$	Back stress tensor
K, n_H, ε_0, $\sigma_{\mathrm{y}0}$, Q, β	Material parameters that describe the isotropic hardening
$\boldsymbol{\eta}$	Relative stress tensor
c, b	Material parameters that describe the kinematic hardening, according to Armstrong-Frederick's law
λ	Plastic multiplier
E	Elastic (Young's) modulus
ψ	Helmholtz free energy per unit volume
ψ_e	Part of the Helmholtz free energy related to the energy stored in the elastic spring

ψ_{kin}	Part of the Helmholtz free energy related to the energy stored in the "hardening" spring
$\boldsymbol{\varepsilon}$	Total small strain tensor
$\boldsymbol{\varepsilon}_{\text{e}}$	Elastic small strain tensor
$\boldsymbol{\varepsilon}_{\text{p}}$	Plastic small strain tensor
$\boldsymbol{\varepsilon}_{\text{p}_\text{e}}$	"Elastic" part of the plastic small strain tensor
$\boldsymbol{\varepsilon}_{\text{p}_\text{i}}$	"Inelastic" part of the plastic small strain tensor
$\mathbb{D}$	Elastic stiffness tensor
μ_{e}	Shear modulus
Λ_{e}	Lamé constant
$\mathbb{I}$	Symmetric fourth order identity tensor
ν	Poisson ratio
R	Scalar-valued stress-like internal variable
$\mathbf{n}$	Plastic flow direction
$\mathbb{D}_{\text{ep}}$	Continuous elastoplastic tangent modulus
H	Rate of change of yield stress with accumulated plastic strain
δ	Auxiliary variable that differentiates elastic ($\delta = 0$) from elastoplastic ($\delta = 1$) behaviour
$\boldsymbol{\sigma}^{\text{trial}}$	Elastic prediction of Cauchy stress tensor
$\boldsymbol{\alpha}^{\text{trial}}$	Elastic prediction of back stress tensor
$\bar{\varepsilon}_{\text{p}}^{\text{trial}}$	Elastic prediction of accumulated plastic strain
$\beta_{\boldsymbol{\eta}}$	Ratio of the increment of stress to be corrected
r_1, $\mathbf{r}_j$	Scalar-valued and second-order tensor-valued auxiliary residua, respectively
$\mathbb{D}_{\text{ep}}^{\text{alg}}$	Consistent (algorithmic) elastoplastic tangent modulus
$\mathbb{E}$, $\mathbb{A}_1$	Fourth-order tensor-valued auxiliary variables
$\mathbf{F}_{\text{e}}$	Elastic deformation gradient tensor
$\mathbf{F}_{\text{p}}$	Plastic deformation gradient
$\overset{\nabla}{(\bullet)}^{\star}$	Objective rate operator
$\boldsymbol{\Omega}^{\star}$	Skew-symmetric spin tensor related to the objective rate $\overset{\nabla}{(\bullet)}^{\star}$
$\mathbf{Q}$	Rotation tensor from the locally rotating configuration to the spatial configuration
$\mathbf{d}_{\text{e}}$	Elastic rate of deformation tensor
$\mathbf{d}_{\text{p}}$	Plastic rate of deformation tensor
$\mathbf{Q}_{\Delta}^{\star}$, $\mathbf{Q}_{\delta}^{\star}$	Incremental rotations from the configurations at n and $n+\alpha$ to the configuration at $n+1$, respectively
$\mathbf{F}_{\text{p}_\text{e}}$	"Elastic" part of the plastic deformation gradient tensor
$\mathbf{F}_{\text{p}_\text{i}}$	"Inelastic" part of the plastic deformation gradient tensor
$\mathbf{C}_{\text{e}}$	Elastic right Cauchy-Green deformation tensor

$\mathbf{C}_{\mathrm{p_e}}$	Elastic right Cauchy-Green deformation tensor related to $\mathbf{F}_{\mathrm{p_e}}$
$\mathbf{d}_{\mathrm{p_i}}$	Symmetric part of $\dot{\mathbf{F}}_{\mathrm{p_i}}\mathbf{F}_{\mathrm{p_i}}^{-1}$
$\mathbf{C}_{\mathrm{p}}$	Plastic right Cauchy-Green deformation tensor
$\mathbf{M}$	Mandel stress tensor
$\mathbf{M}_{\mathrm{kin}}$	"Mandel" stress tensor related to kinematic hardening
$\mathbf{X}$	Back stress tensor in the reference configuration
$\boldsymbol{\chi}$	Back stress tensor in the intermediate configuration
$\boldsymbol{\Sigma}$	Relative stress tensor in the intermediate configuration
$\mathbf{Y}$	Relative stress tensor in the reference configuration
$\mathbf{Y}_{\mathrm{kin}}$	Representation of $\mathbf{M}_{\mathrm{kin}}$ in the reference configuration
$\mathbf{C}_{\mathrm{p_i}}$	Plastic right Cauchy-Green deformation tensor related to $\mathbf{F}_{\mathrm{p_i}}$
$\mathbf{n}_{\mathbf{Y}}$	Derivative of the yield potential with regard to $\mathbf{Y}$
$\bar{\mathbb{A}}$, $\bar{\mathbb{L}}^{(k)}$	Anisotropic tensors that act in the reference configuration
A_{D}	Scalar-valued auxiliary variable
$\mathbf{A}_{\mathrm{N}}$, $\mathbf{f}$, $\mathbf{f}_{\mathrm{kin}}$	Second-order tensor-valued auxiliary variables
$\mathbf{U}_{\mathrm{p}}$	Plastic stretch tensor
$\mathbf{U}_{\mathrm{p_i}}$	Stretch tensor related to $\mathbf{C}_{\mathrm{p_i}}$

Chapter 1

Introduction

1.1 Motivation

The production of metallic components employs procedures that can be classified into four groups, namely: casting, machining, forming, and consolidating smaller pieces (by, e.g., welding or powder metallurgy). Metal forming processes make use of the fact that metals can plastically deform without degradation of their main properties. These processes are usually subdivided into four categories such as squeezing, bending, shearing, and drawing. Drawing of sheet materials (metals) is the process of interest in this work, due to its several benefits. It allows for the production of very diversified industrial items, ranging from simple pots and pans for cooking, sinks, and containers to complex automotive parts such as panels and gas tanks, with a fast production rate and, in some cases, very small waste of raw material.

The process consists of stretching a flat metal sheet or plate into the desired three-dimensional part, with a depth of several times the initial thickness of the initial material. The sheet is mounted between a die and a punch, then the punch is moved downwards (or upwards, depending on the relative position of the tools) forcing the material to flow into the die cavity, and thus shaping the material according to the design of the mating punch-die set. Usually, in order to prevent the formation of wrinkles in the sheet's flange during deformation, the blank is clamped down by a blank holder over the die.

Drawing of sheet metals can be classified as hot or cold drawing. In one hand, hot drawing is a non-isothermal forming process where forming and quenching take place in the same forming step. It is usually chosen to produce parts of simple geometry, from relatively thick metal sheets but with high strength and minimum springback. In hot drawing, the material usually undergoes considerable thinning as it flows through the tools. On the other hand, cold drawing is performed at room temperature, using relatively thin metal sheets, which thickness changes very little comparatively to hot drawing. Although cold drawing is limited by the lower formability of the materials (relatively to hot drawing) and the final parts usually undergo considerable springback, it is one of the most important cold-working operations due to the high variety, in shape and size, of parts that can be produced by this

process, allied to its rapid press cycle times.

When the depth of a stamped part is lesser than its "diameter", it is generally designated as shallow drawing. Otherwise, it is termed deep drawing. In deep drawing, thinning is usually higher, and to achieve the final part's shape several successive drawing steps with progressive dies may be required.

The production of metallic parts by deep drawing is usually preceded by several expensive empirical trial-and-error attempts to design proper tools and stablish adequate features of the process (e.g., lubrication and blank holder force), in order to produce the parts with the required performance (e.g., structural stiffness), fulfilling the dimensional tolerances (which, for example, can be crucial for assembly), and to avoid defects in the final part such as undesired wrinkling, earing, tearing, thinning, springback, and lack or excess of material. The constantly increasing demand for faster and more economical manufacturing allied to the fast development of computational systems, in both hardware and software, has been stimulating the development and production of new parts consistently assisted by virtual tools such as Computer Aided Design (CAD) and Computer Aided Manufacturing (CAM).

The numerical simulation of sheet metal forming, mainly based on the Finite Element Method (FEM), is increasingly being used as a virtual tool in the design of parts of high complexity and performance, with reasonable accuracy and computation time. It is continuously replacing the traditional, expensive and time-consuming, experimental trial-and-error tests by cheaper and faster computational trial-and-error tests using numerical simulations based on FEM. This is not only due to the fact that these computational tests allow the reduction of costs and time relatively to traditional ones, but also the possibility of production of parts with improved quality and performance. Thus, in sheet metal forming industry, numerical simulation has been extensively employed to shorten the design cycle, to reduce the preproduction costs in the design of a new product (due to the high cost and time required to produce metal forming tools), and to assist the design of parts with optimized performance.

The outcome from numerical simulation of sheet metal forming processes is influenced by several features such as the element technology, the contact model, and the material's constitutive model. The latter is crucial, since without a proper constitutive model the final deformed part's shape can not be well predicted, the same for possible defects such as earing, thinning, springback, and tearing. Moreover, during the production of metallic parts by forming, the material experiences large displacements, rotations, and deformations, implying the consideration of material models that encompasses these nonlinearities. Several commercial software codes of numerical simulation, based on the Finite Element Method exist nowadays specifically oriented (or suitable) to sheet metal forming processes. These codes include, usually, a wide database of constitutive models, but is the user's responsibility to select the proper constitutive model to represent the material's behaviour. When an appropriate constitutive model is not available in the software's database, the user has to develop and algorithmically implement a proper one, which often represents a lengthy, difficult, and error-prone task.

The increasing use of advanced materials in industrial applications has stimulated demand for better constitutive descriptions that enable the accurate modelling of complex plastic behaviour at finite strains. Generally, these materials, such as aluminium alloys and advanced high-strength steels, exhibit some inherent planar anisotropy and/or complex cyclic hardening phenomena.

Sheet metal anisotropy is generally related to the presence of preferred orientations on the crystal texture, coming from the thermo-mechanical process associated to the production of metallic sheets (rolling process) and from the plastic deformation during stamping operations. Nevertheless, the assumption that the deformation-induced anisotropy is small and negligible comparatively to the initial anisotropy (induced by rolling operations and heat treatment) is usually adopted. In sheet metal forming processes, anisotropic yielding and flowing are directly associated to the occurrence of earing and thinning.

After the forming step, the metallic parts undergo elastic recovery and springback when they are unloaded and removed from the tooling. The springback, which is related to elastically-driven changes of the part's shape, is dependent on the internal stress distribution within the metal blank. Thus, a correct computation of the material's stress-strain response is required to correctly predict the amount of springback. In addition, during the unloading of the part, some material points in the continuum can experience reverse loading. Some materials exhibit the so-called Bauschinger effect, which describes the reduction of the yield stress upon reverse loading after the occurrence of plastic deformation during the initial loading, hence affecting the amount of springback that occurs. This way, a kinematic hardening model, capable of describing the Bauschinger effect, among with other cyclic hardening phenomena, is required when a good prediction of the springback is desired.

1.2 Objectives

The present work is related to the study, development, and algorithmic implementation of advanced constitutive models, providing a reliable representation of complex plastic behaviour of advanced metallic materials. Moreover, aiming for the correct description of these materials' behaviour in industrial applications, such as in sheet metal forming, models that encompass large deformations and rotations are considered.

Preceding the development of any constitutive model, a thorough study of the state-of-the-art has to be carried out. Here, focus will be given to those models in the literature that comprise plastic yielding anisotropy, by means of anisotropic yield criteria, and/or cyclic hardening phenomena. Based on that search, a constitutive model grounded on the infinitesimal theory is developed. The study, development, and improvement of accurate, efficient, and robust algorithms for the numerical implementation of the small strain model is also considered.

The development of constitutive models that account for large deformations and rotations is carried out by following both hypoelastic and hyperelastic approaches. Whereas the

hypoelastic approach is studied in this work due to its simplicity, efficiency in metallic applications, and vast incorporation into material databases of commercial FEM codes, a model based on the hyperelastic approach is developed due to its theoretically sounder background that, among others advantages, allows its application in a broader range of materials, such as polymers. Efficient numerical methodologies are considered in the algorithmic implementation of the developed finite strain constitutive models, which represent different challenges depending on the approach (hypoelastic- or hyperelastic-based) in question.

The aforementioned models are initially derived following the combined nonlinear hardening law (assumed as standard nowadays), based on the association of nonlinear isotropic hardening with the nonlinear kinematic hardening law of Armstrong and Frederick (1966). Aiming at a better description of complex cyclic hardening phenomena displayed by advanced materials, these models and corresponding algorithmic procedures are adapted, so their kinematic hardening law is improved to include several back stress components. Whereas the employment of such hardening law in the context of hypoelasticity has been presented in several works in the literature, its use in the context of hyperelasticity is very rare in published works. The hyperelastic-based model, considering this hardening law and developed within this Thesis, follows a different approach from the literature, by representing a continuum mechanical extension of a modified rheological model of the Armstrong-Frederick kinematic hardening law.

Also within the objectives of this work is the numerical implementation of the aforementioned algorithmic procedures into material user subroutines of in-house and commercial codes of numerical simulation by the FEM. Doing this way, the numerical performance, accuracy, and robustness of the developed numerical algorithms and corresponding constitutive models can be assessed and compared by means of both academic and industry-relevant numerical examples. An exhaustive analysis is carried out by comparing the obtained results with experimental and numerical data presented in the literature for numerical benchmarks where plastic anisotropy and/or cyclic hardening phenomena have a strong effect in the deformation process.

1.3 Reading guide

Besides this chapter, where after a description of this work's motivation the main objectives of the Thesis are established, the present text is divided in 7 more chapters, organized as follows:

Chapter 2 The basal topics of continuum mechanics, which are the foundation for the material constitutive models developed in Chapters 4 and 5, are presented. Also, it is briefly indicated the basic fundamentals of thermodynamics on which the FEM and the studied constitutive models are based;

Chapter 3 The concepts inherent to computational plasticity are presented. Firstly, a brief

comparison between crystallographic and phenomenological models is given and the choice of using the phenomenological approach in this work is sustained. Secondly, a state-of-the-art of isotropic and anisotropic yield functions suitable for metallic materials is presented. Thirdly, the most common cyclic hardening phenomena are enumerated and the state-of-the-art of hardening laws that enable the description of such behaviours is discussed. Particular attention is given to the classical and modified rheological models of Armstrong-Frederick kinematic hardening, since they are the bases to the constitutive models presented in Chapters 4 and 5;

Chapter 4 A small strain elastoplastic model that represents a continuum mechanical extension of the rheological model of Armstrong-Frederick kinematic hardening to three-dimensional conditions is developed. For the sake of generality, the derivation of the model allows the inclusion of any isotropic or anisotropic (quadratic or nonquadratic) yield function. The algorithmic treatment of the constitutive equations for numerical implementation into codes of numerical simulation is given. Here, the classical forward-Euler and backward-Euler approaches are adapted to the present model and enhanced in order to improve their numerical efficiency;

Chapter 5 Elastoplastic models that account for finite strains and rotations are discussed in this chapter. Firstly, the state-of-the-art of finite strain hypoelastic- and hyperelastic-based models is presented.

Secondly, the constitutive model presented is Chapter 4 is extended to finite strains and rotations in the context of hypoelasticity. Preceding the derivation of the hypoelastic-based model, the concept of objectivity is addressed. The employment of objective integration algorithms for hypoelastic-based models is also discussed. An algorithm that preserves the structure and the inherent simplicity of those for small strain constitutive models, as discussed in Chapter 4, is adapted to the constitutive model in study.

Thirdly, a hyperelastic-based model, that is suitable for any quadratic or nonquadratic yield function and based on the rheological model of Armstrong-Frederick kinematic hardening, is developed. The followed approach express all the constitutive equations in the reference configuration, resulting on symmetric tensor-valued quantities only. Overcoming the limitation to quadratic yield criteria displayed by most hyperelastic-based models in the literature, a new procedure is proposed to ensure that the material's anisotropic axes follow the rigid body motions of the material. For numerical implementation purposes, the algorithmic procedure used to numerically integrate the evolution equations is presented. A backward-Euler scheme based on the exponential map is adapted to the presented hyperelastic-based model.

Fourthly, the kinematic hardening law of the hyperelastic-based model is enhanced by considering a modified rheological model of Armstrong-Frederick kinematic hardening, thus taking into account several back stress components. This is accomplished

by taking several multiplicative decompositions of the plastic part of the deformation gradient into account, resulting on multiple strain-like tensor-valued internal variables that characterize the complex kinematic hardening law. This modification follows a distinct approach comparatively to the few works present in the literature that encompass this hardening law. At the end, the algorithmic procedure is adapted to consider the modifications on the constitutive model;

Chapter 6 A procedure used to identify the material's constitutive parameters employed by the developed constitutive models is presented. This parameters' identification procedure is based on an inverse methodology grounded on an optimization algorithm. The assessment of the presented procedure is carried out by applying it to a virtual (fictitious) material. Then, the presented procedure is used to identify the constitutive parameters of some of the materials used in the numerical simulations of Chapter 7;

Chapter 7 The results obtained from several numerical simulations are presented, by implementing the analysed constitutive models in material user subroutines of a commercial FEM code. Firstly, the correctness of the user subroutines' implementation is assessed. Secondly, some fundamental limitations of the hypoelastic- and hyperelastic-based models are analysed. Thirdly, a comparison of the accuracy and stability of the integration algorithms related to the hypoelastic-based model is given. Fourthly, the performance of the presented constitutive models and numerical algorithms is analysed in industry-relevant benchmarks of sheet metal forming. Finally, the hypoelastic- and hyperelastic-based formulations are compared by means of a numerical example where finite elastic strains occur;

Chapter 8 The main conclusions of this Thesis, along with its contribution to the present literature, are presented. Some perspectives of future developments, giving continuity to the present work, are also outlined.

Chapter 2

Topics of continuum mechanics and thermodynamics

In this chapter the fundamental topics of continuum mechanics, which constitute the foundation of the constitutive models developed in Chapters 4 and 5, are presented, namely the kinematics of continuum bodies as well as strain and stress measures. Furthermore, the basic concepts of thermodynamics, in which the FEM and the studied constitutive models are based, are briefly covered in this chapter.

2.1 Kinematics

2.1.1 Body motion and deformation gradient

Let $\mathfrak{B}$ be a material body which occupies the region Ω and consists of a continuous set of particles defined by the spatial points P (see Fig. 2.1). Every point P is represented in the three-dimensional Euclidean space, $\mathbb{E}^3$, by means of a vector, $\boldsymbol{x}(t) \in \mathbb{E}^3$, that is formed by the point's coordinates with respect to a global Cartesian basis, $\boldsymbol{e}_i$, with $i = 1 \dots 3$. The evolution of each point's position with time is defined by a smooth one-to-one function designated by deformation map, φ, according to

$$\boldsymbol{x} = \varphi(\boldsymbol{X}, t), \tag{2.1}$$

where $\boldsymbol{X}$ represents the point's position at t_0.

This way, $\varphi(\Omega, t)$ denotes the region occupied by $\mathfrak{B}$ at t, which is called current or Eulerian configuration. The motion of $\mathfrak{B}$, given by φ, is commonly defined regarding a fixed reference or Lagrangian configuration. For convenience purposes the reference configuration is usually chosen to be the one at t_0 (undeformed configuration).

The displacement of a material particle between the reference and the current configurations is given by the vector field

$$\boldsymbol{u} = \varphi(\boldsymbol{X}, t) - \boldsymbol{X}, \tag{2.2}$$

as represented in Fig. 2.1. The body $\mathfrak{B}$ may undergo combined stretch and rigid deformations. Rigid deformations occur when the deformation, in the time interval $[t_0, t]$, preserves the distances between all material particles of $\mathfrak{B}$ and can be characterized by rigid translation, rotation, or the combination of both. The time derivative of the point's position in the current configuration provides the spatial velocity,

$$\boldsymbol{v} = \frac{\partial \boldsymbol{x}(\boldsymbol{X}, t)}{\partial t}. \tag{2.3}$$

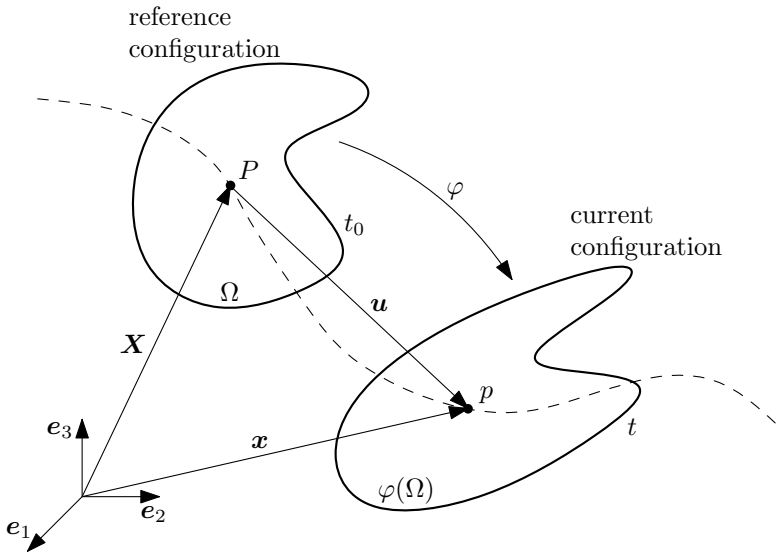

Figure 2.1: Schematic representation of the motion of a continuum body $\mathfrak{B}$.

The deformation gradient, $\mathbf{F}$, of the motion φ, is a key quantity in finite deformation analysis and is expressed by

$$\mathbf{F} = \frac{\partial \boldsymbol{x}(\boldsymbol{X}, t)}{\partial \boldsymbol{X}} = \frac{\partial \varphi(\boldsymbol{X}, t)}{\partial \boldsymbol{X}} = \mathbf{I} + \frac{\partial \boldsymbol{u}(\boldsymbol{X}, t)}{\partial \boldsymbol{X}} = \mathbf{I} + \nabla \boldsymbol{u}, \tag{2.4}$$

where $I_{ij} = \delta_{ij}$ is the second-order identity tensor and $\nabla(\bullet)$ is the gradient operator with regard to $\boldsymbol{X}$. As represented in Fig. 2.2, the deformation gradient is the linear operator that maps infinitesimal material fibres $\mathrm{d}\boldsymbol{X}$, which connects two neighbouring material particles $\boldsymbol{X}$ and $\boldsymbol{X} + \mathrm{d}\boldsymbol{X}$, into their counterparts $\mathrm{d}\boldsymbol{x}$ at t, i.e.,

$$\mathrm{d}\boldsymbol{x} = \mathbf{F}\mathrm{d}\boldsymbol{X}. \tag{2.5}$$

From Equation 2.4 it is trivially concluded that for $t = t_0$ the deformation gradient equals the second-order identity tensor, i.e., $\mathbf{F} = \mathbf{I}$, since the current configuration corresponds to the reference one. Moreover, the deformation gradient is not able to represent rigid body translations, because $\partial \boldsymbol{u}(\boldsymbol{X}, t)/\partial \boldsymbol{X} = \mathbf{0}$.

Let $\mathbf{A}$ be a second-order tensor-valued quantity defined in the reference configuration. It

is mapped into the current configuration through the deformation gradient according to

$$\mathbf{a} = \mathbf{F}\mathbf{A}\mathbf{F}^{\mathrm{T}}. \tag{2.6}$$

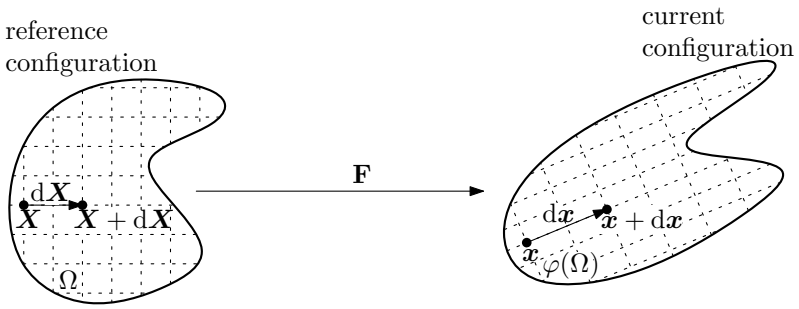

Figure 2.2: Schematic representation of the deformation gradient.

2.1.2 Polar decomposition

Considering that the deformation gradient provides information about stretching and rigid body rotations and such rotations do not affect the shape or size of the body $\mathfrak{B}$, the use of the polar decomposition theorem to $\mathbf{F}$ is particularly interesting and follows

$$\mathbf{F} = \mathbf{R}\mathbf{U} = \mathbf{V}\mathbf{R}, \tag{2.7}$$

where the symmetric tensors $\mathbf{U}$ and $\mathbf{V}$ are the right and left stretch tensors, respectively, and the orthogonal tensor $\mathbf{R}$ is the local rotation tensor, that possesses the properties: $\mathbf{R}^{-1} = \mathbf{R}^{\mathrm{T}}$ and $\det(\mathbf{R}) = 1$. These decompositions are schematically represented in Fig. 2.3, introducing two local configurations. They are denoted as local because the "neighbourhood points" do not "fit together" unless the body is strictly subjected to rigid deformations (Simo and Hughes, 1998). The relation between the right and left stretch tensors is given by

$$\mathbf{V} = \mathbf{R}\mathbf{U}\mathbf{R}^{\mathrm{T}}. \tag{2.8}$$

Since $\mathbf{U}$ and $\mathbf{V}$ encompass only the stretch part of $\mathbf{F}$, they are very important in the definition of strain measures (see Section 2.2). Moreover, from $\mathbf{U}$ and $\mathbf{V}$ the right and left Cauchy-Green strain tensors, $\mathbf{C}$ and $\mathbf{B}$, respectively, are defined by

$$\mathbf{C} = \mathbf{U}^2 = \mathbf{F}^{\mathrm{T}}\mathbf{F} \text{ and } \mathbf{B} = \mathbf{V}^2 = \mathbf{F}\mathbf{F}^{\mathrm{T}}, \tag{2.9}$$

respectively. Considering these expressions, the stretch tensors, $\mathbf{U}$ and $\mathbf{V}$, can be obtained from

$$\mathbf{U} = \sqrt{\mathbf{C}} \text{ and } \mathbf{V} = \sqrt{\mathbf{B}}, \tag{2.10}$$

respectively. Through the spectral decomposition, $\mathbf{C}$ and $\mathbf{B}$ can be represented following

$$\mathbf{C} = \sum_{A=1}^{3} \lambda_A^2 \boldsymbol{c}_A \otimes \boldsymbol{c}_A \text{ and } \mathbf{B} = \sum_{A=1}^{3} \lambda_A^2 \boldsymbol{b}_A \otimes \boldsymbol{b}_A, \tag{2.11}$$

respectively, where λ_A^2 are the eigenvalues of $\mathbf{C}$ and $\mathbf{B}$, and $\boldsymbol{c}_A$ and $\boldsymbol{b}_A$ are the corresponding eigenvectors. Introducing Equation 2.8 into these equations, the relation $\boldsymbol{b}_A = \mathbf{R}\boldsymbol{c}_A$ is obtained. Taking into account the coaxiality of $\mathbf{U}$ and $\mathbf{C}$, and $\mathbf{V}$ and $\mathbf{B}$, respectively, the stretch tensors can be attained from

$$\mathbf{U} = \sum_{A=1}^{3} \lambda_A \boldsymbol{c}_A \otimes \boldsymbol{c}_A \text{ and } \mathbf{V} = \sum_{A=1}^{3} \lambda_A \boldsymbol{b}_A \otimes \boldsymbol{b}_A. \tag{2.12}$$

Due to these relations, λ_A are also named as principal stretches.

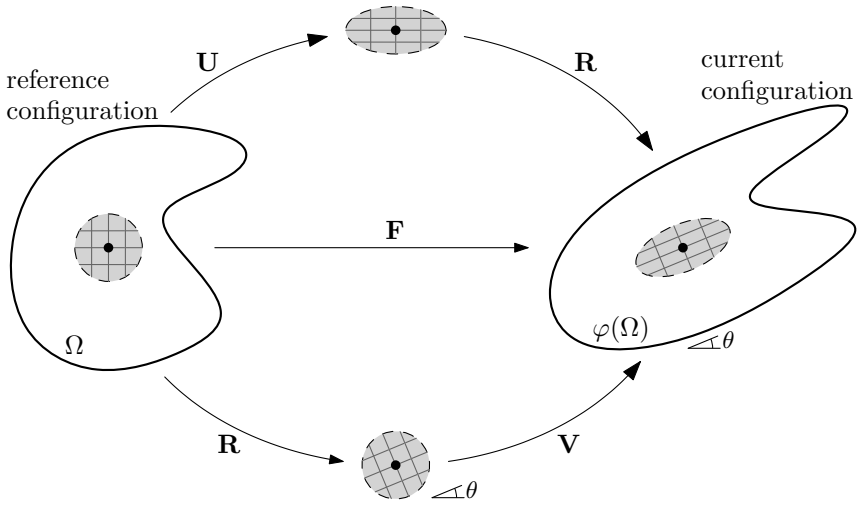

Figure 2.3: Schematic representation of the polar decomposition of the deformation gradient.

2.1.3 Spatial rate of deformation and continuum spin tensor

The spatial velocity gradient, $\mathbf{l}$, is obtained by

$$\mathbf{l} = \frac{\partial \boldsymbol{v}}{\partial \boldsymbol{x}} = \frac{\partial}{\partial t}\left(\frac{\partial \boldsymbol{x}}{\partial \boldsymbol{X}}\right)\frac{\partial \boldsymbol{X}}{\partial \boldsymbol{x}} = \dot{\mathbf{F}}\mathbf{F}^{-1}, \tag{2.13}$$

where the relations

$$\dot{\mathbf{F}} = \mathbf{R}\dot{\mathbf{U}} + \dot{\mathbf{R}}\mathbf{U} \text{ and} \tag{2.14}$$

$$\mathbf{F}^{-1} = (\mathbf{R}\mathbf{U})^{-1} = \mathbf{U}^{-1}\mathbf{R}^{-1}, \tag{2.15}$$

hold. Therefore, it is possible to derive $\mathbf{l}$ as

$$\mathbf{l} = \dot{\mathbf{R}}\mathbf{R}^{\mathrm{T}} + \mathbf{R}\dot{\mathbf{U}}\mathbf{U}\mathbf{R}^{\mathrm{T}}. \tag{2.16}$$

The first term of the right-hand side of this equation is commonly denoted as the rotation rate tensor (or angular velocity of the material) and physically represents the rate of rigid-body rotation at a given material point about a predefined axis (Dienes, 1979). As indicated in Section 5.2.1, this skew-symmetric tensor is used as the spin tensor in the Green-McInnis-Naghdi objective rate, i.e., $\boldsymbol{\Phi}^{\mathrm{GMN}} = \dot{\mathbf{R}}\mathbf{R}^{\mathrm{T}}$.

The spatial velocity gradient can also be additively decomposed into a symmetric, $\mathbf{d}$, and a skew-symmetric, $\mathbf{w}$, parts, i.e.,

$$\mathbf{l} = \mathbf{d} + \mathbf{w}, \tag{2.17}$$

with

$$\mathbf{d} = \frac{1}{2}(\mathbf{l} + \mathbf{l}^{\mathrm{T}}) = \mathbf{R}\mathrm{sym}(\dot{\mathbf{U}}\mathbf{U})\mathbf{R}^{\mathrm{T}} = \mathbf{R}\left(\frac{1}{2}\dot{\mathbf{C}}\right)\mathbf{R}^{\mathrm{T}} \text{ and} \tag{2.18}$$

$$\mathbf{w} = \frac{1}{2}(\mathbf{l} - \mathbf{l}^{\mathrm{T}}) = \dot{\mathbf{R}}\mathbf{R}^{\mathrm{T}} + \mathbf{R}\mathrm{skew}(\dot{\mathbf{U}}\mathbf{U})\mathbf{R}^{\mathrm{T}}, \tag{2.19}$$

where $\mathbf{d}$ is the spatial rate of deformation or stretching tensor and $\mathbf{w}$ is the continuum spin or vorticity tensor.

The continuum spin tensor, $\mathbf{w}$, is used as the spin tensor in the corotational objective rate of Zaremba-Jaumann, i.e., $\boldsymbol{\Phi}^{\mathrm{ZJ}} = \mathbf{w}$ (see Section 5.2.1), and physically represents the rate of rotation of the principal axes of the spatial rate of deformation, $\mathbf{d}$. Moreover, $\mathbf{w}$ has no contribution for straining. When the principal directions of $\mathbf{U}$ and $\dot{\mathbf{U}}$ are kept the same, the tensor $\dot{\mathbf{U}}\mathbf{U}$ is symmetric, hence the relation $\mathbf{w} = \dot{\mathbf{R}}\mathbf{R}^{\mathrm{T}}$ holds, therefore $\boldsymbol{\Phi}^{\mathrm{ZJ}} = \boldsymbol{\Phi}^{\mathrm{GMN}}$.

2.1.4 Determinant of the deformation gradient

Here, an infinitesimal volume defined by $\mathrm{d}\boldsymbol{A}$, $\mathrm{d}\boldsymbol{B}$, and $\mathrm{d}\boldsymbol{C}$ with the corresponding origins at point P, at a position $\boldsymbol{X}$ in the reference configuration, is considered (see Fig. 2.4). The infinitesimal volume is denoted by $\mathrm{d}v_0$ and given by

$$\mathrm{d}v_0 = (\mathrm{d}\boldsymbol{A} \times \mathrm{d}\boldsymbol{B}) \cdot \mathrm{d}\boldsymbol{C}. \tag{2.20}$$

Applying the deformation map φ to the material body, the deformed infinitesimal volume, $\mathrm{d}v$, is obtained by

$$\mathrm{d}v = (\mathbf{F}\mathrm{d}\boldsymbol{A} \times \mathbf{F}\mathrm{d}\boldsymbol{B}) \cdot \mathbf{F}\mathrm{d}\boldsymbol{C}. \tag{2.21}$$

Hence, the local volume change ratio is determined by

$$\frac{\mathrm{d}v}{\mathrm{d}v_0} = \frac{(\mathbf{F}\mathrm{d}\boldsymbol{A} \times \mathbf{F}\mathrm{d}\boldsymbol{B}) \cdot \mathbf{F}\mathrm{d}\boldsymbol{C}}{(\mathrm{d}\boldsymbol{A} \times \mathrm{d}\boldsymbol{B}) \cdot \mathrm{d}\boldsymbol{C}} = J, \tag{2.22}$$

where J is the determinant of the deformation gradient, i.e., $J = \det\mathbf{F}$. The physical meaning of J implies that it is always non-null since the infinitesimal volume would collapse to a point if $J = 0$. Moreover, considering that $J = 1$ for the reference configuration and J would have to "pass" by 0 to reach a configuration where it would present a negative value, yields $J > 0$ regardless to φ.

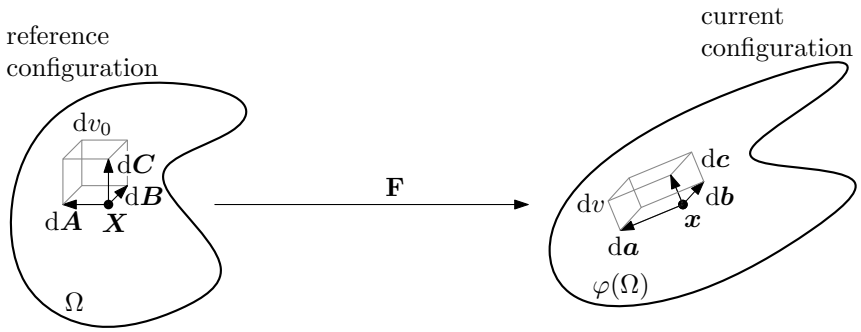

Figure 2.4: Schematic representation of the volume change.

2.2 Strain measures

The polar decomposition of the deformation gradient (see Section 2.1.2) has been used to distinguish pure rigid rotations and pure stretching. The neighbourhood region of P is said to be unstrained when the distances between the material particles are kept constant (in pure rigid deformations) or strained if otherwise (when stretching, characterized by $\mathbf{U}$ and $\mathbf{V}$, occurs).

However, it has not been yet defined a measure to quantify straining. Thus, it is required to introduce a strain measure to rate how much $\mathbf{U}$ and $\mathbf{V}$ deviate from $\mathbf{I}$. There is not a unique strain measure to quantify straining, and the definition of strain measure is still somewhat arbitrary, with its specific choice being prescribed by mathematical and physical convenience (Souza Neto *et al.*, 2008).

A natural way to quantify straining is by using the right and left Cauchy-Green tensors, which can be alternatively represented following

$$\mathbf{C} = \mathbf{I} + \nabla\boldsymbol{u} + (\nabla\boldsymbol{u})^{\mathrm{T}} + (\nabla\boldsymbol{u})^{\mathrm{T}}\nabla\boldsymbol{u} \text{ and} \tag{2.23}$$

$$\mathbf{B} = \mathbf{I} + \nabla\boldsymbol{u} + (\nabla\boldsymbol{u})^{\mathrm{T}} + \nabla\boldsymbol{u}(\nabla\boldsymbol{u})^{\mathrm{T}}, \tag{2.24}$$

respectively. However, it can be seen that these strain measures are not zero for unstrained regions.

A family of Lagrangian strain tensors, based on the right stretch tensor, $\mathbf{U}$, has been

defined by Seth (1962) and Hill (1978), according to

$$\mathbf{E}^{(m)} = \begin{cases} \dfrac{1}{m}(\mathbf{U}^m - \mathbf{I}) & \text{if } m \neq 0 \\ \ln(\mathbf{U}) & \text{if } m = 0 \end{cases} \tag{2.25}$$

where m is a real number. According to the chosen value for the exponent m, some particular strain measures of this family can be given, such as

Green-Lagrange	$m = 2$,
Biot	$m = 1$,
Henchy or logarithmic	$m = 0$,
Swainger	$m = -1$,
Almansi	$m = -2$, and
No strain	$m = -\infty$.

By means of the spectral decomposition (compare with Equation 2.12), the Lagrangian strain tensors can be rewritten as

$$\mathbf{E}^{(m)} = \begin{cases} \displaystyle\sum_{A=1}^{3} \frac{1}{m}(\lambda_A^m - 1)\boldsymbol{c}_A \otimes \boldsymbol{c}_A & \text{if } m \neq 0 \\ \displaystyle\sum_{A=1}^{3} \ln(\lambda_A)\boldsymbol{c}_A \otimes \boldsymbol{c}_A & \text{if } m = 0 \end{cases} \tag{2.26}$$

The adopted term "Lagrangian" is then justified by its representation based on the Lagrangian triad. When local rigid deformation, i.e., $\mathbf{F} = \mathbf{R}$ and $\mathbf{U} = \mathbf{I}$, is considered, for any m it yields $\mathbf{E}^{(m)} = \mathbf{0}$.

Analogously to $\mathbf{E}^{(m)}$, based on the left stretch tensor, $\mathbf{V}$, the Eulerian counterpart of the family of Lagrangian strain measures is defined by

$$\boldsymbol{\varepsilon}^{(m)} = \begin{cases} \dfrac{1}{m}(\mathbf{V}^m - \mathbf{I}) & = \displaystyle\sum_{A=1}^{3} \frac{1}{m}(\lambda_A^m - 1)\boldsymbol{b}_A \otimes \boldsymbol{b}_A & \text{if } m \neq 0 \\ \ln(\mathbf{V}) & = \displaystyle\sum_{A=1}^{3} \ln(\lambda_A)\boldsymbol{b}_A \otimes \boldsymbol{b}_A & \text{if } m = 0 \end{cases} \tag{2.27}$$

Similarly to relation 2.8, the Eulerian and Lagrangian strain tensors are related by

$$\boldsymbol{\varepsilon}^{(m)} = \mathbf{R}\mathbf{E}^{(m)}\mathbf{R}^{\mathrm{T}}. \tag{2.28}$$

An important strain measure used in the hyperelastic-based constitutive model presented in Chapter 5 is, for instance, the Green-Lagrange strain, which, taking Equation 2.23a into

account, can be alternatively rewritten as

$$\mathbf{E}^{(2)} = \frac{1}{2}[\nabla \boldsymbol{u} + (\nabla \boldsymbol{u})^{\mathrm{T}} + (\nabla \boldsymbol{u})^{\mathrm{T}} \nabla \boldsymbol{u}]. \tag{2.29}$$

2.3 Stress measures

In order to mathematically quantify the forces at the boundary and within a body, the concept of stress measure is used, dimensions of which being force per unit area. One of the most used stress measures is the Cauchy stress tensor, denoted as $\boldsymbol{\sigma}$. It is a second-order tensor-valued quantity given by the linear relation of a surface force $\boldsymbol{t}$ that acts across any surface characterized by a normal vector $\boldsymbol{n}$ in the current (deformed) configuration, per unit area also defined in the current configuration, according to

$$\boldsymbol{t} = \boldsymbol{\sigma} \boldsymbol{n}. \tag{2.30}$$

From the balance of angular momentum results the symmetry of $\boldsymbol{\sigma}$, i.e., $\boldsymbol{\sigma} = \boldsymbol{\sigma}^{\mathrm{T}}$ (see Section 2.4.2).

Considering the Cauchy stress tensor, the Kirchhoff stress tensor, $\boldsymbol{\tau}$, which is frequently used in continuum mechanics, can be defined as

$$\boldsymbol{\tau} = J\boldsymbol{\sigma}. \tag{2.31}$$

Owing to the symmetry of the Cauchy stress, the Kirchhoff stress is also a symmetric tensor. For incompressible deformations, i.e., $J = 1$, the Cauchy and Kirchhoff stress tensors provide the same value. Thus, in metal plasticity, where elastic strains are assumed to be small and the plastic behaviour is considered incompressible, the approximation $\boldsymbol{\sigma} \approx \boldsymbol{\tau}$ is commonly employed.

The first Piola-Kirchhoff (or nominal) stress tensor, $\mathbf{P}$, is obtained from the counterpart of the surface force $\boldsymbol{t}$ that acts on surfaces defined in the current configuration per unit area defined in the reference configuration. This stress measure is related to the Cauchy and Kirchhoff stress tensors following

$$\mathbf{P} = J\boldsymbol{\sigma}\mathbf{F}^{-\mathrm{T}} = \boldsymbol{\tau}\mathbf{F}^{-\mathrm{T}}. \tag{2.32}$$

In contrast to the tensors $\boldsymbol{\sigma}$ and $\boldsymbol{\tau}$, the second-order tensor $\mathbf{P}$ is generally nonsymmetric.

Finally, the second Piola-Kirchhoff stress tensor, $\mathbf{S}$, is the representation of the Kirchhoff stress tensor in the reference configuration. It is obtained from the relations

$$\mathbf{S} = J\mathbf{F}^{-1}\boldsymbol{\sigma}\mathbf{F}^{-\mathrm{T}} = \mathbf{F}^{-1}\boldsymbol{\tau}\mathbf{F}^{-\mathrm{T}}. \tag{2.33}$$

Due to the symmetry of $\boldsymbol{\sigma}$, the second Piola-Kirchhoff stress tensor is also a symmetric tensor. As for the strain measures, many other stress measures can be defined, such as the Mandel

stress tensor discussed in Chapter 5.

For all the stress tensors indicated before there is an associated rate of deformation tensor. The conjugated stress-rate of deformation pairs are obtained considering that they provide the same power per unit volume of the reference configuration, i.e., they obey the following stress-power relationships

$$\begin{aligned} \boldsymbol{\tau} : \mathbf{d} &= \mathbf{P} : \dot{\mathbf{F}} \\ &= \mathbf{S} : \dot{\mathbf{E}}^{(2)} = \frac{1}{2}\mathbf{S} : \dot{\mathbf{C}}. \end{aligned} \tag{2.34}$$

2.4 Basic fundamentals of thermodynamics

2.4.1 Conservation of mass

This work refers only to processes where the mass of a subdomain $\mathfrak{B}_\mathrm{p}$ of the body $\mathfrak{B}$, that occupies the region Ω_p in the reference configuration, is maintained constant during the deformation, i.e.,

$$m = \int_{\Omega_\mathrm{p}} \rho_0 \mathrm{d}v_0 = \int_{\varphi(\Omega_\mathrm{p})} \rho \mathrm{d}v, \tag{2.35}$$

where $\rho_0 = \mathrm{d}m/\mathrm{d}v_0$ and $\rho = \mathrm{d}m/\mathrm{d}v$ are the densities of mass of $\mathfrak{B}_\mathrm{p}$ at the reference and current configurations, respectively. From this consideration, the postulate of conservation of mass in its local form can be expressed as

$$\dot{\rho} + \rho \mathrm{div}_{\boldsymbol{x}}(\boldsymbol{v}) = 0, \tag{2.36}$$

where $\mathrm{div}_{\boldsymbol{x}}(\bullet) = \partial(\bullet)_i/\partial x_i$ is the spatial divergence operator. This equation states that the mass of an isolated domain can not vary due to processes that act inside the system.

2.4.2 Momentum balance

The linear momentum of a subdomain of a body, in the current configuration, can be defined by

$$\boldsymbol{I} = \int_{\varphi(\Omega_\mathrm{p})} \rho \boldsymbol{v} \mathrm{d}v. \tag{2.37}$$

When the resultant forces that act on the subdomain are null the subdomain remains in uniform motion, otherwise the change of linear momentum in time equals the resulting volume and surface forces, i.e.,

$$\dot{\boldsymbol{I}} = \frac{\partial}{\partial t} \int_{\varphi(\Omega_\mathrm{p})} \rho \boldsymbol{v} \mathrm{d}v = \int_{\varphi(\Omega_\mathrm{p})} \boldsymbol{b} \mathrm{d}v + \int_{\varphi(\partial\Omega_\mathrm{p})} \boldsymbol{t} \mathrm{d}a, \tag{2.38}$$

where $\partial\Omega_\mathrm{p}$ is the space occupied by the boundary of the subdomain $\mathfrak{B}_\mathrm{p}$ and $\boldsymbol{b}$ are the body forces per unit volume of the deformed body. This relation is known as the linear momentum

balance and can be rewritten in a local form according to

$$\begin{aligned} \operatorname{div}_{\boldsymbol{x}}\boldsymbol{\sigma} + \boldsymbol{b} &= \rho\dot{\boldsymbol{v}} \quad \text{in } \varphi(\Omega_{\mathrm{p}}) \\ \boldsymbol{t} &= \boldsymbol{\sigma}\boldsymbol{n} \quad \text{in } \varphi(\partial\Omega_{\mathrm{p}}). \end{aligned} \tag{2.39}$$

On the other hand, the angular momentum of a subdomain $\mathfrak{B}_{\mathrm{p}}$, respectively to the coordinate system's origin, is defined by

$$\boldsymbol{D} = \int_{\varphi(\Omega_{\mathrm{p}})} \boldsymbol{x} \times \rho\boldsymbol{v}\mathrm{d}v. \tag{2.40}$$

The angular momentum balance states that the rate of the angular momentum equals the resulting applied moments caused by the volume and surface forces, i.e.,

$$\dot{\boldsymbol{D}} = \frac{\partial}{\partial t}\int_{\varphi(\Omega_{\mathrm{p}})} \boldsymbol{x} \times \rho\boldsymbol{v}\mathrm{d}v = \int_{\varphi(\Omega_{\mathrm{p}})} \boldsymbol{x} \times \boldsymbol{b}\mathrm{d}v + \int_{\varphi(\partial\Omega_{\mathrm{p}})} \boldsymbol{x} \times \boldsymbol{t}\mathrm{d}a. \tag{2.41}$$

The local form of the angular momentum balance states the symmetry of the Cauchy stress tensor, i.e., $\boldsymbol{\sigma} = \boldsymbol{\sigma}^{\mathrm{T}}$, and thus also the symmetry of the second Piola-Kirchhoff stress tensor.

2.4.3 First law of thermodynamics

The first law of thermodynamics, also called balance of internal energy, postulates the conservation of total energy and is mathematically expressed, in the current configuration, in a local form, by

$$\rho\dot{e} = \boldsymbol{\sigma} : \mathbf{d} + \rho r - \operatorname{div}_{\boldsymbol{x}}\boldsymbol{q}, \tag{2.42}$$

where e is the specific internal energy per unit mass, r is the heat supply (or heat production) per unit mass and unit time, and $\boldsymbol{q}$ is the heat flux. Thus, the left-hand side term represents the rate of the internal energy per unit deformed volume, the second right-hand side term is the heat supply per unit deformed volume, and $\operatorname{div}_{\boldsymbol{x}}\boldsymbol{q}$ is the spatial divergence of the heat flux. Moreover, the term $\boldsymbol{\sigma} : \mathbf{d}$ is the stress power per unit deformed volume.

2.4.4 Second law of thermodynamics

The entropy of a thermo-mechanical system measures the microscopic randomness and disorder and is used to determine the evolution of the thermodynamic process. The entropy relative to a subdomain of a body, $\mathfrak{B}_{\mathrm{p}}$, is given by the specific entropy per unit mass, s. The rate of the subdomain's entropy is given by

$$\int_{\varphi(\Omega_{\mathrm{p}})} \rho\dot{s}\mathrm{d}v = \int_{\varphi(\Omega_{\mathrm{p}})} \frac{\rho r}{\theta} + \rho\gamma_s\mathrm{d}v - \int_{\varphi(\partial\Omega_{\mathrm{p}})} \frac{1}{\theta}\boldsymbol{q}\cdot\boldsymbol{n}\mathrm{d}a, \tag{2.43}$$

where $\rho r/\theta$ represents the source of entropy inside the subdomain due to evolution of temperature, γ_s is the production of entropy per unit mass and unit time and $-\boldsymbol{q}\cdot\boldsymbol{n}/\theta$ is the

supply of entropy due to heat flux through the boundary surface of the subdomain. Here, $\boldsymbol{n}$ is the normal vector of the area element $\mathrm{d}a$.

The second law of thermodynamics states that in thermodynamic processes the production of entropy is never negative, i.e., $\rho\gamma_s \geq 0$. In other words, it establishes the irreversibility of entropy production. In its local form, this law can be expressed by the inequality

$$\rho\gamma_s = \rho\dot{s} - \frac{\rho r}{\theta} + \mathrm{div}_{\boldsymbol{x}}\frac{\boldsymbol{q}}{\theta} \geq 0. \tag{2.44}$$

2.4.5 Helmholtz free energy

The Helmholtz free energy per unit mass, $\bar{\psi}$, results from the additive split of the internal energy into a part related to the entropy and a part that measures the "available" energy to produce work, i.e.,

$$\bar{\psi} = e - \theta s. \tag{2.45}$$

It can be expressed in a generic form as

$$\bar{\psi} = \bar{\psi}(\boldsymbol{\varepsilon}, \mathbf{A}_i, \boldsymbol{a}), \tag{2.46}$$

where $\boldsymbol{\varepsilon}$ is an appropriated strain measure, $\mathbf{A}_i$, with $i = 1 \ldots N$, are tensor-valued internal variables, and $\boldsymbol{a}$ is a vector given by scalar-valued internal variables and/or constitutive parameters of the material.

2.4.6 Clausius-Duhem inequality

From the combination of the first and second law of thermodynamics, the fundamental inequality

$$\rho\dot{s} - \frac{1}{\theta}(\rho\dot{e} - \boldsymbol{\sigma} : \mathbf{d} + \mathrm{div}_{\boldsymbol{x}}\boldsymbol{q}) + \mathrm{div}_{\boldsymbol{x}}\frac{\boldsymbol{q}}{\theta} \geq 0, \tag{2.47}$$

is obtained. Considering the definition of the Helmholtz free energy (Equation 2.45) and the identity

$$\mathrm{div}_{\boldsymbol{x}}\frac{\boldsymbol{q}}{\theta} = \frac{1}{\theta}\mathrm{div}_{\boldsymbol{x}}\boldsymbol{q} - \frac{1}{\theta^2}\boldsymbol{q}\cdot\nabla_{\boldsymbol{x}}\theta, \tag{2.48}$$

the local form of the so-called Clausius-Duhem inequality is obtained, following the expression

$$-\rho(\dot{\bar{\psi}} + s\dot{\theta}) + \boldsymbol{\sigma} : \mathbf{d} - \frac{1}{\theta}\boldsymbol{q}\cdot\nabla_{\boldsymbol{x}}\theta \geq 0. \tag{2.49}$$

This work is related to isothermal processes only, i.e., $\dot{\theta} = 0$ and $\nabla_{\boldsymbol{x}}\theta = 0$. Thus, for such isothermal conditions, the Clausius-Duhem inequality is reduced to the form

$$-\rho\dot{\bar{\psi}} + \boldsymbol{\sigma} : \mathbf{d} \geq 0. \tag{2.50}$$

Chapter 3

Computational plasticity

In this chapter, the concepts inherent to computational plasticity are presented. Initially, a succinct comparison between crystallographic and phenomenological material models is presented, and the main advantages of phenomenological models over crystallographic ones are outlined to sustain the choice of considering the former in this work. Then, the fundamentals of phenomenological models, along with the state-of-the-art of yield functions and hardening models, are presented. Special attention is given to complex anisotropic yield functions and to the classical and modified rheological models of Armstrong-Frederick kinematic hardening, since they are the bases of the constitutive models presented in the following chapters.

3.1 Cristalographic vs. phenomenological models

Several efforts have been made to model experimental anisotropic mechanical behaviours as accurately as possible, resulting in many micro- and macro-anisotropic models presented in the literature. The description of the (yield and hardening) anisotropy using FEM usually employs either crystallographic texture-based models or phenomenological models.

On the one hand, crystallographic models are grounded on the crystallographic structure of the material and simulate the slip on the crystal's slip systems to determine the elastic and plastic deformations as well as the evolution of the material's properties. Due to the nature of the crystallographic structure of metallic materials, this type of models are inherently anisotropic. The ability of crystal plasticity models to relate the plastic behaviour of crystalline materials to their microstructures represents their main advantage and has motivated several efforts on the development of time-efficient numerical algorithms and constitutive models, which overcome, e.g., the numerical problems due to the interdependency of slip systems. Crystal plasticity models have some more advantages such as the use of the crystallographic texture as an input parameter, thus avoiding the substantial number of mechanical tests required by some complex phenomenological anisotropic models, or the capability to directly follow the evolution of the material's anisotropy through the plastic deformation. Hence, these models have been used for many purposes such as texture design, calculation of evo-

lutionary coefficients of phenomenological yield functions, calculation of damage parameters, evaluation of forming limit diagrams (FLD), and the simulation of microcrack initiation, crack propagation, fatigue, creep in small scale plasticity, and fracture criteria, for crystalline materials.

The simulation of anisotropic metallic materials using crystal plasticity models can be performed by directly modelling aggregates of grains one-by-one, by associating an aggregate to each integration (Gauss) point, and thus providing the mechanical behaviour of the macro structure using polycrystal models (e.g., full or relaxed constraint Taylor's model, self-consistent approach, and N-point model), or even using homogenization techniques by coupling multiple scales through the use of representative volume elements (RVE), for instance. Crystal plasticity has been used to successfully simulate sheet metal forming operations, see e.g., Beaudoin *et al.* (1994), Nakamachi *et al.* (2001), Raabe and Roters (2004), Raabe *et al.* (2005), Böhlke *et al.* (2006), Chen *et al.* (2007), Tikhovskiy *et al.* (2007), and Van Houtte *et al.* (2012). However, despite the significant progress in computational technology and in crystal plasticity modelling, these approaches still involve much heavier calculations comparatively to phenomenological models, turning prohibitive the analyses of complex forming operations. An extensive and comprehensive review of crystal plasticity constitutive modelling in FEM was published by Roters *et al.* (2010).

On the other hand, phenomenological models consist of sets of empirical mathematical relations that describe the experimental macroscopic behaviour of the materials as accurately as possible. Even though the derivation of some of these mathematical relations are physically motivated with bases on the crystallographic structure of the materials, the parameters that characterize a particular material are determined by fitting with experimental data. In other words, the constitutive parameters related to a particular material are obtained by their tuning in order to fit the modelled behaviour with data coming from experimental mechanical tests, rather than from the material's crystallographic structure. The main disadvantage of this type of models consists of the high number of experimental tests usually required to describe the complex anisotropic behaviours of some materials. The yield anisotropy is modelled by a macroscopic anisotropic yield surface characterized by anisotropy parameters, whose determination can be quite complex for some yield criteria. Moreover, in sheet metals the macroscopic characterization of the out-of-the-plane behaviour requires very complex, unconventional and usually very expensive, experimental mechanical tests. Thus, for such characterization of the material, crystallographic models are often employed in the determination of some parameters used in phenomenological models.

Nevertheless, phenomenological models are widely used in both academia and industry in the simulation of a vast range of material behaviours, such as yield anisotropy, cyclic hardening phenomena, damage, fracture, creep, etc. Their main advantages consist of their time efficiency and relative simplicity. On the one hand, phenomenological models require fairly low computational costs, allowing the numerical simulation of industrial complex processes in the production of real parts. On the other hand, their formulations are usually not very

complicated from the point of view of an engineer and thus their adaptation and/or improvement are not such complex tasks. Moreover, even though the algorithmic implementation of phenomenological models represents a challenging, time-consuming, and error-prone task, it is still simpler then the algorithmic implementation of crystallographic models.

Considering these advantages and comparisons, putting special attention to the goal of efficiently modelling industry-relevant sheet metal forming processes, the work developed in this Thesis will only focus on phenomenological models.

3.2 Fundamentals of elastoplastic phenomenological models

In the context of isothermal rate-independent elastoplastic constitutive models, the material's behaviour is characterized by two domains, namely the elastic and elastoplastic ones. In the elastic behaviour domain, where loading and unloading imply no dissipation of energy, the mechanical response is described by an elastic law, in which the stress is given from an energy potential as a function of a suitable measure of the elastic deformation. In elastoplastic models it is assumed that the elastic domain is bounded by a yield criterion. In one-dimensional situations, as in the uniaxial tensile test, the boundary is typically easily distinguishable and characterized by the yield stress, σ_{y}, and the yield criterion simply states that the elastoplastic domain is defined by $\Phi = |\sigma| - \sigma_{\mathrm{y}} = 0$. When this criterion is reached, further loading leads to elastoplastic deformations. The elastoplastic behaviour is characterized by its irreversibility, due to the dissipation of energy inherent to plasticity. The concepts of elastic domain and yield criterion are schematically represented in Fig. 3.1a for one-dimensional conditions.

Considering this, three-dimensional phenomenological elastoplastic models are grounded in three principles, namely:

Yield criterion Its main purpose is to delimit the elastic domain, and expresses mathematically the so-called yield surface in the three-dimensional stress space, also called as the Haig-Westergaard space (see Fig. 3.1b, for two-dimensional plane stress conditions). The state-of-the-art of isotropic and anisotropic yield criteria is presented in Section 3.3. Stress states represented inside this yield surface are in the elastic domain, whereas the ones represented on the yield surface are in the elastoplastic domain. The region outside the yield surface represent stress states that have no physical meaning;

Hardening law When the yield surface is reached, if the material is subjected to further loading it experiences hardening phenomena. This, usually nonlinear, phenomena are described by a hardening law, which may induce expansion, translation, rotation, or distortion of the yield surface with ongoing deformation. Detailed information on this phenomena and the state-of-the-art of hardening laws are presented in Section 3.4;

Plastic flow rule Along with hardening, when the material is subjected to loading after the yield surface being reached, plastic flow, i.e., evolution of plastic deformation, takes

place. The normality flow rule, in which it is assumed that the plastic deformations are normal to a plastic potential of stress, is commonly considered. It encompasses the associated and nonassociated flow rules, which consider that the plastic and yield potentials are equal and different, respectively. Based on its plastic incompressibility, the adoption of the associated flow rule to describe the behaviour of metallic materials is widely accepted.

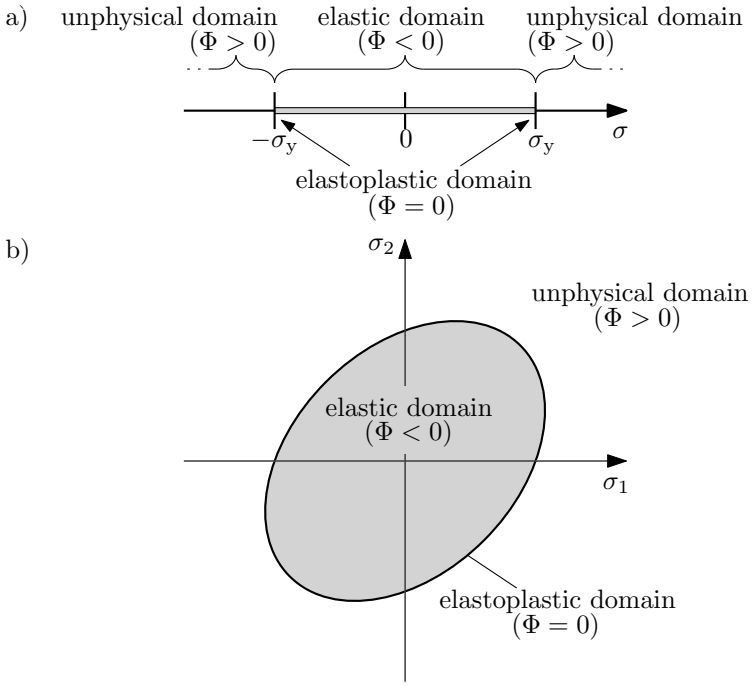

Figure 3.1: Elastic, elastoplastic, and unphysical domains in a) 1D and b) 2D conditions.

3.3 Plastic yielding

As indicated before, plastic yielding occurs when a yield criterion is satisfied. Yield criteria are commonly expressed in terms of a potential of stress (the so-called yield potential), generic definition of which is

$$\Phi(\boldsymbol{\sigma}, \mathbf{A}_i, \boldsymbol{a}) = \bar{\sigma}(\boldsymbol{\sigma}, \mathbf{A}_i, \boldsymbol{a}) - \sigma_{\mathrm{y}}(\mathbf{A}_i, \boldsymbol{a}), \tag{3.1}$$

where $\bar{\sigma}$ is the effective stress, which is a function of the stress tensor, N tensor-valued internal variables ($\mathbf{A}_i$, with $i = 1 \dots N$), and of a vector $\boldsymbol{a}$ given by scalar-valued internal variables and/or constitutive parameters of the material. The dependence of the effective and yield stresses on $\mathbf{A}_i$ and $\boldsymbol{a}$ enables the description of several features, such as yield anisotropy, yield surface's evolution with hardening, yield surface's dependency on the temperature, etc.

With the definition of yield potential in hands, the yield criterion states that the elasto-plastic boundary of the elastic domain is defined by the stress states that verify the condition

$$\Phi(\boldsymbol{\sigma}, \mathbf{A}_i, \boldsymbol{a}) = 0. \tag{3.2}$$

Thus, the representation, in the Haig-Westergaard space, of the set of all stress states that verify this condition is the yield surface. The elastic domain is then characterized mathematically by the set of stress states for which $\Phi(\boldsymbol{\sigma}, \mathbf{A}_i, \boldsymbol{a}) < 0$. The set of all admissible stress states results from the union of the elastic and elastoplastic domains, i.e., $\Phi(\boldsymbol{\sigma}, \mathbf{A}_i, \boldsymbol{a}) \leq 0$. Hence, all stress states that lie outside of the admissible domain, i.e., $\Phi(\boldsymbol{\sigma}, \mathbf{A}_i, \boldsymbol{a}) > 0$, possess no physical meaning, being achievable only mathematically during the algorithmic procedure used to numerically integrate the constitutive equations.

The yield surface must be closed, smooth, and convex (exception is made to the yield criterion of Tresca presented in the following, in which some regions of the surface are flat). Besides its physical motivation, the convexity of the yield surface is a convenient property in the numerical implementation, because together with the absence of singular points (again, exception is made to the yield criterion of Tresca) it ensures a one-to-one relationship between the stress and strain increments, thus ensuring the stability and convergence of the algorithmic procedure.

Based on experimental observations, it is widely assumed that hydrostatic pressure does not cause plastic deformations in metallic materials characterized by low porosity. Thus, the yield surface of such materials is represented in the Haig-Westergaard space by the lateral surface of a prism, axis of which is coincident with the diagonal of the space (defined by the points that satisfy the relation $\sigma_1 = \sigma_2 = \sigma_3$) (see Fig. 3.2a). Since any surface's section normal to this axis is identical, it is convenient to geometrically represent the yield surface by its projection on the deviatoric plane. This plane is normal to the diagonal of the Haig-Westergaard space and includes the origin of the coordinate frame, hence being characterized by the points that verify $\sigma_1 + \sigma_2 + \sigma_3 = 0$ (see Fig. 3.2b).

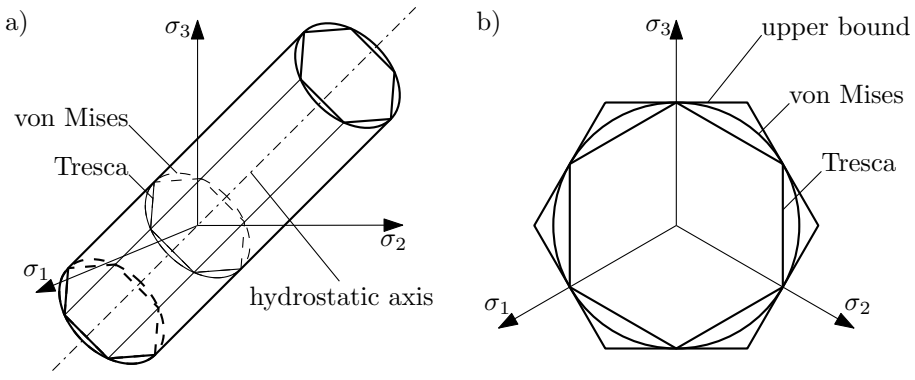

Figure 3.2: Geometric representation of von Mises's and Tresca's yield surfaces a) in Haig-Westergaard space and b) their projection on the deviatoric plane.

Anisotropic yielding is modelled by considering an anisotropic yield potential representing a yield surface that accounts for the variation of the yield stress with the loading direction. Such yield potentials use effective stress functions in which are included specific material

parameters that characterize the yield surface's shape. In constitutive models that consider the associated flow rule, the anisotropic flow is intrinsically modelled and is directly related to the yield anisotropy, when an anisotropic yield potential is taken into account. In the following, the state-of-the-art of isotropic and anisotropic yield criteria is presented.

3.3.1 Isotropic yield functions

A material is assumed isotropic when its properties are independent of the directions considered. Hence, yield criteria used to describe yield isotropy can be expressed by means of some kind of stress invariants only. Several different sets of stress invariants can be used, such as the principal stresses (or eigenvalues of the stress tensor), σ_i, with $i = 1 \dots 3$, or the stress invariants themselves, i.e.,

$$I_1 = \mathrm{tr}(\boldsymbol{\sigma}), \tag{3.3}$$

$$I_2 = \frac{1}{2}\mathrm{tr}(\boldsymbol{\sigma}^2) = \frac{1}{2}\boldsymbol{\sigma} : \boldsymbol{\sigma}, \text{ and} \tag{3.4}$$

$$I_3 = \frac{1}{3}\mathrm{tr}(\boldsymbol{\sigma}^3) = \det(\boldsymbol{\sigma}). \tag{3.5}$$

In the context of metal plasticity, where plastic deformation is independent on the hydrostatic pressure, isotropic yield criteria can be solely represented using the principal deviatoric stresses or the second and third invariants (J_2 and J_3) of the deviatoric stress tensor, given by

$$\mathbf{s} = \boldsymbol{\sigma}^{\mathrm{D}} = \mathbb{P} : \boldsymbol{\sigma} = \boldsymbol{\sigma} - \frac{1}{3}\mathrm{tr}(\boldsymbol{\sigma})\mathbf{I}, \tag{3.6}$$

where $(\bullet)^{\mathrm{D}}$ denotes the deviatoric part of a tensor and the operator $P_{ijkl} = \delta_{ik}\delta_{jl} - \frac{1}{3}\delta_{ij}\delta_{kl}$ maps second-order tensor-valued quantities into their deviatoric part.

Among the most well-known isotropic yield criteria are the ones considered in the following.

Tresca (1864) Based on experimental observations that plastic strains occur by crystallographic slip due to shear stresses, Tresca proposed the oldest yield criterion. It assumes that the elastic limit is established when the maximum shear stress reaches a critical value. Thus, this criterion can be mathematically expressed, for general stress conditions, by

$$\Phi = \max\left\{|\sigma_1 - \sigma_2|, |\sigma_2 - \sigma_3|, |\sigma_3 - \sigma_1|\right\} - \sigma_{\mathrm{y}}. \tag{3.7}$$

The three-dimensional geometric representation of this yield criterion on the Haig-Westergaard space and its projection on the deviatoric plane are presented in Fig. 3.2. It is represented by a hexagonal prism, and due to the presence of singular points (vertices) and flat surfaces its algorithmic treatment for numerical implementation requires special procedures to account for these particularities.

von Mises (1913) This is the most well-known yield criterion and is nowadays the most used in the description of the plastic behaviour of isotropic materials. The von Mises's yield criterion, also denoted as J_2 criterion, states that plastic yielding occurs when the elastic energy of distortion reaches a critical value. It is mathematically expressed by

$$\begin{aligned}\Phi &= \sqrt{3J_2} - \sigma_{\mathrm{y}} \\ &= \sqrt{\frac{1}{2}\left[(\sigma_{11}-\sigma_{22})^2 + (\sigma_{22}-\sigma_{33})^2 + (\sigma_{33}-\sigma_{11})^2\right] + 3(\sigma_{12}^2+\sigma_{13}^2+\sigma_{23}^2)} - \sigma_{\mathrm{y}}.\end{aligned} \tag{3.8}$$

Its corresponding yield surface represents a cylinder of radius σ_{y} in the Haig-Westergaard space that encircles the hexagonal prism given by Tresca's criterion.

Drucker (1949) Considering that the Tresca's criterion assumes that the intermediate principal stresses do not affect plastic yielding, whereas in the von Mises's criterion all principal stresses has equal weight on plastic yielding, Drucker (1949) proposed a more versatile criterion, whose yield surface lies between Tresca's and von Mises's surfaces, according to

$$\Phi = J_2^3 - cJ_3^2 - k^2, \tag{3.9}$$

where c is a material parameter used to weight the effect of all principal stresses (and therefore to fit the yield surface with experimental data) and $k^2 = 27(\sigma_{\mathrm{y}}/3)^6$. The constant c is limited to $[-27/8, 2.25]$ in order to ensure the yield surface's convexity.

Hershey (1954) A nonquadratic generalization of the von Mises's criterion was introduced by Hershey (1954), and later used by Hosford (1972), aiming at a more flexible yield surface, which is expressed by

$$\Phi = \left\{\frac{1}{2}\left[(\sigma_1-\sigma_2)^a + (\sigma_2-\sigma_3)^a + (\sigma_3-\sigma_1)^a\right]\right\}^{\frac{1}{a}} - \sigma_{\mathrm{y}}, \tag{3.10}$$

where the exponent a is a material parameter related to its crystallographic structure. This criterion degenerate to von Mises's criterion for $a = 2$ (or $a = 4$ for plane stress conditions), whereas it reduces to Tresca's criterion for $a = 1$ and in the limit situation $a \to \infty$. Moreover, while for $a \in\ ]1, 2[\ \cup\ ]4, \infty[$ the corresponding yield surface lies between Tresca's and von Mises's surfaces, when $a \in\ ]2, 4[$ it lies outside von Mises's surface. Based on crystal plasticity, Hosford (1972) suggested that the exponent a should be 6 for BCC materials and 8 for FCC materials.

Karafillis and Boyce (1993) Considering the existence of a lower bound for any isotropic yield surface, to which corresponds Tresca's surface, and an upper bound as represented in Fig. 3.2b, Karafillis and Boyce (1993) proposed a generalization of Hershey's

criterion, following

$$\Phi = [(1-c)\bar{\sigma}_1 - c\bar{\sigma}_2]^{\frac{1}{a}} - \sigma_y, \tag{3.11}$$

where $\bar{\sigma}_1$ is given in analogy to Hershey's criterion and expressed by

$$\bar{\sigma}_1 = \frac{1}{2}\left(|s_1 - s_2|^a + |s_2 - s_3|^a + |s_3 - s_1|^a\right), \tag{3.12}$$

and $\bar{\sigma}_2$ is given by

$$\bar{\sigma}_2 = \frac{3^a}{2^a + 2}\left(|s_1|^a + |s_2|^a + |s_3|^a\right). \tag{3.13}$$

Here, the exponent a has the same physical meaning as the exponent of Hershey's criterion and the weighting coefficient c is a material parameter that is used to fit the shape of the yield surface with experimental data. While by considering $a = 1$ both Equations 3.12 and 3.13 reduce to von Mises's criterion, in the limit $a \to \infty$ Equation 3.12 represents Tresca's criterion and Equation 3.13 gives the upper bound of the yield surface (see Fig. 3.2b).

Cazacu and Barlat (2004) The above mentioned criteria assume equal plastic yield conditions for tension and compression, which is an assumption valid for materials that deform by slip in the slip systems only, such as materials with cubic structure (BCC and FCC). However, materials with hexagonal closest packed (HCP) structures deform by slip and by twinning. Since twinning is a directional shear mechanism, HCP materials, such as titanium and magnesium alloys, display the so-called strength differential effect, i.e., the yield stress is different for tension and compression. Usually, twinning is easily activated by compression and not activated by tension in the sheet's plane (Cazacu and Barlat, 2004). The strength differential effect is more pronounced for low levels of plastic deformation, since the occurrence of twinning ceases as plastic deformation takes place. Yield surfaces that consider the strength differential effect are nonsymmetric regarding the origin of the stress space and its projection in the deviatoric plane have a triangular-like shape with rounded corners. A straightforward approach to describe the strength differential effect by means of symmetric (isotropic or anisotropic) yield functions consists of using a modified effective stress, which is composed by the effective stress related to the symmetric yield function and one additional weighted pressure term, i.e., related to the first invariant of the stress tensor (see e.g., Spitzig *et al.* (1975), Stoughton and Yoon (2004), and Lou *et al.* (2013)). Considering the plastic incompressibility of most metallic materials and the fact that the strength differential effect displayed by HCP materials is due to the occurrence of twinning rather than pressure sensibility, it seems that this approach lacks in terms of physical interpretation, when HCP materials are considered.

In order to take this effect into account, Cazacu and Barlat (2004) proposed a yield criterion expressed by

$$\Phi = J_2^{\frac{3}{2}} - cJ_3 - \tau_y^3, \tag{3.14}$$

where τ_y is the yield stress in pure shear and c is a material parameter that "measures" the

strength differential effect, the expression of which being obtained from uniaxial tests in the form

$$c = \frac{3\sqrt{3}(\sigma_{\mathrm{t}}^3 - \sigma_{\mathrm{c}}^3)}{2(\sigma_{\mathrm{t}}^3 + \sigma_{\mathrm{c}}^3)}, \tag{3.15}$$

where σ_{t} and σ_{c} are the yield stresses in in-plane uniaxial tensile and compression tests, respectively. In order to ensure the yield surface's convexity, this parameter is limited to $[-3\sqrt{3}/2,\, 3\sqrt{3}/2]$. Moreover, this criterion reduces to von Mises's criterion for $c = 0$, i.e., no strength differential effect is considered.

Extensions of this yield criterion to include the first invariant of the stress tensor into the expression of the effective stress are found in the works of e.g., Gao *et al.* (2011) and Yoon *et al.* (2014).

Cazacu *et al.* (2006) Aiming at a more flexible yield criterion that accounts for the strength differential effect, Cazacu *et al.* (2006) proposed the so-called *CPB06* criterion, of the form

$$\Phi = (|s_1| - ks_1)^a + (|s_2| - ks_2)^a + (|s_3| - ks_3)^a - \sigma_{\mathrm{y}}, \tag{3.16}$$

where the exponent a is considered to be a positive integer and the material parameter k is related to the strength differential effect, being given by

$$k = \frac{1-h}{1+h}, \;\; \text{with} \;\; h = \left[\frac{2^a - 2\left(\frac{\sigma_{\mathrm{t}}}{\sigma_{\mathrm{c}}}\right)^a}{\left(2\frac{\sigma_{\mathrm{t}}}{\sigma_{\mathrm{c}}}\right)^a - 2}\right]^{\frac{1}{a}}. \tag{3.17}$$

The yield surface defined by this potential is convex for any $a \geq 1$ if $k \in [-1, 1]$, to which corresponds $\sigma_{\mathrm{t}}/\sigma_{\mathrm{c}} \in [2^{(1-a)/a}, 2^{(a-1)/a}]$.

3.3.2 Anisotropic yield functions

Yield anisotropy, i.e., the dependency of the yield stress on the loading direction, is mathematically modelled by yield potentials that are represented by yield surfaces which account for the variation of the yield stress. When an associated flow rule is considered, the anisotropic (plastic) flow is also modelled by the yield potential, thus a flexible yield potential that is able to simultaneously describe yield and flow anisotropies is desirable.

Flow anisotropy of sheet materials is commonly characterized by means of the so-called Lankford r-values. The directional r_θ-values are determined by in-plane uniaxial tensile tests on sheet metals with orientation θ regarding the rolling direction and are defined by

$$r_\theta = \frac{\varepsilon_{22}}{\varepsilon_{33}} = -\frac{\varepsilon_{22}}{\varepsilon_{11} + \varepsilon_{22}}, \tag{3.18}$$

where ε_{11}, ε_{22}, and ε_{33} are the strains in the length, width, and thickness directions, respectively. The r_θ-values can be seen as a measure of resistance to thinning. While if $r_\theta > 1$ the

strains in the width direction are dominant, when $r_\theta < 1$ the thickness strains are dominant, which can lead to excessive thinning and failure in the production of parts. Also, differences in the sheet's plane of r_θ-values are directly related to the formation of earing in the drawing of cylindrical cups.

The right hand expression of Equation 3.18 is usually the preferential one, due to the significant differences between the relative errors of the measurement of in-plane and thickness strains. By convention, the r_θ-values are evaluated at 20% of elongation for comparison purposes (Banabic, 2010). Nevertheless, nowadays the tensile test machines possess systems for continuous measurement of strain, thus allowing the determination of r_θ-value's evolution with the plastic deformation.

Using the r_θ-values regarding 0°, 45°, and 90° from the rolling direction (RD), the so-called normal anisotropy coefficient is obtained by

$$r_\mathrm{n} = \frac{r_0 + 2r_{45} + r_{90}}{4}. \tag{3.19}$$

A higher normal anisotropy represents a higher resistance against thinning, which is preferable for sheet metal forming operations. The variation of the r_θ-values in the sheet's plane is assessed by the so-called planar anisotropy coefficient, expressed by

$$\Delta r = \frac{r_0 - 2r_{45} + r_{90}}{2}. \tag{3.20}$$

A more pronounced earing in the drawing of a cylindrical cup is observed for higher values of planar anisotropy.

Considering that the experimental yield surfaces are not symmetric in the equi-biaxial region, the biaxial r_b-value has been defined. It can be experimentally determined from either the disk compression test (Barlat *et al.*, 2005) or the in-plane biaxial tensile test (Pöhlandt *et al.*, 2002). This measure of anisotropy is determined by the ratio

$$r_\mathrm{b} = \frac{\varepsilon_{22}}{\varepsilon_{11}}. \tag{3.21}$$

Its value is one for isotropy and directly measures the slope of the yield surface at the equi-biaxial stress state. The r_b-value is particularly important for the correct description of the material's anisotropy in sheet metal forming processes, because, usually, the stress state to which several material points are subjected is near the equi-biaxial and plane-strain stress states.

The analytical expressions used to determine the directional and biaxial r-values directly from the yield potential are presented in Appendix D. The use of highly anisotropic advanced materials in the last decades has motivated the development of several anisotropic yield criteria, the most-relevant of which are presented in the following.

Hill's family of anisotropic yield criteria

Hill (1948) - Von Mises proposed the first anisotropic yield criterion for a single crystal. It was later also used for polycrystals and reduces to the yield criterion proposed by Hill (1948) in the case of orthotropy. Nowadays, the criterion proposed by Hill (1948) is still the most well-known and used anisotropic yield criterion to model the behaviour of orthotropic materials, specially steels, due to its simplicity and user-friendliness. This yield criterion is given by a quadratic function expressed by

$$\Phi = \sqrt{F(\sigma_{22}-\sigma_{33})^2 + G(\sigma_{33}-\sigma_{11})^2 + H(\sigma_{11}-\sigma_{22})^2 + 2L\sigma_{23}^2 + 2M\sigma_{13}^2 + 2N\sigma_{12}^2} - \sigma_{\mathrm{y}}, \tag{3.22}$$

where F, G, H, L, M, and N are six material parameters that characterize the material's anisotropy. By using tensorial notation, this criterion can be alternatively written as

$$\Phi = \sqrt{\boldsymbol{\sigma} : \mathbb{A} : \boldsymbol{\sigma}} - \sigma_{\mathrm{y}} = \sqrt{\mathbf{s} : \mathbb{A} : \mathbf{s}} - \sigma_{\mathrm{y}}, \tag{3.23}$$

where the fourth-order tensor $\mathbb{A}$, also denoted as anisotropy tensor, represents the anisotropy of the material and can be expressed by

$$\mathbb{A} = \begin{bmatrix} G+H & -H & -G & 0 & 0 & 0 \\ -H & F+H & -F & 0 & 0 & 0 \\ -G & -F & G+F & 0 & 0 & 0 \\ 0 & 0 & 0 & 2N & 0 & 0 \\ 0 & 0 & 0 & 0 & 2M & 0 \\ 0 & 0 & 0 & 0 & 0 & 2L \end{bmatrix}, \tag{3.24}$$

using Voigt's notation.

The determination of the six anisotropy parameters can be done by calibration with either the yield stresses or the r-values. On the one hand, if the correct description of the variation of the yield stresses is desired, the anisotropy parameters are determined by

$$F = \frac{1}{2}\left[-\left(\frac{\sigma_{\mathrm{y}}}{\sigma_{(\mathrm{RD})}}\right)^2 + \left(\frac{\sigma_{\mathrm{y}}}{\sigma_{(\mathrm{TD})}}\right)^2 + \left(\frac{\sigma_{\mathrm{y}}}{\sigma_{(\mathrm{ND})}}\right)^2\right], \tag{3.25}$$

$$G = \frac{1}{2}\left[\left(\frac{\sigma_{\mathrm{y}}}{\sigma_{(\mathrm{RD})}}\right)^2 - \left(\frac{\sigma_{\mathrm{y}}}{\sigma_{(\mathrm{TD})}}\right)^2 + \left(\frac{\sigma_{\mathrm{y}}}{\sigma_{(\mathrm{ND})}}\right)^2\right], \tag{3.26}$$

$$H = \frac{1}{2}\left[\left(\frac{\sigma_{\mathrm{y}}}{\sigma_{(\mathrm{RD})}}\right)^2 + \left(\frac{\sigma_{\mathrm{y}}}{\sigma_{(\mathrm{TD})}}\right)^2 - \left(\frac{\sigma_{\mathrm{y}}}{\sigma_{(\mathrm{ND})}}\right)^2\right], \tag{3.27}$$

$$L = \frac{1}{2}\left(\frac{\sigma_{\mathrm{y}}}{\tau_{(\mathrm{TD})(\mathrm{ND})}}\right)^2, \tag{3.28}$$

$$M = \frac{1}{2}\left(\frac{\sigma_{\mathrm{y}}}{\tau_{(\mathrm{ND})(\mathrm{RD})}}\right)^2, \text{ and} \tag{3.29}$$

$$N = \frac{1}{2}\left(\frac{\sigma_{\mathrm{y}}}{\tau_{(\mathrm{RD})(\mathrm{TD})}}\right)^2, \tag{3.30}$$

where $\sigma_{(\mathrm{RD})}$, $\sigma_{(\mathrm{TD})}$, and $\sigma_{(\mathrm{ND})}$ are the yield stresses obtained from in-plane uniaxial tensile tests along RD, TD, and ND[1], respectively. Also, $\tau_{(\mathrm{TD})(\mathrm{ND})}$, $\tau_{(\mathrm{ND})(\mathrm{RD})}$, and $\tau_{(\mathrm{RD})(\mathrm{TD})}$ are the yield stresses in pure shear conditions along the corresponding axes of anisotropy. On the other hand, for the simulation of sheet metal forming processes the anisotropy parameters are commonly determined using the r_θ-values along 0°, 45°, and 90° from the rolling direction. Thus, considering $G+H = 1$ along with plane stress conditions, three independent anisotropy parameters have to be determined according to the relations

$$F = \frac{r_0}{r_{90}(1+r_0)}, \;\; G = \frac{1}{1+r_0}, \;\; \text{and} \;\; N = \frac{(r_0+r_{90})(2r_{45}+1)}{2r_{90}(1+r_0)}. \tag{3.31}$$

This anisotropic criterion reduces to von Mises's criterion when $F = G = H = 0.5$ and $L = M = N = 1.5$.

The low flexibility is the main disadvantage of Hill (1948)'s yield criterion. Only three parameters are used to describe the planar anisotropy in metal sheets, thus not allowing the simultaneous accurate description of the yield stress's and r-value's evolution in the plane. Also, Hill (1948)'s criterion can predict only four ears in the drawing of a cylindrical cup, whereas a higher number of ears can be experimentally observed. Moreover, from the work of Pearce (1968), it was concluded that this criterion provides a poor description of the behaviour of some materials with $r_{\mathrm{n}} < 1$ and $\sigma_{\mathrm{b}}/\sigma_0 > 1$, such as aluminium alloys.

Hill (1979) - Considering the drawbacks of Hill (1948)'s yield criterion and based on the fact that nonquadratic functions are required to describe complex anisotropic behaviours, Hill (1979) proposed a nonquadratic yield criterion expressed by

$$\begin{aligned}\Phi = (&F|\sigma_{22}-\sigma_{33}|^m + G|\sigma_{33}-\sigma_{11}|^m + H|\sigma_{11}-\sigma_{22}|^m \\ &+A|2\sigma_{11}-\sigma_{22}-\sigma_{33}|^m + B|-\sigma_{11}+2\sigma_{22}-\sigma_{33}|^m \\ &+C|-\sigma_{11}-\sigma_{22}+2\sigma_{33}|^m)^{\frac{1}{m}} - \sigma_{\mathrm{y}},\end{aligned} \tag{3.32}$$

where A, B, C, F, G, and H are anisotropy parameters and the exponent m must be greater than one to ensure the yield surface's convexity.

This criterion is more flexible than Hill (1948)'s criterion, allowing a better description of experimental yield surfaces. However, because no shear components of the stress tensor are considered in this yield function, this criterion is limited to conditions where the loading directions are coincident with the axes of anisotropy. Also, the criterion is not able to properly describe the anisotropic behaviour of materials having $r_0/r_{90} \neq 1$ and $\sigma_0/\sigma_{90} \neq 1$. Hill proposed four particular forms of his criterion for plane stress conditions. These forms are based on the assumption of planar isotropy and thus the shear components of the stress

[1]Where RD, TD, and ND stand for rolling direction, transverse direction, and normal direction, respectively.

tensor are not required because the axes RD and TD can be arbitrarily oriented in the sheet's plane.

If $A = B = C = 0$ and the exponent m of Equation 3.32 is replaced by the exponent a of Equation 3.10 (given by the crystallographic structure of the material), the generalization of the isotropic yield criterion of Equation 3.10 to orthotropy, proposed by Hosford (1979) independently from Hill, is obtained, i.e.,

$$\Phi = \left(F|\sigma_{11} - \sigma_{22}|^a + G|\sigma_{22} - \sigma_{33}|^a + H|\sigma_{33} - \sigma_{11}|^a\right)^{\frac{1}{a}} - \sigma_{\mathrm{y}}. \tag{3.33}$$

Another disadvantage, due to not considering shear components into account, is the inhibition of describing planar anisotropy, except for RD and TD. To overcome this limitation, several extensions of Hill (1979)'s criterion that include shear components in the sheet's plane have been proposed such as by Zhou (1990), Montheillet *et al.* (1991), and Chu (1995).

Hill (1990) - Later, Hill also proposed a yield criterion including shear components in the sheet's plane, according to

$$\begin{aligned}\Phi = \Bigg\{ \frac{1}{2} \Bigg\{ & |\sigma_{11} + \sigma_{22}|^m + \left(\frac{\sigma_{\mathrm{b}}}{\tau_{\mathrm{y}}}\right)^m \left|(\sigma_{11} - \sigma_{22})^2 + 4\sigma_{12}^2\right|^{\frac{m}{2}} \\ & + \left|\sigma_{11}^2 + \sigma_{22}^2 + 2\sigma_{12}^2\right|^{\frac{m}{2}-1} \left[-2A\left(\sigma_{11}^2 - \sigma_{22}^2\right) + B\left(\sigma_{11} - \sigma_{22}\right)^2\right] \Bigg\} \Bigg\}^{\frac{1}{m}} - \sigma_{\mathrm{b}}.\end{aligned} \tag{3.34}$$

The use of σ_{12} allows the criterion to be expressed in a general coordinate system, i.e., the anisotropy axes are not necessarily coincident with the directions of the principal stresses, and the description of the variation of the yield stress and r-value in the sheet's plane is possible. Here, A, B, and m are material parameters defined as functions of the sets $\{\sigma_0,\ \sigma_{45},\ \sigma_{90},\ \sigma_{\mathrm{b}},\ r_{45}\}$, $\{\sigma_{45},\ \sigma_{\mathrm{b}},\ r_0,\ r_{45},\ r_{90}\}$, or $\{\sigma_{45},\ \sigma_{\mathrm{b}},\ r_{45},\ F,\ G,\ H,\ N\}$ (Hill (1948)'s anisotropy parameters), whereas σ_{b} and τ_{y} are the yield stresses in equi-biaxial tension and pure shear, respectively. In order to allow the description of more mechanical parameters, Lin and Ding (1996) and Leacock (2006) proposed extensions of Hill (1990)'s criterion. The main disadvantages of this criterion is its complexity and the limitation to plane stress conditions.

Hill (1993) - In his work, Hill (1993) showed that his previously presented yield criteria required that if $\sigma_0 = \sigma_{90}$, then the condition $r_0 = r_{90}$ is necessarily imposed and the reciprocal. In order to avoid this restriction and to describe the behaviour of materials in which $r_{\mathrm{n}} < 1$ and $\sigma_{\mathrm{b}}/\sigma_0 > 1$, Hill (1993) proposed the following polynomial yield function,

$$\Phi = \sqrt{\left(\frac{\sigma_{11}}{\sigma_0}\right)^2 - \frac{c\sigma_{11}\sigma_{22}}{\sigma_0\sigma_{90}}\sigma_{11}\sigma_{22} + \left(\frac{\sigma_{22}}{\sigma_{90}}\right)^2 + \left[(p+q) - \frac{p\sigma_{11} + q\sigma_{22}}{\sigma_{\mathrm{b}}}\right]\frac{\sigma_{11}\sigma_{22}}{\sigma_0\sigma_{90}}} - \sigma_{\mathrm{y}}, \tag{3.35}$$

where c, p, and q are material parameters determined as functions of the set $\{\sigma_0,\ \sigma_{90},\ \sigma_{\mathrm{b}},\ r_0,\ r_{90}\}$. The main disadvantages of this yield criterion is its limitation to plane stress conditions and the absence of shear components of the stress tensor in its formulation. Thus, the

anisotropy axes are restricted to the directions of the principal stresses and the description of the evolution of the yield stress and r-value in the sheet's plane is not possible.

Barlat's family of anisotropic yield criteria

Barlat and Lian (1989) (*Yld89*) - A generalization of the isotropic yield function of Hershey (1954) (Equation 3.10) to account with shear components, hence allowing a representation in a general coordinate frame, was proposed by Barlat and Richmond (1987) for plane stress conditions. This criterion was later extended by Barlat and Lian (1989) to include the description of planar anisotropy, according to

$$\Phi = \left\{ \frac{1}{2} \left[(2-c) \left| K_1 + K_2 \right|^a + (2-c) \left| K_1 - K_2 \right|^a + c \left| 2K_2 \right|^a \right] \right\}^{\frac{1}{a}} - \sigma_{\mathrm{y}}, \tag{3.36}$$

with

$$K_1 = \frac{\sigma_{11} + h\sigma_{22}}{2} \text{ and } K_2 = \sqrt{\left(\frac{\sigma_{11} - h\sigma_{22}}{2} \right)^2 + p^2 \sigma_{12}^2}, \tag{3.37}$$

where the exponent a has the same physical meaning as the exponent of Hershey's criterion (Equation 3.10) and c, h, and p are anisotropy parameters determined by either $\{r_0,\ r_{90}\}$ or $\{\sigma_0,\ \sigma_{90}\}$ together with $\{\tau_{\mathrm{y}_1},\ \tau_{\mathrm{y}_2}\}$. Here, τ_{y_1} and τ_{y_2} are the yield stresses relative to two different types of shear tests, namely, $\sigma_{12} = \tau_{\mathrm{y}_1}$ with $\sigma_{11} = \sigma_{22} = 0$ and $\sigma_{12} = 0$ with $\sigma_{22} = -\sigma_{11} = \tau_{\mathrm{y}_2}$. The disadvantages of this criterion include the limitation to plane stress conditions, the poor description of anisotropy in biaxial stress conditions, and the fact of not being able to simultaneously describe the variation of the yield stress and r-value in the sheet's plane.

Barlat *et al.* (1991) (*Yld91*) - Based on Hershey's isotropic criterion, Barlat *et al.* (1991) proposed an anisotropic yield criterion for any three-dimensional loading conditions employing the concept of linear transformations. This concept consists of introducing the anisotropy feature into an isotropic yield function by replacing the components of the stress tensor, $\boldsymbol{\sigma}$, by the components of a "weighted" stress tensor, $\tilde{\mathbf{s}}$, the so-called isotropic plasticity equivalent deviatoric stress tensor. This way, the yield function is isotropic with regard to $\tilde{\mathbf{s}}$ but anisotropic with regard to $\boldsymbol{\sigma}$ (see Fig. 3.3). The concept of linear transformations is very attractive because it allows the use of a high number of anisotropic parameters (improving the description of the anisotropy). Also, due to the linearity of the tensor transformation, the anisotropic yield function is convex if $\bar{\sigma} = \bar{\sigma}(\tilde{\mathbf{s}})$ is convex with respect to its arguments (Barlat *et al.*, 2005).

The extension of the Hershey's criterion to orthotropy, proposed by Barlat *et al.* (1991), is expressed by

$$\Phi = \left[\frac{1}{2} \left(\left| \tilde{s}_1 - \tilde{s}_2 \right|^a + \left| \tilde{s}_2 - \tilde{s}_3 \right|^a + \left| \tilde{s}_3 - \tilde{s}_1 \right|^a \right) \right]^{\frac{1}{a}} - \sigma_{\mathrm{y}}, \tag{3.38}$$

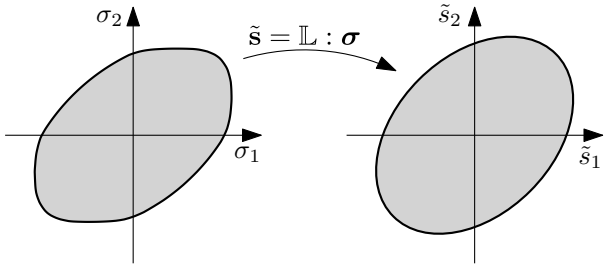

Figure 3.3: Schematic representation of the linear transformation concept.

where the exponent a is given by the crystallographic structure of the material and affects the yield surface only isotropically. Also, $\tilde{s}_i$, with $i = 1 \dots 3$, are the principal values of the weighted stress tensor, which is given by the linear transformation

$$\tilde{\mathbf{s}} = \tilde{\mathbb{L}} : \mathbf{s} = \tilde{\mathbb{L}} : \mathbb{P} : \boldsymbol{\sigma} = \mathbb{L} : \boldsymbol{\sigma}. \tag{3.39}$$

Here, $\tilde{\mathbb{L}}$ is the fourth-order tensor that gives the "weights" to the components of the stress tensor by means of anisotropy parameters. The use of the fourth-order tensor $\mathbb{L}$ to perform the linear transformation was proposed by Karafillis and Boyce (1993) (see Page 39). The tensor $\mathbb{L}$ describes the material's symmetry and is restricted by

i) $L_{ijkl} = L_{jikl} = L_{ijlk}$ and $L_{ijkl} = L_{klij}$,

ii) it is invariant with respect to the orthotropy group, and

iii) $L_{ijkk} = 0$.

The condition $L_{ijkk} = 0$ ensures that the hydrostatic component of $\tilde{s}$ is always zero, thus modelling plastic incompressibility. This condition can be dropped to model compressible materials. By using Voigt's notation, $\mathbb{L}$ can be written as

$$\mathbb{L} = \frac{1}{3} \begin{bmatrix} c_3 + c_2 & -c_3 & -c_2 & 0 & 0 & 0 \\ -c_3 & c_3 + c_1 & -c_1 & 0 & 0 & 0 \\ -c_2 & -c_1 & c_2 + c_1 & 0 & 0 & 0 \\ 0 & 0 & 0 & 3c_4 & 0 & 0 \\ 0 & 0 & 0 & 0 & 3c_5 & 0 \\ 0 & 0 & 0 & 0 & 0 & 3c_6 \end{bmatrix}, \tag{3.40}$$

where c_i, with $i = 1 \dots 6$, are the anisotropy parameters that are used to characterize the material's anisotropy. In plane stress conditions, such as in sheet metal forming processes, four anisotropy coefficients are used to describe planar anisotropy and whose determination can be carried out by numerically solving a set of four nonlinear equations. The four anisotropy parameters can be used to describe either the yield stresses in uniaxial tension for three directions in the sheet's plane and the equi-biaxial yield stress, or the r-values for three

directions in the sheet's plane. In the case of isotropy all coefficients are equal to one and the isotropic criterion of Hershey is recovered. The convexity of Hershey's criterion for $a \geq 1$ ensures the convexity of *Yld91* criterion.

The main advantages of this criterion rely on its generality and flexibility. Nevertheless, for plane stress conditions, its reduced number of anisotropy coefficients does not allow the simultaneously correct description of the evolution of the yield stress and r-value in the sheet's plane.

Barlat *et al.* (1997a) (*Yld94*) - Motivated by the observation that *Yld91* criterion is not able to describe the experimental behaviour of some materials, specially near pure shear conditions, Barlat *et al.* (1997a) proposed an extension to *Yld91*, expressed by

$$\Phi = \left[\frac{1}{2}\left(\alpha_1 \left|\tilde{s}_2 - \tilde{s}_3\right|^a + \alpha_2 \left|\tilde{s}_3 - \tilde{s}_1\right|^a + \alpha_3 \left|\tilde{s}_1 - \tilde{s}_2\right|^a\right)\right]^{\frac{1}{a}} - \sigma_{\mathrm{y}}, \tag{3.41}$$

where $\tilde{\mathbf{s}}$ is obtained from the linear transformation of Equation 3.39 using the same $\mathbb{L}$ as *Yld91* criterion and the parameters α_i, with $i = 1 \ldots 3$, are given by the transformation

$$\alpha_i = \alpha_{\mathrm{x}} p_{1i}^2 + \alpha_{\mathrm{y}} p_{2i}^2 + \alpha_{\mathrm{z}} p_{3i}^2. \tag{3.42}$$

Here, p_{ji}, with $j = 1 \ldots 3$, are the components of the rotation tensor, $\mathbf{p}$, that relates the anisotropic axes with the principal directions of $\tilde{\mathbf{s}}$, and α_{x}, α_{y}, and α_{z} are anisotropy parameters. When $\alpha_{\mathrm{x}} = \alpha_{\mathrm{y}} = \alpha_{\mathrm{z}} = 1$, then *Yld91* is recovered.

For plane stress conditions, this criterion has six independent parameters to describe planar anisotropy, whose determination is carried out by considering the set $\{\sigma_0,\ \sigma_{45},\ \sigma_{90},\ \sigma_{\mathrm{b}},\ r_0,\ r_{90}\}$. The use of only one parameter, c_4, to describe both σ_{45} and r_{45} does not allow their simultaneously accurate description (Barlat *et al.*, 1997b). Moreover, the convexity of the yield surface associated to this criterion has not been mathematically proved, although the positivity of α_{x}, α_{y}, and α_{z} is a necessary condition (Barlat *et al.*, 1997a).

Barlat *et al.* (1997b) (*Yld96*) - Bearing in mind that slight variations of the yield surface's shape may induce significant variations on r_θ and the fact that *Yld94* criterion does not allow the reproduction of the r_{45} experimental, Barlat *et al.* (1997b) proposed a criterion given by Equations 3.41 and 3.42. In this criterion, denoted as *Yld96*, the parameters α_{x}, α_{y}, and α_{z} are assumed to be functions of the angles between the principal directions of $\tilde{\mathbf{s}}$ and the anisotropy axes, rather than constants as in *Yld94*. For plane stress conditions, *Yld96* has seven independent anisotropy parameters, allowing the description of the set $\{\sigma_0,\ \sigma_{45},\ \sigma_{90},\ \sigma_{\mathrm{b}},\ r_0,\ r_{45},\ r_{90}\}$, to be determined by three uniaxial tensile tests and an equi-biaxial test. The convexity of this criterion has not been proved for general three-dimensional conditions, but can be proved numerically, with high probability, for plane stress conditions (Barlat *et al.*, 1997b). This fact, along with the difficulty related to the analytical calculation of its derivatives and the high complexity of its implementation in numerical codes of simulation

(particularly for full 3D stress states) are the main disadvantages of this criterion (Barlat *et al.*, 2003).

Barlat *et al.* (2003) (*Yld2000-2D*) - Considering only plane stress conditions, Barlat *et al.* (2003) proposed an anisotropic criterion, denoted as *Yld2000-2D*, that avoids the disadvantages of *Yld96* and preserves its flexibility. The criterion, convexity of which has been analytically proven, uses two linear transformations and is expressed by

$$\Phi = \left[\frac{1}{2}\left(\bar{\sigma}_1 + \bar{\sigma}_2\right)\right]^{\frac{1}{a}} - \sigma_{\mathrm{y}}, \tag{3.43}$$

where

$$\bar{\sigma}_1 = \left|\tilde{s}_1^{(1)} - \tilde{s}_2^{(1)}\right|^a \text{ and } \bar{\sigma}_2 = \left|2\tilde{s}_2^{(2)} + \tilde{s}_1^{(2)}\right|^a + \left|2\tilde{s}_1^{(2)} + \tilde{s}_2^{(2)}\right|^a. \tag{3.44}$$

Here, the two isotropic plasticity equivalent deviatoric stress tensors, $\tilde{\mathbf{s}}^{(k)}$, with $k = 1, 2$, are obtained by two linear transformations on the deviatoric stress tensor, i.e., $\tilde{\mathbf{s}}^{(k)} = \tilde{\mathbb{L}}^{(k)} : \mathbf{s}$. In the context of plastic incompressibility, the use of the deviatoric stress tensor, $\mathbf{s}$, in detriment of the stress tensor, $\boldsymbol{\sigma}$, avoids the use of the condition $\tilde{L}^{(k)}_{ijll} = 0$, because a yield function expressed in terms of the deviatoric stress tensor ensures the condition of pressure independency, even though $\tilde{\mathbf{s}}^{(k)}$ may not be deviatoric. Doing so, the number of independent anisotropy parameters in $\tilde{\mathbb{L}}^{(k)}$ is increased from six to nine for general conditions and from four to seven for the plane stress case (Barlat *et al.*, 2003). The use of two linear transformations is justified by the fact that in each tensor $\tilde{\mathbb{L}}^{(k)}$ only one parameter, $c^{(k)}_{44}$, is available to describe σ_{45} and r_{45}. Using Voigt's notation, for plane stress conditions the fourth-order anisotropic tensors, $\tilde{\mathbb{L}}^{(k)}$, are given by

$$\tilde{\mathbb{L}}^{(k)} = \begin{bmatrix} \tilde{L}^{(k)}_{1111} & \tilde{L}^{(k)}_{1122} & 0 \\ \tilde{L}^{(k)}_{2211} & \tilde{L}^{(k)}_{2222} & 0 \\ 0 & 0 & \tilde{L}^{(k)}_{1212} \end{bmatrix}. \tag{3.45}$$

For convenience, the fourth-order tensors $\mathbb{L}^{(k)} = \tilde{\mathbb{L}}^{(k)} : \mathbb{P}$, used in the transformations $\tilde{s}^{(k)} = \mathbb{L}^{(k)} : \boldsymbol{\sigma}$, are considered, the components of which are obtained from

$$\begin{bmatrix} L^{(1)}_{1111} \\ L^{(1)}_{1122} \\ L^{(1)}_{2211} \\ L^{(1)}_{2222} \\ L^{(1)}_{1212} \end{bmatrix} = \begin{bmatrix} 2/3 & 0 & 0 \\ -1/3 & 0 & 0 \\ 0 & -1/3 & 0 \\ 0 & 2/3 & 0 \\ 0 & 0 & 1 \end{bmatrix} \begin{bmatrix} \alpha_1 \\ \alpha_2 \\ \alpha_7 \end{bmatrix} \text{ and} \tag{3.46}$$

$$\begin{bmatrix} L^{(2)}_{1111} \\ L^{(2)}_{1122} \\ L^{(2)}_{2211} \\ L^{(2)}_{2222} \\ L^{(2)}_{1212} \end{bmatrix} = \frac{1}{9} \begin{bmatrix} -2 & 2 & 8 & -2 & 0 \\ 1 & -4 & -4 & 4 & 0 \\ 4 & -4 & -4 & 1 & 0 \\ -2 & 8 & 2 & -2 & 0 \\ 0 & 0 & 0 & 0 & 9 \end{bmatrix} \begin{bmatrix} \alpha_3 \\ \alpha_4 \\ \alpha_5 \\ \alpha_6 \\ \alpha_8 \end{bmatrix}, \tag{3.47}$$

where α_i, with $i = 1 \dots 8$, are the eight independent anisotropy parameters of this yield criterion, which reduce to one in the isotropic case. These parameters are determined from the experimental set $\{\sigma_0, \sigma_{45}, \sigma_{90}, \sigma_\mathrm{b}, r_0, r_{45}, r_{90}\}$. Considering that only seven parameters are required to describe the seven experimental data of the set considered, Barlat *et al.* (2003) proposed the restriction $L^{(2)}_{1122} = L^{(2)}_{2211}$ or the use of r_b to deal with the eighth parameter. The description of the planar anisotropy, provided by this criterion, is limited to directions orientated 0°, 45°, and 90° from the rolling one, which is not enough to properly describe the anisotropy of some highly anisotropic materials. Another disadvantage lies on the limitation to plane stress conditions.

Barlat *et al.* (2005) (*Yld2004-18p* and *Yld2004-13p*) - In order to have a better description of the anisotropy in the sheet's plane, by means of the use of a higher number of anisotropy parameters, Barlat *et al.* (2005) proposed a convex anisotropic criterion for general three-dimensional conditions, denoted as *Yld2004-18p*, expressed by

$$\Phi = \left(\frac{1}{4} \sum_{i=1}^{3} \sum_{j=1}^{3} \left| \tilde{s}^{(1)}_i - \tilde{s}^{(2)}_j \right|^a \right)^{\frac{1}{a}} - \sigma_\mathrm{y}, \tag{3.48}$$

where a has the same physical meaning as the exponent of Hershey's criterion. The methodology used in the *Yld2000-2D* to introduce several anisotropy parameters is also used in this criterion, i.e., two linear transformations on the deviatoric stress tensor are considered ($\tilde{\mathbf{s}}^{(k)} = \tilde{\mathbb{L}}^{(k)} : \mathbf{s}$). Using Voigt's notation, the fourth-order anisotropic tensors used by this criterion are expressed by

$$\tilde{\mathbb{L}}^{(k)} = \begin{bmatrix} 0 & -c^{(k)}_{12} & -c^{(k)}_{13} & 0 & 0 & 0 \\ -c^{(k)}_{21} & 0 & -c^{(k)}_{23} & 0 & 0 & 0 \\ -c^{(k)}_{31} & -c^{(k)}_{32} & 0 & 0 & 0 & 0 \\ 0 & 0 & 0 & c^{(k)}_{44} & 0 & 0 \\ 0 & 0 & 0 & 0 & c^{(k)}_{55} & 0 \\ 0 & 0 & 0 & 0 & 0 & c^{(k)}_{66} \end{bmatrix}, \tag{3.49}$$

and made up by eighteen anisotropy parameters to describe anisotropy. Isotropy (Hershey's criterion) is recovered when all these parameters are one, while *Yld91* criterion is obtained if only one linear transformation is taken into account, considering only six independent anisotropy parameters. The relation between the parameters of Equations 3.40 and 3.49 is

given by

$$\begin{aligned}
&c_{12}^1 = c_{12}^2 = \frac{1}{3}\left(c_2 + 2c_3\right), \;\; c_{13}^1 = c_{13}^2 = \frac{1}{3}\left(2c_{31}^1 + 2c_{12}^1 - c_{23}^1\right), \;\; c_{44}^1 = c_{44}^2 = c_4, \\
&c_{23}^1 = c_{23}^2 = \frac{1}{3}\left(c_3 + 2c_1\right), \;\; c_{32}^1 = c_{32}^2 = \frac{1}{3}\left(2c_{23}^1 + 2c_{31}^1 - c_{12}^1\right), \;\; c_{55}^1 = c_{55}^2 = c_5, \\
&c_{31}^1 = c_{31}^2 = \frac{1}{3}\left(c_1 + 2c_2\right), \;\; c_{21}^1 = c_{21}^2 = \frac{1}{3}\left(2c_{12}^1 + 2c_{23}^1 - c_{31}^1\right), \;\; c_{66}^1 = c_{66}^2 = c_6.
\end{aligned} \tag{3.50}$$

For sheet forming applications, the experimental data used to determine the eighteen anisotropic parameters consists of the yield stresses and r-values from in-plane uniaxial tension tests along seven directions in the sheet's plane, e.g., for every 15° from RD to TD, the equi-biaxial yield stress from, e.g., the bulge test, the r_{b}-value from the disk compression test, and four additional data that characterize the out-of-plane properties (Barlat *et al.*, 2005). Since out-of-plane experiments are difficult to perform, Barlat *et al.* (2005) suggested the use of polycrystal simulations to determine the yield stress for uniaxial tension at 45° between RD and ND and between TD and ND and for simple shear in the RD-ND and TD-ND planes, for instance. If no crystallographic texture is available, it is recommended to use isotropic values for the out-of-plane properties (Barlat *et al.*, 2005). The determination of the anisotropy parameters is carried out by numerical minimization of an error function that compares experimental and predicted data.

The high number of anisotropy parameters allows an excellent description of planar anisotropic behaviours, such as the evolution of the yield stress and r-value in the sheet's plane. As a consequence, it enables the prediction of highly anisotropic effects in sheet forming, e.g., the formation of six or more ears in the cylindrical cup forming benchmark (Yoon *et al.*, 2006). Its main disadvantage, however, lies on the high number of experimental tests needed to determine all the anisotropy parameters. Therefore, when the number of experimental data available is limited, the authors (Barlat *et al.*, 2005) have proposed another yield criterion, denoted as *Yld2004-13p*, considering only thirteen anisotropy parameters for general three-dimensional conditions (nine for plane stress conditions), expressed by

$$\begin{aligned}
\Phi = \Big\{ \frac{1}{2} \Big[& \left|\tilde{s}_1^{(1)} - \tilde{s}_2^{(1)}\right|^a + \left|\tilde{s}_2^{(1)} - \tilde{s}_3^{(1)}\right|^a + \left|\tilde{s}_3^{(1)} - \tilde{s}_1^{(1)}\right|^a \\
& - \left(\left|\tilde{s}_1^{(1)}\right|^a + \left|\tilde{s}_2^{(1)}\right|^a + \left|\tilde{s}_3^{(1)}\right|^a\right) + \left|\tilde{s}_1^{(2)}\right|^a + \left|\tilde{s}_2^{(2)}\right|^a + \left|\tilde{s}_3^{(2)}\right|^a \Big] \Big\}^{\frac{1}{a}} - \sigma_{\mathrm{y}}.
\end{aligned} \tag{3.51}$$

This criterion is convex for sufficiently high values of a (larger than about 1.7). The two fourth-order anisotropic tensors are dependent on only thirteen parameters, according to Equations 3.52 and 3.53. Due to the lower number of anisotropy parameters, *Yld2004-13p* is not able to predict planar anisotropy as accurately as *Yld2004-18p*. However, it requires less experimental data, the minimization of the corresponding error function used to determine the anisotropy parameters is faster, and the anisotropy's description provided is at the level

of accuracy to that obtained with *Yld2000-2D* (Barlat *et al.*, 2005).

$$\tilde{\mathbb{L}}^{(1)} = \begin{bmatrix} 0 & -1 & -c_{13}^1 & 0 & 0 & 0 \\ -c_{21}^1 & 0 & -c_{23}^1 & 0 & 0 & 0 \\ -1 & -1 & 0 & 0 & 0 & 0 \\ 0 & 0 & 0 & c_{44}^1 & 0 & 0 \\ 0 & 0 & 0 & 0 & c_{55}^1 & 0 \\ 0 & 0 & 0 & 0 & 0 & c_{66}^1 \end{bmatrix} \tag{3.52}$$

$$\tilde{\mathbb{L}}^{(2)} = \begin{bmatrix} 0 & -c_{12}^2 & -c_{13}^2 & 0 & 0 & 0 \\ -c_{21}^2 & 0 & -c_{23}^2 & 0 & 0 & 0 \\ -1 & -1 & 0 & 0 & 0 & 0 \\ 0 & 0 & 0 & c_{44}^2 & 0 & 0 \\ 0 & 0 & 0 & 0 & c_{55}^2 & 0 \\ 0 & 0 & 0 & 0 & 0 & c_{66}^2 \end{bmatrix} \tag{3.53}$$

Later, an extension of *Yld2004-18p* accounting for 27 parameters and denoted as *Yld2004-27p*, has been proposed by Aretz *et al.* (2010). The use of 27 anisotropy parameters was attained by considering three linear transformations, using three fourth-order anisotropic tensors of the type of Equation 3.49. Aretz *et al.* (2010) determined the additional anisotropy parameters by also considering the yield stress from plane-strain tensile tests in 0°, 45°, and 90° from RD.

Aretz and Barlat (2013) (*Yld2011-18p* and *Yld2011-27p*) - Recently, a new yield criterion with a formulation similar to *Yld2004-18p*, denoted as *Yld2011-18p*, has been proposed by Aretz and Barlat (2013). Its yield potential is expressed by

$$\Phi = \left(\frac{1}{\xi} \sum_{i=1}^{3} \sum_{j=1}^{3} \left| \tilde{s}_i^{(1)} + \tilde{s}_j^{(2)} \right|^m \right)^{\frac{1}{m}} - \sigma_{\mathrm{y}}, \tag{3.54}$$

where the exponent m does not have the physical meaning of Hershey's exponent (also considered in, e.g., *Yld2004-18p*) and the scalar ξ is derived from uniaxial or equi-biaxial tension in the isotropic case and can be determined from $\xi = (4/3)^m + 4(2/3)^m + 4(1/3)^m$. Despite the similarities between *Yld2004-18p* and *Yld2011-18p*, the authors (Aretz and Barlat, 2013) argue that these yield functions can be regarded as complementary.

An extension of *Yld2011-18p* has been also proposed by considering an additional linear transformation. This criterion, denoted as *Yld2011-27p*, is expressed by

$$\Phi = \left[\frac{1}{\xi} \left(\sum_{i=1}^{3} \sum_{j=1}^{3} \left| \tilde{s}_i^{(1)} + \tilde{s}_j^{(2)} \right|^m + \sum_{i=1}^{3} \left| \tilde{s}_i^{(3)} \right|^m \right) \right]^{\frac{1}{m}} - \sigma_{\mathrm{y}}, \tag{3.55}$$

where the scalar ξ reads $\xi = (4/3)^m + 5(2/3)^m + 6(1/3)^m$. As for the *Yld2004-27p*, to deter-

mine the additional anisotropy parameters the yield stress in plane-strain tensile tests along three directions in the sheet's plane have been considered in the parameter's identification procedure. Both *Yld2011-18p* and *Yld2011-27p* are convex for $m \geq 1$ and use fourth-order anisotropic tensors expressed by Equation 3.49. Despite the high flexibility of the criteria with 27 anisotropy parameters, the high amount of experimental data required to determine these parameters is still an obstacle to their use in industrial applications.

Karafillis and Boyce (1993) Independently from Barlat *et al.* (1991), Karafillis and Boyce (1993) developed the concept of linear transformations to introduce anisotropy into isotropic yield criteria. They were the first ones to represent the concept of linear transformations by means of tensorial multiplications (see Equation 3.39). Karafillis and Boyce (1993) used this concept to introduce anisotropy into their isotropic criterion (see Page 25). This way, the anisotropic criterion is given by the potential of Equation 3.11, considering that $\bar{\sigma}_1$ and $\bar{\sigma}_2$ are rewritten by

$$\bar{\sigma}_1 = \frac{1}{2}\left(|\tilde{s}_1 - \tilde{s}_2|^a + |\tilde{s}_2 - \tilde{s}_3|^a + |\tilde{s}_3 - \tilde{s}_1|^a\right) \text{ and} \tag{3.56}$$

$$\bar{\sigma}_2 = \frac{3^a}{2^a + 2}\left(|\tilde{s}_1|^a + |\tilde{s}_2|^a + |\tilde{s}_3|^a\right), \tag{3.57}$$

where the isotropic plasticity equivalent deviatoric stress tensor, $\tilde{\mathbf{s}}$, is obtained from Equations 3.39 and 3.40. Comparatively to *Yld91*, the anisotropic criterion proposed by Karafillis and Boyce (1993) uses the same number of anisotropy parameters and thus presents the same level of accuracy regarding the anisotropy's description. However, the use of the isotropic parameter c (and thus $\bar{\sigma}_2$) increases its flexibility.

Bron and Besson (2003) An extension of Karafillis and Boyce (1993)'s criterion has been proposed by Bron and Besson (2003). In order to take more isotropy parameters into account, the yield function of Equation 3.11 was rewritten to account for the sum of multiple isotropic effective stress components. In their work, it was considered only two effective stress components, following

$$\Phi = \left[(1-c)\left(\bar{\sigma}_1^{1/b^1}\right)^a - c\left(\bar{\sigma}_2^{1/b^2}\right)^a\right]^{\frac{1}{a}} - \sigma_{\mathrm{y}}, \tag{3.58}$$

where c, a, b^1, and b^2 are isotropy parameters that only affect the yield surface's shape isotropically. Comparatively to Karafillis and Boyce (1993), a higher number of anisotropy parameters is considered by using two linear transformations, thus rewriting Equations 3.56 and 3.57 in the form

$$\bar{\sigma}_1 = \frac{1}{2}\left(\left|\tilde{s}_1^{(1)} - \tilde{s}_2^{(1)}\right|^{b^1} + \left|\tilde{s}_2^{(1)} - \tilde{s}_3^{(1)}\right|^{b^1} + \left|\tilde{s}_3^{(1)} - \tilde{s}_1^{(1)}\right|^{b^1}\right) \text{ and} \tag{3.59}$$

$$\bar{\sigma}_2 = \frac{3^{b^2}}{2^{b^2} + 2}\left(\left|\tilde{s}_1^{(2)}\right|^{b^2} + \left|\tilde{s}_2^{(2)}\right|^{b^2} + \left|\tilde{s}_3^{(2)}\right|^{b^2}\right), \tag{3.60}$$

where $\tilde{\mathbf{s}}^{(k)}$, with $k = 1, 2$, are obtained from linear transformations on the stress tensor. Two fourth-order anisotropic tensors with the structure of $\mathbb{L}$ (as in Equation 3.40) are considered, thus allowing the use of twelve parameters to describe the anisotropy (eight for plane stress conditions). The convexity of this yield criterion has mathematically been proven and its main advantage relies on its flexibility due to the four isotropy parameters. Karafillis and Boyce (1993)'s criterion is retained if $a = b^1 = b^2$ and $\tilde{\mathbf{s}}^{(1)} = \tilde{\mathbf{s}}^{(2)}$ and, additionally, *Yld91* criterion is obtained if $c = 0$ is further imposed. Nevertheless, the eight anisotropy parameters are not enough to provide an accurate description of the planar anisotropy of some materials used in sheet forming applications.

Banabic-Balan-Comsa's family of anisotropic yield criteria

Banabic *et al.* (2000) (*BBC2000*) - Based on the anisotropic yield criterion of Barlat and Lian (1989), a new family of yield criteria have been developed since 2000. The first criterion of this family was proposed by Banabic *et al.* (2000), being denoted as *BBC2000* and expressed by

$$\Phi = \left\{ \frac{1}{2} \left[a \left(bK_1 + cK_2 \right)^{2k} + a \left(bK_1 - cK_2 \right)^{2k} + (1-a) \left(2cK_2 \right)^{2k} \right] \right\}^{\frac{1}{2k}} - \sigma_{\mathrm{y}}, \tag{3.61}$$

where the exponent k is related to the material's crystallographic structure. The convexity of this criterion is ensured for $a \in [0, 1]$ and positive integer values of k. Here, K_1 and K_2 are functions of the second and third invariants of $\tilde{\mathbf{s}} = \mathbb{L} : \boldsymbol{\sigma}$ and can be represented by

$$K_1 = M\sigma_{11} + N\sigma_{22} \text{ and } K_2 = \sqrt{\left(P\sigma_{11} + Q\sigma_{22} \right)^2 + R\sigma_{12}^2}, \tag{3.62}$$

where M, N, P, Q, and R are functions of four independent coefficients of $\mathbb{L}$. Apart from the exponent k, this criterion uses seven independent anisotropy parameters determined from the experimental set $\{\sigma_0, \sigma_{45}, \sigma_{90}, \sigma_{\mathrm{b}}, r_0, r_{45}, r_{90}\}$.

In order to introduce one anisotropy parameter, and thus to allow the description of r_{b}, an extension of the *BBC2000* was proposed by Paraianu *et al.* (2003) (*BBC2002*). The flexibility of *BBC2002* was improved by Banabic *et al.* (2005) (*BBC2003*), preserving the number of anisotropy parameters. Later, a modification on these criteria was proposed by Banabic *et al.* (2008) (*BBC2005*).

Comsa and Banabic (2008) (*BBC2008*) - The last version of *BBC*'s criteria, denoted by *BBC2008*, was proposed by Comsa and Banabic (2008), being expressed by

$$\begin{aligned} \Phi = \Bigg\{ (w-1) \sum_{k=1}^{n} \Bigg\{ & w^{i-1} \left[\left(L^{(i)} + M^{(i)} \right)^{2k} + \left(L^{(i)} - M^{(i)} \right)^{2k} \right] + \\ & w^{n-i} \left[\left(L^{(i)} + N^{(i)} \right)^{2k} + \left(L^{(i)} - N^{(i)} \right)^{2k} \right] \Bigg\} \Bigg\}^{\frac{1}{2k}} - \sigma_{\mathrm{y}}, \end{aligned} \tag{3.63}$$

with

$$L^{(i)} = l_1^{(i)}\sigma_{11} + l_2^{(i)}\sigma_{22}, \tag{3.64}$$

$$M^{(i)} = \sqrt{\left(m_1^{(i)}\sigma_{11} - m_2^{(i)}\sigma_{22}\right)^2 + \left[m_3^{(i)}\left(\sigma_{12} + \sigma_{21}\right)\right]^2}, \text{ and} \tag{3.65}$$

$$N^{(i)} = \sqrt{\left(n_1^{(i)}\sigma_{11} - n_2^{(i)}\sigma_{22}\right)^2 + \left[n_3^{(i)}\left(\sigma_{12} + \sigma_{21}\right)\right]^2}, \tag{3.66}$$

where $w = (3/2)^{(1/n)} > 1$ and $l_1^{(i)}$, $l_2^{(i)}$, $m_1^{(i)}$, $m_2^{(i)}$, $m_3^{(i)}$, $n_1^{(i)}$, $n_2^{(i)}$, and $n_3^{(i)}$, with $i = 1 \ldots n$, are anisotropy parameters. When all these parameters are equal to $1/2$, the isotropic criterion of Barlat and Richmond (1987) is recovered. This criterion is convex for integer positive values of k. In Comsa and Banabic (2008), $n = 2$ is used and the determination of the sixteen anisotropy parameters for a 2090-T3 aluminium alloy was carried out considering the yield stress and r_θ-value from in-plane uniaxial tensile tests for every 15° from RD to TD, the equi-biaxial yield stress, and the r_b-value.

The main advantage of this criterion is its flexibility, due to the high amount of anisotropy parameters that can be used, which allows the prediction of severe planar anisotropy, e.g., the formation of twelve ears in the cylindrical cup forming (Vrh *et al.*, 2014). However, the high number of anisotropy parameters demands the use of several experimental data to carry out their determination. As main disadvantages of the *BBC*'s criteria, one can mention that their formulation is not user-friendly, besides being limited to plane stress conditions.

Cazacu and Barlat (2001) An alternative approach to introduce the description of anisotropy into isotropic criteria has been proposed by Cazacu and Barlat (2001). It consists of developing generalizations of the invariants of the deviatoric stress and using them directly in the isotropic criterion. In Cazacu and Barlat (2001) the proposed generalizations of J_2 and J_3 are expressed by

$$\begin{aligned} J_2^0 =& a_1\left(\sigma_{11} - \sigma_{22}\right)^2/6 + a_2\left(\sigma_{22} - \sigma_{33}\right)^2/6 + a_3\left(\sigma_{11} - \sigma_{33}\right)^2/6 \\ &+ a_4\sigma_{12}^2 + a_5\sigma_{13}^2 + a_6\sigma_{23}^2 \text{ and} \end{aligned} \tag{3.67}$$

$$\begin{aligned} J_3^0 =& \left(b_1 + b_2\right)\sigma_{11}^3/27 + \left(b_3 + b_4\right)\sigma_{22}^3/27 + \left[2\left(b_1 + b_4\right) - b_2 - b_3\right]\sigma_{33}^3/27 \\ &- \left(b_1\sigma_{22} + b_2\sigma_{33}\right)\sigma_{11}^2/9 - \left(b_3\sigma_{33} + b_4\sigma_{11}\right)\sigma_{22}^2/9 \\ &- \left[\left(b_1 - b_2 + b_4\right)\sigma_{11} + \left(b_1 - b_3 + b_4\right)\sigma_{22}\right]\sigma_{33}^2/9 + 2\left(b_1 + b_4\right)\sigma_{11}\sigma_{22}\sigma_{33}/9 \\ &- \left[2b_9\sigma_{22} - b_8\sigma_{33} - \left(2b_9 - b_8\right)\sigma_{11}\right]\sigma_{13}^2/3 \\ &- \left[2b_{10}\sigma_{33} - b_5\sigma_{22} - \left(2b_{10} - b_5\right)\sigma_{11}\right]\sigma_{12}^2/3 \\ &- \left[\left(b_6 + b_7\right)\sigma_{11} - b_6\sigma_{22} - b_7\sigma_{33}\right]\sigma_{23}^2/3 + 2b_{11}\sigma_{12}\sigma_{13}\sigma_{23}, \end{aligned} \tag{3.68}$$

respectively. Here, a_i, with $i = 1 \ldots 6$, and b_i, with $i = 1 \ldots 11$, are the anisotropy parameters, which reduce to one in isotropy. Cazacu and Barlat (2001) used this approach to introduce

anisotropy into Drucker's criterion (Equation 3.9), i.e.,

$$\Phi = \left(J_2^0\right)^3 - c\left(J_3^0\right)^2 - k^2. \tag{3.69}$$

This criterion has eighteen anisotropy parameters for three-dimensional conditions, which are reduced to eleven for plane stress conditions. For sheet metal forming applications, the eleven parameters are determined using the uniaxial yield stress and r_θ-value in five directions from RD to TD and the equi-biaxial yield stress. As for Drucker's criterion, this criterion is convex if $c \in [-27/8, 2.25]$.

Cazacu and Barlat (2001) also considered the use of one linear transformation, using Equations 3.39 and 3.40, to introduce anisotropy into Drucker's criterion. However, such an extension used only five anisotropy coefficients in plane stress conditions, not allowing the same accuracy as Equation 3.69. The main advantages of the criterion expressed by Equation 3.69 are its simple and user-friendly formulation and the high number of anisotropy parameters employed.

Cazacu and Barlat (2004) Early works on the simultaneous description of strength differential effect and anisotropy include, e.g., the extensions of Hill (1948) criterion proposed by Hosford (1966) and Liu *et al.* (1997) to include the strength differential effect. However, the low flexibility of these criteria does not allow an accurate description of the behaviour of some materials such as magnesium alloys (Cazacu and Barlat, 2004). Having this in mind, Cazacu and Barlat (2004) proposed an extension of their own isotropic criterion, that accounts for the strength differential effect (see Page 26), to orthotropy using the approach proposed in Cazacu and Barlat (2001). Their anisotropic criterion consists of simply replacing J_2 and J_3 of Equation 3.14 by J_2^0 and J_3^0 given by Equations 3.67 and 3.68. This way, while c is used to describe the strength differential effect, the seventeen anisotropy parameters, a_i and b_i (ten for plane stress conditions), provide the anisotropy's description.

Another extensions of the isotropic criterion of Cazacu and Barlat (2004) to orthotropy have been recently proposed by Nixon *et al.* (2010) and Yoon *et al.* (2014) considering one and two linear transformations, respectively. In these works, the anisotropic tensors are expressed by Equation 3.40 and thus only four and eight anisotropy parameters in plane stress conditions are taken into account, respectively.

Cazacu *et al.* (2006) (*CPB06*) - Aiming at a more flexible anisotropic yield criterion able to describe the strength differential effect, Cazacu *et al.* (2006) proposed an extension of their own isotropic criterion (see Page 27) to orthotropy by means of the concept of linear transformations. Thus, their anisotropic criterion, denoted as *CPB06*, is expressed by

$$\Phi = (|\tilde{s}_1| - k\tilde{s}_1)^a + (|\tilde{s}_2| - k\tilde{s}_2)^a + (|\tilde{s}_3| - k\tilde{s}_3)^a - \sigma_{\mathrm{y}}, \tag{3.70}$$

where $\tilde{\boldsymbol{s}}$ is obtained from a linear transformation on the deviatoric stress tensor, using a

fourth-order anisotropy tensor defined by nine independent anisotropy parameters for three-dimensional conditions (seven for plane stress conditions). The main advantage of this criterion relies on its flexibility. It is worth noting that it uses a yield function with the degree of homogeneity a, whereas Cazacu and Barlat (2004)'s criterion is limited to a third-order expression. In order to have a better description of anisotropy, Plunkett *et al.* (2008) proposed an extension of the *CPB06* criterion, considering two linear transformations on the deviatoric stress tensor. This criterion, denoted as *CPB06ex2*, includes two parameters to describe the strength differential effect and eighteen anisotropy parameters for three-dimensional conditions (fourteen for plane stress conditions). Plunkett *et al.* (2008) also analysed the use of three (*CPB06ex3*) and four (*CPB06ex4*) linear transformations in the description of the planar anisotropy of a 2090-T3 aluminium alloy. As expected, the higher the number of linear transformations used, the better is the anisotropy's description obtained, however at the cost of a high amount of experimental data, the availability of which may not exist (or be easy to obtain) for some materials.

Polynomial yield criteria Seeking for simpler formulations, making easy the corresponding numerical implementation, several polynomial yield functions have been proposed (see e.g., Gotoh (1977), Hu (2007), Soare *et al.* (2008), and Yoshida *et al.* (2013)). The use of polynomial functions are appealing due to the simple calculation of the corresponding derivatives. The recently proposed polynomial yield criteria, such as by Soare *et al.* (2008) and Yoshida *et al.* (2013), ally the simplicity of the polynomial character with high flexibility, by taking a considerable number of anisotropy parameters into account, hence being very attractive for numerical simulations of real processes. As an example, Soare *et al.* (2008) proposed a polynomial yield function of eighth order that uses 25 parameters to describe the anisotropy in plane stress conditions, allowing, e.g., the prediction of eight ears in the forming of a cylindrical cup. In the work of Soare and Barlat (2010) it is shown that some of the recently proposed anisotropic yield criteria based on the concept of linear transformations can be expressed by means of homogeneous polynomial functions, therefore enabling a considerable simplification of their numerical implementation in finite element codes.

Vegter yield criteria Vegter *et al.* (1995) and Vegter and van den Boogaard (2006) have proposed a criterion in which the yield locus is directly built from experimental data by applying Bézier interpolations. For isotropy, four mechanical tests are required to characterize the yield locus, namely a unixial, an equi-biaxial, a plane strain, and a pure shear test.

To characterize the yield locus for planar anisotropy this set of tests, except the equi-biaxial test, must be carried out for several directions. If three directions are used (e.g., 0°, 45°, and 90° from RD), the yield function requires seventeen independent parameters, namely yield stresses and r-values. Even though a high number of anisotropy parameters is considered, their determination is straightforward and does not require the solving of a nonlinear set of equations. The main disadvantages of this criterion rely on the not straightforward

formulation of the yield function, the use of several mechanical tests (including plane strain and pure shear tests), and the limitation to plane stress conditions.

It was shown by Ziegler (1977) that a surface represented in the dual space of strain rates could be related to any yield surface represented in the stress space. Having in mind that strain rate potential formulations are more convenient than stress potential formulations (as the ones indicated before) for implementation into specific finite element analysis and design codes, several strain rate anisotropic potentials have been proposed in the last decades (see e.g., Barlat and Chung (1993, 2005), Barlat *et al.* (2003), Kim *et al.* (2007), Rabahallah *et al.* (2009), and Cazacu *et al.* (2010)). The strain rate potential conjugated to a particular stress potential is determined from the principle of plastic work equivalence. However, this procedure is only carried out for classical quadratic potentials, since the determination of exact duals of nonquadratic stress potentials is a very challenging, perhaps sometimes impossible, task. Nevertheless, some analytical orthotropic strain rate potentials numerically conjugated ("pseudo-conjugated") to nonquadratic stress potentials have been proposed, e.g., in the works of Kim *et al.* (2007) and Cazacu *et al.* (2010).

Usually the assumption of associative flow rule is taken into account, in which the yield and plastic potentials are identical. Nevertheless, and seeking for a higher general character, some researchers have also adopted the nonassociated flow rule in metal plasticity (Stoughton, 2002, Stoughton and Yoon, 2004, Arghavani *et al.*, 2011, Gao *et al.*, 2011, Taherizadeh *et al.*, 2010, 2011). This type of flow rule is usually adopted to describe the behaviour of materials whose plastic behaviour is pressure-dependent, since the plastic flow is not orthogonal to the yield surface. However, since the pressure dependency of the plastic behaviour of most metallic materials is negligible, the use of such models in simulations of sheet metal forming is motivated by the increase of the anisotropy parameters's number. In other words, these constitutive models make use of two different potentials to define the plastic yield anisotropy and the plastic flow. Thus, the number of anisotropy coefficients is higher than in associative models, at the expenses of also requiring a higher amount of experimental data.

3.4 Hardening

A material point experiences hardening phenomena when it reaches the limit of the elastic region and evolution of plastic strain takes place by imposition of further loading. Since hardening is the result of dislocation microstructure and its evolution along the imposed strain path, the experimentally observed abnormal hardening phenomena are always dependent on the material itself and on the loading history.

In proportional uniaxial loading, hardening is characterized by a continuous decrease of the material's stiffness (comparatively to the elastic stiffness) as deformation takes place, exceptions are made for linear hardening and perfect plasticity. Abnormal hardening phenomena are commonly observed for cyclic loading conditions (cyclic hardening phenomena) or for

abrupt changes of the loading direction (e.g., latent hardening for cross-loading conditions). Among the most observed cyclic hardening phenomena are (see Fig. 3.4) the Bauschinger effect (reduction of the yield stress upon reverse loading after the occurrence of plastic deformation during the initial loading), the transient behaviour (smooth elasto-plastic transition characterized by a fast change of work-hardening rate, which occurs when the Bauschinger effect is present), the work-hardening stagnation (transient behaviour in which a plateau in the stress-strain relation is observed), the permanent softening (lower levels of stress after the transient period when compared to monotonic loading at a given accumulated plastic strain), and the ratcheting (cyclic accumulation of plastic strain during cyclic loading with nonzero mean stress). The correct description of these phenomena is crucial for an accurate prediction of defects in parts produced by metal forming processes, e.g., the Bauschinger effect and the permanent softening affect directly the springback (Wagoner *et al.*, 2013).

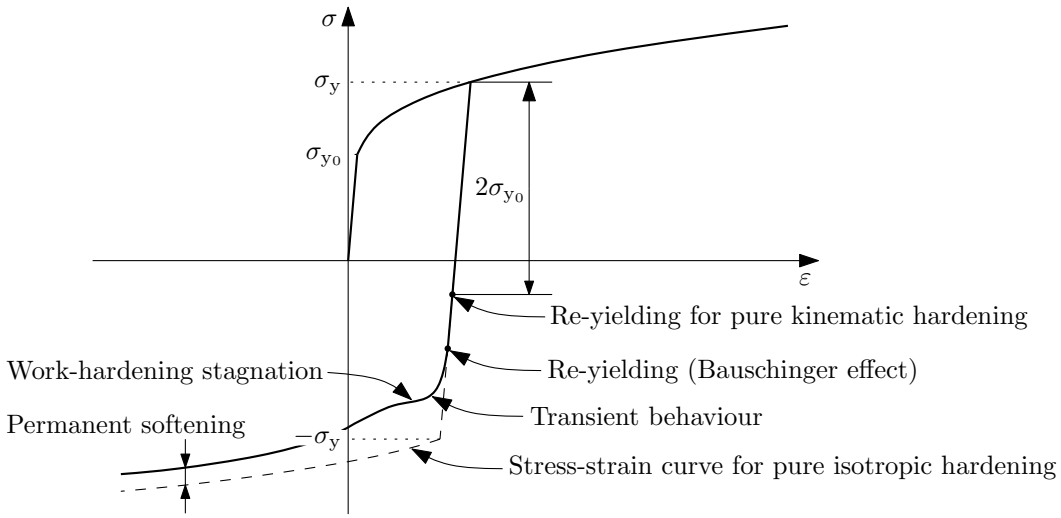

Figure 3.4: Influence of some of the cyclic hardening phenomena on the stress-strain relation during uniaxial tension-compression test.

In the context of phenomenological computational plasticity, hardening is characterized by the evolution of the elastic region, i.e., evolution of the yield surface. This evolution may be an expansion, translation, rotation, or distortion, to which correspond isotropic, kinematic, rotational, and anisotropic (distortion) hardening, respectively (see Fig. 3.5). In order to obtain a better description of complex hardening behaviours displayed by advanced materials, the combination of hardening types are usually considered. The most common combination is the, widely called, combined hardening, in which isotropic and kinematic hardening are simultaneously taken into account (see Fig. 3.5c).

Hardening is mathematically described by the evolution of proper state variables expressed by functions of e.g., the accumulated plastic strain, $\bar{\varepsilon}_{\mathrm{p}}$, which is associated to the effective stress by means of the work-equivalence principle, or the plastic work per unit volume, W_{p}. In the following the state-of-the-art of the hardening models is presented.

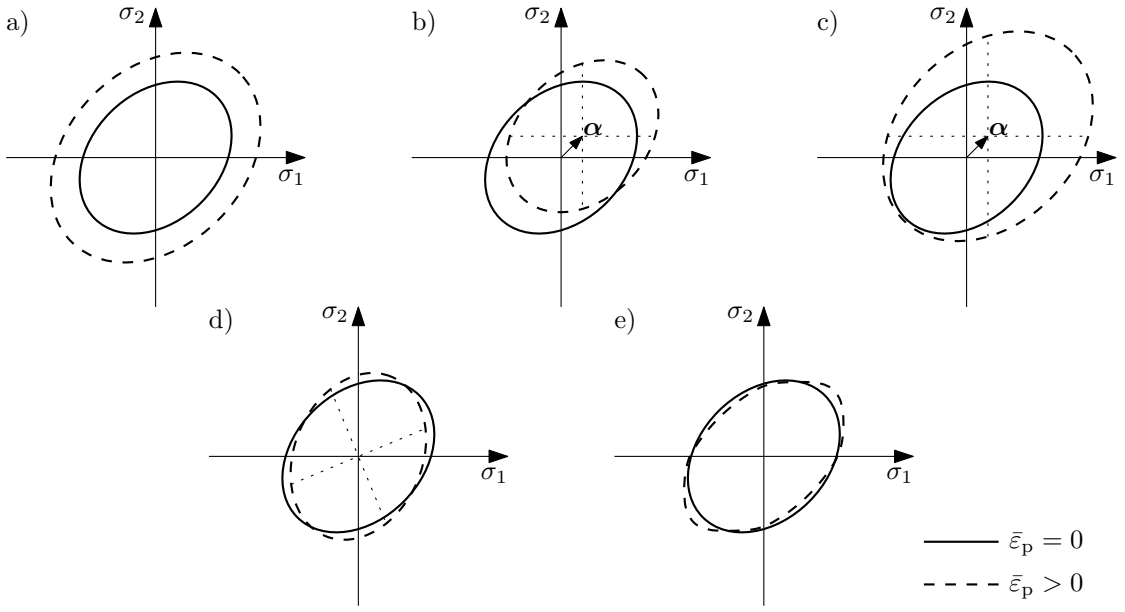

Figure 3.5: Evolution of the yield surface in the $\sigma_1 - \sigma_2$ plane according to a) isotropic, b) kinematic, c) combined, d) rotational, and e) anisotropic hardening.

3.4.1 Isotropic hardening models

The isotropic hardening is the most used hardening model and assumes that the yield surface expands isotropically (see Fig. 3.5a). It is mathematically described by establishing a dependence of the yield stress on suitable internal variables, such as the accumulated plastic strain, i.e., $\sigma_\mathrm{y} = \sigma_\mathrm{y}(\bar{\varepsilon}_\mathrm{p})$. The most well-known isotropic hardening laws are

Linear	$\sigma_\mathrm{y} = \sigma_{\mathrm{y}_0} + K\bar{\varepsilon}_\mathrm{p},$	(3.71)
Hollomon (1945)	$\sigma_\mathrm{y} = K\bar{\varepsilon}_\mathrm{p}^{n_\mathrm{H}},$	(3.72)
Swift (1952)	$\sigma_\mathrm{y} = K\left(\varepsilon_0 + \bar{\varepsilon}_\mathrm{p}\right)^{n_\mathrm{H}},$	(3.73)
Voce (1948)	$\sigma_\mathrm{y} = \sigma_{\mathrm{y}_0} + Q\left(1 - e^{-\beta\bar{\varepsilon}_\mathrm{p}}\right),$	(3.74)
Ludwigson (1971)	$\sigma_\mathrm{y} = K_1\bar{\varepsilon}_\mathrm{p}^{n_1} + e^{(K_2 + n_2\bar{\varepsilon}_\mathrm{p})},$ and	(3.75)
(H/V) Sung *et al.* (2010)	$\sigma_\mathrm{y} = \alpha K\bar{\varepsilon}_\mathrm{p}^{n_\mathrm{H}} + (1-\alpha)\left[\sigma_{\mathrm{y}_0} + Q\left(1 - e^{-\beta\bar{\varepsilon}_\mathrm{p}}\right)\right],$	(3.76)

where K, K_1, K_2, n_H, n_1, n_2, ε_0, σ_{y_0}, Q, β, and α are material parameters. Isotropic hardening laws may be differentiated as either saturation (exponential) or Voce-like models (Voce, 1948), that predict a stress saturation at large stains, or power or Hollomon-like models (Hollomon, 1945, Swift, 1952), stress's evolution of which is unbounded. Saturation and power laws are, generally speaking, employed in the description of the mechanical behaviour of aluminium and steel alloys, respectively. Aiming at a higher flexibility, combinations of these two types of hardening laws were proposed by Ludwigson (1971) and Sung *et al.* (2010).

Although isotropic hardening is widely used, it is unable to describe any of the aforementioned abnormal hardening phenomena. This limitation has motivated the development of

the hardening models presented in the following, which are or may be used in combination with the isotropic hardening.

3.4.2 Kinematic hardening models

Seeking for the description of the Bauschinger effect, the kinematic hardening concept was proposed by Prager (1956). It assumes that the yield surface translates in the stress space, without change of its size, shape, or orientation (see Fig. 3.5b). Such translation is mathematically described by means of the evolution of the so-called back stress tensor, which defines the center of the yield surface in the stress space. Therefore, the effective stresses, $\bar{\sigma}$, related to yield surfaces that undergo kinematic hardening are expressed by means of the relative stress tensor, $\boldsymbol{\eta} = \boldsymbol{\sigma} - \boldsymbol{\alpha}$, rather than of the stress tensor, $\boldsymbol{\sigma}$, alone.

Prager (1956) assumed a linear evolution of the back stress tensor, rate of which is proportional to the rate of the plastic strain tensor. Considering the problems related to Prager's law, such as the monotonously nonproportional plastic straining under monotonously proportional loading, and vice versa, for plane stress conditions even when the von Mises's yield criterion is used, Ziegler (1959) proposed a linear law that establishes a direct relation between the rate of the back stress tensor and the rate of the relative stress tensor. However, the stress-strain response is rarely linear, except, in some cases, in the regime of significant large strains. Moreover, although the kinematic hardening laws of Prager (1956) and Ziegler (1959) are able to describe the Bauschinger effect of some materials, they fail on predicting the remaining abnormal cyclic hardening phenomena. Having this in mind, Armstrong and Frederick (1966) proposed a nonlinear (exponential for a monotonic uniaxial loading) evolution law for the back stress tensor, the so-called Armstrong-Frederick law, by introducing a recall (dynamic recovery) term, collinear with the back stress tensor, to the Prager's evolution law. This evolution law stills nowadays as one of the most used to describe the back stress's evolution, since it enables the prediction of Bauschinger and ratcheting effects, and the smooth transient behaviour. These and some of the evolution laws for the back stress tensor presented in the literature in the last decades are expressed by

Prager (1956)
$$\dot{\boldsymbol{\alpha}} = c\dot{\boldsymbol{\varepsilon}}_{\mathrm{p}}, \tag{3.77}$$

Ziegler (1959)
$$\dot{\boldsymbol{\alpha}} = c\boldsymbol{\eta}\dot{\bar{\varepsilon}}_{\mathrm{p}}, \tag{3.78}$$

Armstrong and Frederick (1966)
$$\dot{\boldsymbol{\alpha}} = c\dot{\boldsymbol{\varepsilon}}_{\mathrm{p}} - b\boldsymbol{\alpha}\dot{\bar{\varepsilon}}_{\mathrm{p}}, \tag{3.79}$$

Chaboche (1991)
$$\dot{\boldsymbol{\alpha}} = \frac{2}{3}c\dot{\boldsymbol{\varepsilon}}_{\mathrm{p}} - \xi\left\langle 1 - \frac{\alpha_{\mathrm{tr}}}{\|\boldsymbol{\alpha}\|}\right\rangle_{c}\boldsymbol{\alpha}\dot{\bar{\varepsilon}}_{\mathrm{p}}, \tag{3.80}$$
$$\text{where } \xi = \frac{c}{c/b - \alpha_{\mathrm{tr}}},$$

Ohno and Wang (1993) (Model I)
$$\dot{\boldsymbol{\alpha}} = \frac{2}{3}c\dot{\boldsymbol{\varepsilon}}_{\mathrm{p}} - bH\left(f\right)\left\langle \mathbf{n} : \frac{\boldsymbol{\alpha}}{\|\boldsymbol{\alpha}\|}\right\rangle\boldsymbol{\alpha}\dot{\bar{\varepsilon}}_{\mathrm{p}}, \tag{3.81}$$
$$\text{where } f = \|\boldsymbol{\alpha}\| - c/b,$$

Ohno and Wang (1993) (Model II)
$$\dot{\boldsymbol{\alpha}} = \frac{2}{3}c\dot{\boldsymbol{\varepsilon}}_{\mathrm{p}} - b\left(\frac{\|\boldsymbol{\alpha}\|}{c/b}\right)^{m}\left\langle \mathbf{n} : \frac{\boldsymbol{\alpha}}{\|\boldsymbol{\alpha}\|}\right\rangle \boldsymbol{\alpha}\dot{\bar{\varepsilon}}_{\mathrm{p}}, \tag{3.82}$$

Abdel-Karim and Ohno (2000)
$$\dot{\boldsymbol{\alpha}} = \frac{2}{3}c\dot{\boldsymbol{\varepsilon}}_{\mathrm{p}} - \mu b\boldsymbol{\alpha}\dot{\bar{\varepsilon}}_{\mathrm{p}} - bH\left(f\right)\left\langle \dot{\lambda}_f\right\rangle \boldsymbol{\alpha}, \tag{3.83}$$
$$\text{where } \dot{\lambda}_f = \dot{\boldsymbol{\varepsilon}}_{\mathrm{p}} : \frac{\boldsymbol{\alpha}}{c/b} - \mu\dot{\bar{\varepsilon}}_{\mathrm{p}},$$

Yoshida and Uemori (2002)
$$\dot{\boldsymbol{\alpha}}_* = \sqrt{\frac{2}{3}}c\left(\mathbf{n} - \sqrt{\frac{\bar{\alpha}_*}{c/b}}\frac{\boldsymbol{\alpha}_*}{\|\boldsymbol{\alpha}_*\|}\right)\dot{\bar{\varepsilon}}_{\mathrm{p}}, \tag{3.84}$$
$$\text{where } \bar{\alpha}_* = \sqrt{\frac{2}{3}\boldsymbol{\alpha}_* : \boldsymbol{\alpha}_*},$$

Chen *et al.* (2005)
$$\dot{\boldsymbol{\alpha}} = \frac{2}{3}c\dot{\boldsymbol{\varepsilon}}_{\mathrm{p}} - b\left\langle \mathbf{n} : \frac{\boldsymbol{\alpha}^{\mathrm{D}}}{\|\boldsymbol{\alpha}^{\mathrm{D}}\|}\right\rangle^{\chi}\left(\frac{\|\boldsymbol{\alpha}\|}{c/b}\right)^{m}\left\langle \mathbf{n} : \frac{\boldsymbol{\alpha}}{\|\boldsymbol{\alpha}\|}\right\rangle \boldsymbol{\alpha}\dot{\bar{\varepsilon}}_{\mathrm{p}}, \text{ and} \tag{3.85}$$

Guo *et al.* (2011)
$$\dot{\boldsymbol{\alpha}} = \frac{2}{3}c\dot{\boldsymbol{\varepsilon}}_{\mathrm{p}} - \left[\mu + H\left(f\right)\left(1-\mu\right)\right]\boldsymbol{\alpha}\dot{\bar{\varepsilon}}_{\mathrm{p}}, \tag{3.86}$$
$$\text{where } \mu = \mu_0 \exp\left(-k\bar{\varepsilon}_{\mathrm{p}}\right),$$

where c, b, α_{tr}, μ, μ_0, m, χ, and k are material parameters, $H(\bullet)$ is the Heaviside's step function, i.e., $H(x) = 0$ if $x < 0$ and $H(x) = 1$ if $x \geq 0$, $\langle\bullet\rangle$ represent the McCauley brackets, i.e., $\langle x\rangle = \left(x + |x|\right)/2$, and λ_f is obtained by using the consistency condition $\dot{f} = 0$. Also, $\boldsymbol{\alpha}_*$ represents the relative kinematic motion between surfaces in the two yield surface model of Yoshida and Uemori (2002), discussed in Section 3.4.3, rather than the conventional back stress tensor, $\boldsymbol{\alpha}$.

In order to obtain a better description of hardening, Chaboche and Rousselier (1983) proposed the addition of several back stress components, e.g., the ones given by Equations 3.77-3.86, with significantly different recall constants, b_j, i.e.,

$$\boldsymbol{\alpha} = \sum_{j=1}^{N}\boldsymbol{\alpha}_j, \text{ with e.g., } \dot{\boldsymbol{\alpha}}_j = c_j\dot{\boldsymbol{\varepsilon}}_{\mathrm{p}} - b_j\boldsymbol{\alpha}_j\dot{\bar{\varepsilon}}_{\mathrm{p}}. \tag{3.87}$$

This methodology increases the flexibility of the model and allows for a good hardening description at a larger strain domain and an accurate reproduction of the transient behaviour at the onset of plastic flow. In addition, the use of one back stress component that evolves linearly together with one or more components that evolve nonlinearly also allows the description of permanent softening. The evolution of the kinematic hardening parameters with the accumulated plastic strain to accurately predict cyclic hardening phenomena (see e.g., Geng *et al.* (2002) and Chung *et al.* (2005)) or its dependency with the temperature (Metzger and Selfert, 2013) have also been considered.

The development of evolution laws for the back stress tensor over the years was mainly motivated by the desire of accurately describe the ratcheting effect. The Armstrong-Frederick law can be used to describe the ratcheting of some materials, but, generally, it overpredicts ratcheting under asymmetric loading with mean stress, because the dynamic recovery term is always active. Considering this, Chaboche (1991) introduced a threshold to the dynamic

recovery term (see Equation 3.80). This way, the back stress evolves linearly below the threshold and nonlinearly, like the Armstrong-Frederick law and attaining the same asymptotic value, when above it. Chaboche (1991) used the superposition (according to Equation 3.87) of a linear model, two classical Armstrong-Frederick models and a fourth with a threshold to describe the ratcheting behaviour of a 316 stainless steel. A generalization of this model was later proposed by Chaboche (1994) aiming at a higher flexibility. Ohno and Wang (1993) proposed a different approach by considering a critical state given by a surface $f = 0$. In their multi-linear Model I, the dynamic recovery term is only active in the critical state, i.e., when the back stress reaches this surface (see Equation 3.81). They also proposed a smooth formulation (Model II, see Equation 3.82), where the Heaviside step function is replaced by a power function, thus providing more realistic predictions. The factor inside the McCauley brackets deactivates the dynamic recovery term during the beginning of the reverse plastic flow, therefore reducing the prediction of ratcheting. One disadvantage of Ohno and Wang (1993) models rely on the high number of $\boldsymbol{\alpha}_j$ components required to describe realistic shapes of stress-strain hysteresis loops, hence employing a high number of material parameters (Yoshida and Uemori, 2002). In the work of Kang *et al.* (2003) Model I, Equation 3.81, is rewritten to explicitly express the back stress's rate as a function of the critical value c/b. This critical value is then assumed to be dependent on the accumulated plastic strain in order to describe strain range dependent cyclic hardening. Modifications on the Model II of Ohno and Wang (1993) include the works of McDowell (1995) and Jiang and Sehitoglu (1996), where, aiming at a better description of multiaxial ratcheting effects, the exponent m was assumed highly nonlinear and dependent on the noncoaxiality of the plastic strain rate and the back stress, rather than as a constant material parameter. Chen *et al.* (2005) also proposed a modification of Model II, by multiplying the recovery term with a factor dependent on the noncoaxiality of the plastic strain rate and the back stress to obtain an accurate prediction of both multiaxial and uniaxial ratcheting simultaneously.

Later, Abdel-Karim and Ohno (2000) proposed a combination of the Armstrong and Frederick (1966)'s model with the Ohno and Wang (1993)'s Model I, by means of a weighting factor μ (see Equation 3.83). This way, the resulting back stress's evolution law includes a dynamic recovery term that is always active and another that is only active when a critical stage is reached, thus having a higher flexibility. Hence, the parameter μ can be tuned in order to obtain an accurate reproduction of experimental ratcheting effects. Due to its flexibility, some modifications to the model of Abdel-Karim and Ohno (2000) have been proposed (Kang (2004); Guo *et al.* (2011)). Kang (2004) proposed the replacement of $< \dot{\lambda}_f >$ by $(1-\mu)\dot{\bar{\varepsilon}}_{\mathrm{p}}$ to describe higher ratcheting under multiaxial cycling compared to uniaxial cycling, as verified for a U71Mn rail steel. And Guo *et al.* (2011) considered that μ evolves exponentially with the accumulated plastic strain to describe the deceleration of ratcheting strain rate with the increasing number of cycles.

3.4.2.1 Rheological model of Armstrong-Frederick kinematic hardening

The key features of the one-dimensional rheological model of the widely used Armstrong-Frederick kinematic hardening law, in which the studied constitutive models (see Chapters 4 and 5) are based, are now presented. The formulation is related to the small strain regime and is restricted to pure kinematic hardening.

The classical elastoplastic rheological model of Armstrong-Frederick kinematic hardening is shown in Fig. 3.6. The elastoplastic behaviour is modelled by means of the additive decomposition of the total strain, ε, into elastic, ε_{e}, and plastic, ε_{p}, parts. Similarly, in order to model the kinematic hardening the plastic strain is also additively decomposed into "elastic", $\varepsilon_{\mathrm{p_e}}$, and "inelastic", $\varepsilon_{\mathrm{p_i}}$, parts, i.e.,

$$\varepsilon = \varepsilon_{\mathrm{e}} + \varepsilon_{\mathrm{p}} \;\text{ and }\; \varepsilon_{\mathrm{p}} = \varepsilon_{\mathrm{p_e}} + \varepsilon_{\mathrm{p_i}}. \tag{3.88}$$

The part $\varepsilon_{\mathrm{p_e}}$ represents the strain in the "hardening" spring, with "elastic" modulus c, and, according to Lion (2000), it is related to local elastic lattice deformations caused by dislocations, while the part $\varepsilon_{\mathrm{p_i}}$ is associated to local plastic deformations due to inelastic slip on crystallographic slip systems. The dashpot, to which $\varepsilon_{\mathrm{p_i}}$ is associated, enables the modelling of the nonlinear kinematic hardening and has a "pseudo"-viscosity of $c/(\dot{\lambda}b)$. The quantity b is a dimensionless material parameter and λ is the so-called plastic multiplier, that is a nonnegative quantity (where $\dot{\lambda} = 0$ for pure elastic deformations and $\dot{\lambda} > 0$ for elastoplastic deformations). Moreover, E is the elastic modulus of the elastic spring and the friction block establishes the yield stress, σ_{y}.

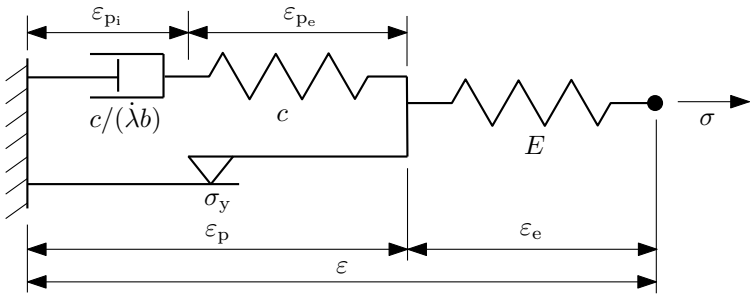

Figure 3.6: Classical rheological model of Armstrong-Frederick kinematic hardening.

The Helmholtz free energy of the model of Fig. 3.6 can be solely defined as a function of the elastic strains, ε_{e} and $\varepsilon_{\mathrm{p_e}}$, and additively decomposed as

$$\psi = \psi_{\mathrm{e}}(\varepsilon_{\mathrm{e}}) + \psi_{\mathrm{kin}}(\varepsilon_{\mathrm{p_e}}) = \frac{1}{2}E(\varepsilon - \varepsilon_{\mathrm{p}})^2 + \frac{1}{2}c(\varepsilon_{\mathrm{p}} - \varepsilon_{\mathrm{p_i}})^2, \tag{3.89}$$

where the two terms ψ_{e} and ψ_{kin} are related to the energy stored in the elastic and "hardening" springs, respectively. For any arbitrary thermodynamic process, the constitutive equations

must fulfil the Clausius-Duhem inequality, which is expressed by

$$-\dot{\psi} + \sigma\dot{\varepsilon} = \left(\sigma - \frac{\partial\psi}{\partial\varepsilon}\right)\dot{\varepsilon} - \frac{\partial\psi}{\partial\varepsilon_{\mathrm{p}}}\dot{\varepsilon}_{\mathrm{p}} - \frac{\partial\psi}{\partial\varepsilon_{\mathrm{p_i}}}\dot{\varepsilon}_{\mathrm{p_i}} \geq 0, \tag{3.90}$$

in the case of isothermal processes (see Equation 2.50). The stress-strain relation in the elastic spring is given by $\sigma = \partial\psi/\partial\varepsilon = E(\varepsilon - \varepsilon_{\mathrm{p}})$. Whereas the stress in the "hardening" spring (back stress) is introduced as

$$\alpha = -\frac{\partial\psi}{\partial\varepsilon_{\mathrm{p_i}}} = c(\varepsilon_{\mathrm{p}} - \varepsilon_{\mathrm{p_i}}). \tag{3.91}$$

From these stress-strain relations the Clausius-Duhem inequality can be reduced to $(\sigma - \alpha)\dot{\varepsilon}_{\mathrm{p}} + \alpha\dot{\varepsilon}_{\mathrm{p_i}} \geq 0$. The evolution equations of the so-called internal variables, ε_{p} and $\varepsilon_{\mathrm{p_i}}$, are then chosen accordingly to the requirement that this inequality must be fulfilled for any thermodynamic process, providing

$$\dot{\varepsilon}_{\mathrm{p}} = \dot{\lambda}\frac{\partial\Phi}{\partial(\sigma - \alpha)} = \dot{\lambda}\mathrm{sign}(\sigma - \alpha) \text{ and } \dot{\varepsilon}_{\mathrm{p_i}} = \dot{\lambda}\frac{\mathrm{b}}{\mathrm{c}}\alpha. \tag{3.92}$$

The evolution of the plastic deformation follows the associated flow rule and is driven by the relative stress $\eta = \sigma - \alpha$. The set of constitutive equations is completed with the Kuhn-Tucker conditions, i.e., $\dot{\lambda} \geq 0$, $\Phi = |\sigma - \alpha| - \sigma_{\mathrm{y}} \leq 0$, and $\dot{\lambda}\Phi = 0$, which are used to compute the rate of the plastic multiplier, $\dot{\lambda}$.

During plastic deformation, the total stress can be represented as the sum of the back stress and the stress in the friction block, i.e., the yield stress, σ_{y}. Thus, since σ_{y} is constant, the stress, $\sigma = \sigma_{\mathrm{y}} + \alpha$, only varies with α. This way, from Equations 3.91 and 3.92b, the evolution of the stress is provided by the nonlinear expression

$$\dot{\sigma} = \dot{\alpha} = c\dot{\varepsilon}_{\mathrm{p}} - \dot{\lambda}b\alpha. \tag{3.93}$$

From this relation and Equation 3.91, one concludes that when σ does not evolve any longer ($\dot{\sigma} = 0$), the relation $\dot{\varepsilon}_{\mathrm{p}} = \dot{\varepsilon}_{\mathrm{p_i}}$ holds, which leads to the statement

$$\dot{\lambda}\mathrm{sign}(\sigma - \alpha) = \dot{\lambda}\frac{b}{c}\alpha \Rightarrow \alpha = \frac{c}{b}\mathrm{sign}(\sigma - \alpha). \tag{3.94}$$

This indicates that the stress value at which the saturation process is finished, is controlled by the ratio c/b. The parameter b defines how fast this value is achieved.

On the other hand, from Equations 3.91 and 3.92b, the evolution equation for the inelastic part of the plastic deformation can be expressed as $\dot{\varepsilon}_{\mathrm{p_i}} = \dot{\lambda}b(\varepsilon_{\mathrm{p}} - \varepsilon_{\mathrm{p_i}})$. So, if the kinematic hardening parameter b tends to zero, it yields that $\dot{\varepsilon}_{\mathrm{p_i}} \to 0$. Thus, the back stress (Equation 3.91) became proportional to the plastic strain, ε_{p}, and hence the linear kinematic hardening is recovered. The same conclusion can be obtained from Equation 3.93.

3.4.2.2 Modified rheological model of kinematic hardening

A modification to the classical rheological model (Fig. 3.6) of Armstrong-Frederick kinematic hardening is now presented in order to include multiple, N, back stress components, hence corresponding to a 1D kinematic hardening description of Equation 3.87. The modification consists of applying multiple, N, sets of "hardening" springs and dashpots in parallel to the friction block, providing the model represented in Fig. 3.7.

The small strain one-dimensional constitutive model is derived analogously to Section 3.4.2.1. Based on Fig. 3.7, and similarly to Equation 3.88, the plastic strain accepts N different additive decompositions into "elastic", $\varepsilon^j_{\mathrm{p_e}}$, and "inelastic", $\varepsilon^j_{\mathrm{p_i}}$, parts, i.e.,

$$\varepsilon_{\mathrm{p}} = \varepsilon^j_{\mathrm{p_e}} + \varepsilon^j_{\mathrm{p_i}} \;\; \forall \;\; j = 1 \ldots N. \tag{3.95}$$

The Helmholtz free energy, that represents the energy stored in the $N+1$ springs of the model of Fig. 3.7, is additively decomposed following

$$\psi = \psi_{\mathrm{e}}(\varepsilon_{\mathrm{e}}) + \sum_{j=1}^{N} \psi^j_{\mathrm{kin}}(\varepsilon^j_{\mathrm{p_e}}) = \frac{1}{2} E(\varepsilon - \varepsilon_{\mathrm{p}})^2 + \sum_{j=1}^{N} \frac{1}{2} c^j (\varepsilon_{\mathrm{p}} - \varepsilon^j_{\mathrm{p_i}})^2. \tag{3.96}$$

Introducing this energy potential on the Clausius-Duhem inequality yields $(\sigma - \alpha)\dot{\varepsilon}_{\mathrm{p}} + \sum_{j=1}^{N} \alpha^j \dot{\varepsilon}^j_{\mathrm{p_i}} \geq 0$, where the total back stress is given by the sum $\alpha = \sum_{j=1}^{N} \alpha^j$ and the

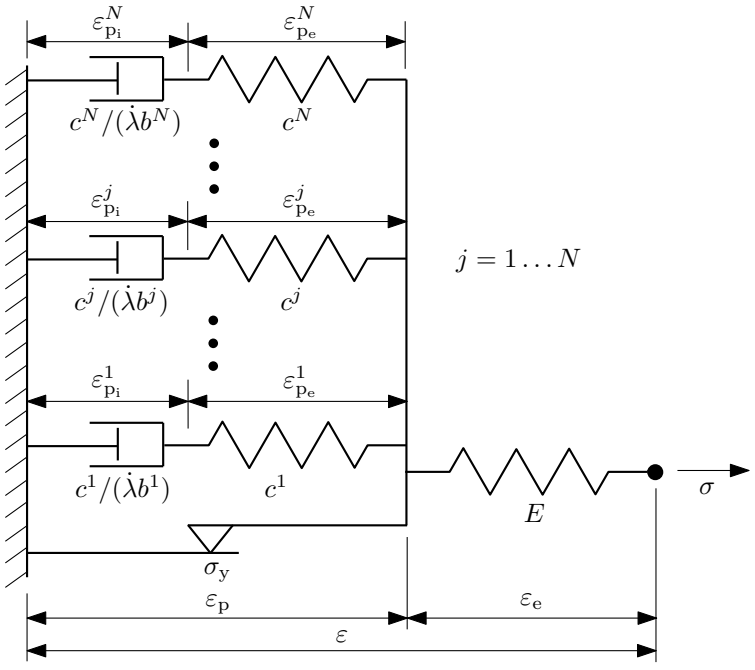

Figure 3.7: Modified rheological model of Armstrong-Frederick kinematic hardening.

back stresses α^j are defined as

$$\alpha^j = -\frac{\partial \psi}{\partial \varepsilon_{\mathrm{p_i}}^j} = c^j(\varepsilon_{\mathrm{p}} - \varepsilon_{\mathrm{p_i}}^j) \ \forall \ j = 1 \ldots N. \tag{3.97}$$

The Clausius-Duhem inequality is fulfilled by Equation 3.92a and

$$\dot{\varepsilon}_{\mathrm{p_i}}^j = \dot{\lambda}\frac{b^j}{c^j}\alpha^j \ \forall \ j = 1 \ldots N. \tag{3.98}$$

From Equations 3.97 and 3.98 the following evolution equation for α^j is obtained,

$$\dot{\alpha}^j = c^j \dot{\varepsilon}_{\mathrm{p}} - \dot{\lambda} b^j \alpha^j \ \forall \ j = 1 \ldots N. \tag{3.99}$$

The set of constitutive equations is completed with the Kuhn-Tucker conditions.

The total stress is given by the sum of the stress in the friction block and the N back stresses, i.e., $\sigma = \sigma_{\mathrm{y}} + \sum_{j=1}^{N} \alpha^j$, and saturates at the value $\sigma = (\sigma_{\mathrm{y}} + \sum_{j=1}^{N} c^j/b^j)\mathrm{sign}(\sigma - \alpha)$. By using multiple back stresses with different b^j a good description of the transient behaviour upon the onset of yielding is obtained. Moreover, if one or more of the back stresses evolves linearly, i.e., $b \approx 0$, the permanent softening effect can be described. This is possible because the back stress that evolves linearly creates an offset in strains (horizontal offset in the stress-accumulated plastic strain strain curve) between the monotonic curve and the one obtained after reverse loading. This methodology to describe the permanent softening effect is schematically represented in Fig. 3.8. The stress-accumulated plastic strain relation for a uniaxial tension-compression test obtained with a pure kinematic hardening model with two back stresses (α_1 and α_2, with nonlinear and linear evolutions, respectively) is depicted. Due to the nature of the kinematic hardening approach, the Bauschinger effect is modelled. For a more flexible description of this effect the combination of isotropic and kinematic hardening

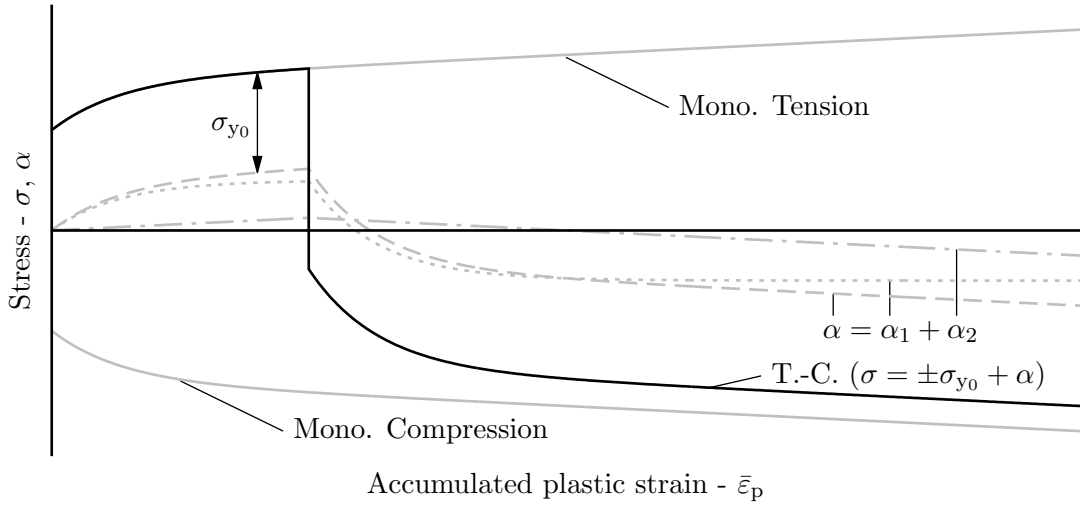

Figure 3.8: Description of the permanent softening effect using multiple back stresses.

law is widely employed. The use of one back stress that evolves nonlinearly models the smooth transient behaviour upon the onset of yielding. More back stresses of this kind can be used to obtain a higher flexibility. Also, in Fig. 3.8, the back stress that evolves linearly enables the modelling of the permanent softening effect.

3.4.3 Multi-surface models

Aiming at a simultaneous description of Bauschinger effect and smooth transient behaviour by means of linear kinematic hardening, Mroz (1967) proposed the multi-surface approach, later modified by Krieg (1975) and Dafalias and Popov (1976). It consists of multiple embedded surfaces that are initially coaxial, for initially isotropic materials, and translate linearly, hence providing a piece-wise linear reproduction of the uniaxial stress-strain relation. The region delimited by the most inner surface is the elastic region. When the material point reaches that surface, it undergoes elastoplastic deformation and the surface translates linearly, rendering a constant elastoplastic modulus, while the remaining surfaces do not evolve. Thereafter, when the second surface is reached, the two surfaces translate together at a lower rate. This way, the nonlinear stress-strain relation is described by multiple regions with constant elastoplastic modulus, hence requiring a high number of yield surfaces to describe a nonlinear curve smoothly.

Dafalias and Popov (1976) proposed a model based on the multi-surface approach, in which a nonlinear stress-strain relation is described by considering only two surfaces and additional state variables. Both inner (loading) and outer (boundary) surfaces are allowed to expand and translate (see Fig. 3.9.) While the evolution of the loading surface, before reaching the boundary surface (see Fig. 3.9b), establishes the transient behaviour, the evolution of the boundary surface provides the long-term hardening behaviour. The state variable that controls the loading surface's evolution is the distance d between the stress point in the loading surface and the corresponding (fictitious) one in the boundary surface (it is usually considered that these stress points have the same normal to the loading and boundary surfaces, respectively).

In addition to the Bauschinger effect and transient behaviour, multi-surface models can describe permanent softening by allowing the boundary surface to translate. Considering its flexibility, several works have been presented on the development of two-yield surface models and algorithmic procedures for its numerical implementation, see e.g., Geng and Wagoner (2002), Yoshida and Uemori (2002), Cardoso and Yoon (2009), and Kim *et al.* (2013). The model proposed by Yoshida and Uemori (2002) has received much attention due to its ability to describe work-hardening stagnation, Bauchinger effect, transient behaviour and permanent softening with reasonably few parameters. On the one hand, they proposed a new evolution equation of the relative kinematic motion of the loading surface with respect to the boundary one (see Equation 3.84), that is more versatile in the description of the transient behaviour when compared with the back stress evolution of Armstrong-Frederick law. On the other

hand, the work-hardening stagnation is modelled by introducing the so-called non-isotropic hardening surface in the stress space. It is then assumed that the boundary surface suffer isotropic hardening only when its center point (back stress) lies on this surface. When the center point of the boundary surface is inside the non-isotropic hardening surface, it can only translate. The increasing of the plastic strain region of work-hardening stagnation with accumulated plastic strain can also be reproduced by assuming the expansion of the non-isotropic hardening surface.

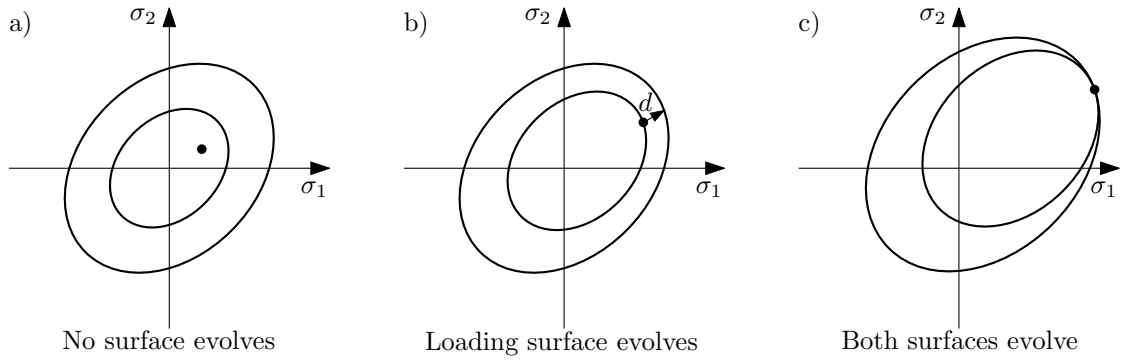

Figure 3.9: Surfaces' evolution in the model of Dafalias and Popov (1976).

3.4.4 Homogeneous anisotropic hardening model

Recently, Barlat *et al.* (2011) proposed the homogeneous anisotropic hardening (HAH) approach, which allows the description of the Bauschinger effect without taking the kinematic hardening concept into account. Following this approach, the yield criterion obeys the isotropic hardening approach, but the yield potential is modified in order to induce asymmetries in the yield surface as plastic deformation takes place, i.e.,

$$\begin{aligned}\Phi &= \left(\bar{\sigma}^q + \bar{\sigma}_{\mathrm{h}}^q\right)^{\frac{1}{q}} - \sigma_{\mathrm{y}} \\ &= \left(\bar{\sigma}^q + f_1^q \left|\mathbf{h}_{\mathrm{s}} : \mathbf{s} - |\mathbf{h}_{\mathrm{s}} : \mathbf{s}|\right|^q + f_2^q \left|\mathbf{h}_{\mathrm{s}} : \mathbf{s} + |\mathbf{h}_{\mathrm{s}} : \mathbf{s}|\right|^q\right)^{\frac{1}{q}} - \sigma_{\mathrm{y}},\end{aligned} \tag{3.100}$$

where the exponent q is a material parameter, $\bar{\sigma}_{\mathrm{h}}$ is a fluctuating component of the yield potential that distorts the yield surface's shape, f_1, and f_2 are functions of proper state variables, and $\mathbf{h}_{\mathrm{s}}$ is the microstructure deviator. This deviator is a state variable that expresses the material deformation's history and thus evolves during plastic deformation.

The hardening mechanism of this approach is represented in Fig. 3.10. When loading is imposed in one direction (direction 1 in this figure), the yield surface expands and flattens in the opposite direction, therefore predicting the Bauschinger effect. The distortion of the yield surface's shape is ruled by the evolution of f_1 and f_2, whereas the deviator, $\mathbf{h}_{\mathrm{s}}$, keeps trace of changes in the loading direction. The HAH approach was later extended independently by Barlat *et al.* (2013) and He *et al.* (2013) to account for cross-hardening. The formulation proposed by He *et al.* (2013) includes a fluctuating component that also allows the descrip-

tion of the work-hardening stagnation. After that, the HAH formulation was improved by Barlat *et al.* (2014), to allow the yield stress in cross-loading conditions to be lower than the corresponding stress on the monotonic flow curve.

In the work of Lee *et al.* (2013b) a dislocation-based hardening model has been incorporated into the HAH approach to describe work-hardening stagnation. Moreover, a model following the HAH approach accounting for the nonlinear elastic behaviour during unloading and reloading according to the quasi-plastic-elastic approach has been presented by Lee *et al.* (2013a), aiming at an accurate prediction of springback. The main disadvantages of this approach rely on the high number of parameters and state variables used, along with the severe complexity of its formulation and corresponding numerical implementation (see the work of Lee *et al.* (2012a) regarding an algorithmic procedure for the HAH approach).

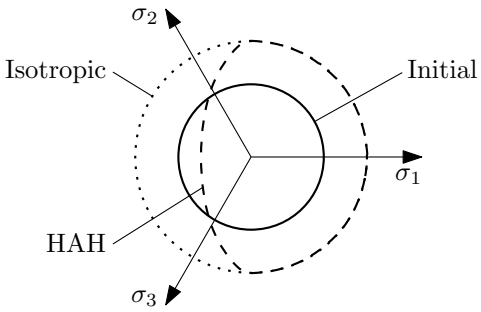

Figure 3.10: Shape's evolution of the yield surface according the HAH approach.

3.4.5 Hardening models for yield anisotropy evolution

The assumption that the yield surface's shape remains unchanged as plastic deformation takes place is widely assumed for sheet metal forming analysis, since it is considered valid for a vast range of metals under moderated strains. However, the changes of the crystallographic texture during plastic deformation may be significant for higher amounts of straining. As a result, along with the crystallographic texture, the yield surface's shape evolves as well, i.e., occurs distortional hardening, as verified experimentally by, e.g., Khan *et al.* (2010).

Constitutive models that account for this type of hardening are usually based on the evolution of either a fourth-order anisotropic tensor (Feigenbaum and Dafalias, 2007, Noman *et al.*, 2010, Pietryga *et al.*, 2012, Shi *et al.*, 2014, Feigenbaum and Dafalias, 2014) or anisotropy parameters directly (Plunkett *et al.*, 2006, Aretz, 2008, Darbandi and Pourboghrat, 2011, Peters *et al.*, 2014, Tuninetti *et al.*, 2015) during plastic deformation.

On the one hand, the fourth-order anisotropic tensor that expresses the material's plastic symmetry is treated as a state variable, whose evolution, with the plastic deformation, follows a nonlinear function of the saturation type. Doing this way, distortional hardening effects are modelled, such as cross-hardening (Noman *et al.*, 2010), directional hardening (i.e., development of a region of high curvature in the direction of loading and flattening in the

opposite direction) (Feigenbaum and Dafalias, 2007, 2014), or both effects (Pietryga *et al.*, 2012, Shi *et al.*, 2014).

On the other hand, for a more general description of the distortional hardening, multiple sets of anisotropy parameters, corresponding to a finite number of fixed levels of either equivalent plastic strain or plastic work, are initially determined. And then, the yield surfaces corresponding to any level of equivalent plastic strain (or plastic work) are obtained from piece-wise linear interpolations (Plunkett *et al.*, 2006, Aretz, 2008, Tuninetti *et al.*, 2015) or by fitting of each anisotropy parameter adopting a proper function (Darbandi and Pourboghrat, 2011, Peters *et al.*, 2014). This approach allows de continuous description of the variation of the yield stress and r-value with the angle from RD along the deformation process. In addition, this procedure can also be used to model the anisotropy's evolution with the temperature (Abedrabbo *et al.*, 2007).

Chapter 4

Small strain elastoplasticity

The continuum mechanical extension of the rheological model of Armstrong-Frederick kinematic hardening to three-dimensional conditions is presented in this chapter under the assumption of small (infinitesimal) strains. Since this rate-independent model is the foundation of the hypoelastic-based model discussed in Chapter 5, the derivation of the constitutive equations and their algorithmic implementation are thoroughly treated here. This is carried out in a general way regarding the yield function, thus allowing for any isotropic or anisotropic (quadratic or nonquadratic) yield function. Moreover, in order to attain a better description of cyclic hardening phenomena, the model is improved so it can consider multiple back stress components.

4.1 Constitutive modelling

4.1.1 Small strain tensor and its additive decomposition

In continuum mechanics, small strain theories are related to infinitesimal deformations of continuum bodies. Deformations are assumed as infinitesimal when the displacement gradient, $\nabla \boldsymbol{u}$, is sufficiently small compared to unity, i.e., $\|\nabla \boldsymbol{u}\| \ll 1$. In this situation, the second-order (nonlinear) terms of Equations 2.23 and 2.24 can be neglected, resulting in the approximation

$$\mathbf{C} \approx \mathbf{B} \approx \mathbf{I} + \nabla \boldsymbol{u} + (\nabla \boldsymbol{u})^{\mathrm{T}}. \tag{4.1}$$

Analogously, applying the same order of approximation to the definitions of the Green-Lagrange strain tensor, $\mathbf{E}^{(2)}$ (Equation 2.29), and its Eulerian counterpart, $\boldsymbol{\varepsilon}^{(2)}$, yields

$$\mathbf{E}^{(2)} \approx \boldsymbol{\varepsilon}^{(2)} \approx \frac{1}{2}[\nabla \boldsymbol{u} + (\nabla \boldsymbol{u})^{\mathrm{T}}]. \tag{4.2}$$

From this approximation, under the assumption of infinitesimal deformations, the small strain tensor is defined as

$$\boldsymbol{\varepsilon} = \frac{1}{2}[\nabla \boldsymbol{u} + (\nabla \boldsymbol{u})^{\mathrm{T}}]. \tag{4.3}$$

It can be shown that all Lagrangian and Eulerian strain measures defined by Equations 2.25 and 2.27, respectively, converge to the same small strain expression, i.e., for any m and within an error of second order in $\nabla \boldsymbol{u}$, stands the approximation $\mathbf{E}^{(m)} \approx \boldsymbol{\varepsilon}^{(m)} \approx \boldsymbol{\varepsilon}$ (Souza Neto *et al.*, 2008).

Analogously to the additive decomposition of Equation 3.88a, the three-dimensional total small strain tensor can be additively decomposed into elastic, $\boldsymbol{\varepsilon}_e$, and plastic, $\boldsymbol{\varepsilon}_p$, parts, i.e.,

$$\boldsymbol{\varepsilon} = \boldsymbol{\varepsilon}_{\mathrm{e}} + \boldsymbol{\varepsilon}_{\mathrm{p}}, \tag{4.4}$$

and to this additive decomposition corresponds the following rate form

$$\dot{\boldsymbol{\varepsilon}} = \dot{\boldsymbol{\varepsilon}}_{\mathrm{e}} + \dot{\boldsymbol{\varepsilon}}_{\mathrm{p}}. \tag{4.5}$$

Moreover, the plastic strain tensor can also be additively decomposed into "elastic", $\varepsilon_{\mathrm{p_e}}$, and "inelastic", $\varepsilon_{\mathrm{p_i}}$, parts, i.e.,

$$\boldsymbol{\varepsilon}_{\mathrm{p}} = \boldsymbol{\varepsilon}_{\mathrm{p_e}} + \boldsymbol{\varepsilon}_{\mathrm{p_i}} \Rightarrow \dot{\boldsymbol{\varepsilon}}_{\mathrm{p}} = \dot{\boldsymbol{\varepsilon}}_{\mathrm{p_e}} + \dot{\boldsymbol{\varepsilon}}_{\mathrm{p_i}}. \tag{4.6}$$

This additional decomposition allows the description of the kinematic hardening and is physically motivated (see Section 3.4.2.1).

4.1.2 Helmholtz free energy potential

It is assumed that the plastic deformation and hardening effects do not affect the elastic properties of the material. This way, the Helmholtz free energy per unit volume, $\psi = \rho\bar{\psi}$, associated to the Armstrong-Frederick model of kinematic hardening, can be additively split into three parts, as

$$\begin{aligned} \psi &= \psi_{\mathrm{e}}(\boldsymbol{\varepsilon}_{\mathrm{e}}) + \psi_{\mathrm{kin}}(\boldsymbol{\varepsilon}_{\mathrm{p_e}}) + \psi_{\mathrm{iso}}(\bar{\varepsilon}_{\mathrm{p}}) \\ &= \frac{1}{2}\boldsymbol{\varepsilon}_{\mathrm{e}} : \mathbb{D} : \boldsymbol{\varepsilon}_{\mathrm{e}} + \frac{1}{2}\boldsymbol{\varepsilon}_{\mathrm{p_e}} : \mathbb{D}_{\mathrm{p}} : \boldsymbol{\varepsilon}_{\mathrm{p_e}} + \psi_{\mathrm{iso}}(\bar{\varepsilon}_{\mathrm{p}}), \end{aligned} \tag{4.7}$$

where the fourth-order tensor $\mathbb{D}$ is the elastic stiffness tensor, given by $\mathbb{D} = \Lambda_{\mathrm{e}}\mathbf{I} \otimes \mathbf{I} + 2\mu_{\mathrm{e}}\mathbb{I}$. The elastic parameters μ_{e} and Λ_{e} are the shear modulus and the Lamé constant, respectively, which are related to the elastic (Young's) modulus, E, and the Poisson ratio, ν, by $\mu_{\mathrm{e}} = E/[2(1+\nu)]$ and $\Lambda_{\mathrm{e}} = \nu E/[(1+\nu)(1-2\nu)]$. Moreover, $\mathbb{D}_{\mathrm{p}} = c\mathbb{I}$ is the fourth-order "elastic stiffness tensor" associated to the hardening spring (see Fig. 3.6) and $\mathbb{I}$ is the symmetric fourth order identity tensor, i.e., $I_{ijkl} = 1/2(\delta_{ik}\delta_{jl} + \delta_{il}\delta_{jk})$.

In Equation 4.7, analogously to Equation 3.89, ψ_{e} is related to the macroscopic elastic material properties and represents the energy stored in the elastic spring, while the term ψ_{kin} is related to the kinematic hardening and represents the elastic energy stored in dislocation

fields (in other words, the energy stored in the hardening spring). Due to the dependence of the yield stress on the accumulated plastic strain, i.e., $\sigma_{\mathrm{y}} = \sigma_{\mathrm{y}}(\bar{\varepsilon}_{\mathrm{p}})$, the additional term ψ_{iso} is taken into account to represent the amount of stored energy due to isotropic hardening (refer to Rice (1971), for a micromechanical motivation). Here, $\bar{\varepsilon}_{\mathrm{p}}$ is the scalar-valued strain-like isotropic hardening variable, i.e., the accumulated (effective) plastic strain, defined by

$$\bar{\varepsilon}_{\mathrm{p}} = \int_0^t \dot{\bar{\varepsilon}}_{\mathrm{p}} dt, \tag{4.8}$$

whose evolution rate, $\dot{\bar{\varepsilon}}_{\mathrm{p}}$, is defined in the following (see Equation 4.13c).

4.1.3 Clausius-Duhem inequality

Taking Equation 4.7 into account, the Clausius-Duhem form of the entropy inequality for isothermal processes (Equation 2.50) is expressed as

$$-\dot{\psi} + \boldsymbol{\sigma} : \dot{\boldsymbol{\varepsilon}} = \left(\boldsymbol{\sigma} - \frac{\partial \psi}{\partial \boldsymbol{\varepsilon}}\right) : \dot{\boldsymbol{\varepsilon}} - \frac{\partial \psi}{\partial \boldsymbol{\varepsilon}_{\mathrm{p}}} : \dot{\boldsymbol{\varepsilon}}_{\mathrm{p}} - \frac{\partial \psi}{\partial \boldsymbol{\varepsilon}_{\mathrm{p_i}}} : \dot{\boldsymbol{\varepsilon}}_{\mathrm{p_i}} - \frac{\partial \psi}{\partial \bar{\varepsilon}_{\mathrm{p}}} \dot{\bar{\varepsilon}}_{\mathrm{p}} \geq 0. \tag{4.9}$$

Employing the definitions of the stress and back stress tensors in the form

$$\boldsymbol{\sigma} = \frac{\partial \psi}{\partial \boldsymbol{\varepsilon}} = \mathbb{D} : \boldsymbol{\varepsilon}_{\mathrm{e}} = \mathbb{D} : (\boldsymbol{\varepsilon} - \boldsymbol{\varepsilon}_{\mathrm{p}}) \text{ and} \tag{4.10}$$

$$\boldsymbol{\alpha} = -\frac{\partial \psi}{\partial \boldsymbol{\varepsilon}_{\mathrm{p_i}}} = c\boldsymbol{\varepsilon}_{\mathrm{p_e}} = c(\boldsymbol{\varepsilon}_{\mathrm{p}} - \boldsymbol{\varepsilon}_{\mathrm{p_i}}), \tag{4.11}$$

and of the scalar-valued stress-like internal variable $R(\bar{\varepsilon}_{\mathrm{p}}) = -\partial\psi/\partial\bar{\varepsilon}_{\mathrm{p}}$, that is related to the isotropic hardening and is energy conjugated to $\bar{\varepsilon}_{\mathrm{p}}$, the inequality 4.9 can be simplified as

$$\boldsymbol{\eta} : \dot{\boldsymbol{\varepsilon}}_{\mathrm{p}} + \boldsymbol{\alpha} : \dot{\boldsymbol{\varepsilon}}_{\mathrm{p_i}} + R\dot{\bar{\varepsilon}}_{\mathrm{p}} \geq 0. \tag{4.12}$$

The expression of the stress tensor (Equation 4.10) is physically motivated, since it ensures that the inequality 4.9 is indifferent to $\dot{\boldsymbol{\varepsilon}}$.

4.1.4 Evolution equations

In order to ensure the second law of thermodynamics, inequality 4.12 must be satisfied for any arbitrary thermodynamic process or, in other words, for any arbitrary $\dot{\boldsymbol{\varepsilon}}$, $\dot{\boldsymbol{\varepsilon}}_{\mathrm{p}}$, $\dot{\boldsymbol{\varepsilon}}_{\mathrm{p_i}}$, and $\dot{\bar{\varepsilon}}_{\mathrm{p}}$. The Clausius-Duhem inequality is sufficiently satisfied by imposing Equation 4.10 along with the evolution equations

$$\dot{\boldsymbol{\varepsilon}}_{\mathrm{p}} = \dot{\lambda}\frac{\partial \Psi}{\partial \boldsymbol{\eta}} = \dot{\lambda}\mathbf{n}, \;\; \dot{\boldsymbol{\varepsilon}}_{\mathrm{p_i}} = \dot{\lambda}\frac{b}{c}\boldsymbol{\alpha}, \text{ and } \dot{\bar{\varepsilon}}_{\mathrm{p}} = \dot{\lambda}\frac{\partial \Phi}{\partial R} = \dot{\lambda}, \tag{4.13}$$

where Ψ is the plastic potential that drives the plastic flow direction, $\mathbf{n} = \partial\Psi/\partial\boldsymbol{\eta}$. The evolution equation for $\boldsymbol{\varepsilon}_{\mathrm{p_i}}$ (Equation 4.13b) has been chosen according to Armstrong and

Frederick (1966). The assumption of Equation 4.13c is useful when the effective stress does not have its conjugate effective strain explicitly defined with respect to the plastic strain tensor, as happens to most of the complex nonquadratic yield functions (Banabic, 2010).

In metal plasticity the difference between the plastic and yield potentials is commonly neglected, i.e., $\Psi = \Phi$, which corresponds to an associated flow rule (usually referred to as normality rule), where

$$\dot{\boldsymbol{\varepsilon}}_{\mathrm{p}} = \dot{\lambda}\frac{\partial \Phi}{\partial \boldsymbol{\eta}}. \tag{4.14}$$

Since this assumption is widely accepted in the modelling of metal plasticity, it will be also taken into account in this work.

Differentiating Equation 4.11 and applying Equation 4.13b, one obtains the evolution equation for the back stress tensor, in the form

$$\dot{\boldsymbol{\alpha}} = c\dot{\boldsymbol{\varepsilon}}_{\mathrm{p}} - \dot{\lambda} b \boldsymbol{\alpha}. \tag{4.15}$$

Finally, the evolution equation for the Cauchy stress tensor is achieved by differentiating Equation 4.10, as

$$\begin{aligned} \dot{\boldsymbol{\sigma}} = \mathbb{D} : \dot{\boldsymbol{\varepsilon}}_{\mathrm{e}} &= \mathbb{D} : (\dot{\boldsymbol{\varepsilon}} - \dot{\boldsymbol{\varepsilon}}_{\mathrm{p}}) \\ &= \mathbb{D} : (\dot{\boldsymbol{\varepsilon}} - \dot{\lambda}\mathbf{n}), \end{aligned} \tag{4.16}$$

which represents the isotropic linear elastic Hooke's law.

4.1.5 Yield potential

In order to account for both kinematic and isotropic hardening, the yield potential for this constitutive model can be written as

$$\Phi(\boldsymbol{\eta}, \bar{\varepsilon}_{\mathrm{p}}) = \bar{\eta}(\boldsymbol{\eta}) - [\sigma_{\mathrm{y}_0} - R(\bar{\varepsilon}_{\mathrm{p}})], \tag{4.17}$$

for general 3D stress states. Here, $\bar{\eta}(\boldsymbol{\eta})$ is the effective stress defined by an isotropic or anisotropic yield function. If the isotropic hardening is assumed to follow, e.g., Voce's exponential law, then

$$\psi_{\mathrm{iso}}(\bar{\varepsilon}_{\mathrm{p}}) = Q\left(\bar{\varepsilon}_{\mathrm{p}} + \frac{1}{\beta}e^{-\beta\bar{\varepsilon}_{\mathrm{p}}}\right) \text{ and } R(\bar{\varepsilon}_{\mathrm{p}}) = -Q\left(1 - e^{-\beta\bar{\varepsilon}_{\mathrm{p}}}\right), \tag{4.18}$$

otherwise, in the case of Swift's power law, it yields

$$\psi_{\mathrm{iso}}(\bar{\varepsilon}_{\mathrm{p}}) = -\frac{K}{n_{\mathrm{H}}+1}(\varepsilon_0 + \bar{\varepsilon}_{\mathrm{p}})^{n_{\mathrm{H}}+1} + K\varepsilon_0^{n_{\mathrm{H}}}\bar{\varepsilon}_{\mathrm{p}} \text{ and } R(\bar{\varepsilon}_{\mathrm{p}}) = -K(\varepsilon_0 + \bar{\varepsilon}_{\mathrm{p}})^{n_{\mathrm{H}}} + K\varepsilon_0^{n_{\mathrm{H}}}. \tag{4.19}$$

4.1.6 Loading/unloading conditions

The set of constitutive equations of the small strain elastoplastic model is completed with the loading/unloading conditions (usually referred to as Kuhn-Tucker conditions),

$$\dot{\lambda} \geq 0, \;\; \Phi \leq 0, \;\; \text{and} \;\; \dot{\lambda}\Phi = 0. \tag{4.20}$$

Thus, elastic and elastoplastic loading paths are differentiated following

$$\begin{cases} \Phi < 0, \;\; \lambda = 0 & \Rightarrow \text{elastic loading/unloading} \\ \Phi = 0, \;\; \lambda > 0, \;\; \text{and} \;\; \dfrac{\partial \Phi}{\partial \boldsymbol{\eta}} : \dot{\boldsymbol{\eta}} > 0 & \Rightarrow \text{elastoplastic loading} \\ \Phi = 0, \;\; \lambda = 0, \;\; \text{and} \;\; \dfrac{\partial \Phi}{\partial \boldsymbol{\eta}} : \dot{\boldsymbol{\eta}} = 0 & \Rightarrow \text{neutral loading} \\ \Phi = 0, \;\; \lambda = 0, \;\; \text{and} \;\; \dfrac{\partial \Phi}{\partial \boldsymbol{\eta}} : \dot{\boldsymbol{\eta}} < 0 & \Rightarrow \text{elastic unloading} \end{cases}$$

From the loading/unloading conditions the consistency condition,

$$\dot{\Phi} = 0, \tag{4.21}$$

can be derived. It states that during plastic loading the point that represents the stress state in the principal stress space is always on the yield surface.

It should now be confirmed that the evolution equations actually fulfil the Clausius-Duhem inequality. By employing Equations 4.13 in Equation 4.12 the second term is clearly nonnegative ($\dot{\lambda}\frac{b}{c}\boldsymbol{\alpha} : \boldsymbol{\alpha} \geq 0$). The inequality 4.12 is then reduced to

$$\boldsymbol{\eta} : \left(\dot{\lambda}\frac{\partial \Phi}{\partial \boldsymbol{\eta}}\right) + R\dot{\lambda} = \dot{\lambda}\left[\boldsymbol{\eta} : \frac{\partial \bar{\eta}(\boldsymbol{\eta})}{\partial \boldsymbol{\eta}} + R\right] = \dot{\lambda}\left[\bar{\eta}(\boldsymbol{\eta}) + R\right] = \dot{\lambda}\left(\Phi + \sigma_{\mathrm{y}_0}\right) \geq 0, \tag{4.22}$$

which is fulfilled by the loading/unloading conditions and by the positivity of the parameter σ_{y_0}. In the above the property $\boldsymbol{\eta} : [\partial \bar{\eta}(\boldsymbol{\eta})/\partial \boldsymbol{\eta}] = a\bar{\eta}(\boldsymbol{\eta})$, of a homogeneous yield function of degree a, was employed[1]. In this work only homogeneous yield functions of degree $a = 1$ are considered, since any homogeneous function of degree a raised to the power of $1/a$ results in a homogeneous function of degree one.

4.1.7 Continuous elastoplastic tangent modulus

The continuous elastoplastic tangent modulus, $\mathbb{D}_{\mathrm{ep}}$, relates the infinitesimal total strain rate tensor to the stress rate tensor, i.e., $\dot{\boldsymbol{\sigma}} = \mathbb{D}_{\mathrm{ep}} : \dot{\boldsymbol{\varepsilon}}$.

[1] A function f of a variable $\mathbf{x}$ is positively homogeneous of a degree a if for any scalar $c \geq 0$, $f(c\mathbf{x}) = c^a f(\mathbf{x})$. Thus, if the tensor variable $\mathbf{x}$ proportionally increases, the surface associated to $f - y = 0$, where y is a scalar that quantifies the size of the surface, expands without changing its shape at a rate given by y.

Applying the consistency condition (Equation 4.21) to the yield potential of Equation 4.17 results

$$\begin{aligned}\dot{\Phi} &= \mathbf{n} : \dot{\boldsymbol{\eta}} - H\dot{\bar{\varepsilon}}_{\mathrm{p}} = 0 \\ &= \mathbf{n} : \Big[\mathbb{D} : \dot{\boldsymbol{\varepsilon}} - \dot{\lambda}\mathbb{D} : \mathbf{n} - \dot{\lambda}(c\mathbf{n} - b\boldsymbol{\alpha})\Big] - H\dot{\lambda} = 0,\end{aligned} \tag{4.23}$$

where the quantity

$$H = -\partial R/\partial \bar{\varepsilon}_p, \tag{4.24}$$

was introduced. In Equation 4.23, the relation $\dot{\boldsymbol{\eta}} = \dot{\boldsymbol{\sigma}} - \dot{\boldsymbol{\alpha}}$ along with Equations 4.13c, 4.15 and 4.16, were employed.

The evolution rate of the plastic multiplier is obtained though mathematical rearrangement of Equation 4.23, yielding

$$\dot{\lambda} = \left[\frac{\mathbf{n} : \mathbb{D}}{\mathbf{n} : (\mathbb{D} : \mathbf{n} + c\mathbf{n} - b\boldsymbol{\alpha}) + H}\right] : \dot{\boldsymbol{\varepsilon}}. \tag{4.25}$$

Inserting this relation into Equation 4.16, provides the following continuous elastoplastic tangent modulus for plastic loading,

$$\mathbb{D}_{\mathrm{ep}} = \frac{\partial \dot{\boldsymbol{\sigma}}}{\partial \dot{\boldsymbol{\varepsilon}}} = \mathbb{D} - \delta \frac{\mathbb{D} : \mathbf{n} \otimes \mathbf{n} : \mathbb{D}}{\mathbf{n} : (\mathbb{D} : \mathbf{n} + c\mathbf{n} - b\boldsymbol{\alpha}) + H}, \tag{4.26}$$

where δ differentiates elastic ($\delta = 0$) from elastoplastic ($\delta = 1$) behaviour.

4.2 Constitutive modelling with multiple back stress components

In this section the constitutive model presented in Section 4.1 will be extended to include a more general nonlinear kinematic hardening law. The derivation will be based on the modified rheological model of kinematic hardening (Section 3.4.2.2), which corresponds to the kinematic hardening law proposed by Chaboche and Rousselier (1983). The derivation of the constitutive equations is analogous to the procedures presented in Section 4.1, thus only the main differences will be outlined here.

Additive decomposition of the plastic strain tensor Based on the rheological model of Fig. 3.7 and similarly to Equations 3.95 and 4.6, the plastic small strain tensor can be additively decomposed following

$$\boldsymbol{\varepsilon}_{\mathrm{p}} = \boldsymbol{\varepsilon}^j_{\mathrm{pe}} + \boldsymbol{\varepsilon}^j_{\mathrm{pi}} \Rightarrow \dot{\boldsymbol{\varepsilon}}_{\mathrm{p}} = \dot{\boldsymbol{\varepsilon}}^j_{\mathrm{pe}} + \dot{\boldsymbol{\varepsilon}}^j_{\mathrm{pi}} \;\; \forall \;\; j = 1 \ldots N. \tag{4.27}$$

Helmholtz free energy potential The additive decomposition of the energy potential is expressed by

$$\begin{aligned}\psi &= \psi_{\mathrm{e}}(\boldsymbol{\varepsilon}_{\mathrm{e}}) + \sum_{j=1}^{N} \psi_{\mathrm{kin}}^{j}(\boldsymbol{\varepsilon}_{\mathrm{p_e}}^{j}) + \psi_{\mathrm{iso}}(\bar{\varepsilon}_{\mathrm{p}}) \\ &= \frac{1}{2}\boldsymbol{\varepsilon}_{\mathrm{e}} : \mathbb{D} : \boldsymbol{\varepsilon}_{\mathrm{e}} + \sum_{j=1}^{N} \frac{1}{2}\boldsymbol{\varepsilon}_{\mathrm{p_e}}^{j} : \mathbb{D}_{\mathrm{p}}^{j} : \boldsymbol{\varepsilon}_{\mathrm{p_e}}^{j} + \psi_{\mathrm{iso}}(\bar{\varepsilon}_{\mathrm{p}}),\end{aligned} \tag{4.28}$$

where $\mathbb{D}_{\mathrm{p}}^{j} = c^{j}\mathbb{I}$ is the fourth-order "elastic stiffness tensor" associated to the hardening spring j (see Fig. 3.7).

Clausius-Duhem inequality Following the procedure presented in Section 4.1.3 for the energy potential 4.28, yields the simplified inequality

$$\boldsymbol{\eta} : \dot{\boldsymbol{\varepsilon}}_{\mathrm{p}} + \sum_{j=1}^{N} \boldsymbol{\alpha}^{j} : \dot{\boldsymbol{\varepsilon}}_{\mathrm{p_i}}^{j} + R\dot{\bar{\varepsilon}}_{\mathrm{p}} \geq 0. \tag{4.29}$$

The relative stress tensor is now given by $\boldsymbol{\eta} = \boldsymbol{\sigma} - \boldsymbol{\alpha}$, where $\boldsymbol{\alpha} = \sum_{j=1}^{N} \boldsymbol{\alpha}^{j}$, with the back stress tensors, $\boldsymbol{\alpha}^{j}$, being defined as

$$\boldsymbol{\alpha}^{j} = -\frac{\partial \psi}{\partial \boldsymbol{\varepsilon}_{\mathrm{p_i}}^{j}} = c^{j}(\boldsymbol{\varepsilon}_{\mathrm{p}} - \boldsymbol{\varepsilon}_{\mathrm{p_i}}^{j}) \ \forall \ j = 1 \ldots N. \tag{4.30}$$

Evolution equations The sufficient conditions to ensure that inequality 4.29 is fulfilled consist of the evolution Equations 4.13c and 4.14 along with

$$\dot{\boldsymbol{\varepsilon}}_{\mathrm{p_i}}^{j} = \dot{\lambda}\frac{b^{j}}{c^{j}}\boldsymbol{\alpha}^{j} \ \forall \ j = 1 \ldots N. \tag{4.31}$$

Analogously to Equation 4.15, the back stress tensors evolve according to

$$\dot{\boldsymbol{\alpha}}^{j} = c^{j}\dot{\boldsymbol{\varepsilon}}_{\mathrm{p}} - \dot{\lambda} b^{j}\boldsymbol{\alpha}^{j} \ \forall \ j = 1 \ldots N. \tag{4.32}$$

Finally, the yield potential (Equation 4.17) and the loading/unloading conditions (Equation 4.20) complete the set of constitutive equations of the constitutive model.

Continuous elastoplastic tangent modulus Applying the procedure presented in Section 4.1.7 to this constitutive model, results in the following continuous elastoplastic tangent modulus

$$\mathbb{D}_{\mathrm{ep}} = \frac{\partial \dot{\boldsymbol{\sigma}}}{\partial \dot{\boldsymbol{\varepsilon}}} = \mathbb{D} - \delta \frac{\mathbb{D} : \mathbf{n} \otimes \mathbf{n} : \mathbb{D}}{\mathbf{n} : \left[\mathbb{D} : \mathbf{n} + \sum_{j=1}^{N}(c^{j}\mathbf{n} - b^{j}\boldsymbol{\alpha}^{j})\right] + H}. \tag{4.33}$$

4.3 Numerical implementation

The implementation of a constitutive model based on rate-type equations in nonlinear finite element analysis requires the integration of the evolution equations of the material's state variables at each integration point within the continuum medium, at any instant of time (pseudo-time), during the deformation process. In this section, the numerical time integration of the constitutive model presented in Section 4.1 is described employing two distinct time integration procedures: forward-Euler and backward-Euler. In addition, the corresponding (algorithmic) consistent elastoplastic tangent moduli are derived. The adaptation of the procedures presented in the following sections to the constitutive model presented in Section 4.2 is straightforward, being therefore presented in Appendix A.

4.3.1 Time discretization of the constitutive equations

The analytical integration of the rate-type constitutive equations can, in general, be obtained only for very simple strain paths. Thus, in realistic engineering problems, numerical schemes that provide an approximate solution are employed. Taking the constitutive model of Section 4.1 into account, the set of differential equations that have to be integrated along the time interval $[t_n, t_{n+1}] \subset [t_0, t_{\text{end}}]$ of duration $\Delta t = t_{n+1} - t_n$ can be summarized as

$$\dot{\boldsymbol{\sigma}} = \mathbb{D} : (\dot{\boldsymbol{\varepsilon}} - \dot{\lambda}\mathbf{n}), \tag{4.34}$$

$$\dot{\boldsymbol{\alpha}} = \dot{\lambda}(c\mathbf{n} - b\boldsymbol{\alpha}), \text{ and} \tag{4.35}$$

$$\dot{\bar{\varepsilon}}_{\text{p}} = \dot{\lambda}, \tag{4.36}$$

obeying the loading/unloading conditions (Equation 4.20). By replacing the time derivatives of these equations by the difference quotient, i.e.,

$$\dot{(\bullet)} = \frac{(\bullet)_{n+1} - (\bullet)_n}{t_{n+1} - t_n} = \frac{\Delta(\bullet)}{\Delta t}, \tag{4.37}$$

leads to the integrated formulas

$$\boldsymbol{\sigma}_{n+1} = \boldsymbol{\sigma}_n + \mathbb{D} : \Delta\boldsymbol{\varepsilon} - \Delta\lambda\mathbb{D} : \mathbf{n}_{n+\alpha}, \tag{4.38}$$

$$\boldsymbol{\alpha}_{n+1} = \boldsymbol{\alpha}_n + \Delta\lambda(c\mathbf{n}_{n+\alpha} - b\boldsymbol{\alpha}_{n+\alpha}), \text{ and} \tag{4.39}$$

$$\bar{\varepsilon}_{\text{p}_{n+1}} = \bar{\varepsilon}_{\text{p}_n} + \Delta\lambda, \tag{4.40}$$

with $\alpha \subset [0, 1]$. At t_n, it is assumed that the system is in global equilibrium and all variables $(\bullet)_n$ are known.

4.3.2 Elastic predictor-plastic corrector strategy

Among the different methodologies that have been proposed to numerically integrate constitutive equations, the predictor-corrector (return mapping) strategy is the most popular stress

integration scheme. This method was firstly introduced by Wilkins (1963), being commonly referred to as radial return procedure for J_2 perfect plasticity.

It consists of two successive procedures: a prediction (elastic) phase, followed by a plastic corrector phase, the geometric interpretation being schematically represented in Fig. 4.1. Initially, the step is assumed to be purely elastic, meaning that there is no plastic flow or evolution of internal variables, i.e.,

$$\Delta\lambda = 0, \tag{4.41}$$

$$\boldsymbol{\varepsilon}_{\mathrm{e}_{n+1}}^{\mathrm{trial}} = \boldsymbol{\varepsilon}_{\mathrm{e}_n} + \Delta\boldsymbol{\varepsilon}, \tag{4.42}$$

$$\boldsymbol{\sigma}_{n+1}^{\mathrm{trial}} = \boldsymbol{\sigma}_n + \mathbb{D} : \Delta\boldsymbol{\varepsilon}, \tag{4.43}$$

$$\boldsymbol{\alpha}_{n+1}^{\mathrm{trial}} = \boldsymbol{\alpha}_n, \text{ and} \tag{4.44}$$

$$\bar{\varepsilon}_{\mathrm{p}_{n+1}}^{\mathrm{trial}} = \bar{\varepsilon}_{\mathrm{p}_n}. \tag{4.45}$$

If the trial relative stress state is within the yield surface, i.e., $\Phi(\boldsymbol{\sigma}_{n+1}^{\mathrm{trial}}, \boldsymbol{\alpha}_{n+1}^{\mathrm{trial}}, \bar{\varepsilon}_{\mathrm{p}_{n+1}}^{\mathrm{trial}}) < 0$, this initial assumption is correct and the material point is effectively in an elastic state. Otherwise, the elastic (predictor) trial relative stress state is at the exterior of the yield surface, hence requiring a corrector phase in order to project the stress onto the yield surface (i.e., to enforce the consistency condition at t_{n+1}). This method is summarized in Box 4.1.

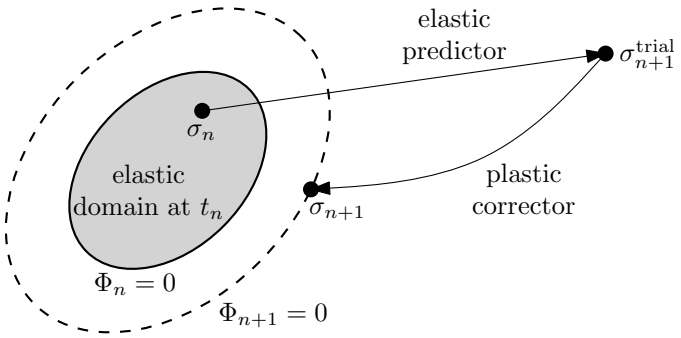

Figure 4.1: Schematic representation of the elastic predictor-plastic corrector method.

To perform the plastic correction, it is necessary to make an assumption for the deformation path. Many integration algorithms have been proposed, mainly differing in how the flow rule is imposed along the corrector phase. Under plane stress conditions, for instance, Ortiz and Pinsky (1981) and Ortiz *et al.* (1983) have proposed the closest point projection method. Ortiz and Simo (1986) also proposed the cutting-plane method, based on an explicit iterative process to meet the consistency condition. Later, Yoon *et al.* (1999) proposed a stress integration method based on the incremental deformation theory, denoted multi-stage return mapping method, which follows the minimum plastic work path. Depending on which time $t_{n+\alpha}$ is employed in the variables' evaluation during the correction step, the stress integration schemes can be categorized in two different approaches, known as forward-Euler ($\alpha = 0$) and backward-Euler ($\alpha = 1$) formulations. In other words, while the

forward-Euler approach makes use of a previous or trial (known) stress state as its reference, the backward-Euler method on the other hand, employs the current (unknown) stress state. Therefore, algorithms based on the forward-Euler method are simple and straightforward to implement, however being conditionally stable. In contrast, backward-Euler formulations are more complex, requiring the use of the 2nd derivatives of the yield function, but providing more accurate results even for large time steps.

In the following sections, the numerical integration of the constitutive equations of the present rate-independent small strain model, adopting the forward-Euler and backward-Euler approaches, is described.

Box 4.1: Scheme of the elastic predictor-plastic corrector method.

Given $\Delta\boldsymbol{\varepsilon}$ and the history data $\boldsymbol{\sigma}_n$, $\boldsymbol{\alpha}_n$ and $\bar{\varepsilon}_{\mathrm{p}_n}$
1. Set initial estimate (trial) values (Equations 4.41-4.45)
2. Evaluate the yield potential
   $\Phi^{\mathrm{trial}} = \bar{\eta}(\boldsymbol{\sigma}_{n+1}^{\mathrm{trial}}, \boldsymbol{\alpha}_{n+1}^{\mathrm{trial}}) - [\sigma_{\mathrm{y}_0} - R(\bar{\varepsilon}_{\mathrm{p}_{n+1}}^{\mathrm{trial}})]$
3. Check for plasticity onset:
   IF ($\Phi^{\mathrm{trial}} \leq 0$) **THEN**
      Set variables at t_{n+1}
         $\boldsymbol{\sigma}_{n+1} = \boldsymbol{\sigma}_{n+1}^{\mathrm{trial}}$, $\boldsymbol{\alpha}_{n+1} = \boldsymbol{\alpha}_{n+1}^{\mathrm{trial}}$, and $\bar{\varepsilon}_{\mathrm{p}_{n+1}} = \bar{\varepsilon}_{p_{n+1}}^{\mathrm{trial}}$
      EXIT
   ELSE
      Perform plastic corrector phase to evaluate $\boldsymbol{\sigma}_{n+1}$, $\boldsymbol{\alpha}_{n+1}$, and $\bar{\varepsilon}_{\mathrm{p}_{n+1}}$
      EXIT
   ENDIF

4.3.3 Forward-Euler algorithm

As mentioned before, algorithms belonging to the forward-Euler category integrate the constitutive equations, along the increment of step/time, based on the variables at a known (previous or trial) stress state. Since the flow direction $\mathbf{n}$ is known (and kept constant along the return procedure) the only unknown variable required to evaluate the stress and the back stress states at t_{n+1} is the plastic multiplier, which can be directly calculated from the consistency condition.

In the forward-Euler algorithm presented in this section, it is convenient to split the increment of total strain in two parts, as $\Delta\boldsymbol{\varepsilon} = (1 - \beta_{\boldsymbol{\eta}})\Delta\boldsymbol{\varepsilon} + \beta_{\boldsymbol{\eta}}\Delta\boldsymbol{\varepsilon}$, where $\beta_{\boldsymbol{\eta}}$ is the ratio of the increment of stress to be corrected, given by

$$\beta_{\boldsymbol{\eta}} = \frac{\bar{\eta}^{\mathrm{trial}} - \sigma_{\mathrm{y}}(\bar{\varepsilon}_{\mathrm{p}_n})}{\bar{\eta}^{\mathrm{trial}} - \bar{\eta}_n}. \tag{4.46}$$

Doing this way, $\boldsymbol{\sigma}_n + (1 - \beta_{\boldsymbol{\eta}})\mathbb{D} : \Delta\boldsymbol{\varepsilon}$ is the last stress state that ensures the yield criterion, and $\beta_{\boldsymbol{\eta}}\mathbb{D} : \Delta\boldsymbol{\varepsilon} - \Delta\lambda\mathbb{D} : \mathbf{n}_n$ is the increment of stress during to plastic loading (see Fig. 4.2).

Although the relation of Equation 4.46 is only valid for monotonic loading, numerical results have shown that this can be a good approximation for nonmonotonic loading paths during sheet metal forming processes.

From the loading/unloading conditions (Equation 4.20), the incremental consistency condition can be stated as

$$\Delta\Phi = 0, \text{ if } (\Phi = 0 \text{ and } \Delta\lambda > 0). \tag{4.47}$$

Thus, applying this condition to Equation 4.17, results

$$\Delta\Phi = \mathbf{n}_n : \Delta\boldsymbol{\eta} - H_n \Delta\bar{\varepsilon}_{\mathrm{p}} = 0. \tag{4.48}$$

Using Equations 4.38-4.40 and the relation $\Delta\boldsymbol{\eta} = \Delta\boldsymbol{\sigma} - \Delta\boldsymbol{\alpha}$ into Equation 4.48 leads to

$$\mathbf{n}_n : [\beta_{\boldsymbol{\eta}}\mathbb{D} : \Delta\boldsymbol{\varepsilon} - \Delta\lambda\mathbb{D} : \mathbf{n}_n - \Delta\lambda(c\mathbf{n}_n - b\boldsymbol{\alpha}_n)] - H_n\Delta\lambda = 0. \tag{4.49}$$

Finally, the increment of the plastic multiplier can be obtained through mathematical rearrangement of Equation 4.49, in the form

$$\Delta\lambda = \frac{\mathbf{n}_n : \Delta\boldsymbol{\sigma}^{\mathrm{trial}}}{\mathbf{n}_n : (\mathbb{D} : \mathbf{n}_n + c\mathbf{n}_n - b\boldsymbol{\alpha}_n) + H_n}, \tag{4.50}$$

where $\Delta\boldsymbol{\sigma}^{\mathrm{trial}}$ is the increment of stress to be corrected, following the equation

$$\Delta\boldsymbol{\sigma}^{\mathrm{trial}} = \beta_{\boldsymbol{\eta}}\mathbb{D} : \Delta\boldsymbol{\varepsilon}. \tag{4.51}$$

By employing the increment of the plastic multiplier (Equation 4.50) on Equations 4.38-4.40 the stress and the state variables are updated. In this work, the plastic flow direction is evaluated at the last known configuration where the yield condition is ensured, i.e., at $\boldsymbol{\sigma}_n + (1 - \beta_{\boldsymbol{\eta}})\mathbb{D} : \Delta\boldsymbol{\varepsilon}$.

Proportioning procedure Since in the forward-Euler method the incremental consistency is not *a-priori* granted, after the return mapping there is still a gap between the predicted stress state after the plastic correction and the correct stress state on the yield surface. In other words, the predicted stress state is not on the updated yield surface (see Fig. 4.2). To eliminate this gap, a proportioning procedure is considered in this work. This procedure consists of applying a radial return to ensure the consistency condition as

$$\boldsymbol{\sigma}_{n+1} = \boldsymbol{\alpha}_{n+1} + \left(\boldsymbol{\eta}_{n+1}\right)^{\mathrm{BP}} \frac{\sigma_{\mathrm{y}}\left(\bar{\varepsilon}_{\mathrm{p}_{n+1}}\right)}{\left(\bar{\eta}_{n+1}\right)^{\mathrm{BP}}}, \tag{4.52}$$

where $(\bullet)^{\mathrm{BP}}$ refers to quantities evaluated before the proportioning procedure. Considering that, generally, the radial direction is not parallel to the normal to the current yield surface for anisotropic yield criteria, the normality condition at the current state is not granted.

Alternatively to the proportioning procedure, the projection (i) along the plastic corrector direction or (ii) normal to the current yield surface can be performed (Hinton, 1992). In order to eliminate this gap, Vrh *et al.* (2010) proposed the next increment corrects error (NICE) algorithm, in which the incremental consistency condition (Equation 4.47) is replaced by a Taylor's power series expansion of Equation 4.20b.

Sub-incrementation technique In order to ensure an algorithmic convergence for larger time increments, the sub-incrementation technique is considered in this work. This technique consists of dividing the increment of stress to be corrected in M equal parts and performing the correction step for each sub-increment, $k = 1 \dots M$, separately and sequentially, thus allowing for larger time steps without the occurrence of divergence. Additionally, the sub-incrementation method help decreasing the gap between the predicted stress state after the plastic correction and the correct stress state on the yield surface, therefore also improving the accuracy of the algorithm. The presented forward-Euler algorithm accounting for the sub-incrementation technique is described in Box 4.2 and schematically represented in Fig. 4.2.

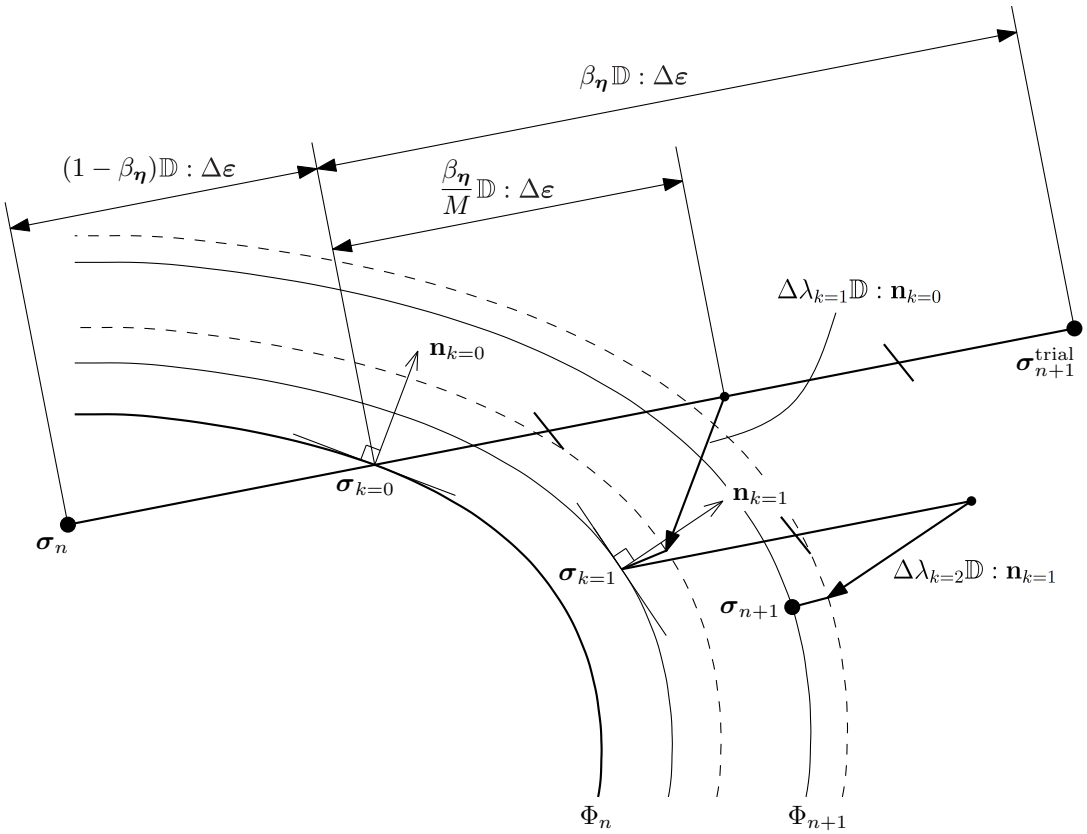

Figure 4.2: Forward-Euler algorithm and the sub-incrementation technique.

In the picture, the material point is initially in an elastic state and the trial stress is outside of the yield surface, thus requiring the correction step to ensure the consistency condition. For the sake of clarity, in Fig. 4.2 only two sub-increments of stress are displayed

and the difference between the yield surfaces before and after the proportioning procedure was represented in an exaggerated way.

Following this technique, the incremental consistency condition (Equation 4.47) is evaluated for each sub-increment k, providing the increment of the plastic multiplier as

$$\Delta\lambda_k = \frac{\mathbf{n}_{k-1} : \Delta\boldsymbol{\sigma}_k^{\text{trial}}}{\mathbf{n}_{k-1} : (\mathbb{D} : \mathbf{n}_{k-1} + c\mathbf{n}_{k-1} - b\boldsymbol{\alpha}_{k-1}) + H_{k-1}}, \tag{4.53}$$

where $\Delta\boldsymbol{\sigma}_k^{\text{trial}}$ is now the sub-increment of stress to be corrected in each iteration k, following the equation

$$\Delta\boldsymbol{\sigma}_k^{\text{trial}} = \frac{\beta_{\boldsymbol{\eta}}}{M}\mathbb{D} : \Delta\boldsymbol{\varepsilon}. \tag{4.54}$$

At each iteration k, after the evaluation of the plastic multiplier (Equation 4.53), the following variables are updated,

$$\begin{aligned}
\boldsymbol{\sigma}_k &= \boldsymbol{\sigma}_{k-1} + \mathbb{D} : (\Delta\boldsymbol{\varepsilon}_k - \Delta\lambda_k\mathbf{n}_{k-1}) \\
&= \boldsymbol{\sigma}_k^{\text{trial}} - \Delta\lambda_k\mathbb{D} : \mathbf{n}_{k-1}, && (4.55)\\
\boldsymbol{\alpha}_k &= \boldsymbol{\alpha}_{k-1} + \Delta\lambda_k\left(c\mathbf{n}_{k-1} - b\boldsymbol{\alpha}_{k-1}\right), \text{ and} && (4.56)\\
\bar{\varepsilon}_{\text{p}_k} &= \bar{\varepsilon}_{\text{p}_{k-1}} + \Delta\lambda_k, && (4.57)
\end{aligned}$$

where $\boldsymbol{\sigma}_k^{\text{trial}}$ is the trial stress at iteration k ($\boldsymbol{\sigma}_k^{\text{trial}} = \boldsymbol{\sigma}_{k-1} + \Delta\boldsymbol{\sigma}_k^{\text{trial}}$). Then, the proportioning procedure is performed,

$$\boldsymbol{\sigma}_k = \boldsymbol{\alpha}_k + (\boldsymbol{\eta}_k)^{\text{BP}}\frac{\sigma_{\text{y}}\left(\bar{\varepsilon}_{\text{p}_k}\right)}{(\bar{\eta}_k)^{\text{BP}}}, \tag{4.58}$$

and the plastic flow direction tensor, $\mathbf{n}$, and the quantity H are finally updated in order to perform the return mapping of the next sub-increment.

The number of sub-increments, M, is assumed to be the higher integer number that respects the condition

$$M = \left[\frac{\bar{\eta}^{\text{trial}} - \sigma_{\text{y}}(\bar{\varepsilon}_{\text{p}_n})}{\sigma_{\text{y}_0}}\right] \times 8 + 1, \tag{4.59}$$

as proposed by Owen and Hinton (1980). This forward-Euler algorithm is presented in Box 4.2. If M is set to be equal to 1, the standard forward-Euler algorithm is recovered.

4.3.4 Backward-Euler algorithm

As indicated before, in backward-Euler formulations the state variables used in the returning procedure are evaluated at t_{n+1}, stress state that is unknown. Consequently, this type of algorithms must account for the variation of the normal to the yield surface (flow direction) during the returning procedure. As a result, they are rather complex, requiring the use of the 2nd derivatives of the yield function. Nevertheless, this methodology provides great accuracy even for large time steps, being more appropriated for an implicit time integration scheme (Cardoso and Yoon, 2009), as chosen for the present work.

Box 4.2: Scheme of the forward-Euler algorithm accounting for the sub-incrementation technique.

1. Determine the number of sub-increments (Equation 4.59)
2. Determine the sub-increments of stress to be corrected (Equation 4.54)
3. Compute the correction step

   Initiate variables

   $\boldsymbol{\sigma}_{k=0} = \boldsymbol{\sigma}_n + (1-\beta_{\boldsymbol{\eta}})\mathbb{D} : \Delta\boldsymbol{\varepsilon}$, $\boldsymbol{\alpha}_{k=0} = \boldsymbol{\alpha}_n$, and $\bar{\varepsilon}_{\mathrm{p}_{k=0}} = \bar{\varepsilon}_{\mathrm{p}_n}$

   Incremental procedure:

   DO $k = 1 : M$

   a) Evaluate the plastic flow direction tensor, $\mathbf{n}_{k-1}$, and the quantity H_{k-1}

   b) Compute the increment of the plastic multiplier (Equation 4.53)

   c) Update of the state variables (Equations 4.55-4.57)

   d) Perform the proportioning procedure (Equation 4.52)

   ENDDO

This type of algorithms relies on iterative procedures to determine the state variables at t_{n+1}. For the constitutive model presented in Section 4.1, the system of nonlinear equations to be iteratively solved (using e.g., the Newton-Raphson procedure) is given by the yield criterion and the implicit versions of Equations 4.38 and 4.39, i.e.,

$$\bar{\eta}(\boldsymbol{\eta}_{n+1}) - [\sigma_{\mathrm{y}_0} - R(\bar{\varepsilon}_{\mathrm{p}_{n+1}})] = 0, \tag{4.60}$$

$$\boldsymbol{\sigma}_{n+1} = \boldsymbol{\sigma}_n + \mathbb{D} : \Delta\boldsymbol{\varepsilon} - \Delta\lambda\mathbb{D} : \mathbf{n}_{n+1}, \text{ and} \tag{4.61}$$

$$\boldsymbol{\alpha}_{n+1} = \boldsymbol{\alpha}_n + \Delta\lambda(c\mathbf{n}_{n+1} - b\boldsymbol{\alpha}_{n+1}). \tag{4.62}$$

In the following, the iterative procedure developed within this work is given. For the sake of simplicity, in the remaining equations of this section the subscripts $n+1$ are omitted. From Equations 4.60-4.62, the following auxiliary residua can be written,

$$r_1 = \bar{\eta}(\boldsymbol{\eta}) - [\sigma_{\mathrm{y}_0} - R(\bar{\varepsilon}_{\mathrm{p}_n} + \Delta\lambda)] = 0, \tag{4.63}$$

$$\mathbf{r}_2 = \mathbb{D}^{-1} : \left(\boldsymbol{\sigma} - \boldsymbol{\sigma}^{\mathrm{trial}}\right) + \Delta\lambda\mathbf{n} = \mathbf{0}, \text{ and} \tag{4.64}$$

$$\mathbf{r}_3 = \boldsymbol{\alpha} - \boldsymbol{\alpha}_n - \Delta\lambda\,(c\mathbf{n} - b\boldsymbol{\alpha}) = \mathbf{0}. \tag{4.65}$$

After convergence these residua should be approximately zero, within a given tolerance. In order to employ the Newton-Raphson method, these nonlinear functions are linearised, at each iteration i, around the current values of the state variables to obtain the increment i of the increment of the plastic multiplier, $\Delta\Delta\lambda^i$. Using the Taylor's series expansion (only the linear terms were considered) the resulting linearised residua, for each iteration, are given as

$$r_1 + \mathbf{n} : \Delta\boldsymbol{\sigma} - \mathbf{n} : \Delta\boldsymbol{\alpha} - H\Delta\Delta\lambda = 0, \tag{4.66}$$

$$\mathbf{r}_2 + \left(\mathbb{D}^{-1} + \Delta\lambda\frac{\partial \mathbf{n}}{\partial \boldsymbol{\eta}}\right) : \Delta\boldsymbol{\sigma} - \Delta\lambda\frac{\partial \mathbf{n}}{\partial \boldsymbol{\eta}} : \Delta\boldsymbol{\alpha} + \mathbf{n}\Delta\Delta\lambda = \mathbf{0}, \text{ and} \tag{4.67}$$

$$\mathbf{r}_3 - c\Delta\lambda\frac{\partial \mathbf{n}}{\partial \boldsymbol{\eta}} : \Delta\boldsymbol{\sigma} + \left[(1 + b\Delta\lambda)\,\mathbb{I} + c\Delta\lambda\frac{\partial \mathbf{n}}{\partial \boldsymbol{\eta}}\right] : \Delta\boldsymbol{\alpha} - (c\mathbf{n} - b\boldsymbol{\alpha})\,\Delta\Delta\lambda = \mathbf{0}. \tag{4.68}$$

Here and in the following, the superscripts i are omitted for the sake of simplicity. This system of nonlinear equations can be represented in matrix form as

$$\begin{bmatrix} \mathbf{n} & -\mathbf{n} & -H \\ \mathbb{D}^{-1} + \Delta\lambda\frac{\partial \mathbf{n}}{\partial \boldsymbol{\eta}} & -\Delta\lambda\frac{\partial \mathbf{n}}{\partial \boldsymbol{\eta}} & \mathbf{n} \\ -c\Delta\lambda\frac{\partial \mathbf{n}}{\partial \boldsymbol{\eta}} & (1 + b\Delta\lambda)\,\mathbb{I} + c\Delta\lambda\frac{\partial \mathbf{n}}{\partial \boldsymbol{\eta}} & -c\mathbf{n} + b\boldsymbol{\alpha} \end{bmatrix} \begin{bmatrix} \Delta\boldsymbol{\sigma} \\ \Delta\boldsymbol{\alpha} \\ \Delta\Delta\lambda \end{bmatrix} = - \begin{bmatrix} r_1 \\ \mathbf{r}_2 \\ \mathbf{r}_3 \end{bmatrix}. \tag{4.69}$$

Although this system of equations can be solved numerically, here the closed form solutions for $\Delta\boldsymbol{\sigma}$, $\Delta\boldsymbol{\alpha}$, and $\Delta\Delta\lambda$ are presented, which are advantageous from the computation point of view when compared to numerical procedures. The equation that describes the evolution of the back stress tensor (Equation 4.70) is obtained through a mathematical arrangement of Equation 4.68 and the evolution equation for the stress tensor (Equation 4.71) is then obtained from Equation 4.67 and Equation 4.70. Finally, these evolution equations are introduced in Equation 4.66, in order to obtain the increment i of the increment of the plastic multiplier (Equation 4.72):

$$\Delta\boldsymbol{\alpha} = \mathbb{A}_1^{-1} : \left[-\mathbf{r}_3 + c\Delta\lambda\frac{\partial \mathbf{n}}{\partial \boldsymbol{\eta}} : \Delta\boldsymbol{\sigma} + (c\mathbf{n} - b\boldsymbol{\alpha})\,\Delta\Delta\lambda\right]; \tag{4.70}$$

$$\Delta\boldsymbol{\sigma} = -\mathbb{E}^{-1} : \left(\mathbf{r}_2 + \Delta\lambda\frac{\partial \mathbf{n}}{\partial \boldsymbol{\eta}} : \mathbb{A}_1^{-1} : \mathbf{r}_3 + \mathbf{a}_2\Delta\Delta\lambda\right); \tag{4.71}$$

$$\Delta\Delta\lambda = \frac{r_1 - \mathbf{a}_3 : \mathbf{r}_2 + \left(\mathbf{n} : \mathbb{A}_1^{-1} - \Delta\lambda\mathbf{a}_3 : \frac{\partial \mathbf{n}}{\partial \boldsymbol{\eta}} : \mathbb{A}_1^{-1}\right) : \mathbf{r}_3}{\mathbf{a}_3 : \mathbf{a}_2 + \mathbf{n} : \mathbb{A}_1^{-1} : (c\mathbf{n} - b\boldsymbol{\alpha}) + H}. \tag{4.72}$$

The auxiliary variables used in Equations 4.70-4.72 are defined as

$$\mathbb{E} = \mathbb{D}^{-1} + \Delta\lambda\frac{\partial \mathbf{n}}{\partial \boldsymbol{\eta}} - c(\Delta\lambda)^2\frac{\partial \mathbf{n}}{\partial \boldsymbol{\eta}} : \mathbb{A}_1^{-1} : \frac{\partial \mathbf{n}}{\partial \boldsymbol{\eta}}, \tag{4.73}$$

$$\mathbb{A}_1 = (1 + b\Delta\lambda)\,\mathbb{I} + c\Delta\lambda\frac{\partial \mathbf{n}}{\partial \boldsymbol{\eta}}, \tag{4.74}$$

$$\mathbf{a}_2 = \mathbf{n} - \Delta\lambda\frac{\partial \mathbf{n}}{\partial \boldsymbol{\eta}} : \mathbb{A}_1^{-1} : (c\mathbf{n} - b\boldsymbol{\alpha}), \text{ and} \tag{4.75}$$

$$\mathbf{a}_3 = \mathbf{n} : \mathbb{E}^{-1} - c\Delta\lambda\mathbf{n} : \mathbf{A}_1^{-1} : \frac{\partial \mathbf{n}}{\partial \boldsymbol{\eta}} : \mathbb{E}^{-1}. \tag{4.76}$$

At the end of each iteration i, the increment of the plastic multiplier and the stress and back

stress tensors are then updated as

$$\Delta\lambda^i = \Delta\lambda^{i-1} + \Delta\Delta\lambda^i, \tag{4.77}$$

$$\boldsymbol{\sigma}^i = \boldsymbol{\sigma}^{i-1} + \Delta\boldsymbol{\sigma}^i, \text{ and} \tag{4.78}$$

$$\boldsymbol{\alpha}^i = \boldsymbol{\alpha}^{i-1} + \Delta\boldsymbol{\alpha}^i. \tag{4.79}$$

The iterative procedure continues until the root-mean-square value of the total residuum (right-hand side of Equation 4.69) reaches a zero value, within a prescribed tolerance.

Multi-stage return mapping procedure For large strain increments the solution of Equation 4.60 can be difficult to be numerically obtained. Here, an algorithm that uses the multi-stage return mapping procedure, as proposed by Yoon *et al.* (1999) and based on the control of the potential residuum, is adapted to the material constitutive model presented.

Following the multi-stage return mapping procedure, the nonlinear Equation 4.60 is solved in N sub-steps performed sequentially (see Fig. 4.3), through the following modification

$$\bar{\eta}(\boldsymbol{\eta}_{n+1}) - [\sigma_{\mathrm{y}_0} - R(\bar{\varepsilon}_{\mathrm{p}_{n+1}})] = \Phi_k, \tag{4.80}$$

where the residuum Φ_k, for each sub-step $k = 1 \ldots N$, has a prescribed value and $\Phi_1 > \Phi_2 > \ldots > \Phi_k > \ldots \Phi_N$ ($\Phi_N \approx 0$).
The residua of Equations 4.63-4.65 are then rewritten for each sub-step k as

$$r_{1_k} = \bar{\eta}(\boldsymbol{\eta}_k) - [\sigma_{\mathrm{y}_0} - R(\bar{\varepsilon}_{\mathrm{p}_n} + \Delta\lambda_k)] - \Phi_k = 0, \tag{4.81}$$

$$\mathbf{r}_{2_k} = \mathbb{D}^{-1} : \left(\boldsymbol{\sigma}_k - \boldsymbol{\sigma}^{\mathrm{trial}}\right) + \Delta\lambda_k \mathbf{n}_k = \mathbf{0}, \text{ and} \tag{4.82}$$

$$\mathbf{r}_{3_k} = \boldsymbol{\alpha}_k - \boldsymbol{\alpha}_n - \Delta\lambda_k \left(c\mathbf{n}_k - b\boldsymbol{\alpha}_k\right) = \mathbf{0}. \tag{4.83}$$

Through the linearisation of these residua around the current state variables, and analogously to the procedure presented before, the increments of the back stress, stress and increment of the plastic multiplier, at each iteration i of each sub-step k, are given, without derivation, by

$$\Delta\boldsymbol{\alpha}_k = \mathbb{A}_{1_k}^{-1} : \left[-\mathbf{r}_{3_k} + c\Delta\lambda_k \frac{\partial \mathbf{n}_k}{\partial \boldsymbol{\eta}_k} : \Delta\boldsymbol{\sigma}_k + \left(c\mathbf{n}_k - b\boldsymbol{\alpha}_k\right)\Delta\Delta\lambda_k\right], \tag{4.84}$$

$$\Delta\boldsymbol{\sigma}_k = -\mathbb{E}_k^{-1} : \left(\mathbf{r}_{2_k} + \Delta\lambda_k \frac{\partial \mathbf{n}_k}{\partial \boldsymbol{\eta}_k} : \mathbb{A}_{1k}^{-1} : \mathbf{r}_{3_k} + \mathbf{a}_{2_k}\Delta\Delta\lambda_k\right), \text{ and} \tag{4.85}$$

$$\Delta\Delta\lambda_k = \frac{r_{1_k} - \mathbf{a}_{3_k} : \mathbf{r}_{2_k} + \left(\mathbf{n}_k : \mathbb{A}_{1_k}^{-1} - \Delta\lambda_k \mathbf{a}_{3_k} : \frac{\partial \mathbf{n}_k}{\partial \boldsymbol{\eta}_k} : \mathbb{A}_{1_k}^{-1}\right) : \mathbf{r}_{3_k}}{\mathbf{a}_{3_k} : \mathbf{a}_{2_k} + \mathbf{n}_k : \mathbb{A}_{1_k}^{-1} : \left(c\mathbf{n}_k - b\boldsymbol{\alpha}_k\right) + H_k}, \tag{4.86}$$

respectively. The auxiliary variables $\mathbb{E}_k$, $\mathbb{A}_{1_k}$, $\mathbf{a}_{2_k}$ and $\mathbf{a}_{3_k}$ are computed from Equations 4.73-4.76 using the quantities related to the sub-step k. And the update of the state variables during the iterative procedure within the sub-step k is performed in analogy to Equations

4.77-4.79. This algorithm is summarized in Box 4.3. It is worth noting that from the presented backward-Euler algorithm with the multi-stage return mapping procedure, the classical backward-Euler algorithm can be derived by imposing the number of sub-steps to be equal to 1.

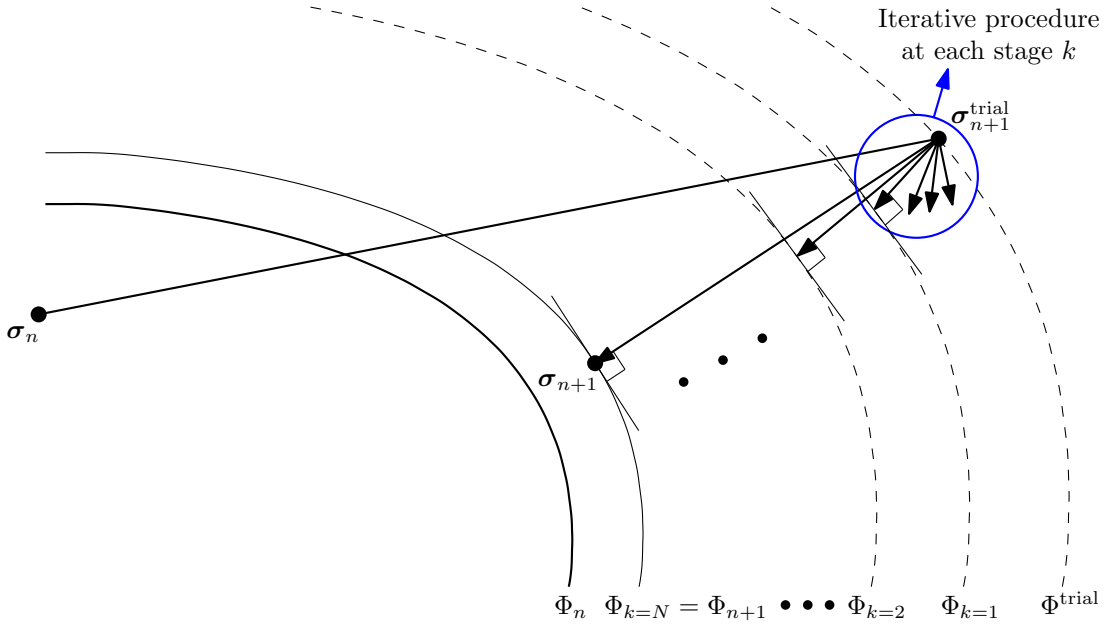

Figure 4.3: Backward-Euler algorithm and the multi-stage return mapping procedure.

4.3.5 Consistent elastoplastic tangent modulus

In order to evaluate the stiffness matrix for nonlinear implicit finite element solvers based on the Newton-Raphson procedure, at each time iteration in each integration point the consistent (algorithmic) elastoplastic tangent modulus (material Jacobian) is required as

$$\mathbb{D}_{\text{ep}}^{\text{alg}} = \left. \frac{\partial(\Delta\boldsymbol{\sigma})}{\partial(\Delta\boldsymbol{\varepsilon})} \right|_{n+1} . \tag{4.87}$$

The elastoplastic tangent modulus should be consistently derived from the implemented integration algorithm is order to ensure the asymptotically quadratic rate of convergence for the Newton-Raphson algorithm of the global equilibrium.

Regarding the computational speed, the use of an analytical closed form expression for the consistent tangent modulus is desired. However, since its derivation for complex nonlinear constitutive models can be a complicated and error-prone task, its numerical computation may be attractive in some situations. This computation is commonly performed by means of the classical perturbation technique that consists of a finite difference approximation (Miehe, 1996b) (see Appendix C). The employment of a numerically obtained consistent tangent modulus does not affect neither the accuracy of the numerical solution nor its convergence rate. Still, this numerical calculation leads to a higher computational effort when compared to

Box 4.3: Scheme of the backward-Euler algorithm accounting for multi-stage return mapping procedure.

Initiate variables
$\boldsymbol{\sigma}_{k=0}^{i=0} = \boldsymbol{\sigma}_n$, $\boldsymbol{\alpha}_{k=0}^{i=0} = \boldsymbol{\alpha}_n$, and $\bar{\varepsilon}_{\mathrm{p}_{k=0}}^{i=0} = \bar{\varepsilon}_{\mathrm{p}_n}$
Multi-stage procedure:
DO $k = 1 : N$
1. Define the residuum Φ_k
$$\Phi_k = \left(1 - \frac{k}{N}\right) \Phi^{\mathrm{trial}}$$
2. Compute the auxiliary residua, $r_{1_k}^0$, $\mathbf{r}_{2_k}^0$, and $\mathbf{r}_{3_k}^0$ (Equations 4.81-4.83)
3. Evaluate the root-mean-square value of the total residuum
$$\| \mathbf{r}^0 \| = \sqrt{(r_{1_k}^0)^2 + \| \mathbf{r}_{2_k}^0 \|^2 + \| \mathbf{r}_{3_k}^0 \|^2}$$
4. Iterative procedure ($TOL = 10^{-8}$):
DO WHILE $\| \mathbf{r} \| > TOL$
a) Compute the auxiliary variables $\mathbb{E}_k^i$, $\mathbb{A}_{1_k}^i$, $\mathbf{a}_{2_k}^i$, and $\mathbf{a}_{3_k}^i$ (Equations 4.73-4.76)
b) Compute the increment i of the increment of the plastic multiplier, $\Delta\Delta\lambda_k^i$ (Equation 4.86)
c) Update the state variables $\Delta\lambda_k^i$, $\boldsymbol{\sigma}_k^i$, and $\boldsymbol{\alpha}_k^i$ (Equations 4.77-4.79)
d) Re-evaluate the auxiliary residua, $r_{1_k}^i$, $\mathbf{r}_{2_k}^i$, and $\mathbf{r}_{3_k}^i$ and the root-mean-square value of the total residuum, $\| \mathbf{r}^i \|$
ENDDO
ENDDO

the computation of analytical expressions. Therefore, in the following the closed form of the consistent elastoplastic tangent modulus for the presented constitutive model is consistently derived from the two integration algorithms presented.

Forward-Euler algorithm From the integrated formula of the stress tensor (Equation 4.38), the relation between the increments of stress and total strain tensors is obtained as

$$\frac{\partial(\Delta\boldsymbol{\sigma})}{\partial(\Delta\boldsymbol{\varepsilon})} = \mathbb{D} - \delta\mathbb{D} : \mathbf{n} \otimes \frac{\partial(\Delta\lambda)}{\partial(\Delta\boldsymbol{\varepsilon})}. \tag{4.88}$$

Treating $\boldsymbol{\varepsilon}$ as a variable, the return mapping procedure presented in the Section 4.3.3 yields the following relation between the increments of the plastic multiplier and total strain tensor

$$\Delta\lambda = \left[\frac{\mathbf{n} : \mathbb{D}}{\mathbf{n} : (\mathbb{D} : \mathbf{n} + c\mathbf{n} - b\boldsymbol{\alpha}) + H}\right] : \Delta\boldsymbol{\varepsilon} = \frac{\partial(\Delta\lambda)}{\partial(\Delta\boldsymbol{\varepsilon})} : \Delta\boldsymbol{\varepsilon}. \tag{4.89}$$

Introducing this relation in Equation 4.88, the final closed-form of the elastoplastic tangent

modulus consistent with the presented forward-Euler algorithm is expressed as

$$\mathbb{D}_{\text{ep}}^{\text{alg}} = \frac{\partial(\Delta\boldsymbol{\sigma})}{\partial(\Delta\boldsymbol{\varepsilon})} = \mathbb{D} - \delta\frac{\mathbb{D} : \mathbf{n} \otimes \mathbf{n} : \mathbb{D}}{\mathbf{n} : (\mathbb{D} : \mathbf{n} + c\mathbf{n} - b\boldsymbol{\alpha}) + H}. \tag{4.90}$$

Backward-Euler algorithm The algorithmic elastoplastic tangent modulus consistent with the backward-Euler algorithm for the presented constitutive model is computed by performing the linearisation of the residua of Equations 4.63-4.65 treating $\boldsymbol{\varepsilon}$ as a variable. Doing so, the increment of the stress tensor (Equation 4.71), after convergence, becomes

$$\Delta\boldsymbol{\sigma} = -\mathbb{E}^{-1} : (-\Delta\boldsymbol{\varepsilon} + \mathbf{a}_2\Delta\Delta\lambda). \tag{4.91}$$

Moreover, the increment of the back stress tensor (Equation 4.70) converges to

$$\Delta\boldsymbol{\alpha} = \mathbb{A}_1^{-1} : \left[c\Delta\lambda\frac{\partial\mathbf{n}}{\partial\boldsymbol{\eta}} : \Delta\boldsymbol{\sigma} + (c\mathbf{n} - b\boldsymbol{\alpha})\,\Delta\Delta\lambda\right]. \tag{4.92}$$

Introducing Equations 4.91 and 4.92 into Equation 4.66, the converged increment of the plastic multiplier is expressed as

$$\Delta\Delta\lambda = \left[\frac{\mathbf{a}_3}{\mathbf{a}_3 : \mathbf{a}_2 + \mathbf{n} : \mathbb{A}_1^{-1} : (c\mathbf{n} - b\boldsymbol{\alpha}) + H}\right] : \Delta\boldsymbol{\varepsilon}. \tag{4.93}$$

The closed-form of the elastoplastic tangent modulus consistent with the backward-Euler algorithm is obtained by replacing Equation 4.93 in Equation 4.91 and solving it in order to the relation between the increments of stress and total strain tensors,

$$\mathbb{D}_{\text{ep}}^{\text{alg}} = \frac{\partial(\Delta\boldsymbol{\sigma})}{\partial(\Delta\boldsymbol{\varepsilon})} = \mathbb{E}^{-1} - \delta\frac{\mathbb{E}^{-1} : \mathbf{a}_2 \otimes \mathbf{a}_3}{\mathbf{a}_3 : \mathbf{a}_2 + \mathbf{n} : \mathbb{A}_1^{-1} : (c\mathbf{n} - b\boldsymbol{\alpha}) + H}. \tag{4.94}$$

Chapter 5

Finite strain elastoplasticity

In industrial forming processes small strain theories are, in general, not valid due to the large deformations and rotations that the material to be processed may suffer. More specifically, one of the limitations of such models consists in the fact that the direct relation between the deformation tensor and the material time derivative of the stress (Equation 4.16) fails on preserving the objectivity when large rotations take place. Therefore the need for models that accurately describe the mechanical behaviour of materials under finite (large) strains has motivated the development of several methodologies, which rely in one of two approaches, namely, hypoelasticity and hyperelasticity formulations.

In this chapter these two approaches are explored. On the one hand, a hypoelastic-based model is derived based on the small strain model presented in Chapter 4. An objective integration algorithm for this hypoelastic-based model that preserves the simplicity of the structure of numerical algorithms for small strain constitutive equations is presented.

On the other hand, an innovative hyperelastic-based model is entirely developed. The model can be suitable for any yield function, overcoming the limitation of hyperelastic-based models, presented in the literature, to quadratic yield functions. Another noteworthy feature of the proposed hyperelastic-based model is that it accounts for nonlinear combined hardening.

In contrast to the majority of the concepts of hyperelastic-based anisotropic modelling presented in the literature, the proposed model is formulated in the reference configuration, hence allowing the use of symmetric tensorial quantities only, which is advantageous from the computational point of view. The numerical implementation of this model is carried out by a backward-Euler procedure based on the exponential map. The exponential map is particularly interesting since it preserves the plastic incompressibility of the material and the symmetry of the tensor-valued quantities. Also, a new procedure taking into account the implementation of any general yield surface is presented in detail.

At the end, the presented hyperelastic-based model is extended to include several back stress components, thus providing a better description of cyclic hardening phenomena. In contrast to the few hyperelastic-based works in the literature that consider such feature,

this model is based on the modified rheological model of Armstrong-Frederick kinematic hardening (see Fig. 3.7) and takes into consideration several multiplicative decompositions of the plastic part of the deformation gradient. This methodology is theoretically sounder when compared to the works of Wallin and Ristinmaa (2005), that considered a nonassociated flow rule where the plastic potential is used to determine multiple strain-like internal variables related to kinematic hardening, and Tsakmakis (1996), back stress tensor of which evolves according to an objective rate.

5.1 State-of-the-art

Early works on finite deformation theory for elastoplasticity consisted mostly on models based on hypoelasticity, e.g., Hibbitt *et al.* (1970), McMeeking and Rice (1975), and Argyris and Kleiber (1977). This approach relies on a hypoelastic relation between the elastic part of the deformation tensor and a proper objective rate of the stress tensor. Moreover, in analogy to the small strain theory, the additive split of the rate of deformation tensor into elastic and plastic parts is taken into account.

However, several shortcomings of this approach were pointed out over the following decades, such as

i) the spurious oscillatory shear stress response during monotonic shear loading conditions if the (widely used) Zaremba-Jaumann rate is considered (Dienes, 1979),

ii) the nonphysical dissipation of energy in elastic deformation paths, thus violating the second law of thermodynamics (Simo and Pister, 1984),

iii) the nonuniqueness respectively to the choice of the objective rate employed (Nemat-Nasser, 1982), and

iv) the noninsurance of objectivity displayed by the early proposed algorithms, that motivated the development of incrementally objective algorithms (Hughes and Winget, 1980).

In order to avoid these issues, the logarithmic objective rate was proposed by Xiao *et al.* (1997). This objective rate was developed in a consistent way to provide an exactly integrable elastic behaviour and, among all possible objective Eulerian rate-type models, those that employ this objective rate are, according to Bruhns *et al.* (1999), the unique self-consistent ones. A recent model based on this objective rate was proposed by Zhu *et al.* (2014), which consists of the extension of the nonlinear kinematic hardening rule developed by Abdel-Karim and Ohno (2000) to finite strains. Despite the shortcomings of classical objective rates, most of the recently proposed constitutive models and in-built material models in commercial finite element codes are based in such hypoelastic approaches, since they are acceptable when the elastic deformations are considered small comparatively to their plastic counterparts. As a consequence, hypoelastic-based models are widely used in the literature to describe a broad

range of features such as evolving elasticity (Zang *et al.*, 2007, Sun and Wagoner, 2011, Lee *et al.*, 2013a), anisotropic plasticity (Yoon *et al.*, 2006, Rabahallah *et al.*, 2009, Taherizadeh *et al.*, 2011, Lee *et al.*, 2012b), anisotropic hardening effects (Yoshida and Uemori, 2003, Chung *et al.*, 2005, Barlat *et al.*, 2012, Cardoso and Yoon, 2009), damage (Haddag *et al.*, 2009), etc.

On the other hand, hyperelastic-based models rely upon a hyperelastic constitutive equation for the stress tensor based on a energy potential (Simo, 1985, Simo and Ortiz, 1985). Due to the nature of the energy potentials, in these models issues related to lack of objectivity and nonpreservation of energy are innately avoided. Regarding elastoplasticity, these models can be categorized into two groups, the ones that consider the multiplicative decomposition of the deformation gradient and those that assume an additive decomposition of generalized strain measures.

Suggested by Kröner (1960) and Lee (1969), among others, the models of the first group assume that the deformation gradient is multiplicatively decomposed into elastic and plastic parts, i.e., $\mathbf{F} = \mathbf{F}_\mathrm{e}\mathbf{F}_\mathrm{p}$. This assumption is widely accepted in the context of finite strains, being conceptually sound and physically motivated. Here, the elastic part, $\mathbf{F}_\mathrm{e}$, is associated to the stretching and rotation of the crystal lattice, whereas the plastic part, $\mathbf{F}_\mathrm{p}$, represents the plastic deformation caused by dislocation motion on crystallographic slip systems (Asaro, 1983, Reina and Conti, 2014). In the last decades this concept has been used in a large variety of scientific areas such as plastic anisotropy (Eidel and Gruttmann, 2003, Menzel and Steinmann, 2003, Svendsen *et al.*, 2006, Sansour *et al.*, 2008, Vladimirov *et al.*, 2010), thermomechanics (Lion, 2000, Håkansson *et al.*, 2005, Rodas *et al.*, 2014), damage mechanics (Menzel *et al.*, 2005, Brünig *et al.*, 2008, Vladimirov *et al.*, 2014), and crystal plasticity (Bargmann *et al.*, 2011, 2014), to name just a few.

The concept of additive decomposition of strain measures was firstly proposed by Green and Naghdi (1965) and later extended for generalized strain measures, i.e., $\mathbf{E}^{(m)} = \mathbf{E}_\mathrm{e}^{(m)} + \mathbf{E}_\mathrm{p}^{(m)}$ (see Equation 2.25) by e.g., Papadopoulos and Lu (1998) for isotropic and Papadopoulos and Lu (2001), Schröder *et al.* (2002), and Löblein *et al.* (2003) for anisotropic response. The particular case of $m = 0$ (logarithmic strain) has been extensively used for quadratic anisotropy in finite strain plasticity (see e.g., Miehe *et al.* (2002), Miehe and Apel (2004), and Ulz (2009)). Due to the additive character, the structure of the classical small strain theory is retained, thus taking advantage of the simplicity inherent to its classical return mapping schemes. However, some inconsistencies of the additive models with the multiplicative approach can been seen.

If the Green-Lagrange strain tensor is considered, $\mathbf{E}^{(2)} = \frac{1}{2}(\mathbf{C} - \mathbf{I})$, as an example and taking into account the multiplicative decomposition of $\mathbf{F}$, yields

$$\begin{aligned}\mathbf{E}^{(2)} &= \frac{1}{2}(\mathbf{F}^{\mathrm{T}}\mathbf{F} - \mathbf{I}) \\ &= \frac{1}{2}(\mathbf{F}_{\mathrm{p}}^{\mathrm{T}}\mathbf{F}_{\mathrm{e}}^{\mathrm{T}}\mathbf{F}_{\mathrm{e}}\mathbf{F}_{\mathrm{p}} - \mathbf{F}_{\mathrm{p}}^{\mathrm{T}}\mathbf{F}_{\mathrm{p}} + \mathbf{C}_{\mathrm{p}} - \mathbf{I}) \\ &= \mathbf{F}_{\mathrm{p}}^{\mathrm{T}}\mathbf{E}_{\mathrm{e}}^{(2)}\mathbf{F}_{\mathrm{p}} + \mathbf{E}_{\mathrm{p}}^{(2)} \\ &\neq \mathbf{E}_{\mathrm{e}}^{(2)} + \mathbf{E}_{\mathrm{p}}^{(2)},\end{aligned} \tag{5.1}$$

showing that the physical meaning of the elastic strain is lost in finite strains. Additive formulations usually prescribe a constitutive equation for the plastic strain, $\mathbf{E}_{\mathrm{p}}^{(m)}$, while the "elastic" strain is obtained from the relation $\mathbf{E}_{\mathrm{e}}^{(m)} = \mathbf{E}^{(m)} - \mathbf{E}_{\mathrm{p}}^{(m)}$. Moreover, Schmidt (2005) has proved that the use of the additive decomposition implies a nonphysical dependence of the elastic parameters on the plastic strain. In addition, under large simple shear deformations in rigid isotropic plasticity the additive formulation of generalized strain measures leads to spurious variations of shear stress regardless the specific value of m (Itskov, 2004). Such phenomena are not verified when the multiplicative approach is considered.

Most of the anisotropic hyperelastic-based models use structural tensors in order to describe the anisotropy of the material. This concept, developed initially by Spencer (1971) and Boehler (1979), consists of using scalar- or tensor-valued isotropic functions dependent on a proper set of second-order tensors (the so-called structural tensors) which represents the symmetry group of the considered material. Doing this way, on the one hand, the elastic anisotropy of the material can be described by the inclusion of structural tensors into an elastic energy potential (Reese, 2003, Eidel and Gruttmann, 2003, Svendsen *et al.*, 2006). On the other hand, if the structural tensors are introduced into the yield function, orthotropic yielding and plastic flow can be attained, as in the models of Eidel and Gruttmann (2003), Menzel and Steinmann (2003), Sansour *et al.* (2006a), Svendsen *et al.* (2006), and Vladimirov *et al.* (2010) for quadratic yield functions. Also, Shi and Mosler (2013) proposed a hyperelastic-based model that accounts for the nonquadratic anisotropic yield criterion of Cazacu and Barlat (2004), which employed (in contrast to the model presented in Section 5.3) nonsymmetric internal variables. Under the limitation of small elastic strains, Badreddine *et al.* (2010) presented a nonassociative finite plastic strain model that accounted for the nonquadratic Karafillis and Boyce (1993)'s yield criterion and isotropic ductile damage.

Generally, hyperelastic-based models including kinematic hardening laws follow one of two main strategies (Dettmer and Reese, 2004). The first strategy, which represents the so-called "Chaboche-type" models, makes use of an evolution equation for the back stress tensor. Hence, these models employ a stress-like internal variable (back stress) and an objective rate of this variable in order to preserve the objectivity (Tsakmakis, 1996, Lührs *et al.*, 1997, Tsakmakis and Willuweit, 2004).

Alternatively, the second strategy employs a strain-like internal variable. It is assumed that a term of the energy potential, related to the kinematic hardening, is dependent on

this variable. Also, the back stress is obtained from the derivative of the energy potential regarding this strain-like quantity (see e.g., Wallin *et al.* (2003) and Sansour *et al.* (2006b), among others). A particular type of models included in the second strategy consists of considering that the plastic part of the deformation gradient is multiplicatively decomposed into elastic and inelastic parts (Lion, 2000, Dettmer and Reese, 2004, Vladimirov *et al.*, 2008, Henann and Anand, 2009, Freund *et al.*, 2012). This decomposition is physically motivated (Lion, 2000) and represents a continuum mechanical extension of the classical rheological model of Armstrong-Frederick kinematic hardening (see Section 3.4.2.1) to finite strains in the context of hyperelasticity. Considering that kinematic hardening can be seen as a specific kind of induced plastic anisotropy, which evolves with the deformation process, some authors have formulated the kinematic hardening effect employing the concept of structural tensors (Svendsen, 2001, Dettmer and Reese, 2004).

The theoretical background of (and comparisons between) hypoelastic- and hyperelastic-based formulations can be found in, e.g., Xiao *et al.* (2006) and Shutov and Ihlemann (2014). Shutov and Ihlemann (2014) proposed the notion of weak invariance, which states that a constitutive model is weakly invariant if, by simply employing suitable transformations on the initial conditions, the constitutive equations are preserved when the local reference configuration is transformed. In their analysis, they concluded that the Zaremba-Jaumann rate (see Section 5.2.1) is the only weakly invariant corotational objective rate. In addition, regarding hyperelastic-based formulations, multiplicative models are weakly invariant, in contrast to additive models using the logarithmic strain. Numerical application-oriented comparisons of hypoelastic- and hyperelastic-based formulations can be found in, e.g., the works of Chatti (2010) and Brepols *et al.* (2014) for anisotropic, following Hill (1948)'s criterion, and isotropic plasticity, respectively.

A comprehensive application-oriented comparison of these two approaches for complex nonquadratic anisotropy is still missing in the literature.

5.2 Finite strain hypoelastoplasticity

In this section, an extension of the previously presented small strain model (Chapter 4) to finite strains in the context of hypoelasticity is shown. Firstly, since Eulerian hypoelastic constitutive models rely on the use of objective constitutive equations, a brief review on the topic of objectivity is given. Then, the derivation of the finite strain hypoelastic-based model is presented. This section ends with the adaptation of an objective integration algorithm to the presented hypoelastic-based model.

5.2.1 Objective constitutive quantities

The principle of objectivity (or frame indifference) requires that any physical process must not be influenced by an arbitrary change of observer. This invariance must be taken into

account by the mathematical constitutive relations that represent the physical phenomena. The relation that defines the change of spatial referential, from observer $\mathcal{O}$ to observer $\mathcal{O}^+$, at the instant t, of an arbitrary vectorial quantity $\boldsymbol{y}$ is defined by

$$\boldsymbol{y}^+(t) = \mathbf{Q}(t)\boldsymbol{y}(t) + \boldsymbol{G}(t), \tag{5.2}$$

where $\mathbf{Q}$ and $\boldsymbol{G}$ denote arbitrary (time-dependent) rotation tensor and translation vector, respectively, between the two observers.

One may consider the two classes of objective second-order tensor-valued quantities (denoted Lagrangean and Eulerian) which transforms under a change of observer according to

$$\boldsymbol{\Gamma}^+(t) = \boldsymbol{\Gamma}(t) \text{ and} \tag{5.3}$$

$$\boldsymbol{\Lambda}^+(t) = \mathbf{Q}(t)\boldsymbol{\Lambda}(t)\mathbf{Q}^{\mathrm{T}}(t), \tag{5.4}$$

respectively. The conventional material time rate of an objective Lagrangean tensor, $\dot{\boldsymbol{\Gamma}}$ is also objective, i.e., $\dot{\boldsymbol{\Gamma}}^+ = \dot{\boldsymbol{\Gamma}}$. In opposite, the conventional material time differentiation of an Eulerian second-order tensor quantity yields

$$\dot{\boldsymbol{\Lambda}}^+ = \dot{\mathbf{Q}}\boldsymbol{\Lambda}\mathbf{Q}^{\mathrm{T}} + \mathbf{Q}\dot{\boldsymbol{\Lambda}}\mathbf{Q}^{\mathrm{T}} + \mathbf{Q}\boldsymbol{\Lambda}\dot{\mathbf{Q}}^{\mathrm{T}} \neq \mathbf{Q}\dot{\boldsymbol{\Lambda}}\mathbf{Q}^{\mathrm{T}}. \tag{5.5}$$

This implies that even though $\boldsymbol{\Lambda}$ is objective and may be used as a constitutive variable, its conventional material time rate should not be used in the constitutive formulation, since it is only objective for a time-independent rotation, i.e., $\dot{\mathbf{Q}} = \mathbf{0}$. Examples of objective Eulerian tensors are the Cauchy stress tensor, $\boldsymbol{\sigma}$, and the rate of deformation, $\mathbf{d}$. Thus, considering that only objective quantities should be used in hypoelastic constitutive relations, the stress rate $\dot{\boldsymbol{\sigma}}$ is not suitable for hypoelastic formulations. This implies that relation 4.16 can not be directly employed to describe the time evolution of the Cauchy stress in the context of hypoelasticity.

In order to avoid this issue, i.e., to ensure that the objectivity is fulfilled, the conventional material time rate of the stress tensor is replaced by a proper objective rate. Considering a generic Eulerian second-order tensor, $\boldsymbol{\Lambda}$, its objective rate can be expressed in general terms according to

$$\overset{\nabla}{\boldsymbol{\Lambda}}{}^{\star} = \dot{\boldsymbol{\Lambda}} + \boldsymbol{\Lambda}\boldsymbol{\Phi}^{\star} + \boldsymbol{\Phi}^{\star\mathrm{T}}\boldsymbol{\Lambda}, \tag{5.6}$$

where $\overset{\nabla}{(\bullet)}{}^{\star}$ stands for the objective rate and $\boldsymbol{\Phi}^{\star}$ is a proper second-order tensor.

Depending on the choice of $\boldsymbol{\Phi}^{\star}$, two distinct subclasses of objective rates of Eulerian tensors may be defined, namely corotational rates if a skew-symmetric tensor ($\boldsymbol{\Phi}^{\star\mathrm{T}} = -\boldsymbol{\Phi}^{\star}$) is considered, or non-corotational rates in the case of non-skew-symmetric tensors ($\boldsymbol{\Phi}^{\star\mathrm{T}} \neq -\boldsymbol{\Phi}^{\star}$). The corotational rate of an objective Eulerian tensor-valued quantity can be seen as the conventional material time rate of that Eulerian quantity when represented in a locally rotating (corotational) coordinate frame, where the spin tensor is defined as $\boldsymbol{\Omega}^{\star} = \boldsymbol{\Phi}^{\star}$. This

means that the structure of classical Galilean space-time is preserved and hence the Leibniz's chain rule for derivatives is respected by the corotational rate. In contrary, regarding non-corotational rates, the structure of the Galilean space-time is distorted implying the violation of the Leibniz's rule (Xiao *et al.*, 2006).

The most common examples of non-corotational rates are

Cotter-Rivlin rate $\quad \boldsymbol{\Phi}^{\mathrm{CR}} = \mathbf{l}$,

Oldroyd rate (Lie derivative) $\quad \boldsymbol{\Phi}^{\mathrm{O}} = -\mathbf{l}^{\mathrm{T}}$, and

Truesdell rate $\quad \boldsymbol{\Phi}^{\mathrm{T}} = -\mathbf{l} + \frac{1}{2}\mathrm{tr}\mathbf{l}$,

which require a special mathematical treatment due to the violation of the Leibniz's rule. Regarding the corotational rates, the representation

$$\overset{\nabla}{\boldsymbol{\Lambda}}{}^{\star} = \dot{\boldsymbol{\Lambda}} + \boldsymbol{\Lambda}\boldsymbol{\Omega}^{\star} - \boldsymbol{\Omega}^{\star}\boldsymbol{\Lambda}, \tag{5.7}$$

is commonly employed and the most important rates are

Zaremba-Jaumann rate $\quad \boldsymbol{\Phi}^{\mathrm{ZJ}} = \mathbf{w}$,

Green-McInnis-Naghdi rate $\quad \boldsymbol{\Phi}^{\mathrm{GMN}} = \dot{\mathbf{R}}\mathbf{R}^{\mathrm{T}}$, and

Logarithmic rate $\quad \boldsymbol{\Phi}^{\mathrm{Log}} = \mathbf{w} + \sum_{\substack{i,j=1 \\ i\neq j}}^{m} \left(\frac{1 + (\lambda_i^2/\lambda_j^2)}{1 - (\lambda_i^2/\lambda_j^2)} + \frac{2}{\ln(\lambda_i^2/\lambda_j^2)} \right) \boldsymbol{b}_i \mathbf{d} \boldsymbol{b}_j$,

where λ_i^2 and $\boldsymbol{b}_i$, with $i = 1 \ldots m$, denote the m distinct eigenvalues and the eigenvectors of the left Cauchy-Green deformation tensor, $\mathbf{B}$, respectively (see Section 2.1.2) (Xiao *et al.*, 1997).

The Zaremba-Jaumann rate is widely used in the context of hypoelastic-based elasto-plasticity. However, it has the disadvantage of predicting spurious phenomena, known as shear oscillations during monotonically progressing simple shear deformation. This phenomena were firstly revealed by Lehmann (1972) for rigid plastic von Mises flow theory with Prager kinematic hardening rule and occurs even when purely elastic behaviour is considered (Dienes, 1979).

Comparatively to the Zaremba-Jaumann rate, the Green-McInnis-Naghdi rate provides a more realistic stress response during simple shear deformations. Nevertheless, Dashner (1986) has questioned the physical meaning of its theoretical basis and the determination of $\boldsymbol{\Phi}^{\mathrm{GMN}}$ is computationally more expensive in comparison to $\boldsymbol{\Phi}^{\mathrm{ZJ}}$, because it requires the polar decomposition of $\mathbf{F}$. In the context of hypoelastic-based elastoplasticity, the continuum spin (see Equation 2.19) can be additively decomposed into an elastic, $\mathbf{w}_{\mathrm{e}} = \dot{\mathbf{R}}\mathbf{R}^{\mathrm{T}}$, and a plastic, $\mathbf{w}_{\mathrm{p}} = \mathbf{R}\mathrm{skew}(\dot{\mathbf{U}}\mathbf{U})\mathbf{R}^{\mathrm{T}}$, parts. Considering that in sheet metal forming shear loading in the normal direction of the sheet's plane is not relevant, the assumption that the plastic spin

is negligible comparatively to its elastic counterpart, i.e., $\mathbf{w}_\mathrm{e} \gg \mathbf{w}_\mathrm{p}$, is commonly accepted (Alves, 2003). In other words, this assumption considers that the Zaremba-Jaumann and Green-McInnis-Naghdi rates are approximately equal, i.e., $\boldsymbol{\Phi}^{\mathrm{ZJ}} = \mathbf{w} \approx \mathbf{w}_\mathrm{e} = \dot{\mathbf{R}}\mathbf{R}^{\mathrm{T}} = \boldsymbol{\Phi}^{\mathrm{GMN}}$, in sheet metal forming processes.

With the exception of the logarithmic one, the well-known objective rates mentioned before are not exactly integrable, except for some particular set of elastic constants, thus predicting nonphysical dissipation of energy during purely "elastic" deformation. The logarithmic rate has been proposed by Xiao *et al.* (1997) based on Prager's yielding stationary criterion[1] and on a new "elastic integrability criterion"[2]. Although this can be considered as the more correct objective rate, the determination of the associated second-order rotation tensor, $\boldsymbol{\Phi}^{\mathrm{Log}}$, is computationally very expensive.

5.2.2 Additive decomposition of the rate of deformation

The rate of deformation, $\mathbf{d}$, is an Eulerian objective tensor quantity, and hence it is a proper deformation rate to be used in the hypoelastic-based formulation. Motivated by the additive decomposition of the strain rate in the small strain theory of elastoplasticity (Equation 4.5), the rate of deformation is assumed to decompose additively according to

$$\mathbf{d} = \mathbf{d}_\mathrm{e} + \mathbf{d}_\mathrm{p}, \tag{5.8}$$

where $\mathbf{d}_\mathrm{e}$ and $\mathbf{d}_\mathrm{p}$ are denoted as elastic and plastic rates of deformation, respectively. It is worth mentioning that, similarly to $\mathbf{d}$, the second-order tensors $\mathbf{d}_\mathrm{e}$ and $\mathbf{d}_\mathrm{p}$ are Eulerian objective quantities and can be used as variables in the constitutive hypoelastic model.

5.2.3 Hypoelastic constitutive law

The hypoelastic constitutive law establishing the relation between any objective rate of stress and the elastic rate of deformation can be generally expressed by

$$\overset{\nabla}{\boldsymbol{\sigma}}{}^{\star} = \mathbf{f}(\boldsymbol{\sigma}, \mathbf{d}_\mathrm{e}), \tag{5.9}$$

where $\mathbf{f}$ is a function of the stress and elastic rate of deformation. In contrast to the hyperelastic-based formulation to be seen in detail in Section 5.3, the constitutive relation of Equation 5.9 is not based on an elastic potential. Thus, during a closed large "elastic" deformation cycle the conservation of energy may not be ensured whereas the work done is not zero, with the exception to models based on the logarithmic rate where the "elastic integrability criterion" is imposed. Due to this nonphysical dissipation of energy, hypoelastic

[1] "The simultaneous vanishing of the stress rate and plastic flow should render yield function stationary" (Xiao *et al.*, 2006).

[2] "For every process of elastic deformations with $\mathbf{d}_\mathrm{e} = \mathbf{d}$, the rate equation $\mathbf{d}_\mathrm{e} = (\partial^2\psi(\boldsymbol{\tau})/\partial\boldsymbol{\tau}^2) : \overset{\nabla}{\boldsymbol{\tau}}$ should be exactly integrable to deliver a dissipationless elastic relation and hence really characterize recoverable elastic behaviour" (Xiao *et al.*, 2006).

constitutive laws are mainly used to describe the elastic behaviour of finite strain elastoplastic models where the elastic strains are expected to be small when compared to the plastic counterparts, i.e., $\mathbf{F}_e \approx \mathbf{I}$, such as in metal elastoplasticity. In this situation, the spatial velocity gradient can be approximately obtained from

$$\begin{aligned} \mathbf{l} &= \dot{\mathbf{F}}_{\mathrm{e}}\mathbf{F}_{\mathrm{e}}^{-1} + \mathbf{F}_{\mathrm{e}}\dot{\mathbf{F}}_{\mathrm{p}}\mathbf{F}_{\mathrm{p}}^{-1}\mathbf{F}_{\mathrm{e}}^{-1} \\ &= \mathbf{l}_{\mathrm{e}} + \mathbf{F}_{\mathrm{e}}\mathbf{l}_{\mathrm{p}}\mathbf{F}_{\mathrm{e}}^{-1} \\ &\approx \mathbf{l}_{\mathrm{e}} + \mathbf{l}_{\mathrm{p}} \Rightarrow \mathbf{d} \approx \mathbf{d}_{\mathrm{e}} + \mathbf{d}_{\mathrm{p}}. \end{aligned} \tag{5.10}$$

Note that the additive decomposition of the rate of deformation (Equation 5.8) is recovered. Considering this, the most used hypoelastic law is the extension of the small strain isotropic linear constitutive relation 4.16 to the objective stress rate, as follows

$$\overset{\nabla}{\boldsymbol{\sigma}}{}^{\star} = \mathbb{D} : \mathbf{d}_{\mathrm{e}} = \mathbb{D} : (\mathbf{d} - \mathbf{d}_{\mathrm{p}}). \tag{5.11}$$

5.2.4 Evolution equations

Considering the Eulerian objective plastic rate of deformation, $\mathbf{d}_{\mathrm{p}}$, the associated flow rule (see Equation 4.14) is expressed as

$$\mathbf{d}_{\mathrm{p}} = \dot{\lambda}\frac{\partial \Phi}{\partial \boldsymbol{\eta}}, \tag{5.12}$$

where the yield potential, Φ, has the same structure as in the small strain theory (see Equation 4.17).

Taking into account that any second-order tensor-valued internal variable must be objective, the above argumentation regarding the objective rate of the Cauchy stress holds for the back stress tensor. Thus the objective back stress rate reads

$$\overset{\nabla}{\boldsymbol{\alpha}}{}^{\star} = c\mathbf{d}_{\mathrm{p}} - \dot{\lambda} b \boldsymbol{\alpha}. \tag{5.13}$$

Finally, the evolution equation of the accumulated plastic strain is given by Equation 4.13c and the loading/unloading conditions (Equation 4.20) complete the set of constitutive equations.

5.2.5 Numerical implementation

In this section the numerical implementation of the considered hypoelastic-based model is presented. The numerical treatment is suitable for most of the rate-independent hypoelastic-based models grounded on the isotropic linear constitutive law of Equation 5.11. Thus, its adaptation to a model in which several back stress components are included can be seen as a straightforward task. Nevertheless, a more general and comprehensive discussion on this topic can be found in, e.g., Simo and Hughes (1998).

5.2.5.1 Objective integration algorithms

The crucial issue in the numerical implementation of hypoelastic-based models stands on the development of numerical integration algorithms that yield discrete equations in which the principle of material frame indifference is ensured in the time discrete frame. This leads to the so-called incrementally objective algorithms (Hughes and Winget, 1980) which preserve the condition of incremental objectivity in order to avoid the occurrence of spurious stresses in rigid body motions (Simo and Hughes, 1998). The development of such algorithms consist of three steps as follows:

1. firstly, the given rate-constitutive equations are mapped from the spatial configuration to a local configuration, in which the rate-type equations are unaffected by superimposed spatial rigid body motions;

2. then, a time integration algorithm is carried out, providing the objective discrete equations in the local configuration;

3. finally, the discrete equations are mapped back from the local to the spacial configuration.

Following this procedure, two basic methodologies exist to define a suitable local configuration (Simo and Hughes, 1998):

Convective representation This methodology considers the convective (reference) configuration as the "local" configuration. It exploits the fact that tensor-based quantities defined in this configuration are independent of, and thus unaffected by, superimposed rigid body motions. As pointed out in Section 2.1.1, the mapping between the reference (material) and current (spacial) configuration is carried out by proper tensorial transformations using the deformation gradient. While this methodology seems interesting from the conceptual point of view, it preserves the simplicity inherent to the state-update integration algorithms used in small strain formulations (e.g., the algorithms presented in Section 4.3) only when the Oldroyd rate of the Kirchhoff stress for J_2-plasticity models is considered (Simo and Hughes, 1998).

Local rotating representation This methodology transforms the rate-type evolution equations to a locally rotating Cartesian coordinate system (also called material corotational coordinate system), properly defined to precisely ensure that the rotated constitutive equations remain unaffected under any superimposed rigid body motion. This methodology has the advantage of leading to state-update integration algorithms whose structures are indeed identical to the ones used in the integration of small strain constitutive equations. It is particularly suitable to models based on corotational objective rates, which involve spin-like tensors such as the Zaremba-Jaumann, Green-McInnis-Naghdi, and logarithmic rates. The crucial computational feature in this methodology relies on

the determination of the locally rotating configuration. This issue is solved by numerically integrating an initial-value problem that produces a subgroup of proper orthogonal transformations, as presented in Section 5.2.5.2.

Considering the advantages of the second methodology, this will be the one analysed in this work. This methodology is based on the theorem stating that, for any given rotation tensor $\mathbf{Q}^\star$, there is a skew-symmetric (spin) tensor $\boldsymbol{\Omega}^\star$ given by $\boldsymbol{\Omega}^\star = \dot{\mathbf{Q}}^\star \mathbf{Q}^{\star\mathrm{T}}$, and which evolution ($\dot{\mathbf{Q}}^\star$) is obtained from the initial-value problem of Equation 5.32. Considering that the rotation tensor $\mathbf{Q}^\star$ is properly computed and is indeed a rotation tensor from the locally rotating (unaffected by superimposed rigid body motions) configuration to the spatial configuration, the hypoelastic constitutive law (Equation 5.11) is mapped to the local configuration by multiplying it with $\mathbf{Q}^{\star\mathrm{T}}$ and $\mathbf{Q}^\star$ from the left and right sides, respectively, resulting in

$$\begin{aligned} \mathbf{Q}^{\star\mathrm{T}} \overset{\nabla}{\boldsymbol{\sigma}}{}^\star \mathbf{Q}^\star = \mathbf{Q}^{\star\mathrm{T}} (\mathbb{D} : \mathbf{d}_\mathrm{e}) \mathbf{Q}^\star = \mathbb{D} : (\mathbf{Q}^{\star\mathrm{T}} \mathbf{d}_\mathrm{e} \mathbf{Q}^\star) \\ \dot{\hat{\boldsymbol{\sigma}}}^\star = \mathbb{D} : \hat{\mathbf{d}}_\mathrm{e}^\star \end{aligned} \tag{5.14}$$

where the isotropy of the constitutive elastic stiffness tensor, $\mathbb{D}$, has been used. Moreover, the following notations have been introduced to denote the rotated Cauchy stress and the rotated rate of deformation,

$$\hat{\boldsymbol{\sigma}}^\star = \mathbf{Q}^{\star\mathrm{T}} \boldsymbol{\sigma} \mathbf{Q}^\star \text{ and} \tag{5.15}$$

$$\hat{\mathbf{d}}^\star = \mathbf{Q}^{\star\mathrm{T}} \mathbf{d} \mathbf{Q}^\star, \text{ with } \hat{\mathbf{d}}^\star = \hat{\mathbf{d}}_\mathrm{e}^\star + \hat{\mathbf{d}}_\mathrm{p}^\star, \tag{5.16}$$

respectively. Also, by simply differentiation one can show that the representation of the complex corotational objective rate of the Cauchy stress in the locally rotating configuration is indeed the simple material time derivative of the rotated Cauchy stress, i.e.,

$$\dot{\hat{\boldsymbol{\sigma}}}^\star = \mathbf{Q}^{\star\mathrm{T}} \overset{\nabla}{\boldsymbol{\sigma}}{}^\star \mathbf{Q}^\star. \tag{5.17}$$

This procedure must be employed to all evolution equations of tensor-valued internal variables of the constitutive model. Hence, applying this procedure to the objective rate of the back stress tensor (Equation 5.13), one obtains

$$\begin{aligned} \mathbf{Q}^{\star\mathrm{T}} \overset{\nabla}{\boldsymbol{\alpha}}{}^\star \mathbf{Q}^\star = \mathbf{Q}^{\star\mathrm{T}} (c\mathbf{d}_\mathrm{p} - b\dot{\lambda}\boldsymbol{\alpha}) \mathbf{Q}^\star = c\mathbf{Q}^{\star\mathrm{T}} \mathbf{d}_\mathrm{p} \mathbf{Q}^\star - b\dot{\lambda} \mathbf{Q}^{\star\mathrm{T}} \boldsymbol{\alpha} \mathbf{Q}^\star \\ \dot{\hat{\boldsymbol{\alpha}}}^\star = c\hat{\mathbf{d}}_\mathrm{p}^\star - b\dot{\lambda}\hat{\boldsymbol{\alpha}}^\star, \end{aligned} \tag{5.18}$$

where the rotated back stress tensor and its material time derivative are given by

$$\hat{\boldsymbol{\alpha}}^\star = \mathbf{Q}^{\star\mathrm{T}} \boldsymbol{\alpha} \mathbf{Q}^\star \text{ and} \tag{5.19}$$

$$\dot{\hat{\boldsymbol{\alpha}}}^\star = \mathbf{Q}^{\star\mathrm{T}} \overset{\nabla}{\boldsymbol{\alpha}}{}^\star \mathbf{Q}^\star, \tag{5.20}$$

respectively.

Remark 1 It is now shown that the representation of an Eulerian objective quantity in the locally rotating configuration, $\hat{\boldsymbol{\Lambda}}^{\star}$, is indeed objective in that configuration. The quantity $\hat{\boldsymbol{\Lambda}}^{\star}$ transforms under a change of observer according to

$$\begin{aligned}(\hat{\boldsymbol{\Lambda}}^{\star})^{+} &= (\mathbf{Q}^{\star\mathrm{T}}\boldsymbol{\Lambda}\mathbf{Q}^{\star})^{+} = (\mathbf{Q}^{\star\mathrm{T}})^{+}(\boldsymbol{\Lambda})^{+}(\mathbf{Q}^{\star})^{+} \\ &= (\mathbf{Q}^{\star\mathrm{T}}\mathbf{Q}^{\mathrm{T}})(\mathbf{Q}\boldsymbol{\Lambda}\mathbf{Q}^{\mathrm{T}})(\mathbf{Q}\mathbf{Q}^{\star})^{+} \\ &= \mathbf{Q}^{\star\mathrm{T}}\boldsymbol{\Lambda}\mathbf{Q}^{\star} = \hat{\boldsymbol{\Lambda}}^{\star},\end{aligned} \tag{5.21}$$

which shows that $\hat{\boldsymbol{\Lambda}}^{\star}$ is precisely objective in the locally rotating configuration. This proves that $\hat{\dot{\boldsymbol{\sigma}}}^{\star}$, $\hat{\boldsymbol{\alpha}}^{\star}$, and $\hat{\mathbf{d}}^{\star}$, and thus the constitutive relations 5.14b and 5.18, are unaffected by superimposed rigid body motions.

At this point the first step of the objective algorithm is concluded. The next step consists of the time discretization of the constitutive relations represented in the local configuration. Following the procedure presented in Section 4.3.1, the rate-type constitutive constitutive Equations 5.14 and 5.18 are integrated along the time interval $[t_n, t_{n+1}] \subset [t_0, t_{\mathrm{end}}]$ by employing the difference quotient (Equation 4.37), leading to the following integrated formulas

$$\hat{\boldsymbol{\sigma}}^{\star}_{n+1} = \hat{\boldsymbol{\sigma}}^{\star}_{n} + \mathbb{D} : \Delta t(\hat{\mathbf{d}}^{\star}_{n+\alpha} - \hat{\mathbf{d}}^{\star}_{\mathrm{p}_{n+\alpha}}) \text{ and} \tag{5.22}$$

$$\hat{\boldsymbol{\alpha}}^{\star}_{n+1} = \hat{\boldsymbol{\alpha}}^{\star}_{n} + c\Delta t\hat{\mathbf{d}}^{\star}_{\mathrm{p}_{n+\alpha}} - b\Delta\lambda\hat{\boldsymbol{\alpha}}^{\star}_{n+\alpha}. \tag{5.23}$$

With the integrated formulas in hand, the final step can be performed. The mapping of these equations back to the spatial configuration is carried out by replacing the rotated quantities by Equations 5.15, 5.16, and 5.19 accordingly, i.e.,

$$\begin{aligned}\mathbf{Q}^{\star\mathrm{T}}_{n+1}\boldsymbol{\sigma}_{n+1}\mathbf{Q}^{\star}_{n+1} &= \mathbf{Q}^{\star\mathrm{T}}_{n}\boldsymbol{\sigma}_{n}\mathbf{Q}^{\star}_{n} + \mathbb{D} : [\mathbf{Q}^{\star\mathrm{T}}_{n+\alpha}(\Delta t\mathbf{d}_{n+\alpha})\mathbf{Q}^{\star}_{n+\alpha} - \mathbf{Q}^{\star\mathrm{T}}_{n+\alpha}(\Delta t\mathbf{d}_{\mathrm{p}_{n+\alpha}})\mathbf{Q}^{\star}_{n+\alpha}] \\ \boldsymbol{\sigma}_{n+1} &= \mathbf{Q}^{\star}_{\Delta}\boldsymbol{\sigma}_{n}\mathbf{Q}^{\star\mathrm{T}}_{\Delta} + \mathbb{D} : [\mathbf{Q}^{\star}_{\delta}(\Delta t\mathbf{d}_{n+\alpha})\mathbf{Q}^{\star\mathrm{T}}_{\delta} - \mathbf{Q}^{\star}_{\delta}(\Delta t\mathbf{d}_{\mathrm{p}_{n+\alpha}})\mathbf{Q}^{\star\mathrm{T}}_{\delta}] \text{ and}\end{aligned} \tag{5.24}$$

$$\begin{aligned}\mathbf{Q}^{\star\mathrm{T}}_{n+1}\boldsymbol{\alpha}_{n+1}\mathbf{Q}^{\star}_{n+1} &= \mathbf{Q}^{\star\mathrm{T}}_{n}\boldsymbol{\alpha}_{n}\mathbf{Q}^{\star}_{n} + c\mathbf{Q}^{\star\mathrm{T}}_{n+\alpha}(\Delta t\mathbf{d}_{\mathrm{p}_{n+\alpha}})\mathbf{Q}^{\star}_{n+\alpha} - b\Delta\lambda\mathbf{Q}^{\star\mathrm{T}}_{n+\alpha}\boldsymbol{\alpha}_{n+\alpha}\mathbf{Q}^{\star}_{n+\alpha} \\ \boldsymbol{\alpha}_{n+1} &= \mathbf{Q}^{\star}_{\Delta}\boldsymbol{\alpha}_{n}\mathbf{Q}^{\star\mathrm{T}}_{\Delta} + c\mathbf{Q}^{\star}_{\delta}(\Delta t\mathbf{d}_{\mathrm{p}_{n+\alpha}})\mathbf{Q}^{\star\mathrm{T}}_{\delta} - b\Delta\lambda\mathbf{Q}^{\star}_{\delta}\boldsymbol{\alpha}_{n+\alpha}\mathbf{Q}^{\star\mathrm{T}}_{\delta},\end{aligned} \tag{5.25}$$

where the incremental rotations from the configurations at n and $n+\alpha$ to the configuration at $n+1$ are denoted by $\mathbf{Q}^{\star}_{\Delta}$ and $\mathbf{Q}^{\star}_{\delta}$, and expressed by

$$\mathbf{Q}^{\star}_{\Delta} = \mathbf{Q}^{\star}_{n+1}\mathbf{Q}^{\star\mathrm{T}}_{n} \text{ and} \tag{5.26}$$

$$\mathbf{Q}^{\star}_{\delta} = \mathbf{Q}^{\star}_{n+1}\mathbf{Q}^{\star\mathrm{T}}_{n+\alpha}, \tag{5.27}$$

respectively.

Note that the integration of evolution equations for scalar variables does not require the use of an objective integration algorithm. Thus, the integration of the evolution of the

equivalent plastic strain is given by the standard integration formula of Equation 4.40.

The main advantage of the methodology using the local rotating representation is that the resulting system of equations (5.24, 5.25 and 4.40) can be numerically integrated using the structure of algorithms for small strain theory, such as those presented in Sections 4.3.3 and 4.3.4. In order to employ the elastic predictor-plastic corrector method the following trial quantities should be considered,

$$\Delta\lambda = 0, \tag{5.28}$$

$$\boldsymbol{\sigma}_{n+1}^{\text{trial}} = \mathbf{Q}_{\Delta}^{\star}\boldsymbol{\sigma}_n\mathbf{Q}_{\Delta}^{\star\text{T}} + \mathbb{D} : [\mathbf{Q}_{\delta}^{\star}(\Delta t\mathbf{d}_{n+\alpha})\mathbf{Q}_{\delta}^{\star\text{T}}], \tag{5.29}$$

$$\boldsymbol{\alpha}_{n+1}^{\text{trial}} = \mathbf{Q}_{\Delta}^{\star}\boldsymbol{\alpha}_n\mathbf{Q}_{\Delta}^{\star\text{T}}, \text{ and} \tag{5.30}$$

$$\bar{\varepsilon}_{\text{p}_{n+1}}^{\text{trial}} = \bar{\varepsilon}_{\text{p}_n}. \tag{5.31}$$

In this work it is assumed that the directions of the anisotropy axes follow the material's rigid body motions, so these axis are assumed to be fixed in the locally rotating (material corotational) coordinate system. This way, for anisotropic materials, the structure of the elastic predictor-plastic corrector algorithms for small strain theory are used to numerically integrate Equations 5.22, 5.23 and 4.40, before the mapping to the spatial configuration.

5.2.5.2 Determination of the rotation tensor

The numerical computation of the incremental rotation tensors is analysed in this section. The rotation tensor $\mathbf{Q}^{\star}$, associated to the skew-symmetric (spin) tensor $\boldsymbol{\Omega}^{\star}$, is obtained by solving the following initial value problem,

$$\dot{\mathbf{Q}}^{\star} = \boldsymbol{\Omega}^{\star}\mathbf{Q}^{\star}, \text{ with } \mathbf{Q}^{\star}\Big|_{t=0} = \mathbf{I}. \tag{5.32}$$

Following the work of Simo and Hughes (1998), this problem can be solved using the exponential map according to

$$\mathbf{Q}_{n+1}^{\star} = \exp(\Delta t\boldsymbol{\Omega}_{n+\alpha}^{\star})\mathbf{Q}_n^{\star}, \text{ with } \mathbf{Q}^{\star}\Big|_{t=0} = \mathbf{I}. \tag{5.33}$$

The use of the exponential map ensures that the rotation tensor $\mathbf{Q}_{n+1}^{\star}$ is indeed a rotation, since a tensorial exponential function exactly maps skew-symmetric tensors onto orthogonal ones. As pointed out by Simo and Hughes (1998), the algorithm of Equation 5.33 is consistent with the initial value problem (5.32) and second-order accurate for the particular case of $\alpha = 1/2$. Moreover, the computation of $\mathbf{Q}_{n+\alpha}^{\star}$ and $\mathbf{Q}_{n+1}^{\star}$ is notably easy and straightforward when $\alpha = 1/2$ is considered. In this situation, one has

$$\mathbf{Q}_{n+\frac{1}{2}}^{\star} = \bar{\mathbf{Q}}^{\star}\mathbf{Q}_n^{\star}, \tag{5.34}$$

$$\mathbf{Q}_{n+1}^{\star} = \bar{\mathbf{Q}}^{\star}\mathbf{Q}_{n+\frac{1}{2}}^{\star}, \text{ thus} \tag{5.35}$$

$$\mathbf{Q}^{\star}_{n+1} = \bar{\mathbf{Q}}^{\star 2}\mathbf{Q}^{\star}_{n}, \tag{5.36}$$

where $\bar{\mathbf{Q}}^{\star}$ is a proper orthogonal tensor.

On the other hand, considering the following property of a tensor exponential function,

$$\exp(\mathbf{A}+\mathbf{B}) = \exp(\mathbf{A})\exp(\mathbf{B}), \;\; \text{if } \mathbf{AB} = \mathbf{BA}, \tag{5.37}$$

and bearing in mind that $(\Delta t \boldsymbol{\Omega}^{\star}_{n+\frac{1}{2}})/2$ commutes with itself, the algorithm of Equation 5.33 can be rewritten as

$$\begin{aligned} \mathbf{Q}^{\star}_{n+1} &= \exp\left(\frac{1}{2}\Delta t \boldsymbol{\Omega}^{\star}_{n+\frac{1}{2}} + \frac{1}{2}\Delta t \boldsymbol{\Omega}^{\star}_{n+\frac{1}{2}}\right)\mathbf{Q}^{\star}_{n} \\ &= \left[\exp\left(\frac{1}{2}\Delta t \boldsymbol{\Omega}^{\star}_{n+\frac{1}{2}}\right)\right]^{2}\mathbf{Q}^{\star}_{n}. \end{aligned} \tag{5.38}$$

Comparison of Equations 5.36 and 5.38 provides the relation

$$\bar{\mathbf{Q}}^{\star} = \exp\left(\frac{1}{2}\Delta t \boldsymbol{\Omega}^{\star}_{n+\frac{1}{2}}\right), \tag{5.39}$$

which can be used to compute $\mathbf{Q}^{\star}_{\Delta}$ and $\mathbf{Q}^{\star}_{\delta}$ by replacing Equations 5.36 and 5.34 into Equations 5.26 and 5.27, respectively.

The computation of the tensor exponential function can be performed using a closed-form expression, for any skew-symmetric tensor $\boldsymbol{\Omega}^{\star}$, using the Rodrigues' formula. Nevertheless, $\mathbf{Q}^{\star}_{\Delta}$ can be computed in an approximated way according to

$$\begin{aligned} \mathbf{Q}^{\star}_{n+1} &= \exp\left(\frac{1}{2}\Delta t \boldsymbol{\Omega}^{\star}_{n+\frac{1}{2}}\right)\exp\left(\frac{1}{2}\Delta t \boldsymbol{\Omega}^{\star}_{n+\frac{1}{2}}\right)\mathbf{Q}^{\star}_{n} \\ \mathbf{Q}^{\star}_{n+1}\mathbf{Q}^{\star\mathrm{T}}_{n} &= \left[\exp\left(-\frac{1}{2}\Delta t \boldsymbol{\Omega}^{\star}_{n+\frac{1}{2}}\right)\right]^{-1}\exp\left(\frac{1}{2}\Delta t \boldsymbol{\Omega}^{\star}_{n+\frac{1}{2}}\right) \\ \mathbf{Q}^{\star}_{\Delta} &\approx \left(\mathbf{I} - \frac{1}{2}\Delta t \boldsymbol{\Omega}^{\star}_{n+\frac{1}{2}}\right)^{-1}\left(\mathbf{I} + \frac{1}{2}\Delta t \boldsymbol{\Omega}^{\star}_{n+\frac{1}{2}}\right), \end{aligned} \tag{5.40}$$

where a first order truncation of the tensor exponential function was considered. This relation can also be obtained if the standard version of the generalized midpoint rule is used to solve the initial value problem 5.32 (Simo and Hughes, 1998).

Considering specific choices for the corotational objective rate, in the case of the Zaremba-Jaumann rate ($\boldsymbol{\Omega}^{\mathrm{ZJ}} = \mathbf{w}$) the spin tensor at $t = n + \alpha$ is computed according to

$$\mathbf{w}_{n+\alpha} = \frac{\mathbf{l}_{n+\alpha} - \mathbf{l}^{\mathrm{T}}_{n+\alpha}}{2\Delta t}. \tag{5.41}$$

The spatial velocity gradient is evaluated at $t = n + \alpha$ from

$$\mathbf{l}_{n+\alpha} = \Delta\mathbf{F}_{n+\alpha}\mathbf{F}^{-1}_{n+\alpha}, \tag{5.42}$$

where the relations

$$\Delta\mathbf{F}_{n+\alpha} = \frac{1}{\alpha}(\mathbf{F}_{n+\alpha} - \mathbf{F}_n) \text{ and} \tag{5.43}$$

$$\mathbf{F}_{n+\alpha} = \alpha\mathbf{F}_{n+1} + (1-\alpha)\mathbf{F}_n, \tag{5.44}$$

hold. This task is simplified if the Green-McInnis-Naghdi rate is considered. In this case, the rotation tensor between the local and the spatial configurations equals the rotation tensor in the polar decomposition, i.e., $\mathbf{Q}^{\mathrm{GMN}}_{n+\alpha} = \mathbf{R}_{n+\alpha}$. Thus, the algorithm presented above can be avoided, since $\mathbf{R}_{n+\alpha}$ can be obtained from the polar decomposition of the deformation gradient $\mathbf{F}_{n+\alpha}$ (Simo and Hughes, 1998).

5.3 Finite strain hyperelastoplasticity

In this section, a continuum mechanical extension of the rheological kinematic hardening model of Armstrong-Frederick to 3D finite strains in the context of hyperelasticity is presented. As in Chapter 4, the constitutive equations are derived in a general way regarding the yield function. This way, the yielding of the material can be described by any isotropic or anisotropic (quadratic or nonquadratic) yield function. Hence, the model is able to successfully overcome the limitation to quadratic yield criteria that is typical of the hyperelastic-based anisotropic models in the literature.

Following the works of Dettmer and Reese (2004) and Vladimirov *et al.* (2008, 2010), the constitutive equations are entirely defined in the reference configuration. Doing this way, the formulations lead to objective tensorial objects only. Moreover, this approach avoids the determination of the plastic spin, leading to the fact that only symmetric tensorial quantities are considered in this model. This is advantageous regarding the numerical implementation of the model into finite element codes, since it drastically reduces the number of nonlinear scalar functions to be numerically integrated at the Gauss point level.

This approach is in contrast to, e.g., the concepts of hyperelastic-based anisotropic plasticity of Eidel and Gruttmann (2003) and Sansour *et al.* (2007). While Eidel and Gruttmann (2003) considers that the plastic spin is zero, coming from the assumption that the yield criterion is dependent on the symmetric part of the relative stress only, in the work of Sansour *et al.* (2007) a "material plastic spin", related to the Mandel's stress tensor, is defined. The use of rate equations for symmetric tensors in finite plasticity has also been discussed by Han *et al.* (2003) and Menzel and Steinmann (2003) for isotropic hardening and by Shutov and Kreißig (2008) and Vladimirov *et al.* (2008, 2010) for isotropic-nonlinear kinematic hardening.

At the end of this section, an algorithm used to numerically integrate the constitutive equations, based on the exponential map, is thoroughly discussed. The exponential map is particularly interesting regarding its application to this constitutive model, since it preserves the plastic isochoric behaviour and the symmetry of the variables (Dettmer and Reese, 2004).

5.3.1 Kinematics

In this work, the widely accepted and physically motivated multiplicative decomposition of the deformation gradient, i.e., $\mathbf{F} = \mathbf{F}_{\mathrm{e}}\mathbf{F}_{\mathrm{p}}$, into elastic, $\mathbf{F}_{\mathrm{e}}$, and plastic, $\mathbf{F}_{\mathrm{p}}$, parts is assumed. This decomposition introduces a (physically fictitious) local intermediate plastic (stress-free) configuration, as shown in Fig. 5.1.

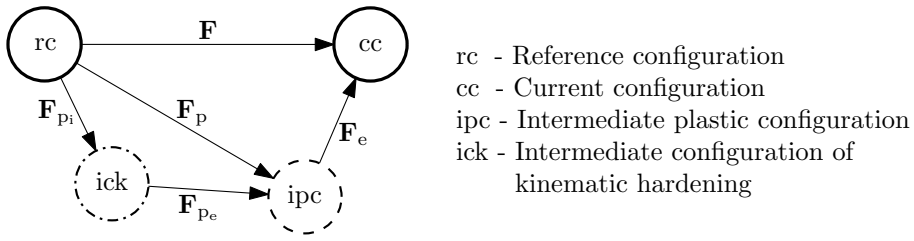

Figure 5.1: Multiplicative decompositions of the deformation gradients.

In the context of the Armstrong-Frederick kinematic hardening law, and in analogy to the additive split of ε_{p}, the multiplicative split of the plastic deformation gradient,

$$\mathbf{F}_{\mathrm{p}} = \mathbf{F}_{\mathrm{p_e}}\mathbf{F}_{\mathrm{p_i}}, \tag{5.45}$$

into "elastic", $\mathbf{F}_{\mathrm{p_e}}$, and "inelastic", $\mathbf{F}_{\mathrm{p_i}}$, parts, is assumed. This decomposition is physically motivated, since $\mathbf{F}_{\mathrm{p_e}}$ and $\mathbf{F}_{\mathrm{p_i}}$ have the same physical interpretations as $\varepsilon_{\mathrm{p_e}}$ and $\varepsilon_{\mathrm{p_i}}$, respectively. Similarly to the decomposition of $\mathbf{F}$, the multiplicative decomposition of $\mathbf{F}_{\mathrm{p}}$ introduces an additional configuration (see Fig. 5.1), usually referred to as the intermediate configuration of kinematic hardening (Lion, 2000).

5.3.2 Helmholtz free energy potential

Taking into account the notion of elastic isomorphism (Bertram, 1998) and the principle of material frame indifference, which impose that the constitutive equations must be independent of superimposed rigid body motions, one can assume that the Helmholtz free energy is only dependent on the elastic right Cauchy-Green deformation tensors $\mathbf{C}_{\mathrm{e}} = \mathbf{F}_{\mathrm{e}}^{\mathrm{T}}\mathbf{F}_{\mathrm{e}}$ and $\mathbf{C}_{\mathrm{p_e}} = \mathbf{F}_{\mathrm{p_e}}^{\mathrm{T}}\mathbf{F}_{\mathrm{p_e}}$. This way, analogously to the decomposition of Equation 4.7, the Helmholtz free energy per unit volume associated to the Armstrong-Frederick model of kinematic hardening can be additively split into three parts, as

$$\psi = \psi_{\mathrm{e}}\left(\mathbf{C}_{\mathrm{e}}\right) + \psi_{\mathrm{kin}}\left(\mathbf{C}_{\mathrm{p_e}}\right) + \psi_{\mathrm{iso}}\left(\bar{\varepsilon}_{\mathrm{p}}\right). \tag{5.46}$$

As in Section 4.1.2, the terms ψ_{e} and ψ_{kin} represent the energy stored in the elastic and in the hardening springs, respectively (see Fig. 3.6), while ψ_{iso} describes the isotropic hardening.

5.3.3 Clausius-Duhem inequality

The constitutive equations of the hyperelastic-based model are derived in a thermodynamically consistent manner in this section. The derivation is grounded on the Clausius-Duhem form of the entropy inequality for isothermal processes (Equation 2.50) expressed in terms of Lagrangian quantities (second Piola-Kirchhoff stress and right Cauchy-Green strain tensors), i.e.,

$$-\dot{\psi} + \mathbf{S} : \frac{1}{2}\dot{\mathbf{C}} \geq 0. \tag{5.47}$$

By introducing the Helmholtz free energy into Equation 5.47 and differentiating with respect to time, the Clausius-Duhem inequality becomes

$$-\left(\frac{\partial \psi_{\mathrm{e}}}{\partial \mathbf{C}_{\mathrm{e}}} : \dot{\mathbf{C}}_{\mathrm{e}} + \frac{\partial \psi_{\mathrm{kin}}}{\partial \mathbf{C}_{\mathrm{p_e}}} : \dot{\mathbf{C}}_{\mathrm{p_e}} + \frac{\partial \psi_{\mathrm{iso}}}{\partial \bar{\varepsilon}_{\mathrm{p}}}\dot{\bar{\varepsilon}}_{\mathrm{p}}\right) + \mathbf{S} : \frac{1}{2}\dot{\mathbf{C}} \geq 0. \tag{5.48}$$

We should now exploit the terms inside the brackets in this inequality. Firstly, the elastic right Cauchy-Green deformation tensor can be rewritten as

$$\mathbf{C}_{\mathrm{e}} = \mathbf{F}_{\mathrm{p}}^{-\mathrm{T}}\mathbf{C}\mathbf{F}_{\mathrm{p}}^{-1}, \tag{5.49}$$

which material time derivative yields

$$\dot{\mathbf{C}}_{\mathrm{e}} = \dot{\mathbf{F}}_{\mathrm{p}}^{-\mathrm{T}}\mathbf{C}\mathbf{F}_{\mathrm{p}}^{-1} + \mathbf{F}_{\mathrm{p}}^{-\mathrm{T}}\dot{\mathbf{C}}\mathbf{F}_{\mathrm{p}}^{-1} + \mathbf{F}_{\mathrm{p}}^{-\mathrm{T}}\mathbf{C}\dot{\mathbf{F}}_{\mathrm{p}}^{-1}. \tag{5.50}$$

From the definition of the inverse of a tensor ($\mathbf{F}_{\mathrm{p}}^{-1}\mathbf{F}_{\mathrm{p}} = \mathbf{I}$) the relation

$$\dot{\mathbf{F}}_{\mathrm{p}}^{-1} = \mathbf{F}_{\mathrm{p}}^{-1}\dot{\mathbf{F}}_{\mathrm{p}}\mathbf{F}_{\mathrm{p}}^{-1} = \mathbf{F}_{\mathrm{p}}^{-1}\mathbf{l}_{\mathrm{p}} \tag{5.51}$$

is obtained, where $\mathbf{l}_{\mathrm{p}} = \dot{\mathbf{F}}_{\mathrm{p}}\mathbf{F}_{\mathrm{p}}^{-1}$ stands for the "plastic" velocity gradient. Taking this relation into account, $\dot{\mathbf{C}}_{\mathrm{e}}$ (Equation 5.50) can be rewritten as

$$\dot{\mathbf{C}}_{\mathrm{e}} = -\mathbf{l}_{\mathrm{p}}^{\mathrm{T}}\mathbf{C}_{\mathrm{e}} + \mathbf{F}_{\mathrm{p}}^{-\mathrm{T}}\dot{\mathbf{C}}\mathbf{F}_{\mathrm{p}}^{-1} - \mathbf{C}_{\mathrm{e}}\mathbf{l}_{\mathrm{p}}. \tag{5.52}$$

Employing the following properties of the double inner product of second-order tensors,

$$\mathbf{A} : \mathbf{B} = \mathrm{tr}(\mathbf{A}^{\mathrm{T}}\mathbf{B}) = \mathrm{tr}(\mathbf{A}\mathbf{B}^{\mathrm{T}}) \text{ and} \tag{5.53}$$

$$\mathrm{sym}(\mathbf{A}) : \mathbf{B} = \mathrm{sym}(\mathbf{A}) : \mathrm{sym}(\mathbf{B}), \tag{5.54}$$

one can arrive at the identities

$$\frac{\partial \psi_{\mathrm{e}}}{\partial \mathbf{C}_{\mathrm{e}}} : (\mathbf{C}_{\mathrm{e}}\mathbf{l}_{\mathrm{p}}) = \left(\mathbf{C}_{\mathrm{e}}\frac{\partial \psi_{\mathrm{e}}}{\partial \mathbf{C}_{\mathrm{e}}}\right) : \mathbf{l}_{\mathrm{p}} = \left(\mathbf{C}_{\mathrm{e}}\frac{\partial \psi_{\mathrm{e}}}{\partial \mathbf{C}_{\mathrm{e}}}\right) : \mathbf{d}_{\mathrm{p}} \text{ and} \tag{5.55}$$

$$\frac{\partial \psi_{\mathrm{e}}}{\partial \mathbf{C}_{\mathrm{e}}} : \left(\mathbf{F}_{\mathrm{p}}^{-\mathrm{T}}\dot{\mathbf{C}}\mathbf{F}_{\mathrm{p}}^{-1}\right) = 2\left(\mathbf{F}_{\mathrm{p}}^{-1}\frac{\partial \psi_{\mathrm{e}}}{\partial \mathbf{C}_{\mathrm{e}}}\mathbf{F}_{\mathrm{p}}^{-\mathrm{T}}\right) : \frac{1}{2}\dot{\mathbf{C}}, \tag{5.56}$$

where the definition of the plastic rate of deformation tensor, $\mathbf{d}_\mathrm{p} = \mathrm{sym}(\mathbf{l}_\mathrm{p})$, was considered. The above derivation exploited the fact that, in this work, it is assumed that the free energy ψ_e and ψ_kin parts are isotropic functions of the elastic right Cauchy-Green tensors $\mathbf{C}_\mathrm{e}$ and $\mathbf{C}_{\mathrm{p_e}}$, respectively. This assumption ensures the coaxiality of the tensors $\mathbf{C}_\mathrm{e}$ and $\partial\psi_\mathrm{e}/\partial\mathbf{C}_\mathrm{e}$ and of the tensors $\mathbf{C}_{\mathrm{p_e}}$ and $\partial\psi_\mathrm{kin}/\partial\mathbf{C}_{\mathrm{p_e}}$, hence also the symmetry of the tensors $\mathbf{C}_\mathrm{e}(\partial\psi_\mathrm{e}/\partial\mathbf{C}_\mathrm{e})$ and $\mathbf{C}_{\mathrm{p_e}}(\partial\psi_\mathrm{kin}/\partial\mathbf{C}_{\mathrm{p_e}})$, respectively.

Applying this procedure to $\mathbf{C}_{\mathrm{p_e}}$, we arrive at

$$\frac{\partial\psi_\mathrm{kin}}{\partial\mathbf{C}_{\mathrm{p_e}}} : \dot{\mathbf{C}}_{\mathrm{p_e}} = \left(2\mathbf{F}_{\mathrm{p_e}}\frac{\partial\psi_\mathrm{kin}}{\partial\mathbf{C}_{\mathrm{p_e}}}\mathbf{F}_{\mathrm{p_e}}^\mathrm{T}\right) : \mathbf{d}_\mathrm{p} - \left(2\mathbf{C}_{\mathrm{p_e}}\frac{\partial\psi_\mathrm{kin}}{\partial\mathbf{C}_{\mathrm{p_e}}}\right) : \mathbf{d}_{\mathrm{p_i}}, \tag{5.57}$$

where the relation

$$\mathbf{d}_\mathrm{p} = \frac{1}{2}\mathbf{F}_\mathrm{p}^{-\mathrm{T}}\dot{\mathbf{C}}_\mathrm{p}\mathbf{F}_\mathrm{p}^{-1} \tag{5.58}$$

was employed. Using the identities of Equations 5.55-5.57 in the Clausius-Duhem inequality (Equation 5.48), it yields

$$\left(\mathbf{S} - 2\mathbf{F}_\mathrm{p}^{-1}\frac{\partial\psi_\mathrm{e}}{\partial\mathbf{C}_\mathrm{e}}\mathbf{F}_\mathrm{p}^{-\mathrm{T}}\right) : \frac{1}{2}\dot{\mathbf{C}} + \left(2\mathbf{C}_\mathrm{e}\frac{\partial\psi_\mathrm{e}}{\partial\mathbf{C}_\mathrm{e}} - 2\mathbf{F}_{\mathrm{p_e}}\frac{\partial\psi_\mathrm{kin}}{\partial\mathbf{C}_{\mathrm{p_e}}}\mathbf{F}_{\mathrm{p_e}}^\mathrm{T}\right) : \mathbf{d}_\mathrm{p} + \left(2\mathbf{C}_{\mathrm{p_e}}\frac{\partial\psi_\mathrm{kin}}{\partial\mathbf{C}_{\mathrm{p_e}}}\right) : \mathbf{d}_{\mathrm{p_i}} - \frac{\partial\psi_\mathrm{iso}}{\partial\bar{\varepsilon}_\mathrm{p}}\dot{\bar{\varepsilon}}_\mathrm{p} \geq 0. \tag{5.59}$$

This inequality must be fulfilled for any arbitrary thermodynamic process, or in other words, for any arbitrary $\dot{\mathbf{C}}$, $\mathbf{d}_\mathrm{p}$, $\mathbf{d}_{\mathrm{p_i}}$, and $\dot{\bar{\varepsilon}}_\mathrm{p}$. Thus, to stablish that this inequality is fulfilled regardless to $\dot{\mathbf{C}}$, the physically motivated expression for the second Piola-Kirchhoff stress tensor, $\mathbf{S}$, is commonly defined as

$$\mathbf{S} = 2\mathbf{F}_\mathrm{p}^{-1}\frac{\partial\psi_\mathrm{e}}{\partial\mathbf{C}_\mathrm{e}}\mathbf{F}_\mathrm{p}^{-\mathrm{T}}. \tag{5.60}$$

One may now introduce the so-called Mandel stress tensor expressed by

$$\mathbf{M} = 2\mathbf{C}_\mathrm{e}\frac{\partial\psi_\mathrm{e}}{\partial\mathbf{C}_\mathrm{e}}, \tag{5.61}$$

and its analogous quantity related to the kinematic hardening,

$$\mathbf{M}_\mathrm{kin} = 2\mathbf{C}_{\mathrm{p_e}}\frac{\partial\psi_\mathrm{kin}}{\partial\mathbf{C}_{\mathrm{p_e}}}. \tag{5.62}$$

The symmetry of these stress tensors is guaranteed by the coaxiality of the tensors $\mathbf{C}_\mathrm{e}$ and $\partial\psi_\mathrm{e}/\partial\mathbf{C}_\mathrm{e}$ and of the tensors $\mathbf{C}_{\mathrm{p_e}}$ and $\partial\psi_\mathrm{kin}/\partial\mathbf{C}_{\mathrm{p_e}}$, respectively.

It is assumed that ψ_kin has the same structure as ψ_e. Thus, by analogy to $\mathbf{S}$, the back stress tensor, $\mathbf{X}$, in the reference configuration is defined as

$$\mathbf{X} = 2\mathbf{F}_{\mathrm{p_i}}^{-1}\frac{\partial\psi_\mathrm{kin}}{\partial\mathbf{C}_{\mathrm{p_e}}}\mathbf{F}_{\mathrm{p_i}}^{-\mathrm{T}}, \tag{5.63}$$

whose push-forward to the intermediate configuration results on the back stress tensor

$$\boldsymbol{\chi} = \mathbf{F}_{\mathrm{p}}\mathbf{X}\mathbf{F}_{\mathrm{p}}^{\mathrm{T}} = 2\mathbf{F}_{\mathrm{p_e}}\frac{\partial \psi_{\mathrm{kin}}}{\partial \mathbf{C}_{\mathrm{p_e}}}\mathbf{F}_{\mathrm{p_e}}^{\mathrm{T}}. \tag{5.64}$$

Introducing the stress tensors indicated before and the stress-like isotropic hardening variable, R, in the Clausius-Duhem inequality (Equation 5.59), it reduces to the form

$$\boldsymbol{\Sigma} : \mathbf{d}_{\mathrm{p}} + \mathbf{M}_{\mathrm{kin}} : \mathbf{d}_{\mathrm{p_i}} + R\dot{\bar{\varepsilon}}_{\mathrm{p}} \geq 0, \tag{5.65}$$

were $\boldsymbol{\Sigma} = \mathbf{M} - \boldsymbol{\chi}$ is the relative stress in the intermediate configuration. This tensor, which results from the subtraction of two symmetric tensors, is also a symmetric tensor.

5.3.4 Evolution equations

The inequality 5.65 is sufficiently satisfied by considering Equation 5.60 and the following evolution equations,

$$\mathbf{d}_{\mathrm{p}} = \dot{\lambda}\frac{\partial \Phi}{\partial \boldsymbol{\Sigma}}, \;\; \mathbf{d}_{\mathrm{p_i}} = \dot{\lambda}\frac{b}{c}\mathbf{M}_{\mathrm{kin}}^{\mathrm{D}}, \;\; \text{and} \;\; \dot{\bar{\varepsilon}}_{\mathrm{p}} = \dot{\lambda}\frac{\partial \Phi}{\partial R} = \dot{\lambda}. \tag{5.66}$$

Similarly to Equations 4.13a and 4.13b, Equation 5.66a represents the associated flow rule and the evolution equation for the deformation variable related to kinematic hardening (Equation 5.66b) has been chosen according to Armstrong and Frederick (1966).

The yield potential and the loading/unloading conditions (Equation 4.20) complete the set of constitutive equations.

The confirmation that the evolutions equations actually fulfil the Clausius-Duhem inequality 5.65 is presented now. It is easy to prove that the second term of Equation 5.65 is naturally nonnegative:

$$\mathbf{M}_{\mathrm{kin}} : \mathbf{d}_{\mathrm{p_i}} = \dot{\lambda}\frac{b}{c}\mathbf{M}_{\mathrm{kin}} : \mathbf{M}_{\mathrm{kin}}^{\mathrm{D}} = \dot{\lambda}\frac{b}{c}\mathbf{M}_{\mathrm{kin}}^{\mathrm{D}} : \mathbf{M}_{\mathrm{kin}}^{\mathrm{D}} \geq 0. \tag{5.67}$$

The remaining of inequality 5.65 can be simplified in the following way,

$$\boldsymbol{\Sigma} : \left(\dot{\lambda}\frac{\partial \Phi}{\partial \boldsymbol{\Sigma}}\right) + R\dot{\lambda} = \dot{\lambda}\left[\boldsymbol{\Sigma} : \frac{\partial \bar{\sigma}(\boldsymbol{\Sigma})}{\partial \boldsymbol{\Sigma}} + R\right] = \dot{\lambda}\left[\bar{\sigma}(\boldsymbol{\Sigma}) + R\right] = \dot{\lambda}\left(\Phi + \sigma_{\mathrm{y_0}}\right) \geq 0. \tag{5.68}$$

Taking into account the loading/unloading conditions and the positivity of the parameter $\sigma_{\mathrm{y_0}}$, this inequality results to be always ensured.

5.3.5 Representation in the reference configuration

Although the set of constitutive equations was consistently and completely derived at this point, it should be noted that these equations are defined in different configurations. While $\mathbf{S}$

(Equation 5.60) acts in the reference configuration, $\boldsymbol{\Sigma}$, $\mathbf{M}$ (Equation 5.61), and $\mathbf{d}_\mathrm{p}$ (Equation 5.66a) are expressed in the intermediate plastic configuration and $\mathbf{M}_\mathrm{kin}$ (Equation 5.62) and $\mathbf{d}_{\mathrm{p_i}}$ (Equation 5.66b) are defined in the intermediate configuration of kinematic hardening. The remaining constitutive equations are scalar functions. In the following, all constitutive equations will be transformed to the reference (undeformed) configuration.

The use of this configuration is advantageous since it is known and kept constant during the deformation process. It will turn out that there is no need to determine the intermediate configurations, avoiding the computation of the (nonsymmetric) $\mathbf{F}_\mathrm{p}$ and $\mathbf{F}_{\mathrm{p_i}}$ tensors. Moreover, in this work the pull-back to the reference configuration is carried out in such a way that the symmetry of the constitutive variables is preserved for any arbitrary thermodynamic process.

By introducing Equation 5.49 in Equation 5.61 and multiplying the left and the right sides by the second-order identity tensor ($\mathbf{I} = \mathbf{F}_\mathrm{p}^{-1}\mathbf{F}_\mathrm{p} = \mathbf{F}_\mathrm{p}^{-\mathrm{T}}\mathbf{F}_\mathrm{p}^{\mathrm{T}}$), yields

$$\begin{aligned}
\mathbf{M} &= 2\mathbf{C}_\mathrm{e}\frac{\partial \psi_\mathrm{e}}{\partial \mathbf{C}_\mathrm{e}} \\
&= \mathbf{F}_\mathrm{p}\mathbf{F}_\mathrm{p}^{-1}\left(2\mathbf{F}_\mathrm{p}^{-\mathrm{T}}\mathbf{C}\mathbf{F}_\mathrm{p}^{-1}\frac{\partial \psi_\mathrm{e}}{\partial \mathbf{C}_\mathrm{e}}\right)\mathbf{F}_\mathrm{p}^{-\mathrm{T}}\mathbf{F}_\mathrm{p}^{\mathrm{T}} \\
&= \mathbf{F}_\mathrm{p}\left(\mathbf{F}_\mathrm{p}^{-1}\mathbf{F}_\mathrm{p}^{-\mathrm{T}}\mathbf{C}2\mathbf{F}_\mathrm{p}^{-1}\frac{\partial \psi_\mathrm{e}}{\partial \mathbf{C}_\mathrm{e}}\mathbf{F}_\mathrm{p}^{-\mathrm{T}}\right)\mathbf{F}_\mathrm{p}^{\mathrm{T}} \\
&= \mathbf{F}_\mathrm{p}\left(\mathbf{C}_\mathrm{p}^{-1}\mathbf{C}\mathbf{S}\right)\mathbf{F}_\mathrm{p}^{\mathrm{T}}.
\end{aligned} \tag{5.69}$$

Introducing this relation and the back stress tensor defined in the intermediate plastic configuration, $\boldsymbol{\chi}$, in the definition of the relative stress tensor, one obtains

$$\begin{aligned}
\boldsymbol{\Sigma} &= \mathbf{M} - \boldsymbol{\chi} \\
&= \mathbf{F}_\mathrm{p}\left(\mathbf{C}_\mathrm{p}^{-1}\mathbf{C}\mathbf{S}\right)\mathbf{F}_\mathrm{p}^{\mathrm{T}} - \mathbf{F}_\mathrm{p}\mathbf{X}\mathbf{F}_\mathrm{p}^{\mathrm{T}} = \mathbf{F}_\mathrm{p}\left(\mathbf{C}_\mathrm{p}^{-1}\mathbf{C}\mathbf{S} - \mathbf{X}\right)\mathbf{F}_\mathrm{p}^{\mathrm{T}} \\
&= \mathbf{F}_\mathrm{p}\mathbf{Y}\mathbf{F}_\mathrm{p}^{\mathrm{T}}.
\end{aligned} \tag{5.70}$$

Here, the representation of the relative stress tensor in the reference configuration, $\mathbf{Y}$, is introduced as

$$\mathbf{Y} = \mathbf{C}_\mathrm{p}^{-1}\mathbf{C}\mathbf{S} - \mathbf{X}. \tag{5.71}$$

In addition, the pull-back of the deviatoric part of the relative stress tensor, $\boldsymbol{\Sigma}^\mathrm{D}$, to the reference configuration is carried out as

$$\begin{aligned}
\boldsymbol{\Sigma}^\mathrm{D} &= \mathbf{F}_\mathrm{p}\mathbf{Y}\mathbf{F}_\mathrm{p}^{\mathrm{T}} - \frac{1}{3}\mathrm{tr}\left(\mathbf{F}_\mathrm{p}\mathbf{Y}\mathbf{F}_\mathrm{p}^{\mathrm{T}}\right)\mathbf{I} \\
&= \mathbf{F}_\mathrm{p}\mathbf{Y}\mathbf{F}_\mathrm{p}^{\mathrm{T}} - \frac{1}{3}\mathrm{tr}\left(\mathbf{F}_\mathrm{p}^{\mathrm{T}}\mathbf{F}_\mathrm{p}\mathbf{Y}\right)\mathbf{F}_\mathrm{p}\mathbf{F}_\mathrm{p}^{-1}\mathbf{F}_\mathrm{p}^{-\mathrm{T}}\mathbf{F}_\mathrm{p}^{\mathrm{T}} \\
&= \mathbf{F}_\mathrm{p}\left[\mathbf{Y} - \frac{1}{3}\mathrm{tr}\left(\mathbf{C}_\mathrm{p}\mathbf{Y}\right)\mathbf{C}_\mathrm{p}^{-1}\right]\mathbf{F}_\mathrm{p}^{\mathrm{T}} \\
&= \mathbf{F}_\mathrm{p}\left[\left(\mathbf{Y}\mathbf{C}_\mathrm{p}\right)^\mathrm{D}\mathbf{C}_\mathrm{p}^{-1}\right]\mathbf{F}_\mathrm{p}^{\mathrm{T}} = \mathbf{F}_\mathrm{p}\left[\mathbf{C}_\mathrm{p}^{-1}\left(\mathbf{C}_\mathrm{p}\mathbf{Y}\right)^\mathrm{D}\right]\mathbf{F}_\mathrm{p}^{\mathrm{T}}.
\end{aligned} \tag{5.72}$$

Analogously, $\mathbf{M}_{\text{kin}}$ can be expressed as

$$\mathbf{M}_{\text{kin}} = \mathbf{F}_{\text{p}_\text{i}} \mathbf{Y}_{\text{kin}} \mathbf{F}_{\text{p}_\text{i}}^{\text{T}}, \tag{5.73}$$

where its representation in the reference configuration is defined as

$$\mathbf{Y}_{\text{kin}} = \mathbf{C}_{\text{p}_\text{i}}^{-1} \mathbf{C}_{\text{p}} \mathbf{X}. \tag{5.74}$$

The deviator of $\mathbf{M}_{\text{kin}}$ can be written by

$$\mathbf{M}_{\text{kin}}^{\text{D}} = \mathbf{F}_{\text{p}_\text{i}} \left[(\mathbf{Y}_{\text{kin}} \mathbf{C}_{\text{p}_\text{i}})^{\text{D}} \mathbf{C}_{\text{p}_\text{i}}^{-1} \right] \mathbf{F}_{\text{p}_\text{i}}^{\text{T}} = \mathbf{F}_{\text{p}_\text{i}} \left[\mathbf{C}_{\text{p}_\text{i}}^{-1} (\mathbf{C}_{\text{p}_\text{i}} \mathbf{Y}_{\text{kin}})^{\text{D}} \right] \mathbf{F}_{\text{p}_\text{i}}^{\text{T}}. \tag{5.75}$$

At this point, attention will be focused on the representations of the evolution equations in the reference configuration. Making use of the relation 5.58 and Equation 5.66a, the evolution equation for the plastic right Cauchy-Green deformation tensor is expressed by

$$\dot{\mathbf{C}}_{\text{p}} = 2\dot{\lambda} \mathbf{F}_{\text{p}}^{\text{T}} \frac{\partial \Phi}{\partial \boldsymbol{\Sigma}} \mathbf{F}_{\text{p}} = 2\dot{\lambda} \mathbf{F}_{\text{p}}^{\text{T}} \left(\frac{\partial \Phi}{\partial \mathbf{Y}} : \frac{\partial \mathbf{Y}}{\partial \boldsymbol{\Sigma}} \right) \mathbf{F}_{\text{p}}. \tag{5.76}$$

Taking into account that

$$\begin{aligned} \left(\frac{\partial Y}{\partial \Sigma} \right)_{ijkl} = \frac{1}{4} [& (F_{\text{p}}^{-1})_{ik} (F_{\text{p}}^{-\text{T}})_{lj} + (F_{\text{p}}^{-1})_{il} (F_{\text{p}}^{-\text{T}})_{kj} \\ & + (F_{\text{p}}^{-1})_{jk} (F_{\text{p}}^{-\text{T}})_{li} + (F_{\text{p}}^{-1})_{jl} (F_{\text{p}}^{-\text{T}})_{ki}], \end{aligned} \tag{5.77}$$

Equation 5.76 now becomes

$$\dot{\mathbf{C}}_{\text{p}} = 2\dot{\lambda} \mathbf{n}_{\mathbf{Y}}, \text{ with } \mathbf{n}_{\mathbf{Y}} = \frac{\partial \Phi}{\partial \mathbf{Y}}. \tag{5.78}$$

Additionally, by using the relation $\dot{\mathbf{C}}_{\text{p}_\text{i}} = 2\mathbf{F}_{\text{p}_\text{i}}^{\text{T}} \mathbf{d}_{\text{p}_\text{i}} \mathbf{F}_{\text{p}_\text{i}}$ and Equation 5.75 into 5.66b the following evolution for $\mathbf{C}_{\text{p}_\text{i}}$ is obtained,

$$\dot{\mathbf{C}}_{\text{p}_\text{i}} = 2\dot{\lambda} \frac{b}{c} (\mathbf{C}_{\text{p}_\text{i}} \mathbf{Y}_{\text{kin}})^{\text{D}} \mathbf{C}_{\text{p}_\text{i}}. \tag{5.79}$$

Remark 2 It will be now detailed the representation and the symmetry of the stress tensors $\mathbf{Y}$ and $\mathbf{Y}_{\text{kin}}$. Taking into account that the free energy ψ_{e} is an isotropic function of $\mathbf{C}_{\text{e}}$, one can represent the tensor $\partial \psi_{\text{e}} / \partial \mathbf{C}_{\text{e}}$ as an isotropic (tensor-valued) function of $\mathbf{C}_{\text{e}}$, as follows

$$\frac{\partial \psi_e}{\partial \mathbf{C}_{\text{e}}} = \alpha_0 \mathbf{I} + \alpha_1 \mathbf{C}_{\text{e}} + \alpha_2 \mathbf{C}_{\text{e}}^2, \tag{5.80}$$

where the scalar factors α_i, with $i = 0 \ldots 2$, are scalar-valued isotropic functions of $\mathbf{C}_{\text{e}}$. Introducing this expression in Equation 5.60 leads to

$$\begin{aligned}\mathbf{S} &= 2\mathbf{F}_{\mathrm{p}}^{-1}\frac{\partial\psi_{\mathrm{e}}}{\partial\mathbf{C}_{\mathrm{e}}}\mathbf{F}_{\mathrm{p}}^{-\mathrm{T}} \\ &= 2\alpha_0\mathbf{C}_{\mathrm{p}}^{-1} + 2\alpha_1\mathbf{C}_{\mathrm{p}}^{-1}\mathbf{C}\mathbf{C}_{\mathrm{p}}^{-1} + 2\alpha_2\mathbf{C}_{\mathrm{p}}^{-1}\left(\mathbf{C}\mathbf{C}_{\mathrm{p}}^{-1}\right)^2.\end{aligned} \tag{5.81}$$

This relation indicates that the second Piola-Kirchhoff stress tensor is in fact symmetric and can be determined solely by means of $\mathbf{C}$ and $\mathbf{C}_{\mathrm{p}}$. Analagously, $\partial\psi_{\mathrm{kin}}/\partial\mathbf{C}_{\mathrm{p_e}}$ is an isotropic function of $\mathbf{C}_{\mathrm{p_e}}$ and can be expressed by

$$\frac{\partial\psi_{\mathrm{kin}}}{\partial\mathbf{C}_{\mathrm{p_e}}} = \beta_0\mathbf{I} + \beta_1\mathbf{C}_{\mathrm{p_e}} + \beta_2\mathbf{C}_{\mathrm{p_e}}^2, \tag{5.82}$$

where the scalar factors β_i, with $i = 0\ldots2$, are scalar-valued isotropic functions of $\mathbf{C}_{\mathrm{p_e}}$. Hence, the expression of the back stress tensor in the reference configuration may be defined as

$$\begin{aligned}\mathbf{X} &= 2\mathbf{F}_{\mathrm{p_i}}^{-1}\frac{\partial\psi_{\mathrm{kin}}}{\partial\mathbf{C}_{\mathrm{p_e}}}\mathbf{F}_{\mathrm{p_i}}^{-\mathrm{T}} \\ &= 2\beta_0\mathbf{C}_{\mathrm{p_i}}^{-1} + 2\beta_1\mathbf{C}_{\mathrm{p_i}}^{-1}\mathbf{C}_{\mathrm{p}}\mathbf{C}_{\mathrm{p_i}}^{-1} + 2\beta_2\mathbf{C}_{\mathrm{p_i}}^{-1}\left(\mathbf{C}_{\mathrm{p}}\mathbf{C}_{\mathrm{p_i}}^{-1}\right)^2,\end{aligned} \tag{5.83}$$

which shows that $\mathbf{X}$ is symmetric and can be fully expressed by $\mathbf{C}_{\mathrm{p}}$ and $\mathbf{C}_{\mathrm{p_i}}$ only.

Introducing Equations 5.81 and 5.83 in the definition of the relative stress tensor in the reference configuration (Equation 5.71) results in

$$\begin{aligned}\mathbf{Y} = 2\alpha_0\mathbf{C}_{\mathrm{p}}^{-1}\mathbf{C}\mathbf{C}_{\mathrm{p}}^{-1} + 2\alpha_1\mathbf{C}_{\mathrm{p}}^{-1}\mathbf{C}\mathbf{C}_{\mathrm{p}}^{-1}\mathbf{C}\mathbf{C}_{\mathrm{p}}^{-1} + 2\alpha_2\mathbf{C}_{\mathrm{p}}^{-1}\mathbf{C}\mathbf{C}_{\mathrm{p}}^{-1}\left(\mathbf{C}\mathbf{C}_{\mathrm{p}}^{-1}\right)^2 \\ - 2\beta_0\mathbf{C}_{\mathrm{p_i}}^{-1} - 2\beta_1\mathbf{C}_{\mathrm{p_i}}^{-1}\mathbf{C}_{\mathrm{p}}\mathbf{C}_{\mathrm{p_i}}^{-1} - 2\beta_2\mathbf{C}_{\mathrm{p_i}}^{-1}\left(\mathbf{C}_{\mathrm{p}}\mathbf{C}_{\mathrm{p_i}}^{-1}\right)^2,\end{aligned} \tag{5.84}$$

which is a symmetric tensor for every arbitrary deformation history. The same procedure can be applied to confirm the symmetry of the tensor $\mathbf{Y}_{\mathrm{kin}}$.

It should be mentioned that some works in the literature, related to the topic of constitutive modelling of quadratic anisotropy and kinematic hardening at finite strains, perform the pull-back according to $\boldsymbol{\Sigma} = \mathbf{F}_{\mathrm{p}}^{-\mathrm{T}}\mathbf{Y}\mathbf{F}_{\mathrm{p}}^{\mathrm{T}}$ and $\mathbf{M}_{\mathrm{kin}} = \mathbf{F}_{\mathrm{p_i}}^{-\mathrm{T}}\mathbf{Y}_{\mathrm{kin}}\mathbf{F}_{\mathrm{p_i}}^{\mathrm{T}}$, thus using the relations

$$\mathbf{Y} = \mathbf{C}\mathbf{S} - \mathbf{C}_{\mathrm{p}}\mathbf{X} \text{ and} \tag{5.85}$$

$$\mathbf{Y}_{\mathrm{kin}} = \mathbf{C}_{\mathrm{p}}\mathbf{X}, \tag{5.86}$$

which are nonsymmetric tensors. Performing the derivation in a consistent way leads to symmetric evolution equations for $\mathbf{C}_{\mathrm{p}}$ and $\mathbf{C}_{\mathrm{p_i}}$ as well. However, in Vladimirov *et al.* (2010) a complex symmetrization procedure was carried out which have affected the clarity of the derivation, leading to additional CPU time effort and reducing the robustness of the numerical implementation. These drawbacks are now completely overcome in the present model.

5.3.6 Yield potential

The yield potential used in this model is expressed by quantities defined in the reference configuration, as follows

$$\Phi(\bar{\mathbb{A}}, \mathbf{Y}, \bar{\varepsilon}_{\mathrm{p}}) = \bar{\sigma}(\bar{\mathbb{A}}, \mathbf{Y}) - [\sigma_{\mathrm{y}_0} - R(\bar{\varepsilon}_{\mathrm{p}})]. \tag{5.87}$$

where $\bar{\mathbb{A}}$ is the anisotropic tensor that acts on stress quantities defined in the reference configuration in the $\mathbf{Y}$ stress space, whose components describe the anisotropy of the material. The effective stress, $\bar{\sigma}$, is not explicitly defined at this point to allow for the possibility of implementation of any isotropic or anisotropic yield function.

Before moving to the description of the implementation of anisotropic yield functions into this model, it is convenient to establish the relation between the relative stress state in the reference configuration, $\mathbf{Y}$, and the relative stress tensor in the current configuration in the material corotational coordinate frame (or locally rotating configuration), $\hat{\boldsymbol{\eta}} = \hat{\boldsymbol{\sigma}} - \hat{\boldsymbol{\alpha}}$.

Firstly, taking into account the relation between the relative stresses represented in the global frame, $\boldsymbol{\eta}$, and in the material corotational coordinate frame, $\hat{\boldsymbol{\eta}} = \mathbf{Q}^{\star\mathrm{T}}\boldsymbol{\eta}\mathbf{Q}^{\star}$, and the relation between the second Piola-Kirchhoff stress tensor and the Cauchy stress tensor (Equation 2.33), the following relation is obtained,

$$\hat{\boldsymbol{\eta}} = J^{-1}\mathbf{Q}^{\star\mathrm{T}}\mathbf{F}\mathbf{T}\mathbf{F}^{\mathrm{T}}\mathbf{Q}^{\star}, \tag{5.88}$$

where $\mathbf{T} = \mathbf{S} - \bar{\boldsymbol{\alpha}}$ is the relative stress in the reference configuration related to the second Piola-Kirchhoff stress space and $\mathbf{Q}^{\star}$ is the rotation tensor between the material corotational and the global (spatial) coordinate frames (Equation 5.32).

Secondly, by employing the identity

$$\mathbf{Y} = \mathbf{C}_{\mathrm{p}}^{-1}\mathbf{C}(\mathbf{S} - \underbrace{\mathbf{C}^{-1}\mathbf{C}_{\mathrm{p}}\mathbf{X}}_{=\bar{\boldsymbol{\alpha}}}) = \mathbf{C}_{\mathrm{p}}^{-1}\mathbf{C}\mathbf{T}, \tag{5.89}$$

the following relation between the relative stresses in the current and reference configurations is obtained,

$$\hat{\boldsymbol{\eta}} = J^{-1}\mathbf{Q}^{\star\mathrm{T}}\mathbf{F}^{-\mathrm{T}}\mathbf{C}_{\mathrm{p}}\mathbf{Y}\mathbf{F}^{\mathrm{T}}\mathbf{Q}^{\star}. \tag{5.90}$$

In this work, it is assumed that the deformation-induced anisotropy of the material (e.g., associated with plastic deformation during stamping operations) is small and negligible compared to the initial anisotropy (induced by rolling and heat treatment of the material's production process). Therefore, the directions of the material's anisotropy axes are fixed in the current configuration in the material corotational (locally rotating) coordinate frame. Quantities defined in this coordinate frame, and thus also the material's anisotropic axis, are unaffected by superposed rigid body motions.

The choice of this approach in detriment of formulations that express the yield function in the intermediate configuration provides an increase of numerical efficiency, since the later would entail the determination of the nonsymmetric tensors $\mathbf{F}_\mathrm{p}$ and $\mathbf{F}_\mathrm{e}$. Special attention should be paid to the representation of the yield function, since it must always obey the principle of material frame indifference.

In the following, a procedure to be carried out in order to represent anisotropic yield criteria as a function of arguments solely defined in the reference configuration is employed for the quadratic criterion proposed by Hill (1948) and for the nonquadratic criterion, *Yld2004-18p*, proposed by Barlat *et al.* (2005). Here, the yield functions are represented by quantities defined in the reference configuration by exploiting the principle of material frame indifference. In the context of yield functions, this principle states that a yield function must provide the same value if expressed by arguments defined in the current or reference configuration, i.e.,

$$\bar{\sigma}\left(\mathbb{A}, \hat{\boldsymbol{\eta}}\right) = \bar{\sigma}\left(\bar{\mathbb{A}}, \mathbf{Y}\right), \tag{5.91}$$

where $\mathbb{A}$ is a fourth-order anisotropic tensor related to stress quantities expressed in the current configuration in the material corotational coordinate frame.

(Quadratic) Hill 1948 yield function Regarding the yield function proposed by Hill (1948), the effective stress is given by $\bar{\sigma} = \sqrt{\hat{\boldsymbol{\eta}} : \mathbb{A} : \hat{\boldsymbol{\eta}}}$. Introducing the relation 5.90 in this yield function, one obtains

$$\begin{aligned}
\hat{\boldsymbol{\eta}} : \mathbb{A} : \hat{\boldsymbol{\eta}} &= \hat{\eta}_{ij} A_{ijkl} \hat{\eta}_{kl} \\
&= J^{-2} (\mathbf{Q}^{\star\mathrm{T}} \mathbf{F}^{-\mathrm{T}} \mathbf{C}_\mathrm{p})_{im} Y_{mn} (\mathbf{F}^\mathrm{T} \mathbf{Q}^\star)_{nj} A_{ijkl} (\mathbf{Q}^{\star\mathrm{T}} \mathbf{F}^{-\mathrm{T}} \mathbf{C}_\mathrm{p})_{ko} Y_{op} (\mathbf{F}^\mathrm{T} \mathbf{Q}^\star)_{pl} \\
&= Y_{mn} \bar{A}_{mnop} Y_{op} = \mathbf{Y} : \bar{\mathbb{A}} : \mathbf{Y}.
\end{aligned} \tag{5.92}$$

The fourth-order tensor $\bar{\mathbb{A}}$ is related to the anisotropic tensor $\mathbb{A}$ following the expression

$$\bar{A}_{mnop} = J^{-2} (\mathbf{C}_\mathrm{p} \mathbf{F}^{-1} \mathbf{Q}^\star)_{mi} (\mathbf{F}^\mathrm{T} \mathbf{Q}^\star)_{nj} (\mathbf{C}_\mathrm{p} \mathbf{F}^{-1} \mathbf{Q}^\star)_{ok} (\mathbf{F}^\mathrm{T} \mathbf{Q}^\star)_{pl} A_{ijkl}. \tag{5.93}$$

The fourth-order anisotropic tensor $\mathbb{A}$ can in turn be represented by means of structural tensors (Vladimirov *et al.*, 2010), following

$$\mathbb{A} = a_1 \mathbb{I} + a_2 \mathbf{M}_1 \otimes \mathbf{M}_1 + a_3 \mathbf{M}_2 \otimes \mathbf{M}_2 + a_4 (\mathbf{M}_1 \otimes \mathbf{M}_2 + \mathbf{M}_2 \otimes \mathbf{M}_1) + a_5 \mathbb{G}_1 + a_6 \mathbb{G}_2, \tag{5.94}$$

where the auxiliary fourth-order tensors $\mathbb{G}_1$ and $\mathbb{G}_2$ are given by

$$(G_\alpha)_{ijkl} = \frac{1}{2} \left[(M_\alpha)_{ik} \delta_{jl} + (M_\alpha)_{il} \delta_{jk} + (M_\alpha)_{jk} \delta_{il} + (M_\alpha)_{jl} \delta_{ik} \right] \ \forall \ \alpha = 1, 2. \tag{5.95}$$

The coefficients a_i, with $i = 1 \ldots 6$, are related to the classical Hill's coefficients (F, G, H, L, M, and N). The structural tensors represent the symmetry of the material and are expressed

as

$$\mathbf{M}_i = \mathbf{N}_i \otimes \mathbf{N}_i \ \ \forall \ \ i = 1 \dots 3, \tag{5.96}$$

where $\mathbf{N}_i$ are the privileged directions of the material.

Applying Equation 5.93 to the anisotropic tensor defined by Equation 5.94 and considering, for the sake of simplicity, only the second term, yields

$$\begin{aligned}\mathbf{M}_1 \otimes \mathbf{M}_1 \rightarrow J^{-2}(\mathbf{C}_\mathrm{p}\mathbf{F}^{-1}\mathbf{Q}^\star)_{mi}(\mathbf{F}^\mathrm{T}\mathbf{Q}^\star)_{nj}(\mathbf{C}_\mathrm{p}\mathbf{F}^{-1}\mathbf{Q}^\star)_{ok}(\mathbf{F}^\mathrm{T}\mathbf{Q}^\star)_{pl}(\mathbf{M}_1)_{ij}(\mathbf{M}_1)_{kl} \\ = (\bar{\mathbf{M}}_1)_{mn}(\bar{\mathbf{M}}_1)_{op},\end{aligned} \tag{5.97}$$

where the structural tensor in the reference configuration is expressed as

$$\begin{aligned}\bar{\mathbf{M}}_1 &= J^{-1}\mathbf{C}_\mathrm{p}\mathbf{F}^{-1}\mathbf{Q}^\star\mathbf{M}_1\mathbf{Q}^{\star\mathrm{T}}\mathbf{F} \\ &= J^{-1}(\mathbf{C}_\mathrm{p}\mathbf{F}^{-1}\mathbf{Q}^\star\mathbf{N}_1) \otimes (\mathbf{N}_1\mathbf{Q}^{\star\mathrm{T}}\mathbf{F}) \\ &= \bar{\mathbf{N}}_1' \otimes \bar{\mathbf{N}}_1'',\end{aligned} \tag{5.98}$$

which is dependent on two privileged directions that distinctly evolve according to

$$\bar{\mathbf{N}}_1' = J^{-\frac{1}{2}}\mathbf{C}_\mathrm{p}\mathbf{F}^{-1}\mathbf{Q}^\star\mathbf{N}_1 \ \text{ and } \ \bar{\mathbf{N}}_1'' = J^{-\frac{1}{2}}\mathbf{N}_1\mathbf{Q}^{\star\mathrm{T}}\mathbf{F}. \tag{5.99}$$

The representation of the remaining terms of Equation 5.94 in the reference configuration may be done following the same procedure.

(Nonquadratic) Yld2004-18p yield function As mentioned in Section 3.3.2, this anisotropic yield function employs the concept of linear transformations in order to introduce the anisotropy into an isotropic yield function (see Equations 3.48 and 3.49). This way, the *Yld2004-18p* yield function is an isotropic convex function with respect to $\tilde{\mathbf{s}}^{(k)}$ $(k = 1, 2)$, i.e.,

$$\Phi(\tilde{\mathbf{s}}^{(1)}, \tilde{\mathbf{s}}^{(2)}, \bar{\varepsilon}_\mathrm{p}) = \bar{\sigma}(\tilde{\mathbf{s}}^{(1)}, \tilde{\mathbf{s}}^{(2)}) - [\sigma_{\mathrm{y}_0} - R(\bar{\varepsilon}_\mathrm{p})]. \tag{5.100}$$

Taking this isotropy into account, the condition 5.91 is fulfilled for this yield function by ensuring that the stress tensors $\tilde{\mathbf{s}}^{(k)}$ are independent of the configuration in which the stress tensor used in the linear transformations is defined, i.e.,

$$\tilde{\mathbf{s}}^{(k)} = \mathbb{L}^{(k)} : \hat{\boldsymbol{\eta}} = \bar{\mathbb{L}}^{(k)} : \mathbf{Y}, \tag{5.101}$$

where $\bar{\mathbb{L}}^{(k)}$ stands for the fourth-order anisotropic tensors that act in the reference configuration.

Employing the relation 5.91 in the condition 5.101, yields

$$\begin{aligned}\tilde{s}_{ij}^{(k)} &= L_{ijmn}^{(k)}\hat{\eta}_{mn} \\ &= L_{ijmn}^{(k)}J^{-1}(\mathbf{Q}^{\star\mathrm{T}}\mathbf{F}^{-\mathrm{T}}\mathbf{C}_{\mathrm{p}})_{mo}Y_{op}(\mathbf{F}^{\mathrm{T}}\mathbf{Q}^{\star})_{pn} \\ &= \bar{L}_{ijop}^{(k)}Y_{op},\end{aligned} \tag{5.102}$$

where

$$\bar{L}_{ijop}^{(k)} = J^{-1}(\mathbf{C}_{\mathrm{p}}\mathbf{F}^{-1}\mathbf{Q}^{\star})_{om}(\mathbf{F}^{\mathrm{T}}\mathbf{Q}^{\star})_{pn}L_{ijmn}^{(k)}. \tag{5.103}$$

This fourth-order anisotropic tensor ensures that the equality 5.101 is always fulfilled.

From relations 5.99 and 5.103 it can be seen that, if the material's anisotropy was assumed to be constant in the reference configuration, the orthotropic symmetry of the material in the current configuration would be destroyed when deformation occurred. This is an issue in the large deformation regime, because it leads to unrealistic evolution of the material's anisotropy. In previous works on finite anisotropic plasticity (Vladimirov *et al.*, 2010) employing the Hill (1948)'s quadratic yield criterion, the fourth-order anisotropic tensor was assumed to be constant in the reference configuration. Thus, from Equation 5.93 one can easily see that the anisotropy was, in contrast to the present formulation, dependent on $\mathbf{F}$.

5.3.7 Continuous elastoplastic tangent modulus

As the presented constitutive model is formulated in the reference configuration, the Lagrangian continuous elastoplastic tangent modulus relates the rate of the right Cauchy-Green deformation tensor to the rate of the second Piola-Kirchhoff stress tensor, according to

$$\dot{\mathbf{S}} = \mathbb{D}_{\mathrm{ep}} : \dot{\mathbf{E}}^{(2)} = \mathbb{D}_{\mathrm{ep}} : \frac{1}{2}\dot{\mathbf{C}}. \tag{5.104}$$

Bearing in mind that $\mathbf{S}$ is fully defined by $\mathbf{C}$, $\mathbf{C}_{\mathrm{p}}$ and proper scalar-factors (see Equation 5.81), its rate can be represented in the form

$$\dot{\mathbf{S}} = 2\frac{\partial \mathbf{S}}{\partial \mathbf{C}} : \frac{1}{2}\dot{\mathbf{C}} + 2\delta\frac{\partial \mathbf{S}}{\partial \mathbf{C}_{\mathrm{p}}} : \mathbf{n}_{\mathbf{Y}}\dot{\lambda}, \tag{5.105}$$

where the rate of $\mathbf{C}_{\mathrm{p}}$, given by Equation 5.78, is taken into account. During plastic loading, $\dot{\lambda} \neq 0$, the consistency condition implies

$$\dot{\Phi} = \mathbf{n}_{\mathbf{Y}} : \dot{\mathbf{Y}} - H\dot{\lambda} = 0. \tag{5.106}$$

Differentiating Equation 5.71 in order to the time, the rate of the stress tensor $\mathbf{Y}$ is expressed as

$$\begin{aligned}\dot{\mathbf{Y}} &= \dot{(\mathbf{C}_\mathrm{p}^{-1})}\mathbf{C}\mathbf{S} + \mathbf{C}_\mathrm{p}^{-1}\dot{\mathbf{C}}\mathbf{S} + \mathbf{C}_\mathrm{p}^{-1}\mathbf{C}\dot{\mathbf{S}} - \dot{\mathbf{X}} \\ &= -2\mathbf{C}_\mathrm{p}^{-1}\mathbf{n}_\mathbf{Y}\mathbf{C}_\mathrm{p}^{-1}\mathbf{C}\mathbf{S}\dot{\lambda} + \mathbf{C}_\mathrm{p}^{-1}\dot{\mathbf{C}}\mathbf{S} + \mathbf{C}_\mathrm{p}^{-1}\mathbf{C}\left(2\frac{\partial \mathbf{S}}{\partial \mathbf{C}} : \frac{1}{2}\dot{\mathbf{C}} + 2\frac{\partial \mathbf{S}}{\partial \mathbf{C}_\mathrm{p}} : \mathbf{n}_\mathbf{Y}\dot{\lambda}\right) \\ &\qquad - 2\frac{\partial \mathbf{X}}{\partial \mathbf{C}_\mathrm{p}} : \mathbf{n}_\mathbf{Y}\dot{\lambda} - 2\frac{b}{c}\frac{\partial \mathbf{X}}{\partial \mathbf{C}_{\mathrm{p_i}}} : \left[(\mathbf{C}_{\mathrm{p_i}}\mathbf{Y}_\mathrm{kin})^\mathrm{D}\mathbf{C}_{\mathrm{p_i}}\right]\dot{\lambda},\end{aligned} \tag{5.107}$$

where the Equations 5.78 and 5.105 and the relation $\dot{(\mathbf{A}^{-1})} = -\mathbf{A}^{-1}\dot{\mathbf{A}}\mathbf{A}^{-1}$ are considered. Moreover, in the above expression, the following rate of the back stress is taken into account,

$$\dot{\mathbf{X}} = 2\frac{\partial \mathbf{X}}{\partial \mathbf{C}_\mathrm{p}} : \mathbf{n}_\mathbf{Y}\dot{\lambda} + 2\frac{b}{c}\frac{\partial \mathbf{X}}{\partial \mathbf{C}_{\mathrm{p_i}}} : \left[(\mathbf{C}_{\mathrm{p_i}}\mathbf{Y}_\mathrm{kin})^\mathrm{D}\mathbf{C}_{\mathrm{p_i}}\right]\dot{\lambda}, \tag{5.108}$$

where the evolution rates of $\mathbf{C}_\mathrm{p}$ and $\mathbf{C}_{\mathrm{p_i}}$ (Equations 5.78 and 5.79, respectively) are employed.

By introducing Equation 5.107 into the consistency condition (Equation 5.106) and solving the relation in order to the rate of the plastic multiplier, it is obtained

$$\dot{\lambda} = \frac{\mathbf{A}_\mathrm{N}}{A_\mathrm{D}} : \frac{1}{2}\dot{\mathbf{C}}, \tag{5.109}$$

where the auxiliary variables

$$(A_\mathrm{N})_{ij} = (n_\mathrm{Y})_{kl}\left[(C_\mathrm{p}^{-1})_{ki}S_{jl} + (C_\mathrm{p}^{-1})_{km}C_{mn}\left(\frac{\partial S}{\partial C}\right)_{nlij}\right] \quad \text{and} \tag{5.110}$$

$$\begin{aligned}A_\mathrm{D} = \mathbf{n}_\mathbf{Y} : \Bigg\{&\mathbf{C}_\mathrm{p}^{-1}\mathbf{n}_\mathbf{Y}\mathbf{C}_\mathrm{p}^{-1}\mathbf{C}\mathbf{S} - \mathbf{C}_p^{-1}\mathbf{C}\frac{\partial \mathbf{S}}{\partial \mathbf{C}_\mathrm{p}} : \mathbf{n}_\mathbf{Y} \\ &+ \frac{\partial \mathbf{X}}{\partial \mathbf{C}_\mathrm{p}} : \mathbf{n}_\mathbf{Y} + \frac{b}{c}\frac{\partial \mathbf{X}}{\partial \mathbf{C}_{\mathrm{p_i}}} : \left[(\mathbf{C}_{\mathrm{p_i}}\mathbf{Y}_\mathrm{kin})^\mathrm{D}\mathbf{C}_{\mathrm{p_i}}\right]\Bigg\} + H,\end{aligned} \tag{5.111}$$

are introduced. The continuous elastoplastic tangent modulus is finally obtained by replacing Equation 5.109 into Equation 5.105,

$$\mathbb{D}_\mathrm{ep} = \frac{\partial \dot{\mathbf{S}}}{\partial \dot{\mathbf{E}}^{(2)}} = 2\frac{\partial \mathbf{S}}{\partial \mathbf{C}} + 2\delta\frac{\partial \mathbf{S}}{\partial \mathbf{C}_\mathrm{p}} : \mathbf{n}_\mathbf{Y} \otimes \frac{\mathbf{A}_\mathrm{N}}{A_\mathrm{D}}. \tag{5.112}$$

5.3.8 Summary of the constitutive model

The set of constitutive equations of the present model are summarized in Box 5.1. All tensor-valued equations are formulated in the reference configuration and are defined solely by the symmetric tensors $\mathbf{C}$, $\mathbf{C}_\mathrm{p}$, and $\mathbf{C}_{\mathrm{p_i}}$, and the plastic multiplier $\dot{\lambda}$. The quantities $\mathbf{C}_\mathrm{p}$, $\mathbf{C}_{\mathrm{p_i}}$, and $\bar{\varepsilon}_\mathrm{p}$ are the so-called internal variables of the constitutive model which describe the evolutions of the plastic deformation, kinematic hardening, and isotropic hardening, respectively. It is worth to highlight that the present constitutive model have been derived in a general way, hence it is suitable for any yield criterion and isotropic hardening law.

For the sake of generality of the model, up to this point $\mathbf{S}$ and $\mathbf{X}$ are determined by

derivatives of the Helmholtz free energy, the particular form of which has not been specified yet. To perform the numerical simulations discussed in Chapter 7, the free energy terms ψ_{e} and ψ_{kin} are assumed to follow the well-known Neo-Hookean form. Consequently, the model is able to represent the behaviour of materials under both finite elastic and finite plastic strains. Doing this way, the model can be applied to describe the behaviour of materials where finite elastic strains take place, e.g., polymeric materials. The free energy terms are then particularized as

$$\psi_{\mathrm{e}}\left(\mathbf{C}_{\mathrm{e}}\right)=\frac{\mu_{\mathrm{e}}}{2}\left(\mathrm{tr}\mathbf{C}_{\mathrm{e}}-3\right)-\mu_{\mathrm{e}}\ln\left(\sqrt{\det\mathbf{C}_{\mathrm{e}}}\right)+\frac{\Lambda_{\mathrm{e}}}{4}\left[\det\mathbf{C}_{\mathrm{e}}-1-2\ln\left(\sqrt{\det\mathbf{C}_{\mathrm{e}}}\right)\right]\ \text{and} \tag{5.113}$$

$$\psi_{\mathrm{kin}}\left(\mathbf{C}_{\mathrm{p_e}}\right)=\frac{c}{4}\left(\mathrm{tr}\mathbf{C}_{\mathrm{p_e}}-3\right)-\frac{c}{2}\ln\left(\sqrt{\det\mathbf{C}_{\mathrm{p_e}}}\right). \tag{5.114}$$

Following this assumption, the second Piola-Kirchhoff stress tensor and the back stress tensor in the reference configuration are expressed as

$$\mathbf{S}=\mu_{\mathrm{e}}(\mathbf{C}_{\mathrm{p}}^{-1}-\mathbf{C}^{-1})+\frac{\Lambda_{\mathrm{e}}}{2}\left(\frac{\det\mathbf{C}}{\det\mathbf{C}_{\mathrm{p}}}-1\right)\mathbf{C}^{-1}\ \text{and} \tag{5.115}$$

$$\mathbf{X}=\frac{c}{2}(\mathbf{C}_{\mathrm{p_i}}^{-1}-\mathbf{C}_{\mathrm{p}}^{-1}), \tag{5.116}$$

respectively.

Box 5.1: Hyperelastoplastic constitutive model

Kinematics	$\mathbf{F}=\mathbf{F}_{\mathrm{e}}\mathbf{F}_{\mathrm{p}},\ \mathbf{F}_{\mathrm{p}}=\mathbf{F}_{\mathrm{p_e}}\mathbf{F}_{\mathrm{p_i}},$ $\mathbf{C}_{\mathrm{p}}=\mathbf{F}_{\mathrm{p}}^{\mathrm{T}}\mathbf{F}_{\mathrm{p}},\ \mathbf{C}_{\mathrm{p_i}}=\mathbf{F}_{\mathrm{p_i}}^{\mathrm{T}}\mathbf{F}_{\mathrm{p_i}}$
Helmholtz free energy	$\psi=\psi_{\mathrm{e}}\left(\mathbf{C}_{\mathrm{e}}\right)+\psi_{\mathrm{kin}}\left(\mathbf{C}_{\mathrm{p_e}}\right)+\psi_{\mathrm{iso}}\left(\bar{\varepsilon}_{\mathrm{p}}\right)$
Stress tensors	$\mathbf{S}=2\mathbf{F}_{\mathrm{p}}^{-1}\dfrac{\partial\psi_{\mathrm{e}}}{\partial\mathbf{C}_{\mathrm{e}}}\mathbf{F}_{\mathrm{p}}^{-\mathrm{T}},\ \mathbf{X}=2\mathbf{F}_{\mathrm{p_i}}^{-1}\dfrac{\partial\psi_{\mathrm{kin}}}{\partial\mathbf{C}_{\mathrm{p_e}}}\mathbf{F}_{\mathrm{p_i}}^{-\mathrm{T}},$ $\mathbf{Y}=\mathbf{C}_{\mathrm{p}}^{-1}\mathbf{C}\mathbf{S}-\mathbf{X},\ \mathbf{Y}_{\mathrm{kin}}=\mathbf{C}_{\mathrm{p_i}}^{-1}\mathbf{C}_{\mathrm{p}}\mathbf{X}$
Evolution equations	$\dot{\mathbf{C}}_{\mathrm{p}}=2\dot{\lambda}\mathbf{n}_{\mathbf{Y}},\ \dot{\mathbf{C}}_{\mathrm{p_i}}=2\dot{\lambda}\dfrac{b}{c}(\mathbf{C}_{\mathrm{p_i}}\mathbf{Y}_{\mathrm{kin}})^{\mathrm{D}}\mathbf{C}_{\mathrm{p_i}},\ \dot{\bar{\varepsilon}}_{\mathrm{p}}=\dot{\lambda}$
Yield function	$\Phi(\mathbf{Y},\bar{\varepsilon}_{\mathrm{p}})=\bar{\sigma}(\mathbf{Y})-[\sigma_{\mathrm{y_0}}-R(\bar{\varepsilon}_{\mathrm{p}})],$
Loading/unloading conditions	$\dot{\lambda}\geq 0,\ \Phi\leq 0,\ \dot{\lambda}\Phi=0$
Continuous tangent modulus	$\mathbb{D}_{\mathrm{ep}}=2\dfrac{\partial\mathbf{S}}{\partial\mathbf{C}}+2\delta\dfrac{\partial\mathbf{S}}{\partial\mathbf{C}_{\mathrm{p}}}:\mathbf{n}_{\mathbf{Y}}\otimes\dfrac{\mathbf{A}_{\mathrm{N}}}{A_{\mathrm{D}}}.$

5.3.9 Numerical implementation

In this section the procedures to be followed in order to implement the hyperelastoplastic constitutive model into a numerical simulation code are presented. An integration algorithm based on the elastic predictor-plastic corrector method is presented, along with its consistent (algorithmic) elastoplastic tangent modulus. The tensor-valued evolution equations are implicitly integrated according to the exponential map.

5.3.9.1 Integration of the evolution equations based on the exponential map

The numerical implementation of the presented constitutive model require the integration of the differential evolution equations presented in Box 5.1 along the time interval $[t_n, t_{n+1}] \subset [t_0, t_{\text{end}}]$ of duration $\Delta t = t_{n+1} - t_n$. Here, a backward-Euler scheme is built based on the exponential map in order to integrate the tensor-valued evolution equations of $\mathbf{C}_{\text{p}}$ and $\mathbf{C}_{\text{p}_\text{i}}$. The exponential map was firstly introduced in the context of computational plasticity by Weber and Anand (1990). Its application ranges from problems of crystal plasticity (Miehe, 1996a, Souza Neto, 2001), viscoelasticity (Reese and Govindjee, 1998), isotropic elastoplasticity (Simo, 1992) to combined isotropic-nonlinear kinematic elastoplasticity (Dettmer and Reese, 2004, Vladimirov *et al.*, 2008, 2010). The exponential map is very attractive for models defined by evolution equations of deviatoric character, since it exactly preserves the inelastic incompressibility of the material, i.e., $\det\mathbf{C}_{\text{p}} = 1$. Another feature of the exponential map is the fact that it automatically preserves the symmetry of the internal variables, hence allowing the use of the spectral decomposition of the tensor-valued arguments.

The evolution equations of $\mathbf{C}_{\text{p}}$ (Equation 5.78) and $\mathbf{C}_{\text{p}_\text{i}}$ (Equation 5.79) can be written in a more general form as

$$\dot{\mathbf{A}} = \dot{\lambda}\mathbf{f}(\mathbf{C}, \mathbf{C}_{\text{p}}, \mathbf{C}_{\text{p}_\text{i}}) = \mathbf{g}(\mathbf{C}, \mathbf{C}_{\text{p}}, \mathbf{C}_{\text{p}_\text{i}})\mathbf{A}, \tag{5.117}$$

where $\mathbf{g} = \dot{\lambda}\mathbf{f}\mathbf{A}^{-1}$ is a nonsymmetric tensor. It is worth noting that the function $\mathbf{f}$ is a symmetric tensor, since $\mathbf{A}$ is symmetric. If the function $\mathbf{g}$ is constant ($\mathbf{g} = \mathbf{g}_0$), the exact solution of the differential equation $\dot{\mathbf{A}} = \mathbf{g}_0\mathbf{A}$ is given analytically by $\mathbf{A}(t) = \exp[(t - t_n)\mathbf{g}_0]\mathbf{A}(t_n)$. Nevertheless, the function $\mathbf{g}$ is, in general, nonlinear in the time interval $[t_n, t_{n+1}]$ and thus an analytical solution of the Equation 5.117 is not available. For that reason, an approximated solution is used following

$$\mathbf{A}(t) = \exp(\bar{\mathbf{g}})\mathbf{A}(t_n) = \exp(\Delta\lambda\mathbf{f}\mathbf{A}^{-1})\mathbf{A}(t_n), \tag{5.118}$$

where the term $\bar{\mathbf{g}} = \Delta\lambda\mathbf{f}\mathbf{A}^{-1}$ is kept piecewise constant in the time interval $[t_n, t_{n+1}]$. Since in this work we employ a implicit integration scheme, this term refer to the time t_{n+1} and thus it is updated iteratively. For the sake of simplicity, the subscript $n+1$ is omitted in the following equations. Thus, and unless otherwise indicated, all quantities refer to t_{n+1}.

The nonsymmetry of $\bar{\mathbf{g}}$ imposes the use of the power series representation,

$$\exp(\bar{\mathbf{g}}) = \sum_{k=0}^{\infty} \frac{1}{k!} \bar{\mathbf{g}}^k, \tag{5.119}$$

if the implicit integration formula (Equation 5.118) is directly employed to solve Equation 5.117. Pietryga *et al.* (2014) assessed the performance of integration algorithms that use the power series representation and the spectral decomposition (see Equation 5.122), in the context of elastoplasticity and viscoplasticity. They concluded that the use of the power series representation is computationally faster if a small number of terms is considered, at the expense of some accuracy.

Dettmer and Reese (2004) suggested a methodology to preserve the symmetry of the internal variable $\mathbf{A}$, by multiplying the approximated solution (Equation 5.118) by $\mathbf{A}_n^{-1}\mathbf{A}$ from the right side. Applying this methodology to the evolution equation of $\mathbf{C}_\mathrm{p}$, it yields

$$\begin{aligned}
\mathbf{C}_\mathrm{p}\mathbf{C}_{\mathrm{p}_n}^{-1}\mathbf{C}_\mathrm{p} &= \exp(\Delta\lambda \mathbf{f}\mathbf{C}_\mathrm{p}^{-1})\mathbf{C}_{\mathrm{p}_n}\mathbf{C}_{\mathrm{p}_n}^{-1}\mathbf{C}_\mathrm{p} \\
&= \sum_{k=0}^{\infty} \frac{1}{k!}(\Delta\lambda \mathbf{f}\mathbf{C}_\mathrm{p}^{-1})^k \mathbf{C}_\mathrm{p} \\
&= \left[\mathbf{I} + \Delta\lambda \mathbf{f}\mathbf{C}_\mathrm{p}^{-1} + \frac{\Delta\lambda^2}{2}(\mathbf{f}\mathbf{C}_\mathrm{p}^{-1})^2 + \dots\right]\mathbf{C}_\mathrm{p} \\
&= \left\{\mathbf{U}_\mathrm{p}\left[\mathbf{I} + \Delta\lambda \mathbf{U}_\mathrm{p}^{-1}\mathbf{f}\mathbf{U}_\mathrm{p}^{-1} + \frac{\Delta\lambda^2}{2}(\mathbf{U}_\mathrm{p}^{-1}\mathbf{f}\mathbf{U}_\mathrm{p}^{-1})^2 + \dots\right]\mathbf{U}_\mathrm{p}^{-1}\right\}\mathbf{C}_\mathrm{p} \\
&= \mathbf{U}_\mathrm{p}\exp(\Delta\lambda \mathbf{U}_\mathrm{p}^{-1}\mathbf{f}\mathbf{U}_\mathrm{p}^{-1})\mathbf{U}_\mathrm{p},
\end{aligned} \tag{5.120}$$

where the definition

$$\mathbf{f} = 2\mathbf{n}_\mathbf{Y}, \tag{5.121}$$

holds and $\mathbf{U}_\mathrm{p} = \sqrt{\mathbf{C}_\mathrm{p}}$, is the plastic right stretch tensor. Since $\mathbf{U}_\mathrm{p}^{-1}\mathbf{f}\mathbf{U}_\mathrm{p}^{-1}$ is a symmetric tensor, $\exp(\Delta\lambda \mathbf{U}_\mathrm{p}^{-1}\mathbf{f}\mathbf{U}_\mathrm{p}^{-1})$ can be represented by means of the spectral decomposition, i.e.,

$$\mathbf{Z} = \mathbf{Z}^\mathrm{T} = \sum_{A=1}^{3} Z_A \boldsymbol{n}_A \otimes \boldsymbol{n}_A \Rightarrow \exp\mathbf{Z} = \sum_{A=1}^{3} (\exp Z_A)\, \boldsymbol{n}_A \otimes \boldsymbol{n}_A, \tag{5.122}$$

where Z_A and $\boldsymbol{n}_A$ are the eigenvalues and eigenvectors of the symmetric tensor $\mathbf{Z}$, respectively. The final form of the integrated plastic flow rule is derived from Equation 5.120 and is expressed as

$$\mathbf{C}_{\mathrm{p}_n}^{-1} = \mathbf{U}_\mathrm{p}^{-1}\exp(\Delta\lambda \mathbf{U}_\mathrm{p}^{-1}\mathbf{f}\mathbf{U}_\mathrm{p}^{-1})\mathbf{U}_\mathrm{p}^{-1}. \tag{5.123}$$

We should now confirm that the inelastic incompressibility is ensured throughout the numerical analysis, i.e, $\det\mathbf{C}_\mathrm{p} = 1$. By applying the determinant operator in Equation 5.123

and making use of the identity $\det[\exp(\mathbf{Z})] = \exp[\mathrm{tr}(\mathbf{Z})]$, the relation

$$\begin{aligned} \det\mathbf{C}_{\mathrm{p}_n}^{-1} &= \det\mathbf{U}_{\mathrm{p}}^{-1}\det[\exp(\Delta\lambda\mathbf{U}_{\mathrm{p}}^{-1}\mathbf{f}\mathbf{U}_{\mathrm{p}}^{-1})]\det\mathbf{U}_{\mathrm{p}}^{-1} \\ &= (\det\mathbf{U}_{\mathrm{p}})^{-1}\exp[\mathrm{tr}(\Delta\lambda\mathbf{U}_{\mathrm{p}}^{-1}\mathbf{f}\mathbf{U}_{\mathrm{p}}^{-1})](\det\mathbf{U}_{\mathrm{p}})^{-1}, \end{aligned} \tag{5.124}$$

is obtained. One can rewrite the trace of the product $\Delta\lambda\mathbf{U}_{\mathrm{p}}^{-1}\mathbf{f}\mathbf{U}_{\mathrm{p}}^{-1}$ as

$$\begin{aligned} \mathrm{tr}\left(2\Delta\lambda\mathbf{U}_{\mathrm{p}}^{-1}\mathbf{n}_{\mathbf{Y}}\mathbf{U}_{\mathrm{p}}^{-1}\right) &= 2\Delta\lambda\mathrm{tr}\left[\mathbf{U}_{\mathrm{p}}^{-1}\left(\mathbf{n} : \frac{\partial\hat{\boldsymbol{\eta}}}{\partial\mathbf{Y}}\right)\mathbf{U}_{\mathrm{p}}^{-1}\right] \\ &= 2\Delta\lambda\mathrm{tr}\left[J^{-1}\mathbf{U}_{\mathrm{p}}^{-1}\mathbf{C}_{\mathrm{p}}\mathbf{F}^{-1}\mathbf{Q}^{\star}\mathbf{n}\mathbf{Q}^{\star\mathrm{T}}\mathbf{F}\mathbf{U}_{\mathrm{p}}^{-1}\right] \\ &= 2\Delta\lambda J^{-1}\mathrm{tr}\left(\mathbf{Q}^{\star\mathrm{T}}\mathbf{F}\mathbf{C}_{\mathrm{p}}^{-1}\mathbf{C}_{\mathrm{p}}\mathbf{F}^{-1}\mathbf{Q}^{\star}\mathbf{n}\right) \\ &= 2\Delta\lambda J^{-1}\mathrm{tr}\left(\mathbf{n}\right) = 0, \end{aligned} \tag{5.125}$$

where the property $\mathrm{tr}\left(\mathbf{n}\right) = 0$ was employed. In the above equation, from the relation 5.90, the following identity was inserted,

$$\left(\frac{\partial\hat{\eta}}{\partial Y}\right)_{ijkl} = J^{-1}(\mathbf{Q}^{\star\mathrm{T}}\mathbf{F}^{-\mathrm{T}}\mathbf{C}_{\mathrm{p}})_{ik}(\mathbf{F}^{\mathrm{T}}\mathbf{Q}^{\star})_{lj}. \tag{5.126}$$

Introducing Equation 5.125 in the expression of the determinant of $\mathbf{C}_{\mathrm{p}_n}^{-1}$ (Equation 5.124), results into

$$\begin{aligned} \det\mathbf{C}_{\mathrm{p}_n}^{-1} &= (\det\mathbf{U}_{\mathrm{p}})^{-1}\exp\left[2\Delta\lambda J^{-1}\mathrm{tr}\left(\mathbf{n}\right)\right](\det\mathbf{U}_{\mathrm{p}})^{-1} \\ (\det\mathbf{C}_{\mathrm{p}_n})^{-1} &= (\det\mathbf{U}_{\mathrm{p}})^{-2} \\ &= (\det\mathbf{C}_{\mathrm{p}})^{-1}, \end{aligned} \tag{5.127}$$

which confirms that $\det\mathbf{C}_{\mathrm{p}} = \det\mathbf{C}_{\mathrm{p}_n} = 1$.

Following the same line of though, the integrated formula for the kinematic hardening rule (Equation 5.79) can be obtained analogously as

$$\mathbf{C}_{\mathrm{p_i}_n}^{-1} = \mathbf{U}_{\mathrm{p_i}}^{-1}\exp(\Delta\lambda\mathbf{U}_{\mathrm{p_i}}^{-1}\mathbf{f}_{\mathrm{kin}}\mathbf{U}_{\mathrm{p_i}}^{-1})\mathbf{U}_{\mathrm{p_i}}^{-1}, \tag{5.128}$$

where the definition

$$\mathbf{f}_{\mathrm{kin}} = 2\frac{b}{c}(\mathbf{C}_{\mathrm{p_i}}\mathbf{Y}_{\mathrm{kin}})^{\mathrm{D}}\mathbf{C}_{\mathrm{p_i}}, \tag{5.129}$$

stands.

Remark 3 The standard backward-Euler integration scheme can be used to integrate the evolution equation represented by Equation 5.117. Following this scheme the time derivative is replaced by the difference quotient (Equation 4.37), leading to the implicit integration formula

$$\mathbf{A}_{n+1} = \mathbf{A}_n + \mathbf{g}_{n+1}\mathbf{A}_{n+1}\Delta t. \tag{5.130}$$

However, the fact that the standard backward-Euler scheme does not preserve the plastic incompressibility represents a major drawback. It leads to nonphysical solutions with large errors if large step sizes are considered. In order to eliminate these errors additional assumptions must be included so that the condition $\det\mathbf{C}_{\mathrm{p}} = 1$ is fulfilled (Lührs *et al.*, 1997, Helm, 2006, Vladimirov *et al.*, 2008, Shutov and Kreißig, 2008). In addition, the exponential map provides a better performance comparatively to the standard backward-Euler scheme for large strain increments, as shown by Vladimirov *et al.* (2008) for finite strain and by Artioli *et al.* (2006, 2007) for small strain formulations.

Finally, the time discretization of the scalar evolution equation for the isotropic hardening variable (Equation 5.66c) is carried out following the classical backward-Euler integration scheme by employing the difference quotient (Equation 4.37), resulting on Equation 4.40.

5.3.9.2 Integration algorithm

The elastic predictor-plastic corrector method presented in Section 4.3.2 is used here to numerically integrate the constitutive equations of the hyperelastic-based model.

Firstly, the rotation tensor $\mathbf{Q}^{\star}_{n+1}$ is computed according to Equation 5.36 and the trial quantities are computed based of the assumption that no plastic flow, and thus no evolution of internal variables, occurs, i.e.,

$$\Delta\lambda = 0, \tag{5.131}$$

$$\mathbf{C}^{\mathrm{trial}}_{\mathrm{p}_{n+1}} = \mathbf{C}_{\mathrm{p}_n} = \mathbf{U}^2_{\mathrm{p}_n}, \tag{5.132}$$

$$\mathbf{C}^{\mathrm{trial}}_{\mathrm{p_i}_{n+1}} = \mathbf{C}_{\mathrm{p_i}_n} = \mathbf{U}^2_{\mathrm{p_i}_n}, \tag{5.133}$$

$$\mathbf{S}^{\mathrm{trial}}_{n+1} = \mu_{\mathrm{e}}(\mathbf{C}^{-1}_{\mathrm{p}_n} - \mathbf{C}^{-1}_{n+1}) + \frac{\Lambda_{\mathrm{e}}}{2}\left(\frac{\det\mathbf{C}_{n+1}}{\det\mathbf{C}_{\mathrm{p}_n}} - 1\right)\mathbf{C}^{-1}_{n+1}, \tag{5.134}$$

$$\mathbf{X}^{\mathrm{trial}}_{n+1} = \frac{c}{2}(\mathbf{C}^{-1}_{\mathrm{p_i}_n} - \mathbf{C}^{-1}_{\mathrm{p}_n}), \tag{5.135}$$

$$\mathbf{Y}^{\mathrm{trial}}_{n+1} = \mathbf{C}^{-1}_{\mathrm{p}_n}\mathbf{C}_{n+1}\mathbf{S}^{\mathrm{trial}}_{n+1} - \mathbf{X}^{\mathrm{trial}}_{n+1}, \tag{5.136}$$

$$\bar{\mathbb{A}}^{\mathrm{trial}}_{n+1} = \bar{\mathbb{A}}\left(\mathbb{A}, \mathbf{F}_{n+1}, \mathbf{Q}^{\star}_{n+1}, \mathbf{C}_{\mathrm{p}_n}\right), \text{ and} \tag{5.137}$$

$$\bar{\varepsilon}^{\mathrm{trial}}_{\mathrm{p}_{n+1}} = \bar{\varepsilon}_{\mathrm{p}_n}. \tag{5.138}$$

Secondly, the yield condition is evaluated based on the trial quantities, i.e.,

$$\Phi^{\mathrm{trial}} = \Phi(\mathbf{Y}^{\mathrm{trial}}_{n+1}, \bar{\mathbb{A}}^{\mathrm{trial}}_{n+1}, \bar{\varepsilon}^{\mathrm{trial}}_{\mathrm{p}_{n+1}}). \tag{5.139}$$

Then, if the initial assumption is not verified ($\Phi^{\mathrm{trial}} > 0$), the plastic corrector phase is performed by solving the nonlinear evolution equations, implicit integration formulas of which are presented in Section 5.3.9.1, imposing that the yield condition must be satisfied at t_{n+1}. The system of equations to be solved can be represented in residuum format as

$$r_1 = \Phi(\mathbf{Y}) = 0, \tag{5.140}$$

$$\mathbf{r}_2 = -\mathbf{C}_{\mathrm{p}_n}^{-1} + \mathbf{U}_{\mathrm{p}}^{-1} \exp(\Delta\lambda \mathbf{U}_{\mathrm{p}}^{-1} \mathbf{f} \mathbf{U}_{\mathrm{p}}^{-1}) \mathbf{U}_{\mathrm{p}}^{-1} = \mathbf{0}, \text{ and} \tag{5.141}$$

$$\mathbf{r}_3 = -\mathbf{C}_{\mathrm{p_i}_n}^{-1} + \mathbf{U}_{\mathrm{p_i}}^{-1} \exp(\Delta\lambda \mathbf{U}_{\mathrm{p_i}}^{-1} \mathbf{f}_{\mathrm{kin}} \mathbf{U}_{\mathrm{p_i}}^{-1}) \mathbf{U}_{\mathrm{p_i}}^{-1} = \mathbf{0}. \tag{5.142}$$

This system of equations consists of 13 nonlinear scalar functions and has to be solved iteratively, employing e.g., Newton's method, until the residua converge to zero within a prescribed tolerance. Due to the fact that the symmetry of the constitutive model's variables was exploited, the second-order tensor-valued residua, $\mathbf{r}_2$ and $\mathbf{r}_3$, can be represented as six-dimensional arrays following the Voigt's notation. This is in contrast to constitutive models which use $\mathbf{F}_{\mathrm{p}}$ and $\mathbf{F}_{\mathrm{p_i}}$ as internal variables. Such models involve the solution of 19 equations at the Gauss point level which leads to a significantly higher CPU time effort and higher memory allocation.

If the system of Equations 5.140-5.142 is solved according to the Newton method, the residua are linearised around the current values of the state variables. The linearisation of the residua 5.140-5.142 is presented in Appendix B. Then, the increments, at each iteration i, of the state variables are obtained from

$$\begin{bmatrix} \Delta\Delta\lambda \\ \Delta\mathbf{U}_{\mathrm{p}}^{-1} \\ \Delta\mathbf{U}_{\mathrm{p_i}}^{-1} \end{bmatrix} = - \begin{bmatrix} r_1 \\ \mathbf{r}_2 \\ \mathbf{r}_3 \end{bmatrix} \begin{bmatrix} \frac{\partial r_1}{\partial(\Delta\lambda)} & \frac{\partial r_1}{\partial \mathbf{U}_{\mathrm{p}}^{-1}} & \frac{\partial r_1}{\partial \mathbf{U}_{\mathrm{p_i}}^{-1}} \\ \frac{\partial \mathbf{r}_2}{\partial(\Delta\lambda)} & \frac{\partial \mathbf{r}_2}{\partial \mathbf{U}_{\mathrm{p}}^{-1}} & \frac{\partial \mathbf{r}_2}{\partial \mathbf{U}_{\mathrm{p_i}}^{-1}} \\ \frac{\partial \mathbf{r}_3}{\partial(\Delta\lambda)} & \frac{\partial \mathbf{r}_3}{\partial \mathbf{U}_{\mathrm{p}}^{-1}} & \frac{\partial \mathbf{r}_3}{\partial \mathbf{U}_{\mathrm{p_i}}^{-1}} \end{bmatrix}^{-1}, \tag{5.143}$$

where the superscripts i are omitted for the sake of simplicity. At each iteration, the state variables are updated following

$$\Delta\lambda^i = \Delta\lambda^{i-1} + \Delta\Delta\lambda^i, \tag{5.144}$$

$$(\mathbf{U}_{\mathrm{p}}^{-1})^i = (\mathbf{U}_{\mathrm{p}}^{-1})^{i-1} + (\Delta\mathbf{U}_{\mathrm{p}}^{-1})^i, \text{ and} \tag{5.145}$$

$$(\mathbf{U}_{\mathrm{p_i}}^{-1})^i = (\mathbf{U}_{\mathrm{p_i}}^{-1})^{i-1} + (\Delta\mathbf{U}_{\mathrm{p_i}}^{-1})^i. \tag{5.146}$$

This integration algorithm is summarized in Box 5.2.

5.3.9.3 Consistent elastoplastic tangent modulus

In analogy to the continuous elastoplastic tangent modulus presented in Section 5.3.7, the algorithmic elastoplastic tangent modulus, consistent with the numerical algorithm used to integrate the constitutive equations of the hyperelastic-based model, relates the increments

Box 5.2: Implicit numerical integration of the hyperelastic-based model.

Given $\mathbf{F}_{n+1}$ and the history data $\mathbf{Q}_n^\star$, $\bar{\varepsilon}_{\mathrm{p}_n}$, $\mathbf{U}_{\mathrm{p}_n}$, and $\mathbf{U}_{\mathrm{p_i}_n}$

1. Compute $\mathbf{C}_{n+1}$ and $\mathbf{Q}_{n+1}^\star$ (Equation 5.36)
2. Set initial estimate (trial) values (Equations 5.131-5.138)
3. Evaluate the yield potential (Equation 5.139)
4. Check for plasticity onset:

IF ($\Phi^{\mathrm{trial}} \leq 0$) **THEN**

a) Set variables at t_{n+1}

$$\mathbf{S}_{n+1} = \mathbf{S}_{n+1}^{\mathrm{trial}},\ \bar{\varepsilon}_{\mathrm{p}_{n+1}} = \bar{\varepsilon}_{\mathrm{p}_{n+1}}^{\mathrm{trial}},\ \mathbf{U}_{\mathrm{p}_{n+1}} = \mathbf{U}_{\mathrm{p}_{n+1}}^{\mathrm{trial}},\ \text{and}\ \mathbf{U}_{\mathrm{p_i}_{n+1}} = \mathbf{U}_{\mathrm{p_i}_{n+1}}^{\mathrm{trial}}$$

b) **EXIT**

ELSE

a) Compute the auxiliary residua r_1^0, $\mathbf{r}_2^0$, and $\mathbf{r}_3^0$ (Equations 5.140-5.142)

b) Evaluate the root-mean-square value of the total residuum

$$\| \mathbf{r}^0 \| = \sqrt{(r_1^0)^2 + \| \mathbf{r}_2^0 \|^2 + \| \mathbf{r}_3^0 \|^2}$$

c) Iterative procedure ($TOL = 10^{-8}$):

DO WHILE $\| \mathbf{r} \| > TOL$

i) Linearise the residua (Appendix B)

ii) Compute the increments $\Delta\Delta\lambda^i$, $(\Delta\mathbf{U}_{\mathrm{p}}^{-1})^i$, and $(\Delta\mathbf{U}_{\mathrm{p_i}}^{-1})^i$ (Equation 5.143)

iii) Update the state variables $\Delta\lambda^i$, $(\mathbf{U}_{\mathrm{p}}^{-1})^i$, and $(\mathbf{U}_{\mathrm{p_i}}^{-1})^i$ (Equations 5.144-5.146)

iv) Re-evaluate the auxiliary residua, r_1^i, $\mathbf{r}_2^i$, and $\mathbf{r}_3^i$ and the root-mean-square value of the total residuum, $\| \mathbf{r}^i \|$

ENDDO

d) **EXIT**

ENDIF

5. Compute the Cauchy stress tensor at t_{n+1}

$\boldsymbol{\sigma}_{n+1} = J^{-1}\mathbf{F}\mathbf{S}_{n+1}\mathbf{F}^{\mathrm{T}}$

of the right Cauchy-Green deformation tensor to the increment of the second Piola-Kirchhoff stress tensor, according to

$$\Delta\mathbf{S} = \mathbb{D}_{\mathrm{ep}}^{\mathrm{alg}} : \Delta\mathbf{E}^{(2)} = \mathbb{D}_{\mathrm{ep}}^{\mathrm{alg}} : \frac{1}{2}\Delta\mathbf{C}. \tag{5.147}$$

Here, $\mathbb{D}_{\mathrm{ep}}^{\mathrm{alg}}$ is obtained following the procedure presented in the works of Dettmer and Reese (2004) and Vladimirov *et al.* (2010). Taking into account that $\mathbf{S}$ is a function of the tensors $\mathbf{C}$ and $\mathbf{C}_{\mathrm{p}}$ (Equation 5.81), the last relation can be expressed as

$$\Delta\mathbf{S} = \left(2\frac{\partial\mathbf{S}}{\partial\mathbf{C}} + 2\delta\frac{\partial\mathbf{S}}{\partial\mathbf{C}_{\mathrm{p}}} : \frac{\partial\mathbf{C}_{\mathrm{p}}}{\partial\mathbf{C}} \right) : \frac{1}{2}\Delta\mathbf{C}, \tag{5.148}$$

where the right Cauchy-Green deformation tensor $\mathbf{C}$ is now treated as a variable, whereas during the local iteration procedure it was treated as a known constant. This way, after convergence of the local solution the residua 5.140-5.142 can be represented as

$$r_1 = r_1(\Delta\lambda, \mathbf{C}, \mathbf{C}_\mathrm{p}, \mathbf{C}_{\mathrm{p_i}}) = 0, \tag{5.149}$$

$$\mathbf{r}_2 = \mathbf{r}_2(\Delta\lambda, \mathbf{C}, \mathbf{C}_\mathrm{p}, \mathbf{C}_{\mathrm{p_i}}) = \mathbf{0}, \text{ and} \tag{5.150}$$

$$\mathbf{r}_3 = \mathbf{r}_3(\Delta\lambda, \mathbf{C}_\mathrm{p}, \mathbf{C}_{\mathrm{p_i}}) = \mathbf{0}. \tag{5.151}$$

Note that there is no dependency of $\mathbf{r}_3$ on $\mathbf{C}$ due to the independence of $\mathbf{f}_\mathrm{kin}$ with regard to $\mathbf{C}$. Linearising and solving this system of equations in order to $\Delta\mathbf{C}_\mathrm{p}$, the following relation between $\Delta\mathbf{C}$ and $\Delta\mathbf{C}_\mathrm{p}$ is obtained,

$$\Delta\mathbf{C}_\mathrm{p} = \frac{\partial\mathbf{C}_\mathrm{p}}{\partial\mathbf{C}} : \Delta\mathbf{C} = -\mathbb{A}_\mathrm{p}^{-1} : \mathbb{A}_\mathrm{c} : \Delta\mathbf{C}, \tag{5.152}$$

where the auxiliary fourth-order tensors $\mathbb{A}_\mathrm{c}$ and $\mathbb{A}_\mathrm{p}$ are expressed, without derivation, as

$$\mathbb{A}_\mathrm{c} = \mathbb{M}_\mathrm{c}^{(2)} - \mathbb{M}_{\mathrm{p_i}}^{(2)} : (\mathbb{M}_{\mathrm{p_i}}^{(3)})^{-1} : \mathbb{M}_\mathrm{c}^{(3)} \text{ and} \tag{5.153}$$

$$\mathbb{A}_\mathrm{p} = \mathbb{M}_\mathrm{p}^{(2)} - \mathbb{M}_{\mathrm{p_i}}^{(2)} : (\mathbb{M}_{\mathrm{p_i}}^{(3)})^{-1} : \mathbb{M}_\mathrm{p}^{(3)}. \tag{5.154}$$

which are functions of the fourth-order tensors

$$\mathbb{M}_\mathrm{c}^{(k)} = \frac{\partial\mathbf{r}_k}{\partial\mathbf{C}} - \left[\frac{\partial r_1}{\partial(\Delta\lambda)}\right]^{-1} \frac{\partial\mathbf{r}_k}{\partial(\Delta\lambda)} \otimes \frac{\partial r_1}{\partial\mathbf{C}}, \tag{5.155}$$

$$\mathbb{M}_\mathrm{p}^{(k)} = \frac{\partial\mathbf{r}_k}{\partial\mathbf{C}_\mathrm{p}} - \left[\frac{\partial r_1}{\partial(\Delta\lambda)}\right]^{-1} \frac{\partial\mathbf{r}_k}{\partial(\Delta\lambda)} \otimes \frac{\partial r_1}{\partial\mathbf{C}_\mathrm{p}}, \text{ and} \tag{5.156}$$

$$\mathbb{M}_{\mathrm{p_i}}^{(k)} = \frac{\partial\mathbf{r}_k}{\partial\mathbf{C}_{\mathrm{p_i}}} - \left[\frac{\partial r_1}{\partial(\Delta\lambda)}\right]^{-1} \frac{\partial\mathbf{r}_k}{\partial(\Delta\lambda)} \otimes \frac{\partial r_1}{\partial\mathbf{C}_{\mathrm{p_i}}}, \tag{5.157}$$

with $k = 2, 3$. The algorithmic tangent for the numerical integration procedure presented in Section 5.3.9.2, associated to the present constitutive model, is finally expressed by

$$\mathbb{D}_\mathrm{ep}^\mathrm{alg} = 2\frac{\partial\mathbf{S}}{\partial\mathbf{C}} - 2\delta\frac{\partial\mathbf{S}}{\partial\mathbf{C}_\mathrm{p}} : \mathbb{A}_\mathrm{p}^{-1} : \mathbb{A}_\mathrm{c}. \tag{5.158}$$

5.4 Finite strain hyperelastoplasticity with multiple back stress components

Based on the modified rheological model of kinematic hardening presented in Section 3.4.2.2, the hyperelastic-based constitutive model presented in Section 5.3 is extended in this section. The following modifications allow for a better description of the nonlinear cyclic hardening behaviour due to the use of multiple back stress components. For the sake of simplicity only the main modifications are presented in this section.

Similarly to the present model, the hyperelastic-based formulations proposed by Tsakmakis (1996) and Wallin and Ristinmaa (2005) incorporates several back stress components. Their works are limited to the isotropic criterion of von Mises and are not based on the multiplicative slip of $\mathbf{F}_{\mathrm{p}}$, which is in contrast to the formulation presented in this section. While in Wallin and Ristinmaa (2005) it is employed a nonassociated flow rule, where the plastic potential, distinct from the yield potential, is used to compute the strain-like internal variables related to the kinematic hardening, in Tsakmakis (1996) the back stress tensor usually used in the yield function is replaced by the quantity $\mathbf{k} = \boldsymbol{\chi} + (2/c)\boldsymbol{\chi}\boldsymbol{\chi}$ and an objective rate of the back stress tensor, $\boldsymbol{\chi}$, in the intermediate configuration, that follows the classical Armstrong-Frederick evolution law (similarly to Equation 5.18), is employed.

In this work an innovative and distinct approach is followed. By considering the modified rheological model of Armstrong-Frederick kinematic hardening, several multiplicative decompositions of $\mathbf{F}_{\mathrm{p}}$ are taken into account, resulting on multiple strain-like variables ($\mathbf{C}^{j}_{\mathrm{p_i}}$, see Equation 5.167) that describe the complex kinematic hardening behaviour. Moreover, since the derivation of the constitutive equations follows the same approach as for the hyperelastic-based model presented in Section 5.3, all the resultant tensor-valued quantities are symmetric.

Kinematics The kinematic hardening law with multiple (N) back stress components is described in this model through N multiplicative decompositions of the plastic part of the deformation gradient into elastic and inelastic parts, i.e.,

$$\mathbf{F}_{\mathrm{p}} = \mathbf{F}^{j}_{\mathrm{p_e}}\mathbf{F}^{j}_{\mathrm{p_i}} \;\; \forall \;\; j = 1 \ldots N. \tag{5.159}$$

Moreover, this decomposition introduces N additional configurations, as schematically represented in Fig. 5.2.

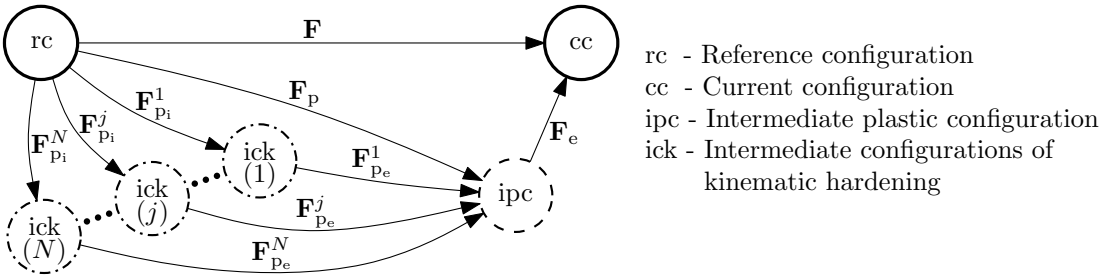

Figure 5.2: Multiplicative decompositions of the deformation gradients considering multiple back stress components.

Helmholtz free energy potential Multiple energy parts, ψ^{j}_{kin}, related to the hardening springs (see Fig. 3.7) are included in the Helmholtz free energy potential. Similarly to

the split of Equation 5.46, the Helmholtz potential can be additively split according to

$$\psi = \psi_{\mathrm{e}}\left(\mathbf{C}_{\mathrm{e}}\right) + \sum_{j=1}^{N} \psi_{\mathrm{kin}}^{j}\left(\mathbf{C}_{\mathrm{p_e}}^{j}\right) + \psi_{\mathrm{iso}}\left(\bar{\varepsilon}_{\mathrm{p}}\right). \tag{5.160}$$

Clausius-Duhem inequality Introducing the Helmholtz free energy potential into the Clausius-Duhem inequality (Equation 5.47) and considering the procedure presented in Section 5.3.3, the following simplified inequality is obtained,

$$\boldsymbol{\Sigma} : \mathbf{d}_{\mathrm{p}} + \sum_{j=1}^{N} \mathbf{M}_{\mathrm{kin}}^{j} : \mathbf{d}_{\mathrm{p_i}}^{j} + R\dot{\bar{\varepsilon}}_{\mathrm{p}} \geq 0, \tag{5.161}$$

where the relative stress in the intermediate configuration is now given by $\boldsymbol{\Sigma} = \mathbf{M} - \sum_{j=1}^{N} \boldsymbol{\chi}^{j}$. The component j of the back stress tensor in the intermediate configuration is defined as $\boldsymbol{\chi}^{j} = \mathbf{F}_{\mathrm{p}}\mathbf{X}^{j}\mathbf{F}_{\mathrm{p}}^{\mathrm{T}}$, whose representation in the reference configuration is expressed by $\mathbf{X}^{j} = 2(\mathbf{F}_{\mathrm{p_i}}^{j})^{-1}(\partial\psi_{\mathrm{kin}}^{j}/\partial\mathbf{C}_{\mathrm{p_e}}^{j})(\mathbf{F}_{\mathrm{p_i}}^{j})^{-\mathrm{T}}$. Moreover, the stress quantities $\mathbf{M}_{\mathrm{kin}}^{j}$, analogous to the Mandel stress tensor and related to the kinematic hardening, are defined by $\mathbf{M}_{\mathrm{kin}}^{j} = 2\mathbf{C}_{\mathrm{p_e}}^{j}(\partial\psi_{\mathrm{kin}}^{j}/\partial\mathbf{C}_{\mathrm{p_e}}^{j})$, and $\mathbf{d}_{\mathrm{p_i}}^{j} = \mathrm{sym}[\dot{\mathbf{F}}_{\mathrm{p_i}}^{j}(\mathbf{F}_{\mathrm{p_i}}^{j})^{-1}]$.

Evolution equations The inequality 5.161 is sufficiently satisfied by assuming that

$$\mathbf{d}_{\mathrm{p_i}}^{j} = \dot{\lambda}\frac{b^{j}}{c^{j}}(\mathbf{M}_{\mathrm{kin}}^{j})^{\mathrm{D}} \;\; \forall \;\; j = 1 \ldots N, \tag{5.162}$$

and taking the evolution Equations of 5.66a and 5.66c into account.

Finally, the yield function (Equation 5.87) and the loading/unloading conditions (Equation 4.20) complete the set of constitutive equations.

Representation in the reference configuration Analogously to the pull-back of Equation 5.70, the representation of the relative stress, that accounts for multiple back stress components, in the reference configuration is expressed by

$$\mathbf{Y} = \mathbf{C}_{\mathrm{p}}^{-1}\mathbf{C}\mathbf{S} - \sum_{j=1}^{N} \mathbf{X}^{j}. \tag{5.163}$$

The pull-back of $\mathbf{M}_{\mathrm{kin}}^{j}$ from the intermediate configuration j of the kinematic hardening to the reference configuration is carried out, analogously to Equation 5.73, according to

$$\mathbf{M}_{\mathrm{kin}}^{j} = \mathbf{F}_{\mathrm{p_i}}^{j}\mathbf{Y}_{\mathrm{kin}}^{j}(\mathbf{F}_{\mathrm{p_i}}^{j})^{\mathrm{T}} \;\; \forall \;\; j = 1 \ldots N, \tag{5.164}$$

representation of which in the reference configuration is defined as

$$\mathbf{Y}_{\mathrm{kin}}^{j} = (\mathbf{C}_{\mathrm{p_i}}^{j})^{-1}\mathbf{C}_{\mathrm{p}}\mathbf{X}^{j} \;\; \forall \;\; j = 1 \ldots N, \tag{5.165}$$

and deviator of which can be expressed by

$$(\mathbf{M}^j_{\text{kin}})^{\text{D}} = \mathbf{F}^j_{\text{p}_\text{i}} \left[\left(\mathbf{Y}^j_{\text{kin}} \mathbf{C}^j_{\text{p}_\text{i}} \right)^{\text{D}} (\mathbf{C}^j_{\text{p}_\text{i}})^{-1} \right] (\mathbf{F}^j_{\text{p}_\text{i}})^{\text{T}} = \mathbf{F}^j_{\text{p}_\text{i}} \left[(\mathbf{C}^j_{\text{p}_\text{i}})^{-1} \left(\mathbf{C}^j_{\text{p}_\text{i}} \mathbf{Y}^j_{\text{kin}} \right)^{\text{D}} \right] (\mathbf{F}^j_{\text{p}_\text{i}})^{\text{T}}. \quad (5.166)$$

Finally, by employing the relation $\dot{\mathbf{C}}^j_{\text{p}_\text{i}} = 2(\mathbf{F}^j_{\text{p}_\text{i}})^{\text{T}} \mathbf{d}^j_{\text{p}_\text{i}} \mathbf{F}^j_{\text{p}_\text{i}}$ and the above equation in Equation 5.162 the evolution equation of $\mathbf{C}^j_{\text{p}_\text{i}}$ can be expressed by

$$\dot{\mathbf{C}}^j_{\text{p}_\text{i}} = 2\dot{\lambda} \frac{b^j}{c^j} (\mathbf{C}^j_{\text{p}_\text{i}} \mathbf{Y}^j_{\text{kin}})^{\text{D}} \mathbf{C}^j_{\text{p}_\text{i}} \ \forall \ j = 1 \dots N. \quad (5.167)$$

Continuous elastoplastic tangent modulus Following the procedure presented in Section 5.3.7, the continuous elastoplastic tangent modulus related to the model that accounts for multiple back stress components is expressed, without derivation, by

$$\mathbb{D}_{\text{ep}} = \frac{\partial \dot{\mathbf{S}}}{\partial \dot{\mathbf{E}}^{(2)}} = 2 \frac{\partial \mathbf{S}}{\partial \mathbf{C}} + 2\delta \frac{\partial \mathbf{S}}{\partial \mathbf{C}_{\text{p}}} : \mathbf{n}_{\mathbf{Y}} \otimes \frac{\mathbf{A}_{\text{N}}}{A^{\Sigma}_{\text{D}}}, \quad (5.168)$$

where $\mathbf{A}_{\text{N}}$ is given by Equation 5.110 and

$$A^{\Sigma}_{\text{D}} = \mathbf{n}_{\mathbf{Y}} : \left\{ \mathbf{C}^{-1}_{\text{p}} \mathbf{n}_{\mathbf{Y}} \mathbf{C}^{-1}_{\text{p}} \mathbf{C}\mathbf{S} - \mathbf{C}^{-1}_{\text{p}} \mathbf{C} \frac{\partial \mathbf{S}}{\partial \mathbf{C}_{\text{p}}} : \mathbf{n}_{\mathbf{Y}} \right.$$
$$\left. + \sum_{j=1}^{N} \left\{ \frac{\partial \mathbf{X}^j}{\partial \mathbf{C}_{\text{p}}} : \mathbf{n}_{\mathbf{Y}} + \frac{b^j}{c^j} \frac{\partial \mathbf{X}^j}{\partial \mathbf{C}^j_{\text{p}_\text{i}}} : \left[\left(\mathbf{C}^j_{\text{p}_\text{i}} \mathbf{Y}^j_{\text{kin}} \right)^{\text{D}} \mathbf{C}^j_{\text{p}_\text{i}} \right] \right\} \right\} + H. \quad (5.169)$$

Summary of the constitutive model Box 5.3 summarizes the set of constitutive equations of the present model. The evolutions of the plastic deformation and hardening (isotropic and kinematic) are described by $N + 2$ internal variables, namely $\mathbf{C}_{\text{p}}$, $\mathbf{C}^j_{\text{p}_\text{i}}$, and $\bar{\varepsilon}_{\text{p}}$. In analogy to Equation 5.114, the free energy terms ψ^j_{kin} are assumed to follow the Neo-Hookean form, i.e.,

$$\psi^j_{\text{kin}} \left(\mathbf{C}^j_{\text{p}_\text{e}} \right) = \frac{c^j}{4} \left(\text{tr} \mathbf{C}^j_{\text{p}_\text{e}} - 3 \right) - \frac{c^j}{2} \ln \left(\sqrt{\det \mathbf{C}^j_{\text{p}_\text{e}}} \right) \ \forall \ j = 1 \dots N. \quad (5.170)$$

Hence, the back stress components in the reference configuration are expressed as

$$\mathbf{X}^j = \frac{c^j}{2} \left[(\mathbf{C}^j_{\text{p}_\text{i}})^{-1} - \mathbf{C}^{-1}_{\text{p}} \right] \ \forall \ j = 1 \dots N. \quad (5.171)$$

Numerical implementation Following the procedure presented in Section 5.3.9.1, the implicit integrated formulas based on the exponential map for the state variables $\mathbf{C}^j_{\text{p}_\text{i}}$ are expressed by

$$(\mathbf{C}^j_{\text{p}_{\text{i}_n}})^{-1} = (\mathbf{U}^j_{\text{p}_\text{i}})^{-1} \exp[\Delta\lambda (\mathbf{U}^j_{\text{p}_\text{i}})^{-1} \mathbf{f}^j_{\text{kin}} (\mathbf{U}^j_{\text{p}_\text{i}})^{-1}] (\mathbf{U}^j_{\text{p}_\text{i}})^{-1}, \quad (5.172)$$

Box 5.3: Hyperelastoplastic constitutive model with multiple back stress components.

Kinematics	$\mathbf{F} = \mathbf{F}_\mathrm{e}\mathbf{F}_\mathrm{p},\ \mathbf{F}_\mathrm{p} = \mathbf{F}^j_{\mathrm{p_e}}\mathbf{F}^j_{\mathrm{p_i}}\ \forall\ j = 1\ldots N,$ $\mathbf{C}_\mathrm{p} = \mathbf{F}_\mathrm{p}^\mathrm{T}\mathbf{F}_\mathrm{p},\ \mathbf{C}^j_{\mathrm{p_i}} = (\mathbf{F}^j_{\mathrm{p_i}})^\mathrm{T}\mathbf{F}^j_{\mathrm{p_i}}$
Helmholtz free energy	$\psi = \psi_\mathrm{e}\left(\mathbf{C}_\mathrm{e}\right) + \sum_{j=1}^{N}\psi^j_\mathrm{kin}\left(\mathbf{C}^j_{\mathrm{p_e}}\right) + \psi_\mathrm{iso}\left(\bar{\varepsilon}_\mathrm{p}\right)$
Stress tensors	$\mathbf{S} = 2\mathbf{F}_\mathrm{p}^{-1}\dfrac{\partial\psi_\mathrm{e}}{\partial\mathbf{C}_\mathrm{e}}\mathbf{F}_\mathrm{p}^{-\mathrm{T}},\ \mathbf{X}^j = 2(\mathbf{F}^j_{\mathrm{p_i}})^{-1}\dfrac{\partial\psi^j_\mathrm{kin}}{\partial\mathbf{C}^j_{\mathrm{p_e}}}(\mathbf{F}^j_{\mathrm{p_i}})^{-\mathrm{T}},$ $\mathbf{Y} = \mathbf{C}_\mathrm{p}^{-1}\mathbf{C}\mathbf{S} - \sum_{j=1}^{N}\mathbf{X}^j,\ \mathbf{Y}^j_\mathrm{kin} = (\mathbf{C}^j_{\mathrm{p_i}})^{-1}\mathbf{C}_\mathrm{p}\mathbf{X}^j$
Evolution equations	$\dot{\mathbf{C}}_\mathrm{p} = 2\dot{\lambda}\mathbf{n}_\mathbf{Y},\ \dot{\mathbf{C}}^j_{\mathrm{p_i}} = 2\dot{\lambda}\dfrac{b^j}{c^j}(\mathbf{C}^j_{\mathrm{p_i}}\mathbf{Y}^j_\mathrm{kin})^\mathrm{D}\mathbf{C}^j_{\mathrm{p_i}},\ \dot{\bar{\varepsilon}}_\mathrm{p} = \dot{\lambda}$
Yield function	$\Phi(\mathbf{Y}, \bar{\varepsilon}_\mathrm{p}) = \bar{\sigma}(\mathbf{Y}) - [\sigma_{\mathrm{y}_0} - R(\bar{\varepsilon}_\mathrm{p})]$
Loading/unloading conditions	$\dot{\lambda} \geq 0,\ \Phi \leq 0,\ \dot{\lambda}\Phi = 0$
Continuous tangent modulus	$\mathbb{D}_\mathrm{ep} = 2\dfrac{\partial\mathbf{S}}{\partial\mathbf{C}} + 2\delta\dfrac{\partial\mathbf{S}}{\partial\mathbf{C}_\mathrm{p}} : \mathbf{n}_\mathbf{Y} \otimes \dfrac{\mathbf{A}_\mathrm{N}}{A^\Sigma_\mathrm{D}}$

where

$$\mathbf{f}^j_\mathrm{kin} = 2\frac{b^j}{c^j}(\mathbf{C}^j_{\mathrm{p_i}}\mathbf{Y}^j_\mathrm{kin})^\mathrm{D}\mathbf{C}^j_{\mathrm{p_i}}\ \forall\ j = 1\ldots N. \tag{5.173}$$

The numerical implementation of this model is carried out using the algorithm previously shown in Box 5.2. The system of nonlinear equations to be solved is constituted by the residua related to the yield condition (r_1) and to the evolutions of $\mathbf{C}_\mathrm{p}$ ($\mathbf{r}_2$) and $\mathbf{C}^j_{\mathrm{p_i}}$ ($\mathbf{r}_{2+j}$), i.e.,

$$r_1 = \Phi(\mathbf{Y}) = 0, \tag{5.174}$$

$$\mathbf{r}_2 = -\mathbf{C}^{-1}_{\mathrm{p}_n} + \mathbf{U}_\mathrm{p}^{-1}\exp(\Delta\lambda\mathbf{U}_\mathrm{p}^{-1}\mathbf{f}\mathbf{U}_\mathrm{p}^{-1})\mathbf{U}_\mathrm{p}^{-1} = \mathbf{0},\ \text{and} \tag{5.175}$$

$$\mathbf{r}_{2+j} = -(\mathbf{C}^j_{\mathrm{p_i}_n})^{-1} + (\mathbf{U}^j_{\mathrm{p_i}})^{-1}\exp[\Delta\lambda(\mathbf{U}^j_{\mathrm{p_i}})^{-1}\mathbf{f}^j_\mathrm{kin}(\mathbf{U}^j_{\mathrm{p_i}})^{-1}](\mathbf{U}^j_{\mathrm{p_i}})^{-1} = \mathbf{0}. \tag{5.176}$$

The linearisation of these residua is presented in Appendix B. Due to the fact that the symmetry of the internal variables of the constitutive model was systematically exploited, the number of scalar equations that represent this system of equations is significantly reduced from $10 + 9j$ to $7 + 6j$, through the representation of the tensor-valued residua as six-dimensional arrays following the Voigt's notation.

Consistent elastoplastic tangent modulus The algorithmic elastoplastic tangent modulus consistent with the numerical algorithm presented above is obtained from Equation 5.147. The closed form expression of the tangent modulus can be obtained following the

procedure presented in Section 5.3.9.3, by linearising and solving the system of equations

$$r_1 = r_1(\Delta\lambda, \mathbf{C}, \mathbf{C}_\mathrm{p}, \mathbf{C}^j_{\mathrm{p_i}}) = 0, \tag{5.177}$$

$$\mathbf{r}_2 = \mathbf{r}_2(\Delta\lambda, \mathbf{C}, \mathbf{C}_\mathrm{p}, \mathbf{C}^j_{\mathrm{p_i}}) = \mathbf{0}, \text{ and} \tag{5.178}$$

$$\mathbf{r}_{2+j} = \mathbf{r}_{2+j}(\Delta\lambda, \mathbf{C}_\mathrm{p}, \mathbf{C}^j_{\mathrm{p_i}}) = \mathbf{0}. \tag{5.179}$$

in order to $\mathbf{C}_\mathrm{p}$, after convergence of the local iteration procedure. Although this derivation is straightforward, when a high number of back stress components is considered, it can be a very lengthy and error prone task. Thus, a numerical computation by means of the classical perturbation technique (Miehe, 1996b) presented in Appendix C is advised. As mentioned in Section 4.3.5, the numerical computation of the consistent elastoplastic tangent modulus requires a higher effort comparatively to the use of the analytical closed form, but its use does not affect neither the accuracy of the numerical solution nor its convergence rate.

Chapter 6

Identification of constitutive parameters

This section presents the procedures used to identify the constitutive parameters of the materials used in some of the numerical examples presented in Chapter 7. Firstly, the inverse methodology developed is presented and assessed through its application considering a virtual (fictitious) material. Secondly, the procedure is used to identify the constitutive parameters of the 6022-T43 and 5182-O aluminium alloys and for the DP590 steel.

6.1 Introduction

The identification of the constitutive parameters is an important, and mandatory, task that precedes the numerical simulation of realistic processes, since the quality of the numerical results depends on a reliable set of parameters used as input for analysis. Over the years, several identification strategies have been developed with the purpose of properly determine constitutive parameters to be used in numerical simulation models. Generally, they can be divided in three categories (Haddadi and Belhabib, 2012), namely (i) the identification of constitutive parameters using stress-strain data obtained by conventional mechanical tests, performed using standard specimens and characterized by homogeneous strain distributions, (ii) the parameters' identification by using the total applied force and total elongation of the specimens, where the mechanical behaviour is dependent on the specimen's shape and thus the real shape of the sample must be taken into account in each iteration of the identification procedure, and (iii) the use of full-field measurement methods, which are based on the experimentally obtained measurements of the applied force and strain maps and, therefore, involves the acquisition of a large amount of information data. Usually, conventional tests are used to identify the anisotropy parameters of anisotropic yield functions, such as the ones considered in this work. Therefore, a suitable parameters' identification strategy based on stress-strain input data should be considered. This strategy consists of an inverse methodology, as the one presented in the following.

6.2 Inverse methodology

The inverse methodology used in this work is illustrated in Fig. 6.1, and consists of an iterative procedure that aims the minimization of an objective function that compares the experimental data with analytical and/or numerically obtained one.

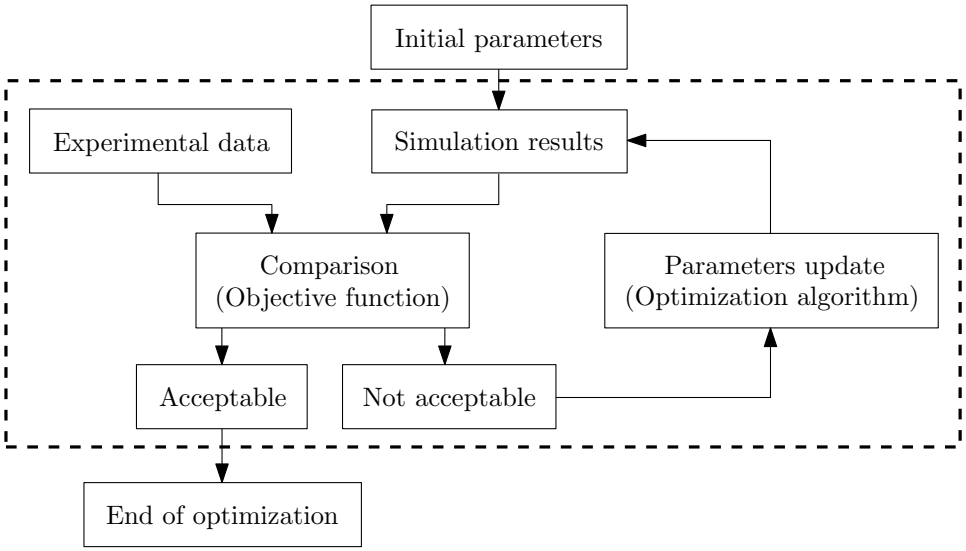

Figure 6.1: Inverse methodology used to identify the constitutive parameters.

From an initial set of constitutive parameters, suitable data (stress-strain relations, r-values, etc.) are analytically and/or numerically computed. Then, a proper objective function is used to compare the experimental data with the data obtained from the current set of constitutive parameters. If the value provided by the objective function is higher than a satisfactory limit, an optimization algorithm is used to update the set of constitutive parameters accounting for the minimization of the objective function's value. The iterative procedure continues until the satisfactory limit is reached.

In this work, the numerically obtained data is attained by using the commercial Finite Element code ABAQUS, by means of the material subrotine, UMAT, used to implement the presented constitutive models. The verification of the correct implementation of the constitutive models is presented in Sections 7.1 and 7.2. In this section, the hypoelastic-based model with the Zaremba-Jaumann rate presented in Section 5.2 is employed and the backward-Euler algorithm is considered.

6.3 Objective function

As aforementioned, the identification procedure is guided by the minimization of a predefined objective function. Therefore, the success of the optimization methodology demands a suitable definition of this function. The experimental data used in this type of optimization problem is composed by discrete values representing, e.g., a set of stress-strain measured

points. Moreover, the numerical results are defined by a curve, hence interpolations for each experimental point are required in order to compare both data. This is schematically represented in Fig. 6.2 for a stress-strain relation. One of the most common objective functions applied in parameters' identification consists of the sum of the squares of the difference of relevant data and can be written as

$$f_{\text{obj}}(x) = \frac{1}{n_{\text{curves}}} \sum_{j=1}^{n_{\text{curves}}} \frac{1}{n_{\text{points}_j}} \sum_{i=1}^{n_{\text{points}_j}} \left(\frac{Y_{i,j}^{\text{exp}} - Y_{i,j}^{\text{num}}(x)}{W_{Y_j}} \right)^2 + \frac{1}{n_r} \sum_{k=1}^{n_r} \left(\frac{r_k^{\text{exp}} - r_k^{\text{num}}}{W_{r_k}} \right)^2, \quad (6.1)$$

where Y is a quantity of interest, such as stress or force defined as a function of strain or displacement, respectively. Also, n_{curves} is the number of curves compared and n_{points_j} is the number of points that represents the curve j. The superscripts exp and num refer to experimental and analytical or numerical data, respectively. The directional and biaxial r-values are represented by r_k. The constants W_{Y_j} and W_{r_k} are weighting factors used to differentiate the quantity of interest Y_j and the r-value k, respectively. Due to the different orders of magnitude of the quantities of interest considered in the parameters' identification processes presented in the following, in this work, these weighting factors are chosen so the difference $(\bullet)^{\text{exp}} - (\bullet)^{\text{num}}$ is normalized in terms of its order of magnitude. Furthermore, the value provided by the objective function is independent of the number of experimental points considered, due to the use of the term $1/n_{\text{points}_j}$, and independent of the number of curves and r-values taken into account by using the terms $1/n_{\text{curves}}$ and $1/n_r$, respectively.

During the optimization procedure, the value of the objective function moves towards to zero and reaches that value if a perfect correspondence between numerical and experimental points is obtained (global minimum). Although the square difference objective function is the most used in parameters' identification procedures, some alternative objective functions have been proposed in the last years such as by Cao and Lin (2008) and Andrade-Campos *et al.* (2012), among others.

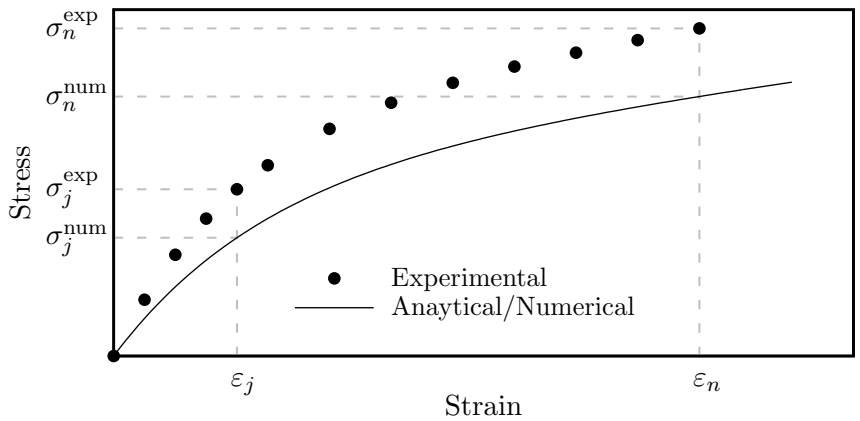

Figure 6.2: Scheme of the comparison between experimental and analytical or numerical data.

6.4 Optimization algorithm

Optimization numerical methods are applied to update the set of constitutive parameters during the identification procedure, with the aim of minimizing the value provided by the objective function. A large number of optimization methods can be used for this purpose, which can be divided in two main groups, namely (i) heuristic methods and (ii) classic gradient-based methods. The objective function is composed by several local minima and some of the optimization methods do not have mechanisms to avoid these points. Therefore, the selection of the optimization method assumes a great importance because it controls the efficiency of the parameters' identification process.

On the one hand, in heuristic methods the nature inspired algorithms can be distinguished. These are probabilistic optimization methods based on biological evolution mechanisms such as the reproduction or natural selection (Andrade-Campos *et al.*, 2007). It is used a population where each individual can be a possible solution. These optimization methods are very robust because the search is initiated with a set of possible solutions, only using the information of the objective function value (Furukawa and Yagawa, 1997). However, they require a large number of iterations and, consequently, large computational time.

On the other hand, the gradient-based methods are characterized by using the information of the derivative of the objective function to successively update the solution until a satisfactory limit is satisfied. Usually, the results obtained with this type of algorithms are characterized of being dependent on the initial set of parameters, since they do not have mechanisms that hinder the convergence for local minima (Andrade-Campos *et al.*, 2007). However, these algorithms are widely used in optimization since they show an excellent relationship between efficiency and required computational time. In this work, the widely used Levenberg-Marquardt gradient-based algorithm (Levenberg, 1944, Marquardt, 1963) is utilized in the parameters' identification process. This algorithm consists of an evolution of the classic Newton method and calculates a search direction between the Gauss-Newton direction and the steepest descent direction. The algorithm is characterized by alternating between a slow descending (when moved away from a minimum) and a quick convergence (when in the neighbourhood of a minimum).

6.5 Assessment of the identification procedure

The presented constitutive parameters' identification procedure is here assessed by applying it to a virtual (fictitious) material. This means that the identification procedure is carried out using the mechanical behaviour of the virtual material as "experimental" data. This kind of analysis is very interesting in the assessment of the ability and accuracy of the developed procedure in determining the best optimal solution (global minimum), since that solution is known.

The considered virtual material's parameters, to which correspond the ideal (optimal)

solution, are depicted in Table 6.1. It is considered an aluminium-like material with isotropic (Swift's law) and nonlinear kinematic (one back stress component) hardening, and anisotropic behaviour described by the *Yld2004-18p* yield function. From these constitutive parameters the "experimental" data that characterize its mechanical behaviour is reproduced by

i) stress-strain relations for in-plane uniaxial tensile tests at every 15° (0°, 15°, 30°, 45°, 60°, 75°, and 90°) from RD,

ii) directional r-values obtained from in-plane uniaxial tensile tests at every 15° from RD,

iii) stress-strain relations for uniaxial tensile tests at 45° from RD in the RD-ND and TD-ND planes of the sheet,

iv) hydraulic pressure-polar displacement relation in the hydraulic bulge test,

v) shear stress-shear strain relations for in-plane shear tests at 0° and 45° from RD,

vi) shear stress-shear strain relations for shear tests in RD in the RD-ND and TD-ND planes of the sheet, and

vii) shear stress-shear strain relations for three in-plane Bauschinger shear tests in the RD, with inversion of loading direction at 10%, 20%, and 30% of shear strain, respectively.

Table 6.1: Constitutive parameters of the virtual material.

Elasticity									
E [GPa]	ν [-]								
69.0	0.33								
Isotropic hardening						Kinematic hardening			
K [MPa]	ε_0 [-]	n_{H} [-]				c [MPa]	b [-]		
500.8	$4.78\text{x}10^{-3}$	0.20				68.2	2.2		
Yld2004-18p anisotropy parameters ($a = 8$)									
c_{12}^1	c_{13}^1	c_{21}^1	c_{23}^1	c_{31}^1	c_{32}^1	c_{44}^1	c_{55}^1	c_{66}^1	
1.2410	1.0783	1.2165	1.2239	1.0931	0.8892	1.3491	0.5019	0.5572	
c_{12}^2	c_{13}^2	c_{21}^2	c_{23}^2	c_{31}^2	c_{32}^2	c_{44}^2	c_{55}^2	c_{66}^2	
0.7754	0.9227	0.7655	0.7934	0.9187	1.0276	0.5898	1.1158	1.1123	

The procedure framework is conducted by an interface program, developed in Fortran, that is linked to the commercial Finite Element code ABAQUS, in order to perform the numerical simulations, being also linked to the optimization software SDL (Andrade-Campos *et al.*, 2007), to verify if the stagnation criterion is satisfied and to update the set of constitutive parameters at each iteration of the identification procedure.

Regarding the numerical modelling, 3D models of a single element are used for the uniaxial tensile, shear, and Bauschinger tests. In the case of the hydraulic bulge test, a converged and structured mesh composed by 128 elements is used considering the setup schematically depicted in Fig. 6.3, following the work of Alves de Sousa *et al.* (2007). Due to the symmetry

of the process and the orthotropy of the material only a quarter section of the specimen is analysed. In all simulations 8-node trilinear finite elements with reduced integration (C3D8R, in ABAQUS) are employed. Concerning the r-values, they can be directly computed from the in-plane uniaxial tensile tests by computing the ratio $r_\theta = \varepsilon_{\mathrm{p}22}/\varepsilon_{\mathrm{p}33}$, or analytically following Appendix D.

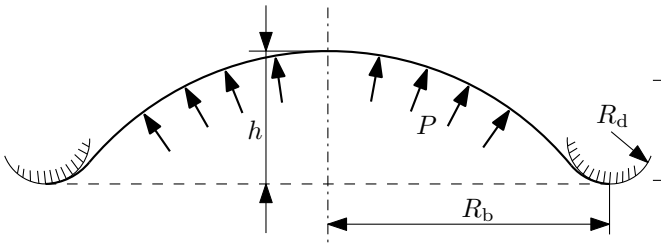

Blank radius	$R_\mathrm{b} = 81.0$
Die profile radius	$R_\mathrm{d} = 12.70$
Initial blank thickness	$t = 1.24$
	[mm]

Figure 6.3: Schematic setup of the hydraulic bulge test.

Concerning the optimization process, some conditions have to be established such as, the derivatives of the objective function are numerically computed through a finite difference with a perturbation value of $5\text{x}10^{-3}$, the maximum number of allowed iterations is 500, and the stagnation stopping criterion equals to 10^{-30}. Moreover, the weighting factors are normalized so that all features of interest (stress-strain curve, r-value, etc.) have the same importance. Additionally, some material parameters are not subjected to the identification process, namely the elastic modulus, E, the Poisson ratio, ν, and the exponent of the yield function a. This means that these parameters are kept constant during the optimization process and assume the same values as the virtual material.

In Table 6.2 it is shown the initial, reference, and optimal identified set of parameters. Additionally, the relative errors between the reference and the optimal identified values are presented. The initially chosen anisotropy parameters are all equal to 1.0, and therefore the identification process started with the description of the Hershey's isotropic yield function (Barlat *et al.*, 2005). The identification process performed 500 iterations and the optimal solution corresponds to a local minimum. Indeed, the relative errors between reference and identified parameters clearly elucidates their difference. It should be mentioned that obtention of the global minimum in the identification process of the constitutive parameters for the considered material model is a quite difficult task due to the high number of parameters taken into account. Moreover, one has to bear in mind that the gradient-based nature of the Levenberg-Marquardt algorithm makes the solution to be dependent on the initial estimation of the parameters, leading, in general, the optimization process to a local minimum of the objective function.

The evolution of the normalized value of the objective function is presented in Fig. 6.4. The value of the objective function is reduced significantly to 0.34% of its initial value. This reduction mainly occurs until iteration 300 and a stabilization of the objective function's value is observed in the following iterations. This type of behaviour is justified by the fact that the Levenberg-Marquardt always seeks the best descent direction, accelerating to convergence.

Table 6.2: Initial, reference, and optimal identified set of parameters for the virtual material.

Parameters	Initial	Optimal	Reference	Rel. Error (%)
K [MPa]	400.0	492.4	500.8	-1.7
ε_0 [-]	2.0x10^{-3}	2.561x10^{-3}	4.78x10^{-3}	-46.4
n_{H} [-]	0.12	0.184	0.20	-8.0
c [MPa]	51.5	55.04	68.2	-19.3
b [-]	6.0	3.69	2.2	67.7
c_{12}^1	1.0	1.1912	1.2410	-4.0
c_{13}^1	1.0	1.0333	1.0783	-4.2
c_{21}^1	1.0	1.0752	1.2165	-11.6
c_{23}^1	1.0	0.8853	1.2239	-27.7
c_{31}^1	1.0	0.8032	1.0931	-26.5
c_{32}^1	1.0	0.5231	0.8892	-41.2
c_{44}^1	1.0	1.2771	1.3491	-5.3
c_{55}^1	1.0	0.4651	0.5572	-16.5
c_{66}^1	1.0	0.4151	0.5019	-17.3
c_{12}^2	1.0	0.8300	0.7754	7.0
c_{13}^2	1.0	1.1956	0.9227	29.6
c_{21}^2	1.0	0.8962	0.7655	17.1
c_{23}^2	1.0	1.0896	0.7934	37.3
c_{31}^2	1.0	1.0681	0.9187	16.3
c_{32}^2	1.0	1.3796	1.0276	34.3
c_{44}^2	1.0	0.6981	0.5898	18.4
c_{55}^2	1.0	1.2260	1.1123	10.2
c_{66}^2	1.0	1.2218	1.1158	9.5

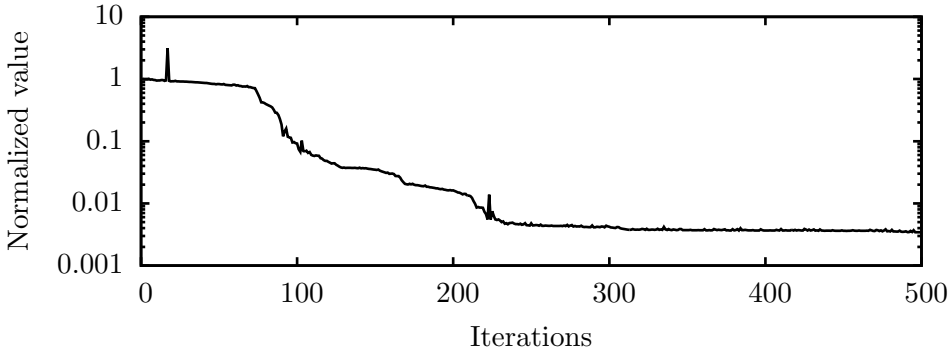

Figure 6.4: Evolution of the objective function's value in the parameters' identification process.

However, when the objective function is close to a possible solution, its value tends to stabilize until a stopping condition is satisfied. In the carried out identification process, the maximum number of iterations was reached. Nevertheless, considering the relationship between required computational time and obtained results, it is important to refer that, in this case, only 300 iterations would be enough to obtain similar results comparatively to those achieved at iteration 500.

Regardless the difference between the optimal identified and the reference parameters, in order to infer about the real quality of the obtained solution, it is mandatory to compare the experimental and numerical data by visual analysis. For that purpose, the "experimental" and numerical data are presented in Figs. 6.5-6.7 for all data considered in the identification process. The extremely good prediction of the r-values evolution in the sheet's plane is presented in Fig. 6.5. In addition to the seven values used in the identification process, the analytical curves obtained with the reference and optimal identified parameters are also depicted. It is worth noting that, even though only the discrete values at every 15° are used in this identification process, the overall predicted evolution of the r-values in the sheet plane is in excellent agreement with the "experimental" evolution. An accurate reproduction of the "experimental" stress-strain curves for the uniaxial tensile, shear, and Bauschinger tests by the identified parameters is seen in Fig. 6.6. This means that although there is a significant difference between the reference and identified hardening parameters (Table 6.2), the obtained solution provides a reliable reproduction of the combined isotropic-nonlinear kinematic hardening of the virtual material. Finally, the hydraulic bulge test results and the "experimental" data are also in excellent agreement for polar displacement up to 35 mm, with a small deviation for larger displacements (Fig. 6.7). It is worth mentioning that even though the equi-biaxial stress-strain curve provides more information about the hardening and anisotropy of the material relatively to the hydraulic pressure-polar displacement curve, the latter is considered in this example to confirm that the developed identification procedure can be applied to a wide range of different type of data.

In Fig. 6.8 the "experimental" yield surfaces with 0.25 increments of normalized shear contours, along with the ones predicted by the initial and identified set of parameters, are depicted. Considering the noticeable similarity of the yield surfaces and the excellent agreement between the "experimental" and numerical data presented in Figs. 6.5-6.7, one may conclude that the developed parameters' identification procedure is able to predict the complex anisotropic behaviour described by the considered constitutive model.

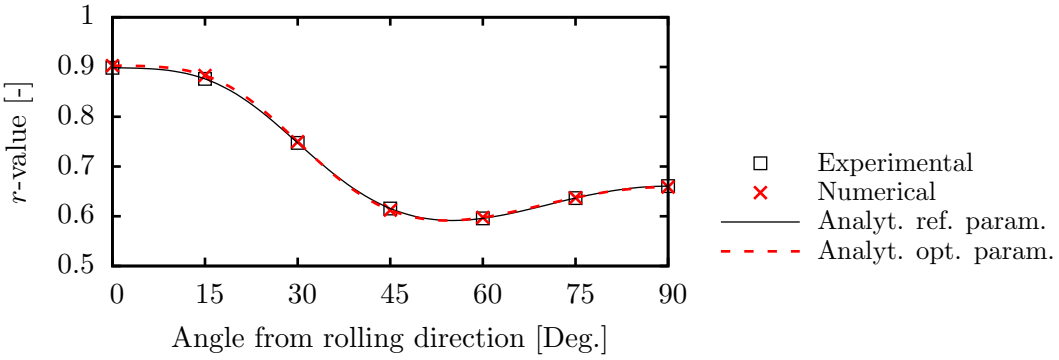

Figure 6.5: Virtual material - "Experimental" and analytically obtained, with the identified parameters, directional r-values.

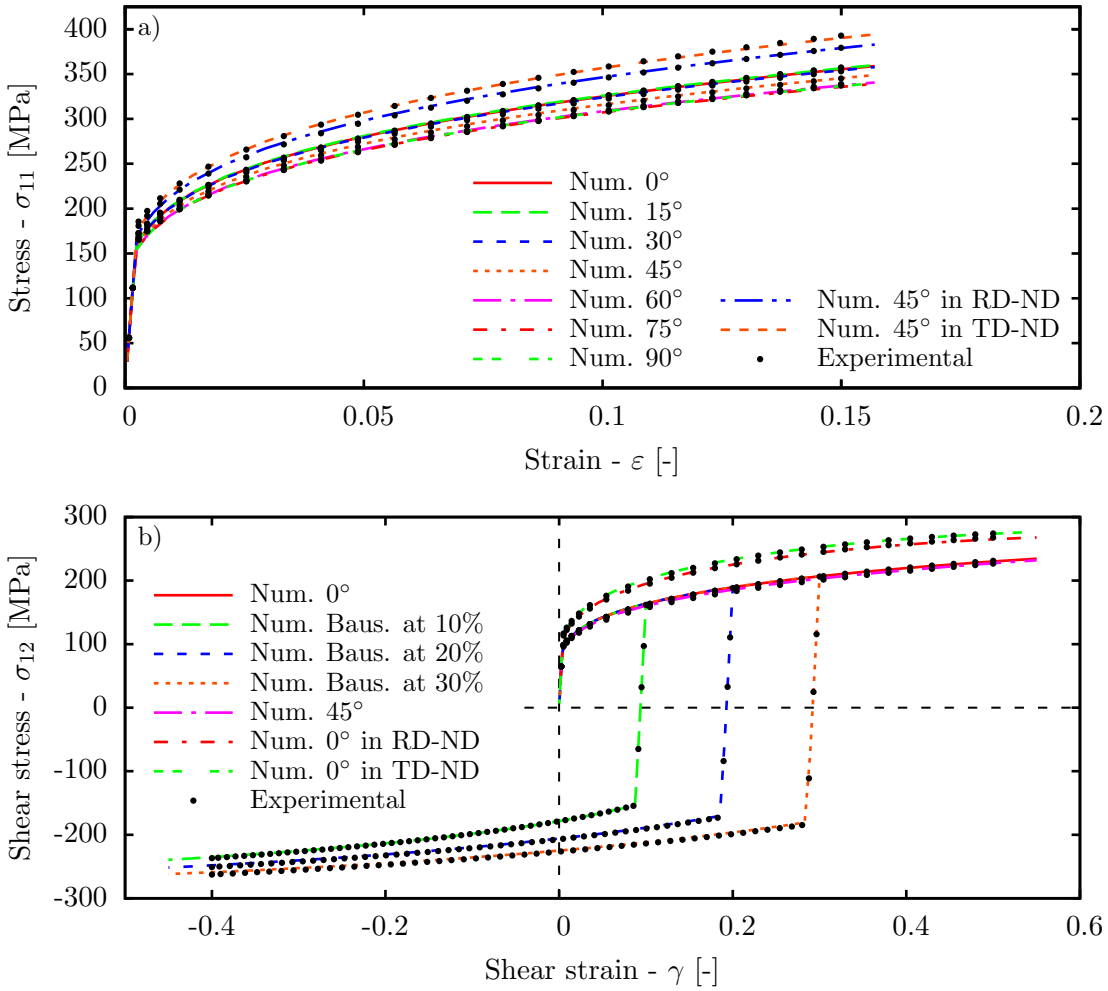

Figure 6.6: Virtual material - "Experimental" and numerically obtained, with the identified parameters, stress-strain curves for a) uniaxial tensile tests and b) monotonic and Bauschinger shear tests.

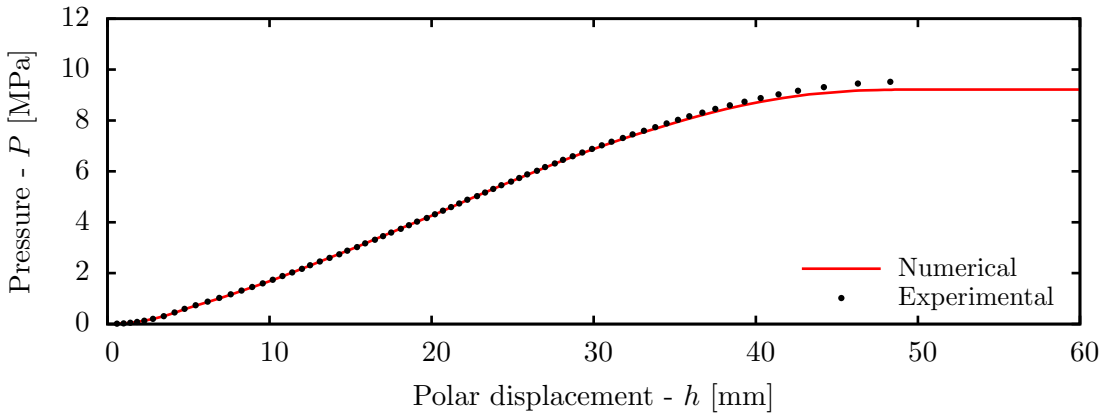

Figure 6.7: Virtual material - "Experimental" and numerically obtained, with the identified parameters, hydraulic pressure-polar displacement relation for the hydraulic bulge test.

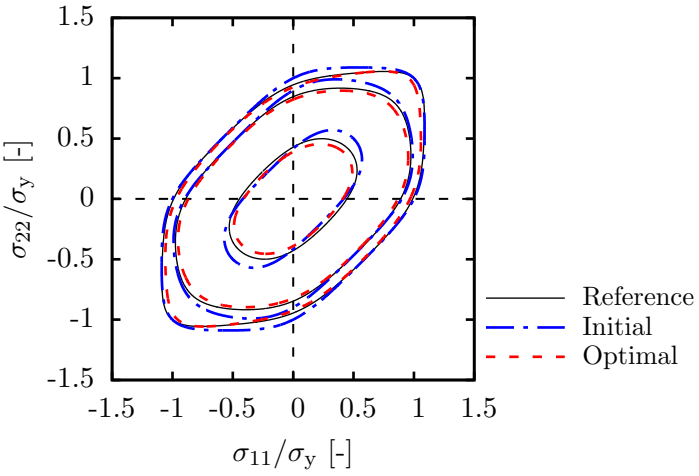

Figure 6.8: Virtual material - "Experimental" and numerically obtained, with the initial and identified parameters, normalized yield surfaces.

6.6 6022-T43 aluminium alloy - Hardening parameters' identification

The identification methodology presented before is now applied to the 6022-T43 aluminium alloy, which is employed in the numerical example of Section 7.9 related to the benchmark #3 of NUMISHEET'05 international conference. Here, the parameters related to the material's elasticity and anisotropy are known and assume the values provided by Stoughton *et al.* (2005), i.e., $E = 70.2$ [GPa] and $\nu = 0.363$ [-], while the anisotropy is described by the *Yld2004-18p* yield function considering the anisotropy parameters depicted in Table 6.3. Due to the lack of information in Stoughton *et al.* (2005) regarding the hardening parameters related to the kinematic hardening, the identification of the isotropic and nonlinear kinematic hardening parameters is presented here. Also, the experimental data for the in-plane uniaxial tensile and tension-compression/Bauschinger tests presented in Taherizadeh *et al.* (2011) are considered as reference data. It is assumed that the isotropic hardening follow the Voce's exponential law, while the kinematic hardening is described using only one back stress component.

Table 6.3: Al6022-T43's anisotropy parameters ($a = 8$) (Stoughton *et al.*, 2005).

c_{12}^1	c_{13}^1	c_{21}^1	c_{23}^1	c_{31}^1	c_{32}^1	c_{44}^1	c_{55}^1	c_{66}^1
0.9499	1.1099	1.0641	1.3281	1.1431	1.2537	1.2752	1.0025	1.0033
c_{12}^2	c_{13}^2	c_{21}^2	c_{23}^2	c_{31}^2	c_{32}^2	c_{44}^2	c_{55}^2	c_{66}^2
0.9170	0.8469	0.9086	0.6211	0.7359	0.7974	0.5219	0.9889	1.0134

The set of optimal identified hardening parameters is presented in Table 6.4. The experimental data and the numerical curves obtained with the identified parameters are depicted in Fig. 6.9. It can be seen an excellent representation of the experimental hardening evolu-

tion, including cyclic phenomena, namely the Bauschinger effect and the transient behaviour. Since only one back stress component is required to describe the behaviour of this material (with excellent accuracy) no additional identification procedures, including more than one back stress component, are carried out.

Table 6.4: 6022-T43 aluminium alloy - Identified hardening parameters.

Isotropic hardening			Kinematic hardening	
σ_{y_0} [MPa]	Q [MPa]	β [-]	c [MPa]	b [-]
129.26	208.73	7.705	1385.50	142.43

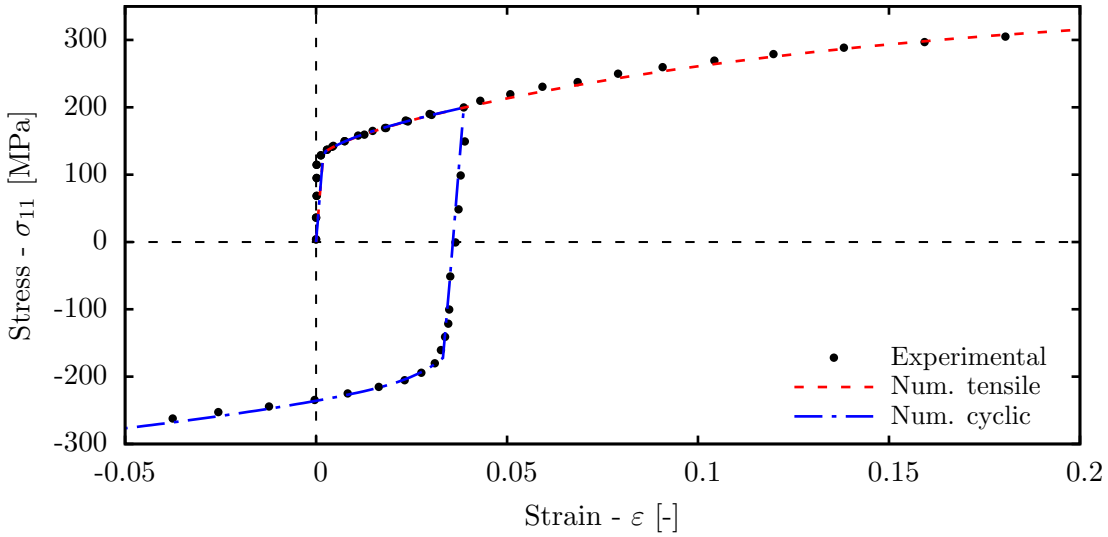

Figure 6.9: 6022-T43 aluminium alloy - Experimental and numerically obtained, with the identified parameters, stress-strain curves for uniaxial tensile and tension-compression / Bauschinger tests.

6.7 DP590 steel - Hardening parameters' identification

The hardening parameters of the DP590 steel to be considered in the numerical example of Section 7.8, related to a benchmark of the NUMISHEET'93 international conference, are here determined using the described identification procedure. The material is assumed to be isotropic (von Mises yield function) and its elasticity is described by $E = 190.0$ [GPa] and $\nu = 0.33$ [-] (Lee *et al.*, 2012b). The experimental data employed in the identification process consist of i) in-plane uniaxial tensile test, ii) in-plane monotonic shear test, and iii) in-plane Bauschinger shear tests with reverse loading at 3%, 8%, and 13% of pre-strain. Three different hardening models are considered, namely, 1) pure isotropic hardening following the Swift's power law, 2) pure nonlinear kinematic hardening using only one back stress component, and 3) pure nonlinear kinematic hardening using two back stress components. Due to the inability

of isotropic hardening laws to describe cyclic hardening phenomena, the parameters of Model 1 are identified using only stress-strain data related to monotonic tests, i.e., experimental data i) and ii).

The sets of optimal identified hardening parameters for the three hardening models are presented in Table 6.5, along with the corresponding objective function's values.

Table 6.5: DP590 steel - Identified hardening parameters.

Model 1 - Isotropic hardening					Obj. func. value	
K [MPa]	ε_0 [-]	n_{H} [-]			f_{obj}	(Rel.)
948.9	0.00356	0.153			8.38	(11.2%)
Model 2 - Kinematic hardening (1)						
σ_{y_0} [MPa]	c^1 [MPa]	b^1 [-]				
403.5	5142.2	24.7			142.52	(190.9%)
Model 3 - Kinematic hardening (2)						
σ_{y_0} [MPa]	c^1 [MPa]	b^1 [-]	c^2 [MPa]	b^2 [-]		
380.5	7066.3	71.7	1589.9	9.6	74.65	(100.0% - Ref.)

The experimental data, coming from Lee *et al.* (2012b), and the numerical curves obtained from the identified parameters for the three hardening models are depicted in Fig. 6.10. From this figure, an accurate reproduction of the experimental stress-strain curves is observed especially for Model 3. Comparatively to Model 2, the use of more than one back stress component in Model 3 enables a better reproduction of the Bauschinger effect and the transient behaviour after reverse loading, resulting in a significant reduction of the objective function's values (see Table 6.5). With Model 1 an excellent reproduction of the monotonic curves is obtained, hence a considerable small value of the objective function is achieved. However, this model does not take cyclic hardening phenomena into account, and therefore its overall reproduction of the experimental data for the five mechanical tests can be considered fairly poor.

6.8 5182-O aluminium alloy - Hardening and anisotropy parameters' identification

In order to perform the numerical example of Section 7.10 related to the benchmark #2 of NUMISHEET'14 international conference, the constitutive (hardening and anisotropy) parameters of the 5182-O aluminium alloy are determined using the described identification procedure. The experimental data used in the identification process, coming from Stoughton *et al.* (2013), consists of

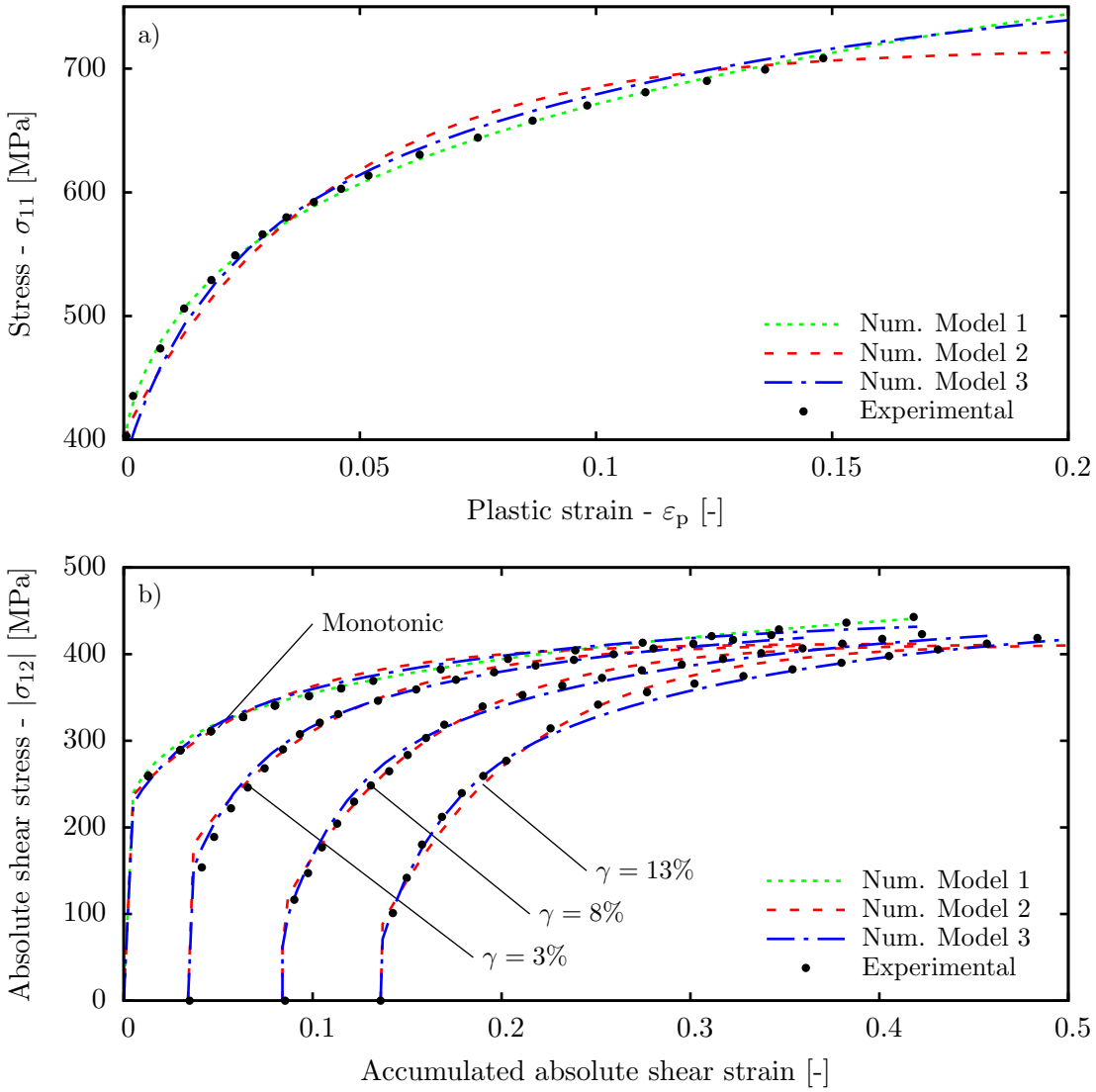

Figure 6.10: DP590 steel - Experimental data (Lee *et al.*, 2012b) and numerically obtained, with the identified parameters, stress-strain curves for a) uniaxial tensile test and b) monotonic and Bauschinger shear tests, considering three different hardening models.

i) stress-plastic strain relations for in-plane uniaxial tensile tests at every 15° from RD,

ii) directional r-values obtained from in-plane uniaxial tensile tests at every 15° from RD,

iii) biaxial stress-plastic thickness strain relation in the hydraulic bulge test,

iv) biaxial r_b-value obtained from the disk compression test, and

v) stress-plastic strain relation for in-plane uniaxial cyclic test in RD.

The *Yld2004-18p* yield function is used to model the anisotropy of the material, the hardening behaviour of which being described using a combined isotropic-nonlinear kinematic hardening law considering two back stress components. The nonlinear isotropic expansion of the yield surface is represented using a modified Voce's law, i.e., $\sigma_{y_0} - R(\bar{\varepsilon}_p) = \sigma_{y_0} + Q[1 - \exp(-\beta\bar{\varepsilon}_p)] +$

$K\bar{\varepsilon}_{\mathrm{p}}$. This hardening law represents a particular case of the H/V law, proposed by Sung *et al.* (2010), considering $\alpha = 1/2$ and $n_{\mathrm{H}} = 1$ (see Equation 3.76). As for the previous materials, the elastic parameters are not subjected to the identification process, therefore having those particular values provided by Stoughton *et al.* (2013), i.e., $E = 70.0$ [GPa] and $\nu = 0.333$ [-]. Additionally, the yield function's exponent a is assumed to be equal to 8 (FCC material). Moreover, due to the lack of information about the out-of-plane properties of the material, the corresponding anisotropy parameters take their isotropic value, i.e., $c_{55}^1 = c_{55}^2 = c_{66}^1 = c_{66}^2 = 1.0$.

The set of optimal identified constitutive parameters for the 5182-O aluminium alloy is presented in Table 6.6. The numerical results obtained with the optimal identified set of constitutive parameters and the experimental data, coming from Stoughton *et al.* (2013), are presented in Figs. 6.11-6.13. An accurate reproduction of the experimental data is observed regarding both material's hardening and anisotropy. The excellent description of the anisotropy can be seen particularly in the great reproduction of the directional and biaxial r-values (see Fig. 6.12). From Figs. 6.11 and 6.13 the good description of the hardening behaviour provided by the employed combined hardening law can by observed. In addition to the considered hardening model, the numerical results obtained with combined hardening with only one back stress component are also depicted in Fig. 6.13. The improvement of the experimental data's reproduction given by the use of two back stress components, comparatively to the use of only one, is remarkable, in particular concerning the transient behaviour of the material. The constitutive hardening parameters of this hardening model (combined with one back stress component) were obtained from a new identification process and read: $\sigma_{\mathrm{y}_0} = 83.8$ [MPa], $Q = 204.6$ [MPa], $\beta = 9.0$ [-], $K = 174.3$ [MPa], $c = 4937.4$ [MPa] and $b = 100.0$ [-].

Table 6.6: 5182-O aluminium alloy - Identified hardening parameters.

Isotropic hardening									
σ_{y_0} [MPa]	Q [MPa]	β [-]	K [MPa]						
40.2	164.5	12.4	173.3						
Kinematic hardening									
c^1 [MPa]	b^1 [-]	c^2 [MPa]	b^2 [-]						
20670.8	404.9	166.4	4.8						
Yld2004-18p anisotropy parameters ($a = 8$)									
c_{12}^1	c_{13}^1	c_{21}^1	c_{23}^1	c_{31}^1	c_{32}^1	c_{44}^1	c_{55}^1	c_{66}^1	
0.7300	0.9137	0.6485	1.1986	0.3905	0.9065	0.8019	1.0	1.0	
c_{12}^2	c_{13}^2	c_{21}^2	c_{23}^2	c_{31}^2	c_{32}^2	c_{44}^2	c_{55}^2	c_{66}^2	
1.0320	0.3568	1.0460	0.3539	1.0970	0.7676	1.0540	1.0	1.0	

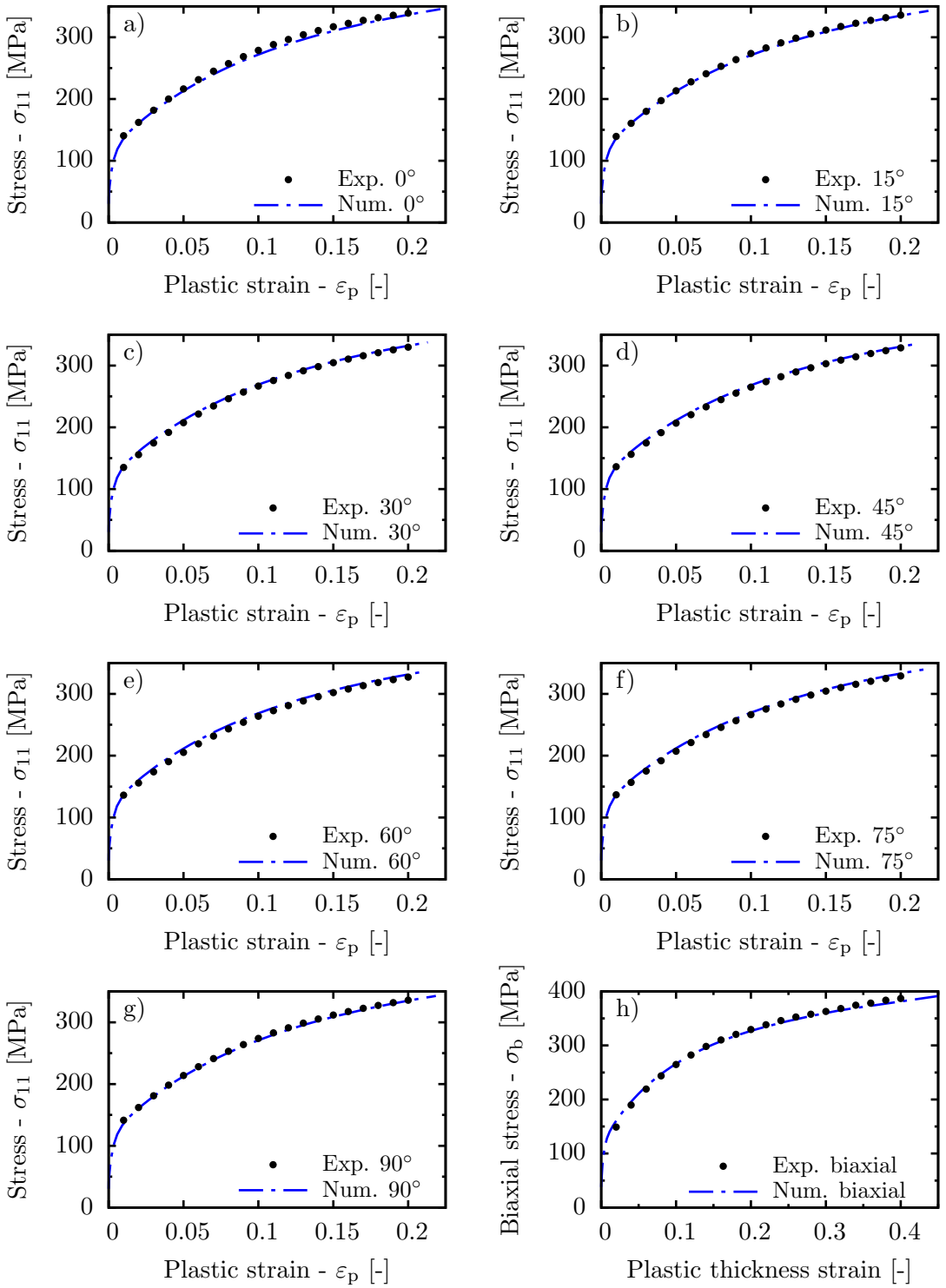

Figure 6.11: 5182-O aluminium alloy - Experimental data (Stoughton *et al.*, 2013) and numerically obtained, with the identified parameters, stress-strain curves for a)-g) uniaxial tensile tests at every 15° from RD and h) hydraulic bulge test.

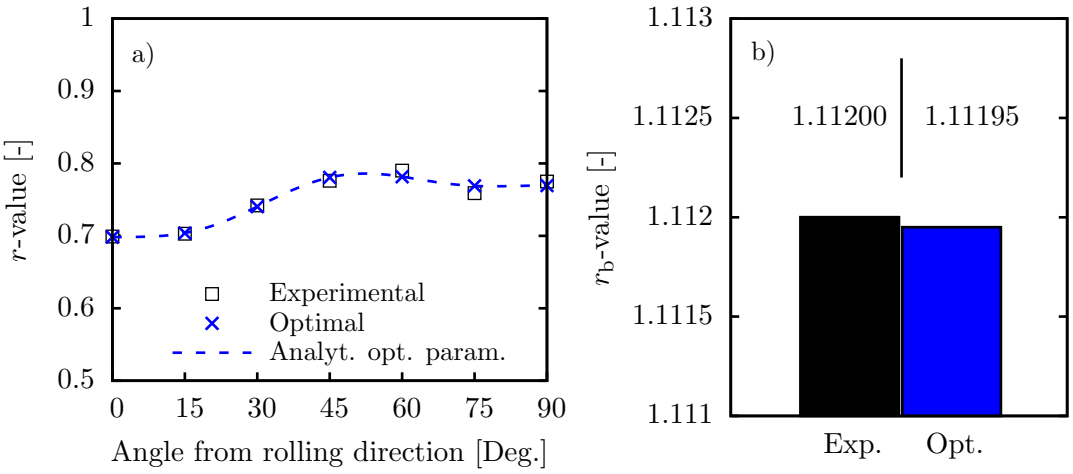

Figure 6.12: 5182-O aluminium alloy - Experimental (Stoughton *et al.*, 2013) and analytically obtained, with the identified parameters, a) directional r-values and b) biaxial r_b-values.

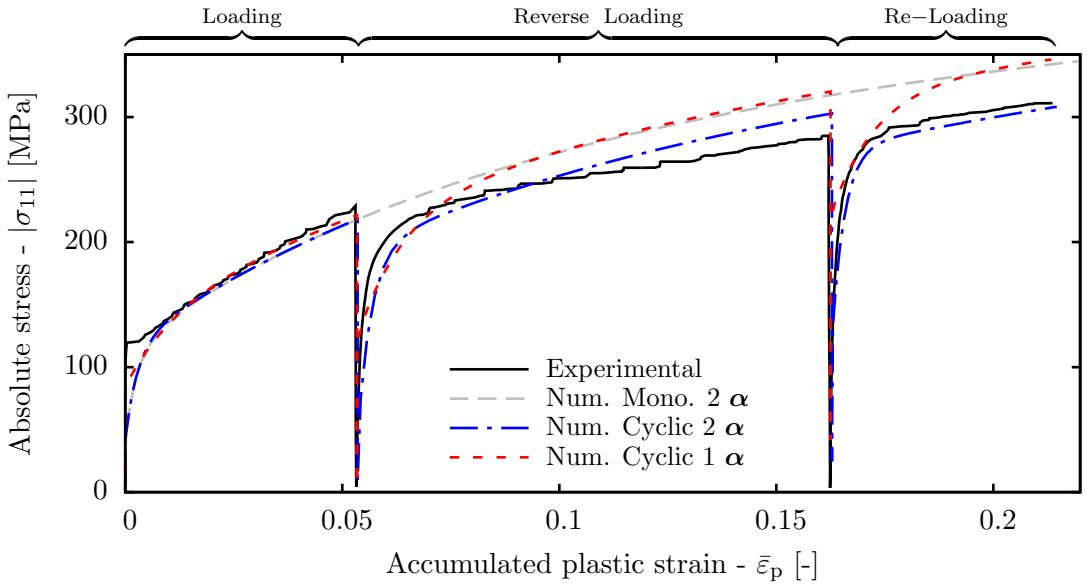

Figure 6.13: 5182-O aluminium alloy - Experimental data (Stoughton *et al.*, 2013) and numerically obtained, with the identified parameters, stress-strain curves for in-plane uniaxial cyclic test, considering one and two back stress components.

Chapter 7

Numerical results and discussion

The description of the anisotropic elastoplasticity provided by the finite strain constitutive models presented in Chapter 5, as well as the numerical performance of the algorithms presented in Sections 4.3 and 5.3.9, are assessed in this section by means of numerical simulations. To this purpose, the considered constitutive models have been implemented with the presented algorithms into the commercial Finite Element code ABAQUS/Standard, via material user subroutines, UMATs, which have been developed in Fortran.

In this section, the numerically obtained results related to the hypoelastic- and hyperelastic-based models are referred to as "Hypoelastic" and "Hyperelastic", respectively, followed by a suffix that characterizes the algorithm and/or the methodology to define the corotational coordinate frame. This way, regarding the hypoelastic-based formulation, the following suffixes are considered,

i) BE1 - Standard backward-Euler algorithm,

ii) BE - Backward-Euler algorithm with the multi-stage return mapping procedure,

iii) FE1 - Standard forward-Euler algorithm,

iv) FE - Forward-Euler algorithm with the sub-incrementation technique,

v) ZJ - Zaremba-Jaumann objective rate, and

vi) GMN - Green-McInnis-Naghdi objective rate.

Also, the suffixes considered for the hyperelastic-based formulation are $\mathbf{R}$ and $\mathbf{R}^{\mathrm{ZJ}}$, whether the rotation tensor between the global and the material corotational coordinates frames is obtained from the polar decomposition of $\mathbf{F}$ or from the spin tensor, $\mathbf{w}$, respectively.

This section is organized as follows. Firstly, the correctness of the UMATs' implementation is assessed by means of the comparison of numerically obtained Lankford r-values and obtained results for the tensile test at finite strains with analytical data (Section 7.1 and 7.2). Secondly, some fundamental limitations of the hypoelastic- and hyperelastic-based formulations are analysed considering the numerical simulation of the shear test at finite strains (Section 7.3). Thirdly, the accuracy and stability of the integration algorithms related to the

hypoelastic-based model are compared by means of the so-called iso-error maps (Section 7.4). Fourthly, the performance of the considered constitutive models and numerical algorithms is assessed in industry-relevant benchmarks of sheet metal forming (Sections 7.5-7.10). Finally, the hypoelastic- and hyperelastic-based formulations are compared using the numerical simulation of the thermoforming of a polymeric sheet, where finite elastic strains occur (Section 7.11).

7.1 Numerical prediction of Lankford r-values

The correct numerical implementation of the anisotropic yield functions into the material user subroutine, UMAT, can be confirmed by computing the Lankford r-values numerically. In addition to the anisotropic yield function, this numerical test also assesses the implementation of its derivatives, as well as the accuracy of the integration procedure. This two-step numerical procedure consists of a 1x1x0.1 mm single element, which is elongated up to 5% and subsequently unloaded to eliminate the effects of elasticity. This procedure is schematically represented in Fig. 7.1 and is carried out for every 15° from the rolling direction. For each orientation the respective r_θ value is determined according to $r_\theta = \varepsilon_{22}/\varepsilon_{33}$.

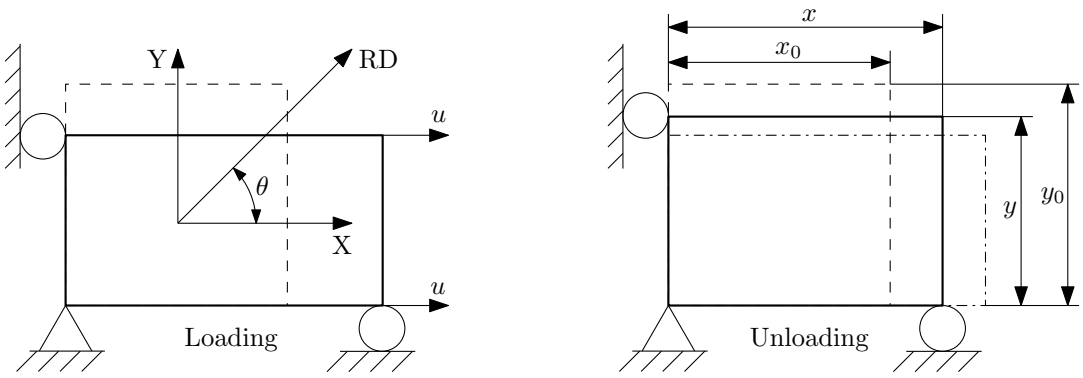

Figure 7.1: r-values prediction - Scheme of the procedure followed.

The numerical simulations are carried out for a 2090-T3 aluminium alloy. Its mechanical behaviour is described by the following parameters: $E = 70$ [GPa]; $\nu = 0.30$ [-]; isotropic hardening following Swift's law as $\sigma_{y_0} - R(\bar{\varepsilon}_p) = 646.0(0.025+\bar{\varepsilon}_p)^{0.227}$ [MPa]; and no kinematic hardening, i.e., $c = 0.0$ [MPa] and $b = 10^{-8} \approx 0$ [-] (Yoon *et al.*, 2006).

Here, the assessment of the implementation of the *Yld91* and *Yld2004-18p* yield criteria is presented. Since *Yld91* employs the concept of linear transformations to introduce anisotropy character into an isotropic yield function, its incorporation into the hyperelastic-based model is carried out similarly to *Yld2004-18p* (see Section 5.3.6). The assessment of the implementation of these yield criteria is of interest in this section because they are employed in the numerical examples that follow. This way, the anisotropy of the 2090-T3 aluminium alloy is described by the *Yld91* and *Yld2004-18p* anisotropy parameters listed in Table 7.1 (Yoon *et al.*, 2000, Barlat *et al.*, 2005).

Table 7.1: Al2090-T3's anisotropy parameters ($a = 8$) (Yoon *et al.*, 2000, Barlat *et al.*, 2005).

Yld91								
c_1	c_2	c_3	c_4	c_5	c_6			
1.0674	0.8559	1.1296	1.2970	1.0000	1.0000			
Yld2004-18p								
c^1_{12}	c^1_{13}	c^1_{21}	c^1_{23}	c^1_{31}	c^1_{32}	c^1_{44}	c^1_{55}	c^1_{66}
−0.0698	0.9364	0.0791	1.0030	0.5247	1.3631	0.9543	1.0690	1.0237
c^2_{12}	c^2_{13}	c^2_{21}	c^2_{23}	c^2_{31}	c^2_{32}	c^2_{44}	c^2_{55}	c^2_{66}
0.9811	0.4767	0.5753	0.8668	1.1450	−0.0792	1.4046	1.1471	1.0516

The UMATs related to the hyperelastic-based model employing $\mathbf{R}^{\mathrm{ZJ}}$ (obtained from the spin tensor $\mathbf{w}$) and $\mathbf{R}$ (obtained from the polar decomposition of $\mathbf{F}$), as well as the UMATs related to the hypoelastic-based model using the Zaremba-Jaumann and the Green-McInnis-Naghdi rates considering the forward-Euler and backward-Euler algorithms, are assessed in this numerical example. The numerically predicted r-values are presented in Figs. 7.2a and 7.3a for *Yld91* and *Yld2004-18p*, respectively, along with the analytical values, computed according to a procedure shown in Appendix D, and the experimental data comes from Yoon *et al.* (2000). In addition to the r-values, the normalized yield stresses are also computed, providing the results presented in Figs. 7.2b and 7.3b. The plots present an excellent agree-

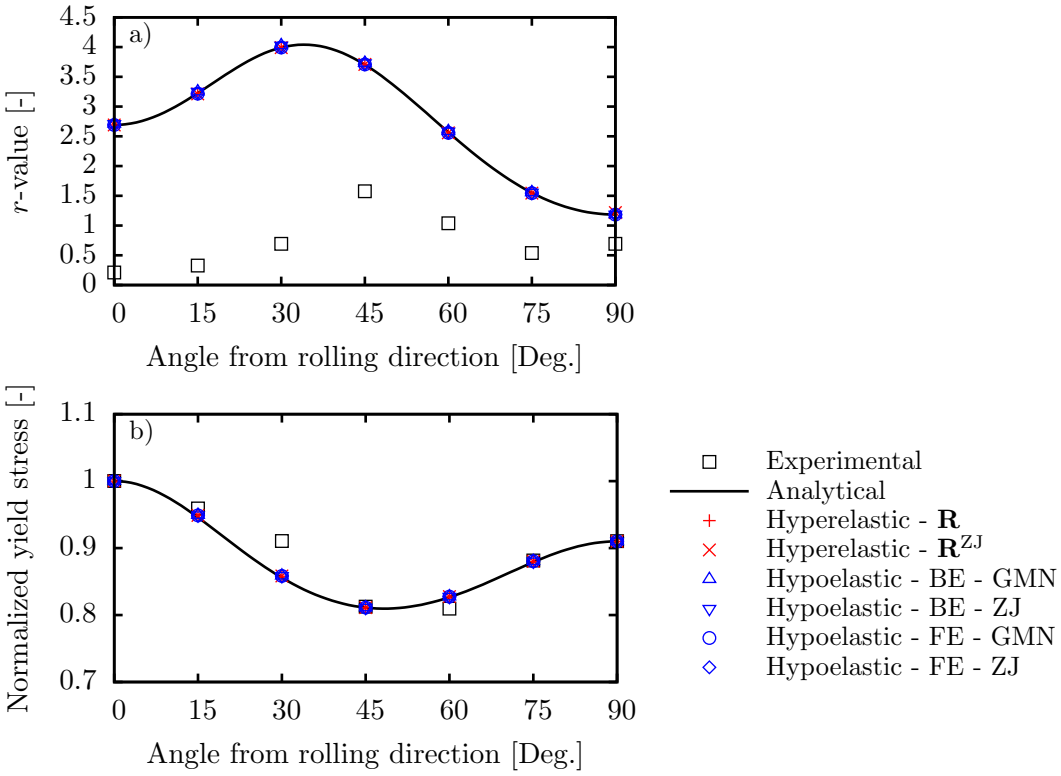

Figure 7.2: r-values prediction - Numerically, analytically, and experimentally (Yoon *et al.*, 2000) obtained a) r-values and b) normalized yield stresses, considering *Yld91* criterion.

ment between the obtained results and the analytical curves, hence confirming the correct implementation of the yield functions. It is visible the excellent description of the anisotropy for this material when the *Yld2004-18p* criterion is considered, comparatively to the *Yld91* criterion. Such description is possible due to the considerable flexibility of this yield function related to the high number of anisotropy parameters.

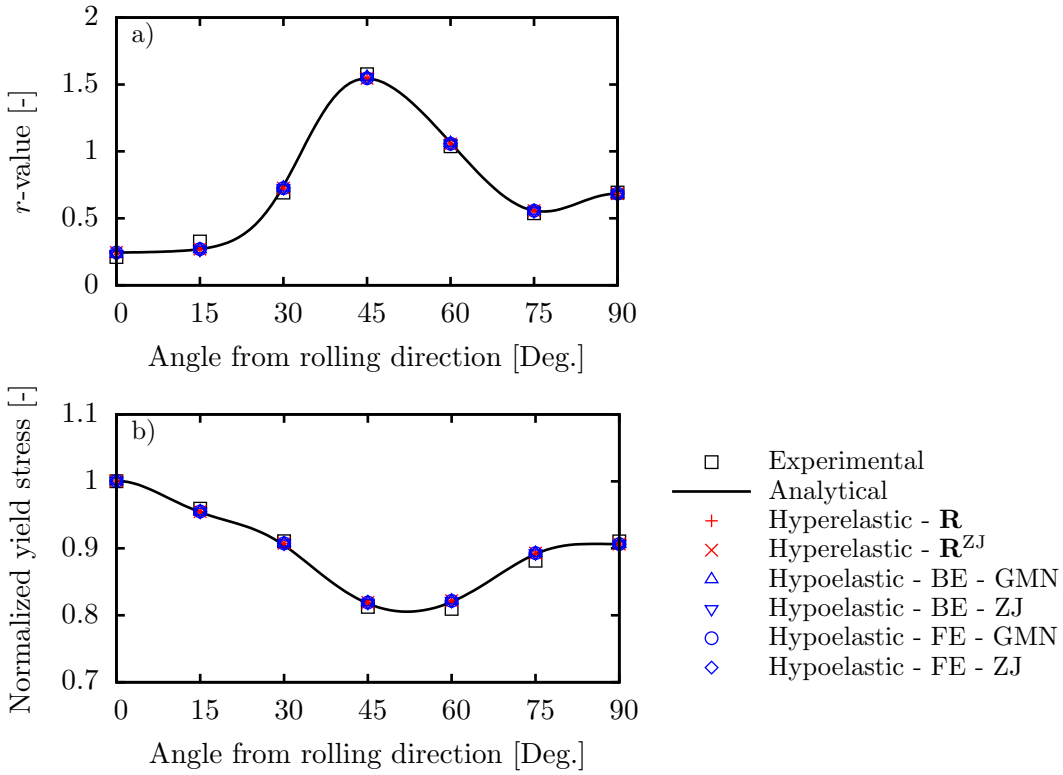

Figure 7.3: r-values prediction - Numerically, analytically, and experimentally (Yoon *et al.*, 2000) obtained a) r-values and b) normalized yield stresses, considering *Yld2004-18p* criterion.

7.2 Tensile test at finite strains

Here, the numerical simulation of the uniaxial tensile test, employing a single element, is used to validate the description of the anisotropy at finite strains and the implementation of the kinematic hardening law.

Anisotropy at finite strains Firstly, the plastic yielding of the material is assumed to be anisotropic, while isotropic hardening is adopted. To confirm the assumption that the anisotropic yielding is described with accuracy in the finite strain regime, the uniaxial tensile test is performed up to 300% of accumulated plastic strain, along 0° and 90° from the rolling direction. It is worth mentioning that the materials analysed in this work would not undergo such large deformations experimentally, since failure would occur before reaching

the imposed 300% of accumulated plastic strain. Nevertheless, such large deformations are taken into account in these simulations to assess the performance of the proposed material constitutive models in extreme conditions. The numerical simulations are carried out for a 2090-T3 aluminium alloy, whose material parameters are indicated in Section 7.1. Here, for the sake of particularization the anisotropy of the material is described by the *Yld2004-18p* function.

The obtained results for the hyperelastic-based model employing $\mathbf{R}^{\mathrm{ZJ}}$ and $\mathbf{R}$, as well as the ones related to the hypoelastic-based model using the Zaremba-Jaumann and the Green-McInnis-Naghdi rates and considering the forward-Euler and backward-Euler algorithms are compared to the analytical stress-accumulated plastic strain curves in Fig. 7.4. The analytical curves are obtained considering that the relation $[\sigma_{\mathrm{y}_\theta}(\bar{\varepsilon}_{\mathrm{p}_0})]/[\sigma_{\mathrm{y}}(\bar{\varepsilon}_{\mathrm{p}_0})] = [\sigma_{\mathrm{y}_\theta}(\bar{\varepsilon}_{\mathrm{p}})]/[\sigma_{\mathrm{y}}(\bar{\varepsilon}_{\mathrm{p}})]$ holds during the deformation process, since it is assumed that the anisotropy does not evolve with the plastic deformation. The excellent agreement between the obtained results and the analytical curves proves the correct description of the yielding anisotropy in the large plastic strain regime, regardless the elasticity law, the choice of the rotation tensor that transforms quantities from the locally rotating configuration to the spatial configuration, or the algorithms used to implement the hypoelastic-based model.

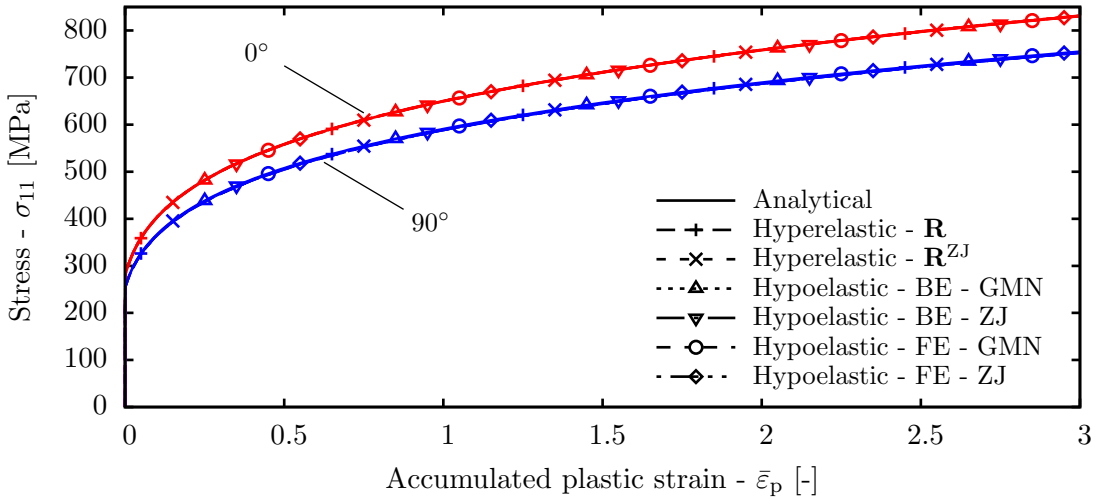

Figure 7.4: Uniaxial tensile test - Stress-accumulated plastic strain relationships for the Al2090-T3 along RD (red) and TD (blue).

Uniaxial tension/compression Secondly, in order to verify the implementation of the combined isotropic-nonlinear kinematic hardening law, one cycle of uniaxial tension/compression with inversion of loading direction at 25% of total strain is simulated. This time, the hardening parameters of the material used in the simulations are those identified for the 5182-O aluminium alloy in Section 6.8. Hence, nonlinear isotropic hardening and nonlinear kinematic hardening considering two back stress components are now taken into account. Isotropic yielding (von Mises yield criterion) is assumed. This way, the analytical

integration of the kinematic hardening law provides the following back stress-accumulated plastic strain response for each back stress component (see e.g., Chaboche (2008)),

$$\alpha^j_{\mathrm{xx}} = v\frac{3c^j}{2b^j} + \left(\alpha^j_0 - v\frac{3c^j}{2b^j}\right)\exp[-vb^j(\bar{\varepsilon}_{\mathrm{p}} - \bar{\varepsilon}_{\mathrm{p}_0})], \tag{7.1}$$

where $v = \pm 1$ defines the flow direction and $\bar{\varepsilon}_{\mathrm{p}_0}$ and α^j_0 are the values of the accumulated plastic strain and back stress at the beginning of the loading branch considered. Taking into account that for a uniaxial loading the von Mises criterion is reduced to $v(\sigma_{\mathrm{xx}} - \sum_{j=1}^{N}\alpha^j_{\mathrm{xx}}) - [\sigma_{\mathrm{y}_0} - R(\bar{\varepsilon}_{\mathrm{p}})] = 0$, the relation of stress-accumulated plastic strain in uniaxial conditions is given by

$$\sigma_{\mathrm{xx}} = v(\sigma_{\mathrm{y}_0} - R(\bar{\varepsilon}_{\mathrm{p}})) + \sum_{j=1}^{N}\left\{v\frac{3c^j}{2b^j} + \left(\alpha^j_0 - v\frac{3c^j}{2b^j}\right)\exp[-vb^j(\bar{\varepsilon}_{\mathrm{p}} - \bar{\varepsilon}_{\mathrm{p}_0})]\right\}. \tag{7.2}$$

Regarding the hyperelastic-based elastoplastic model, due to the plastic isotropy of the material, the specific choice of the rotation tensor (Equation 5.32) used to determine the corotational coordinate system in the current configuration (in which the yield function is evaluated) is irrelevant, as the obtained results are independent of that choice. From Fig. 7.5 it can be seen the excellent agreement between the obtained results and the analytical curves for one cycle of tension/compression, confirming the correct implementation of the combined hardening law in the large plastic strain regime. The analytical curve related to monotonic loading is additionally presented for a better visualisation of the Bauschinger and transient phenomena.

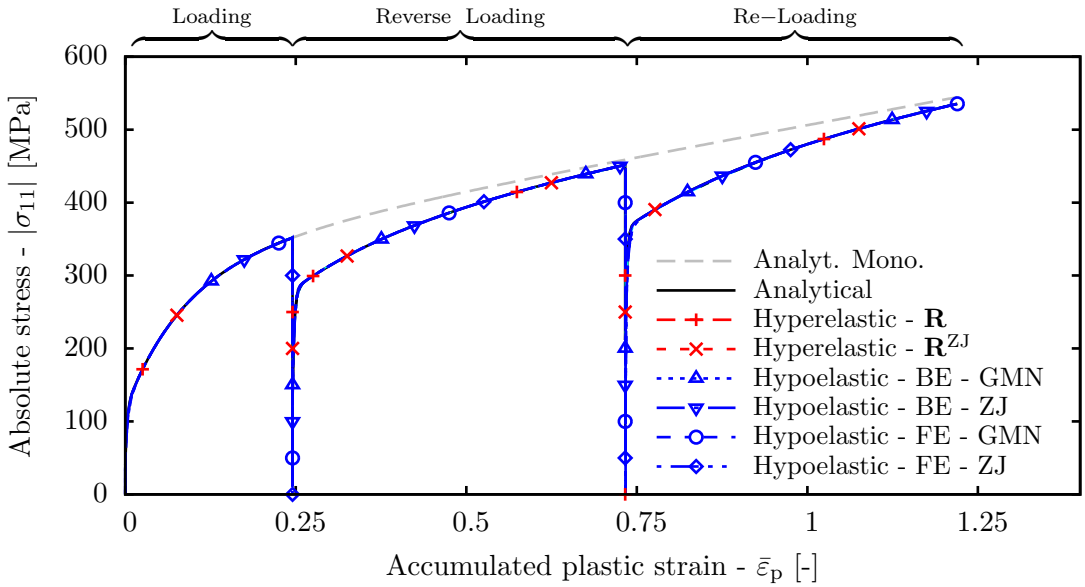

Figure 7.5: Uniaxial tensile test - Absolute stress-accumulated plastic strain relationships during one cycle of tension/compression considering combined hardening with two back stress components.

7.3 Shear test at finite strains

Some limitations subjacent to the hypoelastic- and hyperelastic-based models presented in Section 5 are now pointed out and analysed by investigating the monotonic simple shear test, characterized by the deformation gradient $\mathbf{F} = \mathbf{I} + \gamma \boldsymbol{e}_1 \otimes \boldsymbol{e}_2$, where γ is the shear strain. The accurate prediction of the shear stress in this fundamental mode of deformation represents a challenging task due to the complexity induced by the rotation of the principal directions of $\mathbf{F}$. Most of the results presented in this section are well-known in the literature and have lead to several research works on this topic, such as the works cited below (and references therein). They are presented here to compare the two approaches employed and sustain the results' discussion of the following sections.

Shear test at finite elastic strains The elastic response of the two approaches are assessed for a generic polymeric material, elastic properties of which are assumed to be $E = 7$ [MPa] and $\nu = 0.4$ [-]. The numerical results are depicted in Fig. 7.6. The previously mentioned shear stress oscillations in hypoelasticity using the Zaremba-Jaumann rate is clearly seen in this figure. This spurious phenomenon motivated the development of several objective rates such as the Green-McInnis-Naghdi rate, which fails to predict a linear behaviour at finite strains. Comparison of the most used objective rates in hypoelastic simple shear conditions can be found in, e.g., Liu and Hong (1999).

Regardless the abnormal behaviour predicted by the hypoelastic models, they succeed to describe the linear response of the hyperelastic model for elastic shear strains up to 50%. The high elastic stiffness of metallic materials precludes the occurrence of such amount of elastic strains during sheet metal forming processes and hence allows the use of hypoelastic-based models in the numerical simulation of industry-relevant processes.

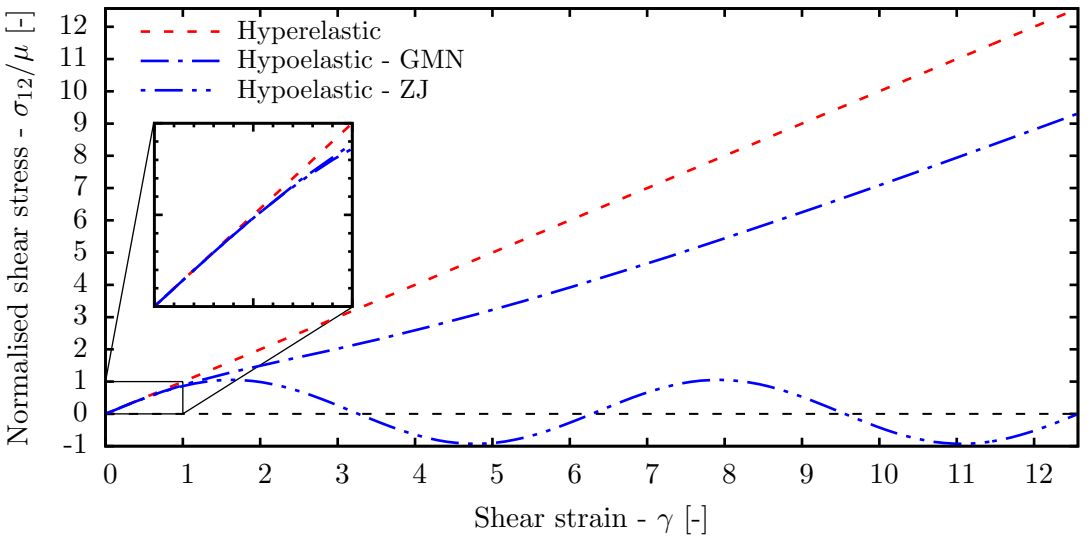

Figure 7.6: Simple shear test - Hypoelastic vs. hyperelastic response.

Shear test at finite strains with kinematic hardening A different phenomenon of oscillating shear stresses is related to the kinematic hardening. In order to solely assess the influence of the kinematic hardening, the material considered in this example is a generic aluminium alloy, $E = 70$ [GPa] and $\nu = 0.33$, with isotropic (von Mises) yielding and no isotropic hardening, $\sigma_{y_0} = 100$ [MPa] (thus small elastic strains). Regarding the kinematic hardening, two situations are considered, namely a) "linear", $b = 10^{-8} \approx 0$ [-], and b) nonlinear, $b = 2.0$ [-], cases. In both situations the kinematic "stiffness" is assumed to be equal to $c = 1000.0$ [MPa].

The obtained numerical results (see Fig. 7.7) are in agreement with the literature. On the one hand, considering "linear" kinematic hardening the hyperelastic-based model predicts, similarly to the results of Dettmer and Reese (2004), a monotonously crescent curve resembling the ones of the saturation-type. The hypoelastic-based models using the Zaremba-Jaumann and the Green-McInnis-Naghdi rates predict oscillatory and nonlinear monotonously crescent responses, respectively, as seen in the work of Svendsen *et al.* (1998). Regardless the nonlinear responses at finite strains, the hypoelastic-based models predict a linear behaviour for shear strains up to 75%, whereas the linearity of the shear stress-

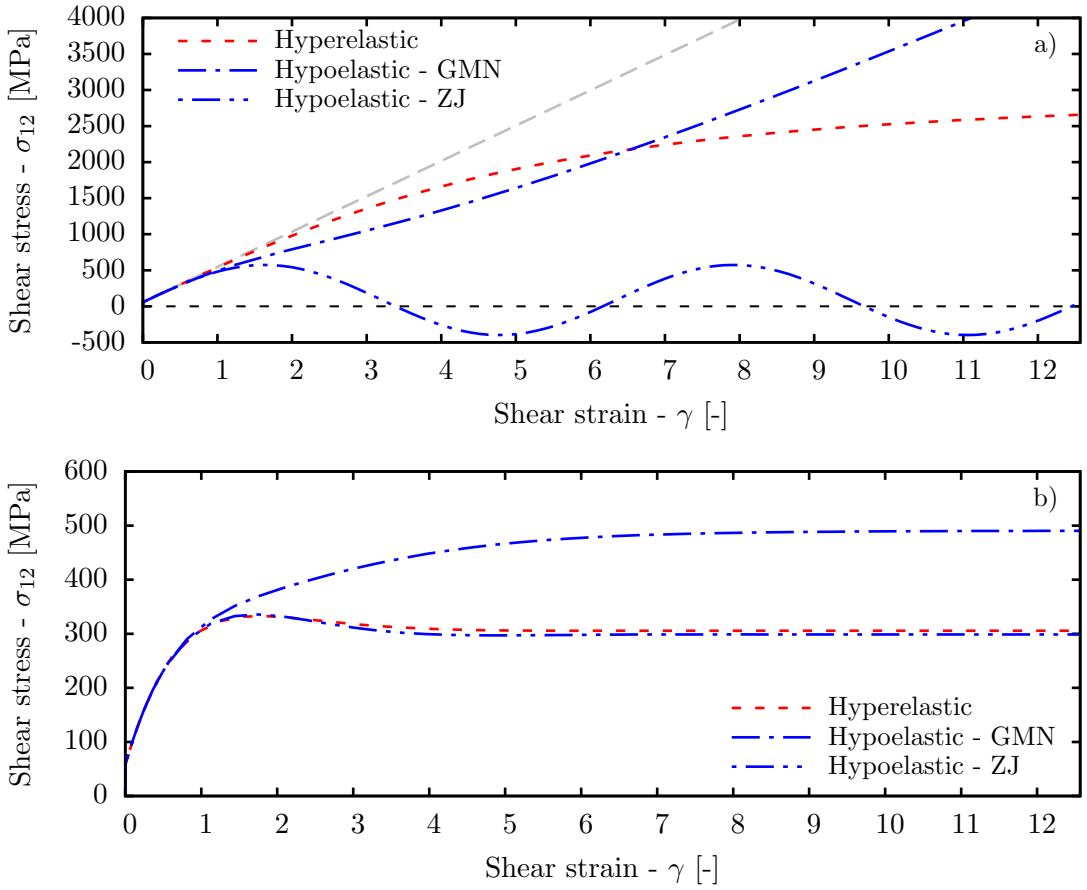

Figure 7.7: Simple shear test - Hypoelastic-based vs. hyperelastic-based plasticity response with a) "linear" and b) nonlinear kinematic hardening.

shear strain curve is maintained until 150% of shear strain for the hyperelastic-based model. On the other hand, considering nonlinear kinematic hardening, only the hypoelastic-based model using the Green-McInnis-Naghdi rate predicts a monotonously crescent response of the saturation-type. Interestingly, the hypoelastic-based model using the Zaremba-Jaumann rate and the hyperelastic-based model provide similar results, namely they exhibit softening followed by stress stagnation. Such abnormal behaviour in hyperelastic-based models was also predicted in the work of, e.g., Dettmer and Reese (2004). It is worth to mention, as pointed out by Dettmer and Reese (2004), that finite strain models predict considerably high normal stresses in simple shear conditions. These stress components clearly affect the material's behaviour, resulting in complex abnormal shear stress-shear strain responses.

Shear test at finite strains with plastic anisotropy Finally, oscillating shear stresses can also be predicted in anisotropic plasticity due to the rigid body rotation to which the material is subjected. In order to solely assess the influence of the plastic anisotropy, the material considered in this example is a generic aluminium alloy, $E = 70$ [GPa] and $\nu = 0.33$ [-], with no isotropic hardening, $\sigma_{y_0} = 100$ [MPa], and no kinematic hardening, $c = 0$ [MPa] and $b = 10^{-8} \approx 0$ [-] (thus small elastic strains). It is assumed that this fictitious material possesses the same anisotropic behaviour as the 2090-T3 aluminium alloy, i.e., the anisotropy is described by the *Yld2004-18p* criterion considering the parameters presented in Table 7.1.

The obtained results, presented in Fig. 7.8a, have an oscillatory character dependent on the rotation tensor employed to determine the corotational coordinate system in the current configuration. On the one hand, the hypoelastic-based model using the Zaremba-Jaumann rate and the hyperelastic-based model employing $\mathbf{R}^{\mathrm{ZJ}}$ (obtained from the spin tensor $\mathbf{w}$) reflect the orthotropic symmetry of the material in, almost identical, periodical stress responses. This periodicity is due to the linearly increasing rotation governed by $\mathbf{R}^{\mathrm{ZJ}}$ (see Fig. 7.8b). This periodical oscillatory behaviour is in agreement with the response obtained by multiplicative hyperelastic-based models that define the anisotropy in the intermediate configuration and have motivated several works on the elimination of these oscillations (Dafalias, 1985, Aravas, 1992, Cleja-Ţigoiu, 2000, Itskov and Aksel, 2004, Johansson, 2008). Considering that shear stress oscillations occur when the plastic spin is neglected, Cleja-Ţigoiu (2000) and Itskov and Aksel (2004), among others, established a proper constitutive relation for the plastic spin which is introduced in the evolution equations. A different approach was employed by Johansson (2008), that consists of considering evolving anisotropy of the affine saturation type to suppress stress oscillations.

On the other hand, the angle associated to the rotation tensor $\mathbf{R}$, obtained from the polar decomposition of $\mathbf{F}$, converges asymptotically to 90° (see Fig. 7.8b). Thus, the shear stress responses provided by the hypoelastic-based model using the Green-McInnis-Naghdi rate and the hyperelastic-based model employing $\mathbf{R}$ converge to the value relative to 90° after an initial oscillation (associated to the rotation from 0° to 90°) (see Fig. 7.8a). Once more, considering this rotation tensor, the hypoelastic-based and hyperelastic-based models

provide very similar results.

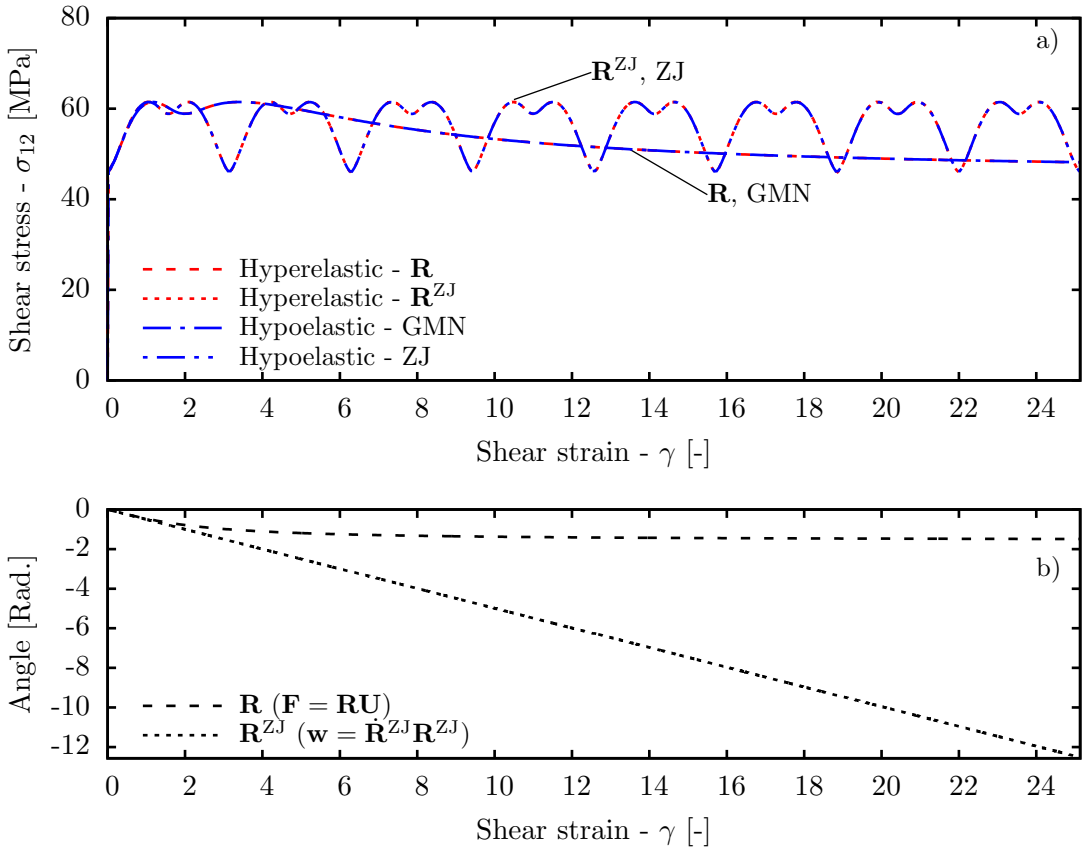

Figure 7.8: Simple shear test - Anisotropic plasticity, a) hypoelastic-based vs. hyperelastic-based shear stress-shear strain response and b) angle of rotation from the polar decomposition of $\mathbf{F}$ and associated to the spin tensor, $\mathbf{w}$.

7.4 Iso-error maps

The so-called iso-error maps are widely used in the literature as a tool to assess the accuracy and stability of integration algorithms, in particular when a large time discretization is considered (Ortiz and Simo, 1986, Yoon *et al.*, 1999, Artioli *et al.*, 2007). The construction of these iso-error maps consists of considering a point on the initial yield surface from which a sequence of strain increments is applied. Then, for each strain increment, the numerical algorithm is used to compute a corresponding approximated stress tensor, $\boldsymbol{\sigma}^{\text{num}}$, which is compared to the exact stress tensor, $\boldsymbol{\sigma}^{\text{exact}}$. The iso-error maps are usually drawn based on the percentage of the relative root mean square errors, i.e.,

$$ERR = \frac{\| \boldsymbol{\sigma}^{\text{num}} - \boldsymbol{\sigma}^{\text{exact}} \|}{\| \boldsymbol{\sigma}^{\text{exact}} \|} \times 100 \ \ [\%]. \tag{7.3}$$

Here, iso-error maps are used to compare the performance of the developed and implemented

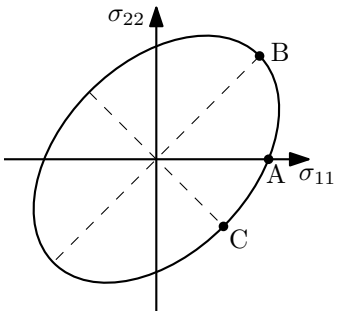

Figure 7.9: Iso-error maps - Points considered in the plane stress yield surface.

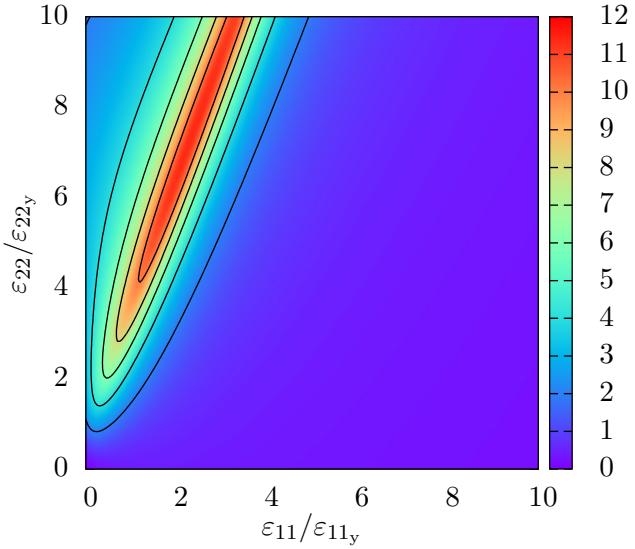

(a) BE - $ERR_{\max} = 11.385\%$ (contours of 2%).

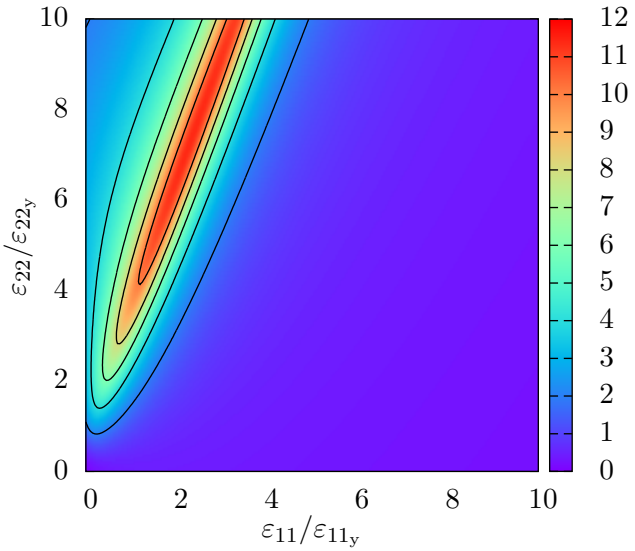

(b) BE1 - $ERR_{\max} = 11.385\%$ (contours of 2%).

Figure 7.10: Iso-error maps - Point A (uniaxial).

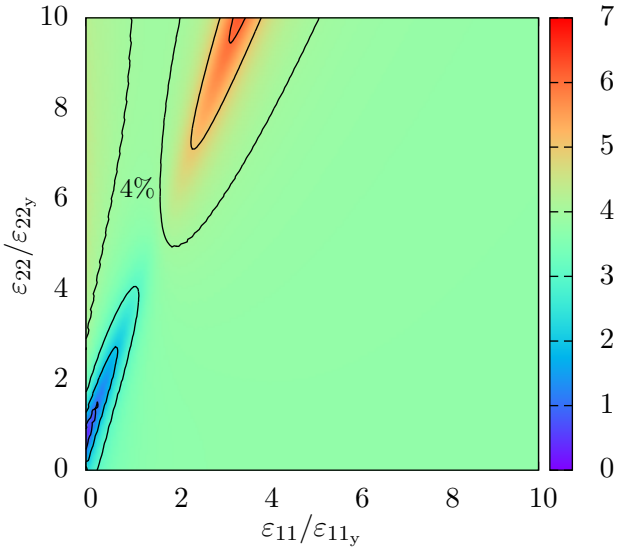

(c) FE - $ERR_{\max} = 6.196\%$ (contours of 1%).

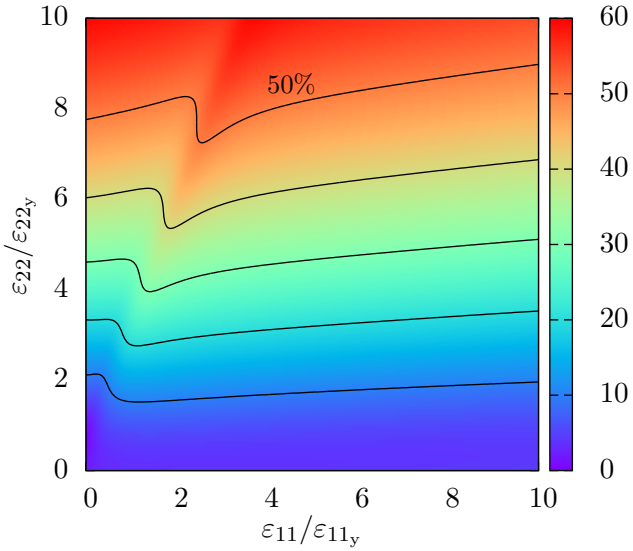

(d) FE1 - $ERR_{\max} = 59.501\%$ (contours of 10%).

Figure 7.10: Iso-error maps - Point A (uniaxial) (cont.).

algorithms for the hypoelastic-based model at three different stress points, namely: A) uniaxial, B) biaxial, and C) pure shear, as depicted in Fig. 7.9. Due to the lack of an analytical solution, the exact stress is obtained numerically considering 1000 sub-increments of strain and using the backward-Euler algorithm with the multi-stage return mapping procedure (BE). Both combined hardening and yield anisotropy are taken into account in this example by employing the 6022-T43 aluminium allow, constitutive parameters of which are presented in Section 6.6. The analysis is carried out for the forward-Euler algorithm with and without the sub-incrementation technique (FE and FE1, respectively) and for the backward-Euler algorithm with and without the multi-stage return mapping procedure (BE and BE1, respec-

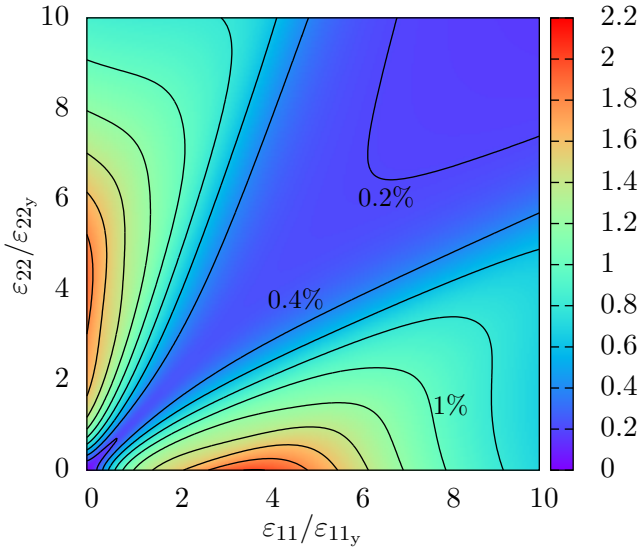

(a) BE - $ERR_{\max} = 2.012\%$ (contours of 0.2%).

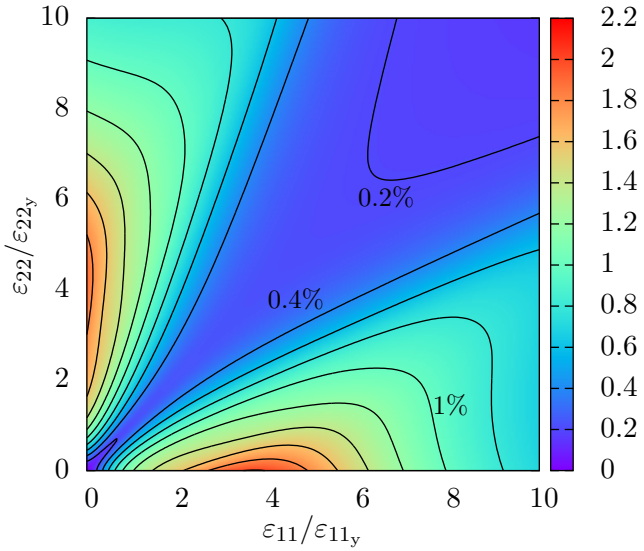

(b) BE1 - $ERR_{\max} = 2.012\%$ (contours of 0.2%).

Figure 7.11: Iso-error maps - Point B (biaxial).

tively).

The obtained results are presented in Figs. 7.10-7.12. Regarding the backward-Euler algorithm, the multi-stage return mapping procedure does not affect the accuracy of the algorithm, since for all three cases BE and BE1 provided the same results. On the contrary, the use of the sub-incrementation technique in the forward-Euler algorithm significantly improves the accuracy of the algorithm. In all three cases the standard forward-Euler algorithm (FE1) provides the worse accuracy and its error reaches considerable high values (above 50%) for moderate strain increments. From the obtained results it can be seen that, generally, the backward-Euler algorithms (BE and BE1) are more accurate than the forward-Euler ones

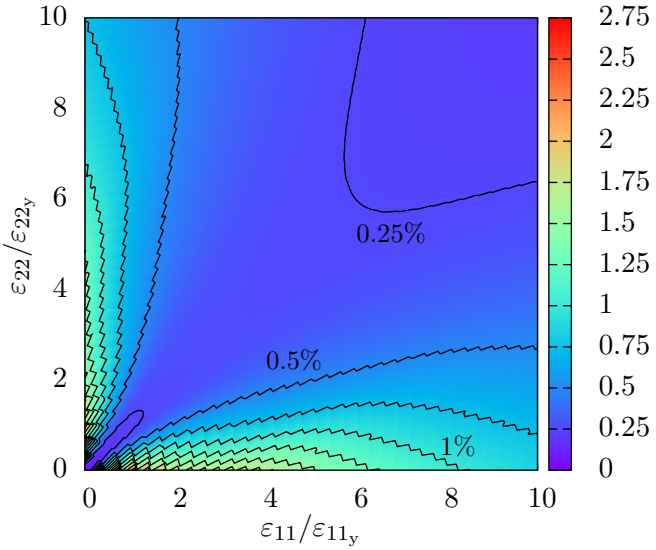

(c) FE - $ERR_{\max} = 2.571\%$ (contours of 0.25%).

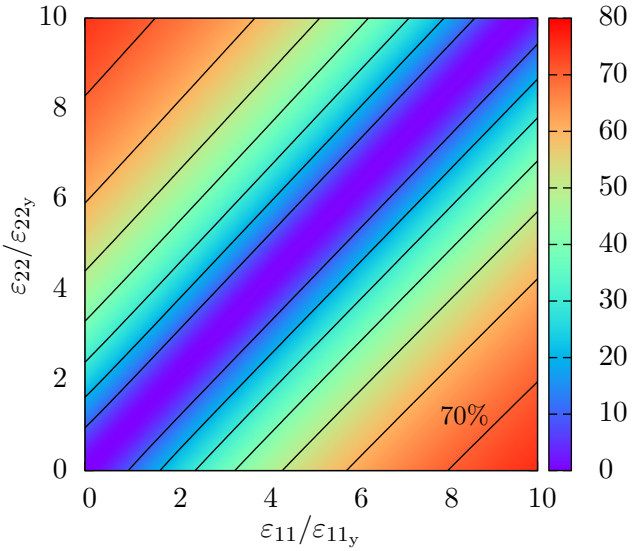

(d) FE1 - $ERR_{\max} = 75.506\%$ (contours of 10%).

Figure 7.11: Iso-error maps - Point B (biaxial) (cont.).

(FE and FE1), as expected. The shape of the iso-error maps of the FE algorithm is similar to the ones of BE and BE1 and it is worth noting that, surprisingly, FE is more accurate than BE and BE1 in some situations. For case A, even though the general accuracy of FE is poorer comparatively to BE and BE1, its maximum error is smaller than the maximum error obtained with BE and BE1. In opposite, for case B, FE is generally more accurate than BE and BE1, but reaches a higher maximum value. The good accuracy of FE is related to the high number of sub-increments considered by the sub-incrementation technique, which consists of performing several return mappings with small increments of strain instead of only one return mapping.

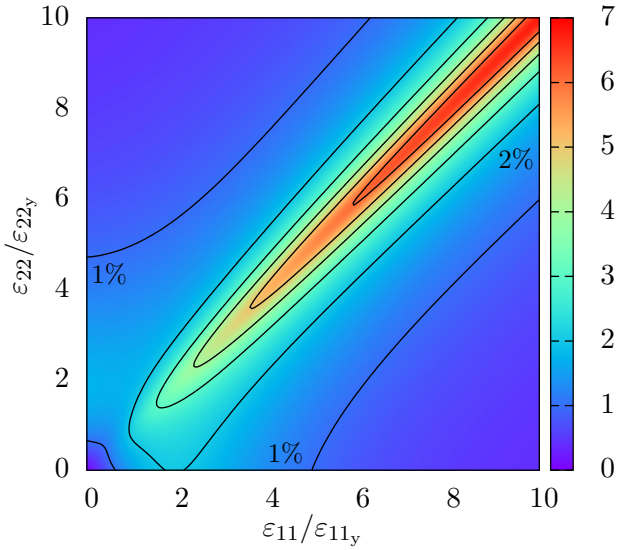

(a) BE - $ERR_{\max} = 6.754\%$ (contours of 1%).

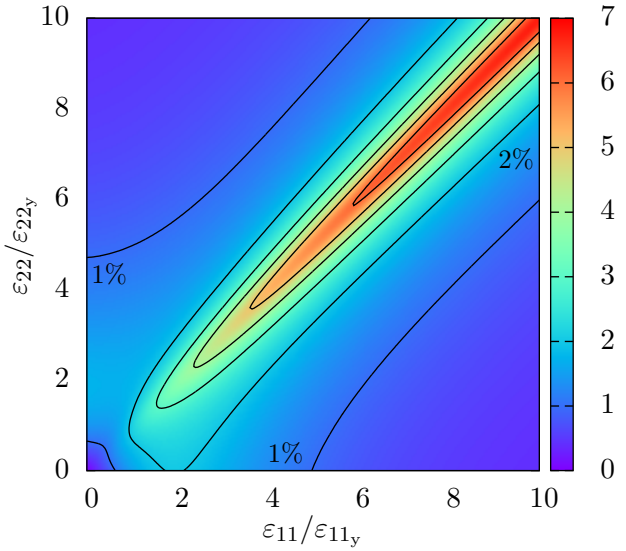

(b) BE1 - $ERR_{\max} = 6.754\%$ (contours of 1%).

Figure 7.12: Iso-error maps - Point C (pure shear).

7.5 Drawing of a thin circular flange

This benchmark, proposed by Papadopoulos and Lu (2001) and analysed in the works of Miehe *et al.* (2002), Miehe and Apel (2004), and Caminero *et al.* (2011), concerns the drawing process of a thin circular flange and is considered for the analysis of anisotropic elasto-plasticity. This drawing process, schematically represented in Fig. 7.13, can be seen as a simplification of the flange's drawing in the cylindrical cup drawing test, without modelling contact. For that purpose, only planar deformations are taken into account by simply supporting the lower and upper node layers of the discretized blank, whereas an inward radial displacement of 75 [mm] is uniformly imposed to the inner rim, while the outer rim is free from

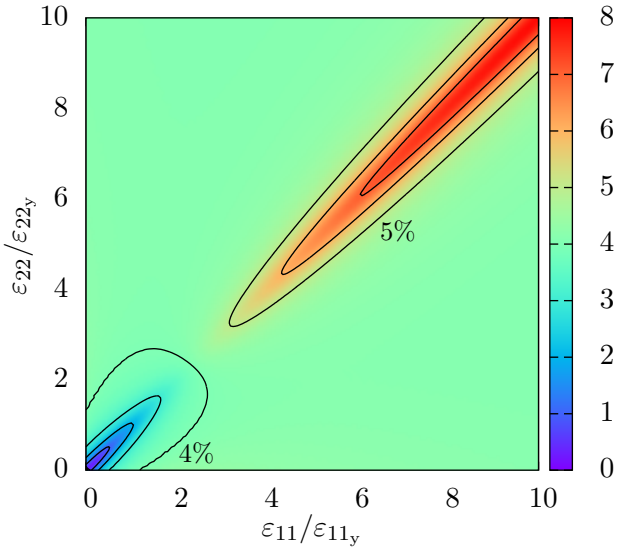

(c) FE - $ERR_{\max} = 7.899\%$ (contours of 1%).

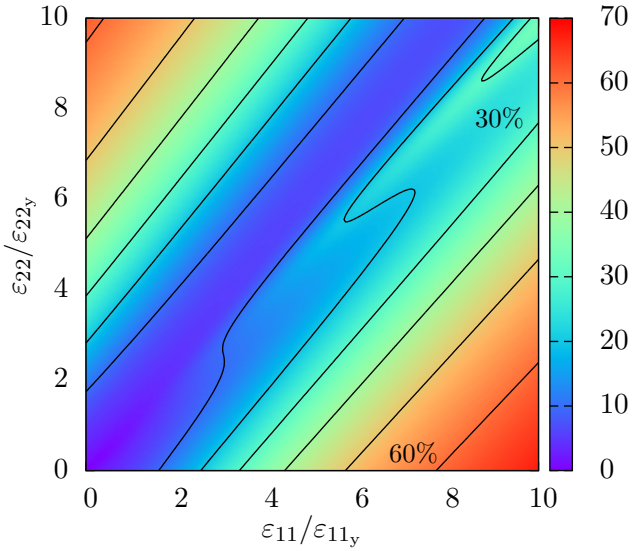

(d) FE1 - $ERR_{\max} = 67.259\%$ (contours of 10%).

Figure 7.12: Iso-error maps - Point C (pure shear) (cont.).

in-plane constraints. The obtained earing profile, a consequence of the material's anisotropy, can be seen as a rough approximation of the one obtained with the cylindrical cup drawing process, since in the latter more drawing is considered and the material experiences distinct loading/unloading conditions as it flows into the die (see Section 7.6).

Due to the geometrical and material symmetry, only a quarter section of the flange is analysed in this work. The flange has a thickness of 10 mm and has been discretized by 900 (30x30, radial x angular directions) 8-node trilinear finite elements with reduced integration (C3D8R, in ABAQUS), with one element along the thickness direction.

Three different materials are employed in this numerical problem, the 2090-T3 aluminium

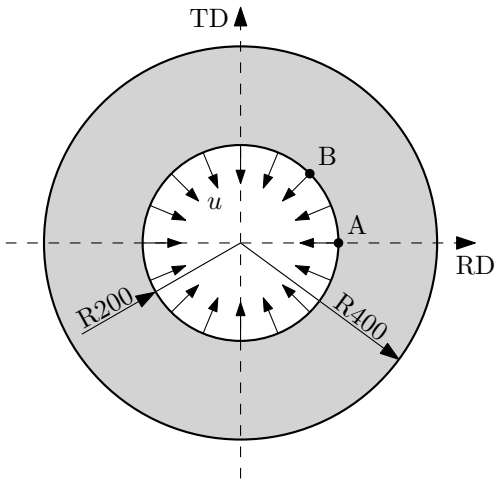

Figure 7.13: Circular flange's drawing - Scheme of the drawing process (units in mm).

alloy (the constitutive parameters of which were presented in Section 7.1), and fictitious isotropic and anisotropic materials, the latter introduced by Yoon *et al.* (2006) and denoted as FM8. The fictitious materials are assumed to have the same hardening behaviour as the Al2090-T3 alloy, while the anisotropic yielding behaviour of FM8 is described by the *Yld2004-18p* anisotropy parameters listed in Table 7.2 (Yoon *et al.*, 2006).

The obtained deformed configurations and distributions of accumulated plastic strain, $\bar{\varepsilon}_{\mathrm{p}}$, related to the hyperelastic-based model using $\mathbf{R}$, are shown in Fig. 7.14. In order to quantify the effect of the anisotropy on the earing, Fig. 7.15 shows the comparison of the obtained profiles (for 1/4 of the plate) considering the implemented constitutive models and algorithms. The isotropic material plate preserves the axisymmetry of its shape and distribution of $\bar{\varepsilon}_{\mathrm{p}}$ during the deformation process, as expected. On the other hand, the anisotropy of the Al2090-T3 alloy and FM8 material induces non-axisymmetric distributions of $\bar{\varepsilon}_{\mathrm{p}}$ and earing in the outer rim. The Al2090-T3 and FM8 reveal 4 and 8 ears in the final configuration, respectively, with the shape and alignment regarding the rolling direction being considerably different from each other. In Fig. 7.16 the development of the in-plane nodal forces acting at the nodes A and B, specified in Fig. 7.13, is depicted. When comparing the forces' evolution at A and B for the two considered anisotropic materials with the ones of the isotropic material, the anisotropy is easily seen. Regarding the different models and algorithms analysed, once more, the obtained results are in excellent agreement between each other.

Table 7.2: FM8's anisotropic coefficients ($a = 8$) (Yoon *et al.*, 2006).

c^1_{12}	c^1_{13}	c^1_{21}	c^1_{23}	c^1_{31}	c^1_{32}	c^1_{44}	c^1_{55}	c^1_{66}
0.7297	0.8777	0.4252	0.7268	1.1386	1.0000	1.3485	1.0000	1.0000
c^2_{12}	c^2_{13}	c^2_{21}	c^2_{23}	c^2_{31}	c^2_{32}	c^2_{44}	c^2_{55}	c^2_{66}
1.0513	1.0389	1.3289	1.1775	0.7651	0.9169	0.0432	1.0000	1.0000

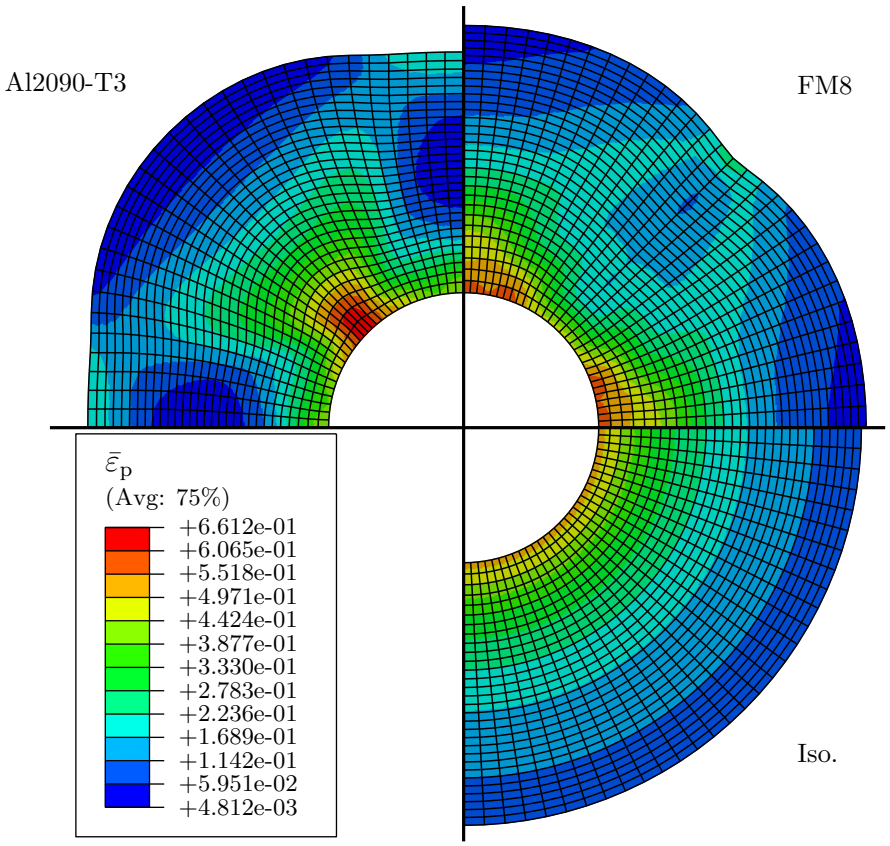

Figure 7.14: Circular flange's drawing - Deformed configurations and distributions of the accumulated plastic strain for an isotropic material, Al2090-T3, and FM8.

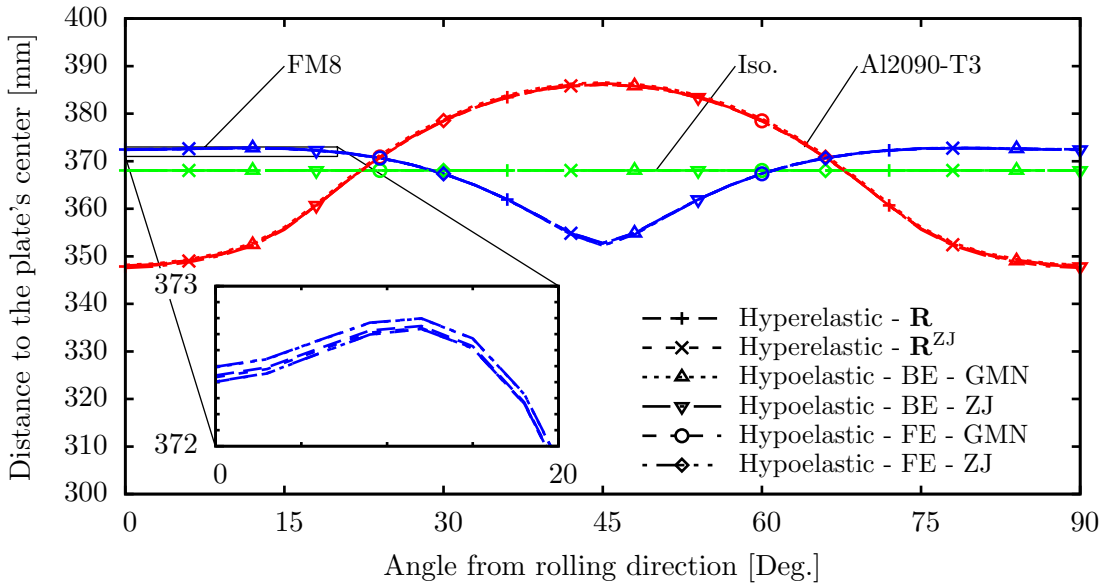

Figure 7.15: Circular flange's drawing - Obtained earing profiles for an isotropic material (green), Al2090-T3 (red), and FM8 (blue).

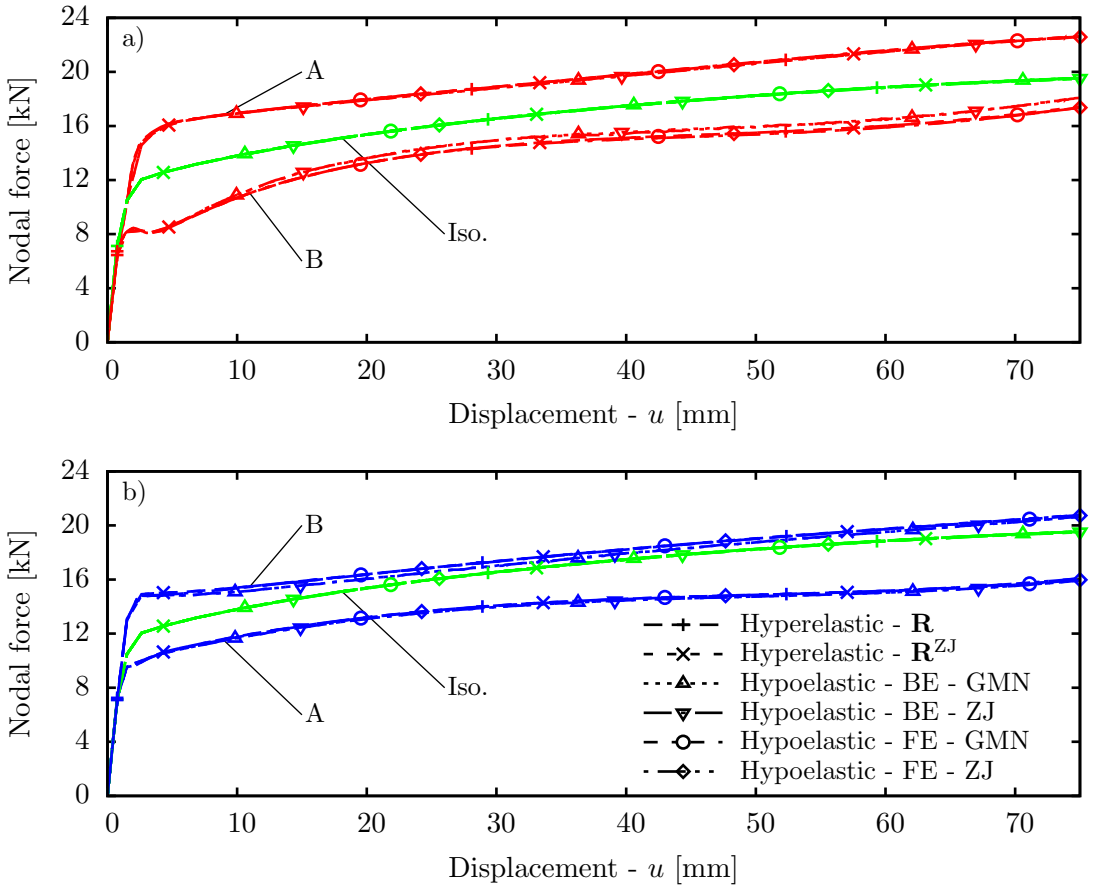

Figure 7.16: Circular flange's drawing - Nodal forces' evolution at A and B for an isotropic material (green) along with a) Al2090-T3 and b) FM8.

7.6 Cylindrical cup drawing test

One of the most used benchmarks in the analysis of the anisotropic planar behaviour and formability of metallic sheets is the cylindrical cup drawing test. Similarly to the numerical example of Section 7.5, the planar anisotropy of the material induces asymmetric flow of the material, resulting on an uneven periodic edge profile at the top of the formed cup (earing). This earing is an undesirable effect, since in the production of metallic parts it implies an additional processing step (trimming of the uneven top edge), leading to waste of material, reduction of production rate and thus increased costs. In the last years, several works have been presented on the study of this deep drawing process, e.g., in contrast to the usual practice of considering solely isotropic hardening with constant anisotropy, the influence of the use of combined isotropic-kinematic (Thuillier *et al.*, 2010, Vladimirov *et al.*, 2011) and combined rotational-isotropic-kinematic hardening laws (Choi *et al.*, 2006), and evolving anisotropy (Yoon *et al.*, 2010) have been studied. Although the prediction of the earing profile is usually carried out numerically, some analytical approaches have also been proposed by e.g., Chung *et al.* (2011) and Yoon *et al.* (2006). Here, this benchmark test is

used to assess the performance of the developed and implemented material models in real deep drawing forming processes regarding the anisotropy description. To that purpose, two materials are considered, namely the 2090-T3 aluminium alloy and the fictitious material FM8, whose constitutive parameters were presented in Sections 7.1 and 7.5, respectively.

This forming process is schematically represented in Fig. 7.17 and consists of forcing the blank to flow into the axisymmetric cavity of the die by means of moving the axisymmetric punch downwards. In order to prevent buckling on the blank's flange a blank holder is utilized. A blank holder force of 22.2 [kN] (5.55 [kN] for a quarter section of the blank) and a Coulomb's friction coefficient of 0.1 between the surfaces in contact are considered. The adopted value of the blank holder force is just enough to prevent wrinkling and thus minimize its influence on the earing formation. The specific dimensions of the sheet and tools as well as the process parameters are chosen according to Yoon *et al.* (2006).

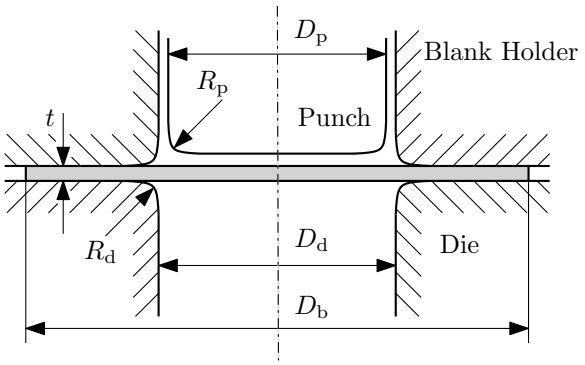

Punch diameter	$D_p = 97.46$
Punch profile radius	$R_p = 12.70$
Die opening diameter	$D_d = 101.48$
Die profile radius	$R_d = 12.70$
Blank diameter	$D_b = 158.76$
Initial sheet thickness	$t_0 = 1.6$

[mm]

Figure 7.17: Cilindrical cup drawing test - Scheme of the drawing process.

As in the previous section, due to the orthotropic material symmetry, as well as the process symmetry, only a quarter section of the blank is modelled and analysed. A total of 7500 8-node trilinear finite elements with reduced integration (C3D8R, in Abaqus), distributed in the sheet's plane as represented in Fig. 7.18, with 4 layers along the thickness direction, are used to discretize the blank, whereas the tools are modelled as analytical rigid bodies.

In Fig. 7.19 it is shown the deformed configurations and the non-axisymmetric evolution of the distribution of the accumulated plastic strain, $\bar{\varepsilon}_p$, at different punch displacements, u, for the 2090-T3 aluminium alloy considering the hyperelastic-based model using **R** and the *Yld2004-18p* function.

The obtained earing profiles related to the analysed materials are depicted in Fig. 7.20 considering the implemented constitutive models and algorithms. As in Fig. 7.15, only the earing profile between 0° and 90° is presented, since the entire profile can be obtained by mirroring, due to the orthotropic material symmetry. The results obtained with the *Yld2004-18p* criterion predicted 8 ears in the entire earing profile for both Al2090-T3 and FM8 materials. For the Al2090-T3 using the *Yld2004-18p* criterion, 4 additional ears at 0°, 90°, 180° and 270° are predicted comparatively to Fig. 7.15, because more drawing is considered. This is due to the additional stretching coming from the friction between the blank and

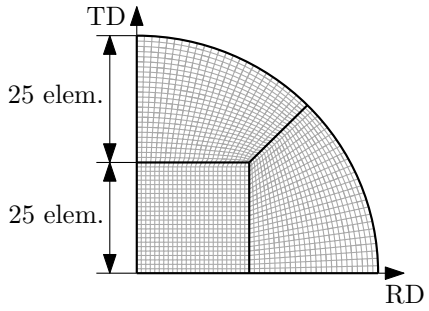

Figure 7.18: Cylindrical cup drawing test - Blank discretization.

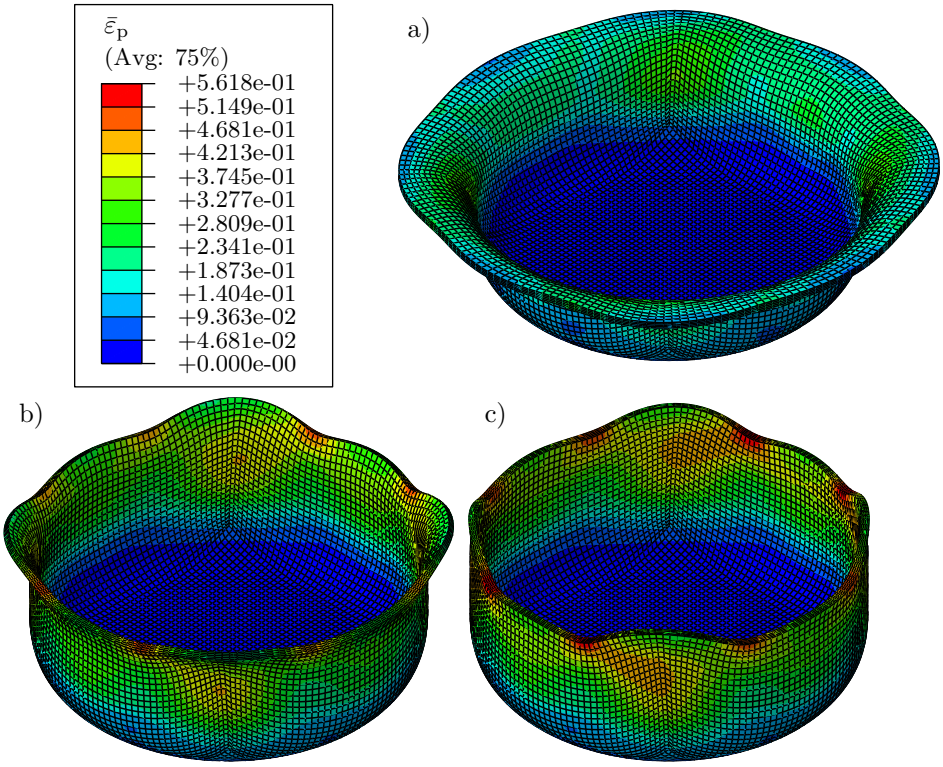

Figure 7.19: Cylindrical cup drawing test - Deformed configurations and distributions of the accumulated plastic strain at a) $u = 30$ mm, b) $u = 45$ mm, and c) $u = 65$ mm (final configuration).

the tools, as well as the higher amount of material flow. Moreover, the bending/unbending conditions to which the material is subjected when it is drawn through the die profile may also affect the earing profile. When the *Yld91* criterion is used to describe the Al2090-T3's anisotropy, its lower flexibility, comparatively to *Yld2004-18p*, allows the prediction of only 4 ears in the entire earing profile. Regarding FM8, the 8 ears are already obtained during the drawing of the circular flange (see Fig. 7.15), but have now more pronounced height and new positions for the cylindrical cup drawing test. These 8 ears have been also predicted by Yoon *et al.* (2006). As expected, when the von Mises criterion is employed an axisymmetric profile is obtained.

The predicted evolution of the punch's force during the forming process is presented in

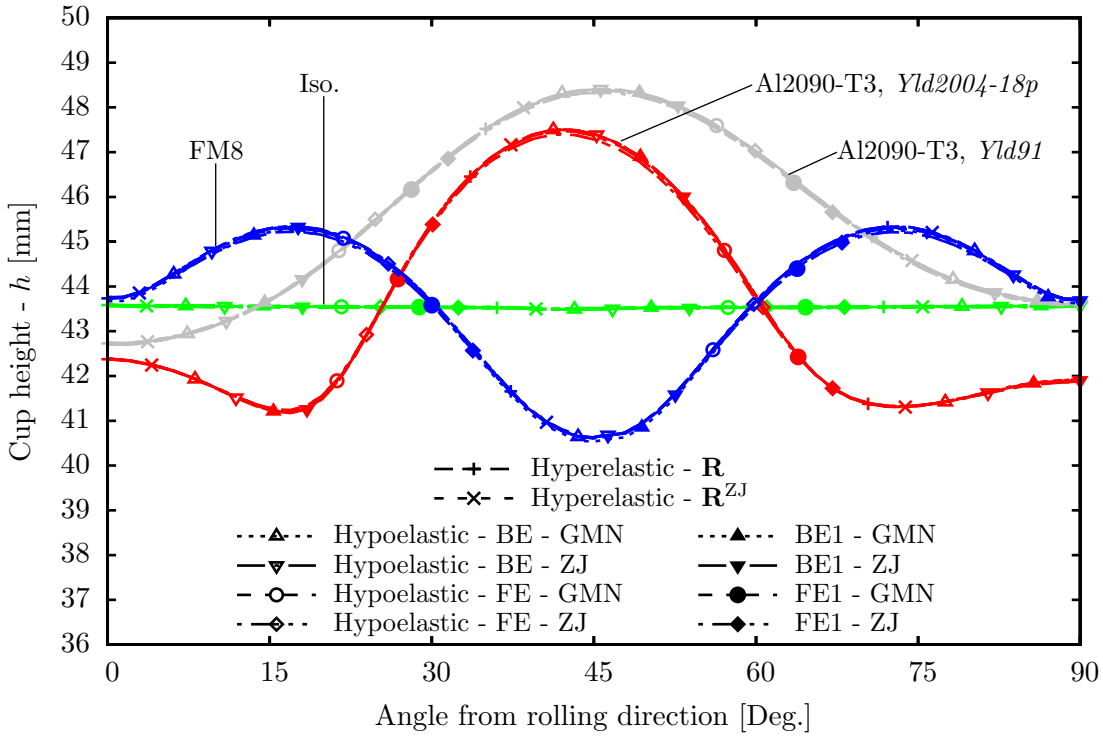

Figure 7.20: Cylindrical cup drawing test - Obtained cup height profiles for an isotropic material (green), Al2090-T3 using *Yld91* (gray) and *Yld2004-18p* (red) yield criteria, and FM8 (blue).

Fig. 7.21. It is interesting to observe that differences of about 20% on the maximum punch force are predicted, even though all results were obtained considering the same hardening law. Moreover, regarding the Al2090-T3, significant differences occurs when two different yield criteria are used to describe the same anisotropic behaviour. The results obtained with the considered finite strain formulations and algorithms are in great agreement with each other, regarding both earing profiles and punch force-punch displacement relationship.

The number of increments required to completely drawn the cup (only the forming step is taken into account) for each constitutive model with the considered integration algorithms and the corresponding relative times of computation (considering the hypoelastic-BE-ZJ as reference) are presented in Table 7.3. Although the differences between the obtained results (see Figs. 7.20 and 7.21) are negligible, the performances of the employed algorithms regarding the computational time are quite different. Concerning the hypoelastic-based model, on the one hand, the backward-Euler algorithms (with and without the multi-stage return mapping procedure) provide very similar results. Because of the small size of the step increments, mainly imposed by the contact algorithm, a fast convergence of the return mapping is obtained with only one stage, thus the advantage of using the multi-stage return mapping procedure is wasted.

On the other hand, relatively to the forward-Euler algorithms, an improvement of performance is observed in both the number of step increments and the time of computation

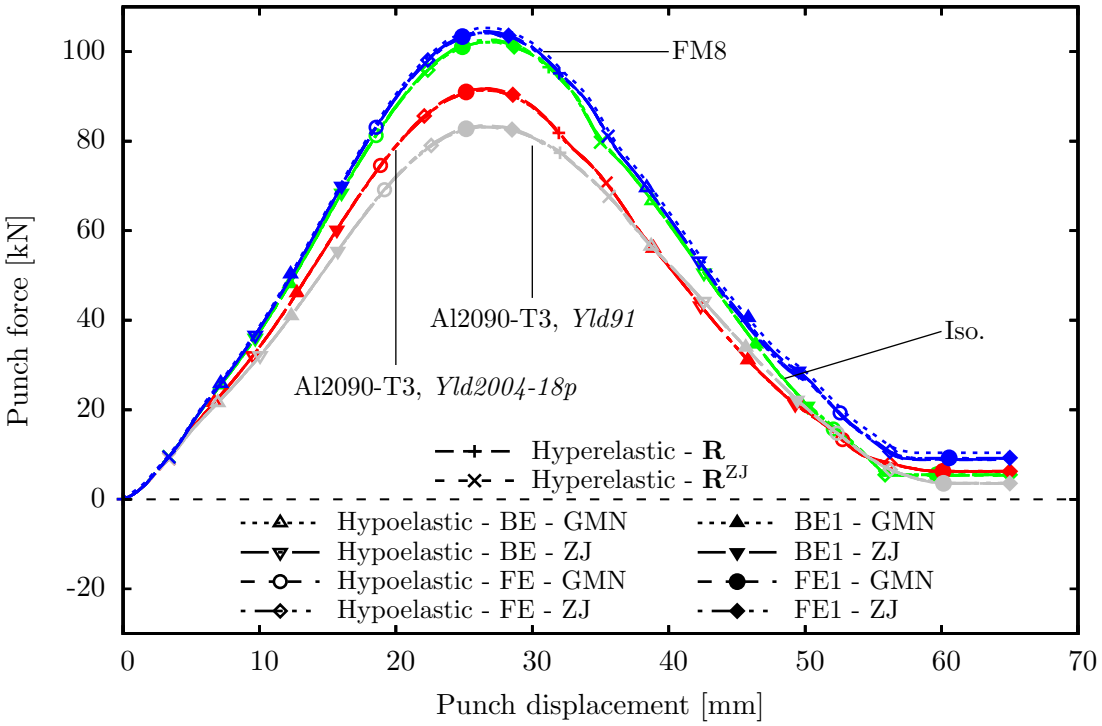

Figure 7.21: Cylindrical cup drawing test - Predicted punch force-punch displacement relationships for an isotropic material (green), Al2090-T3 using *Yld91* (gray) and *Yld2004-18p* (red) yield criteria, and FM8 (blue).

Table 7.3: Cylindrical cup drawing test - Number of increments and relative times to completely drawn the cup.

Model	Algorithm	Objective rate	Al2090-T3 (*Yld2004-18p*) # inc.	Al2090-T3 (*Yld2004-18p*) Rel. time	FM8 # inc.	FM8 Rel. time
Hypo-	BE	ZJ	78	1.00 (Ref.)	81	1.04
		GMN	78	1.05	81	0.98
	BE1	ZJ	78	1.03	81	0.97
		GMN	78	0.97	82	1.00
	FE	ZJ	128	2.04	113	1.74
		GMN	136	2.20	116	1.81
	FE1	ZJ	134	2.47	119	2.16
		GMN	138	2.50	115	2.18
	Rotation tensor					
Hyper-	$\mathbf{R}$		95	6.26	98	5.65
	$\mathbf{R}^{ZJ}$		95	6.26	89	5.33

when the sub-incrementation technique is considered. Nevertheless, even when the sub-incrementation technique is used, the forward-Euler algorithm takes more than twice the time required by the backward-Euler algorithms.

In this numerical example, the hypoelastic-based model is considerably more efficient than

the hyperelastic-based one. The differences in the required times of computation are understandable considering the employed algorithms to integrate the constitutive equations. For the hyperelastic model, the used algorithm (see Section 5.3.9.2) requires a complex linearization of the residua (see Equations 5.140-5.142) at each iteration of the iterative procedure if plastic deformation occurs. In turn, for the hypoelastic model the plastic multiplier is computed using a single equation: at each iteration for the backward-Euler algorithm (see Equation 4.86); and at each sub-increment for the forward-Euler algorithm considering the sub-incrementation technique (see Equation 4.53). Comparing the obtained results between the two materials, one can conclude that the anisotropy affects both the number of increments required and the time of computation. This is related to the fact that the more pronounced the yield surface's anisotropy, the higher the number of iterations required to perform the return mapping (in backward-Euler algorithms) or the error at the end of the return mapping (in forward-Euler algorithms), specially at cornered regions of the yield surface.

In Fig. 7.22 the results obtained with the hyperelastic-based model using **R** for the 2090-T3 aluminium alloy are compared with the experimental data coming from Yoon *et al.* (2000) and with the numerical results obtained by Yoon *et al.* (2006), Alves de Sousa *et al.* (2007), and Kim *et al.* (2008). In the (reference) experimental earing profile the cup height evolution between 90° and 180° is not an exact mirror image of the cup height profile between 0° and 90°. It was argued by Yoon *et al.* (2000) that this probably results from an inexact alignment between the centre of the blank and the corresponding centre of the tools during the forming experiment. The obtained earing profile is in good agreement with the experimental data and with the works of Yoon *et al.* (2006) (based on a solid element formulation), Alves de Sousa *et al.* (2007) (for an enhanced assumed strain solid-shell formulation), and also with

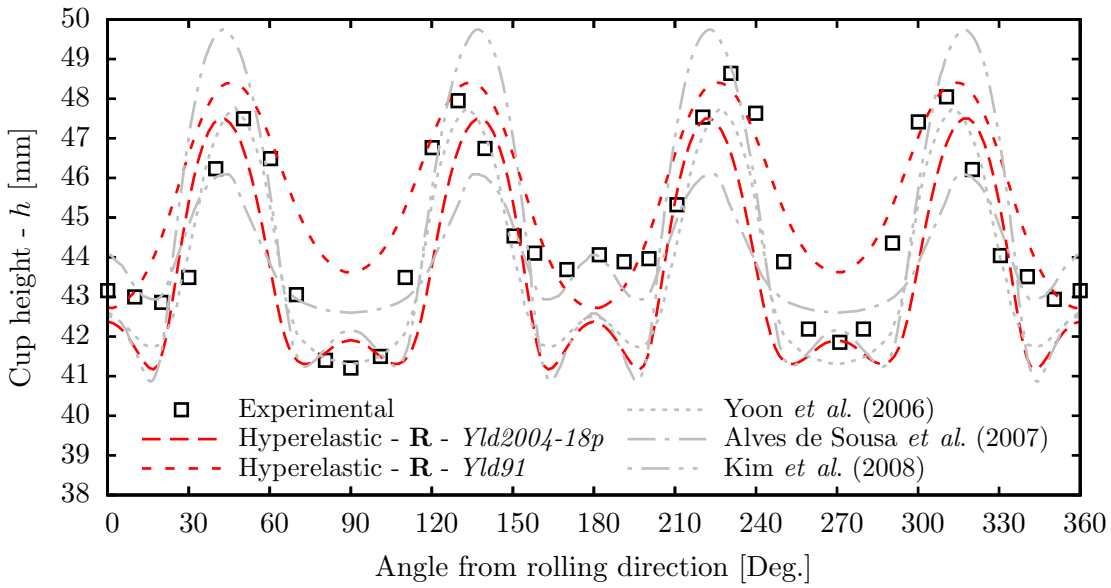

Figure 7.22: Cylindrical cup drawing test - Comparison of the obtained results for the Al2090-T3 with experimental (Yoon *et al.*, 2000) and numerical data presented in the literature.

Kim *et al.* (2008) (using shell elements). However, two unexpected ears at 90° and 270°, which did not occur experimentally, are also predicted. The same ears were also predicted in the work of Kim *et al.* (2008), which used the same commercial FEM code (ABAQUS).

7.7 S-rail forming benchmark

The plastic forming of an S-shaped channel, so-called "S-rail", was proposed in the NUMISHEET (1996) international conference as a benchmark problem. It was designed to compare different numerical results with each other as well as with experiments. The complex geometry of this problem makes it an interesting validation test about the springback prediction capabilities of numerical formulations. Although some analytical approaches to predict springback have been proposed (see e.g., Moon *et al.* (2008)), they are limited to simple forming processes and material properties, not being suitable, in general, to the springback analyses of real forming processes. Hence, the analysis of such complex forming processes, as the forming of an S-rail, implies the use of numerical approaches, as the FEM.

The geometry of the blank and tools, as well as the initial setup, are shown in Fig. 7.23. The initial blank thickness is 0.92 [mm]. The blank is placed between the die and the blank holder and the imposed upward movement of the punch draws the blank into the curved cavity of the die. After an imposed displacement of 37 [mm], the deformed part is removed from the tooling and allowed to spring back. In this work, a blank holding force of 10 [kN] is considered following the indications of the NUMISHEET benchmark's board. A Coulomb's friction coefficient of 0.1 is assumed between the surfaces in contact. The simulation of this problem is carried out for the 6111-T4 aluminium alloy, constitutive parameters of which are presented in Table 7.4, after (Yoon *et al.*, 1999). The hardening of the material is solely defined by the isotropic Swift's law (no kinematic hardening is considered, i.e., $c = 0.0$ [MPa] and $b = 10^{-8} \approx 0$ [-]), and the material's anisotropy is described by the *Yld91* yield function.

Table 7.4: Al6111-T4's constitutive parameters (Yoon *et al.*, 1999).

Elasticity			Isotropic hardening		
E [GPa]	ν [-]		K [MPa]	ε_0 [-]	n_{H} [-]
69.0	0.33		488.0	7.1x10^{-3}	0.232
Yld91 anisotropy parameters ($a = 8$)					
c_1	c_2	c_3	c_4	c_5	c_6
0.9503	0.8347	1.0240	0.9800	1.0000	1.000

The adopted mesh consists of 6000 8-node trilinear finite elements fully integrated with incompatible deformation modes (C3D8I, in Abaqus), disposed in the sheet plane as illustrated in Fig. 7.24. The choice of the C3D8I formulation over conventional 3D formulations (e.g., C3D8 or C3D8R in Abaqus) is due to the fact that preliminary simulations showed that conventional 3D formulations were not able to properly reproduce the wrinkling patterns, ex-

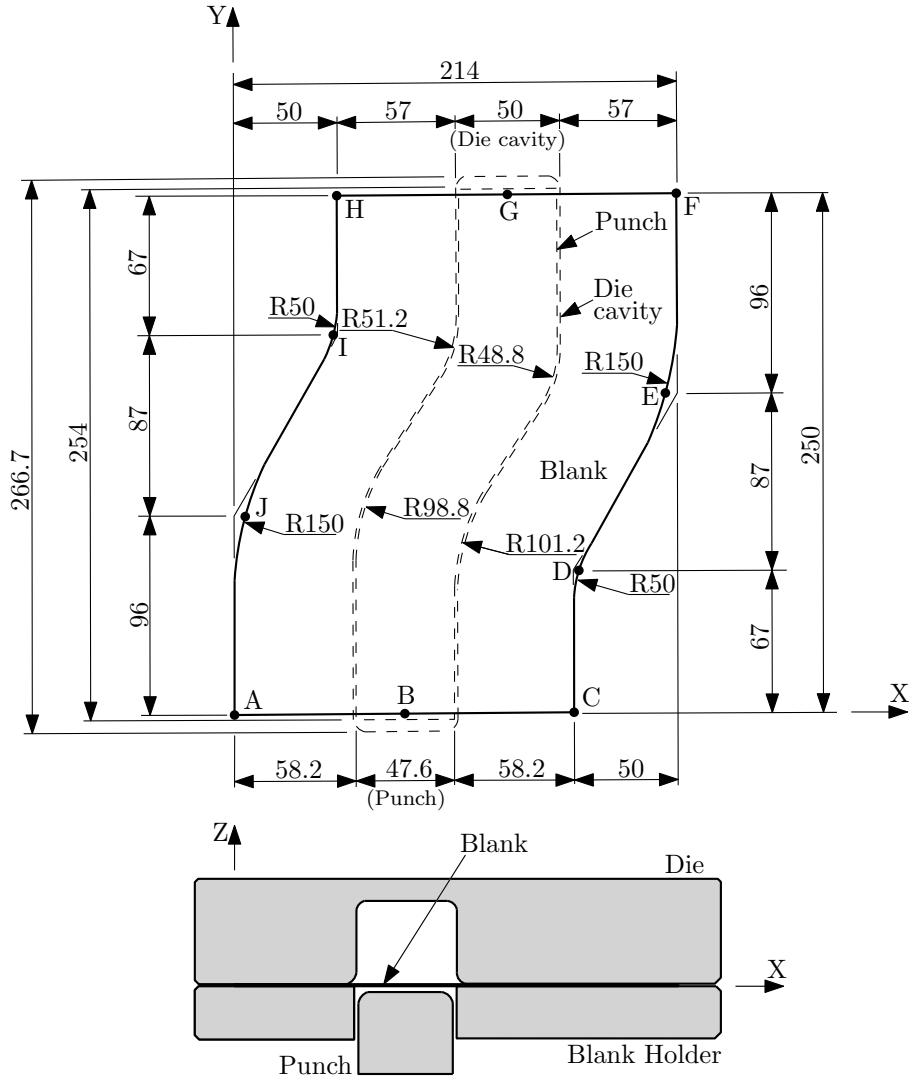

Figure 7.23: S-rail forming - Scheme of the drawing process (units in mm).

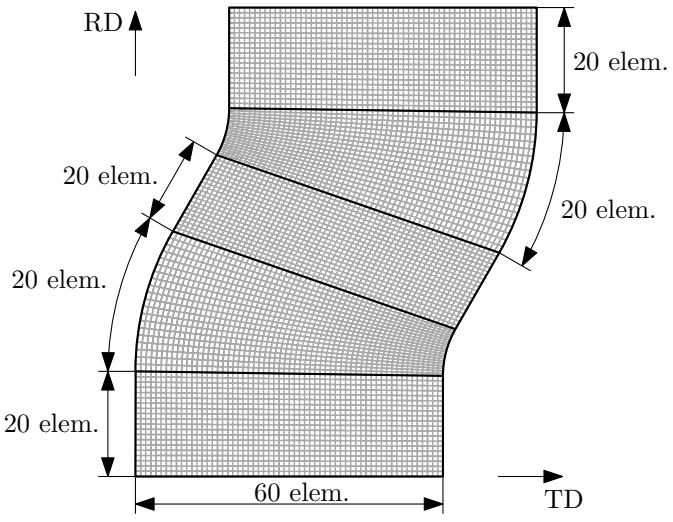

Figure 7.24: S-rail forming - Blank discretization.

perimentally observed, in the final formed part. The tools are assumed to be rigid bodies modelled by 4-node bilinear quadrilateral rigid elements (R3D4, in Abaqus). The deformed configurations and distributions of *Yld91* effective stress after the forming step and after the springback are shown in Fig. 7.25, considering the hyperelastic-based model using **R**. As shown in this figure, some wrinkles are revealed at the top of the formed part during the forming step, shape of which suffer a small variation during the springback. The effective stresses decrease considerably and the flanges of the part are slightly twisted, due to elastic unloading, when the tools are removed.

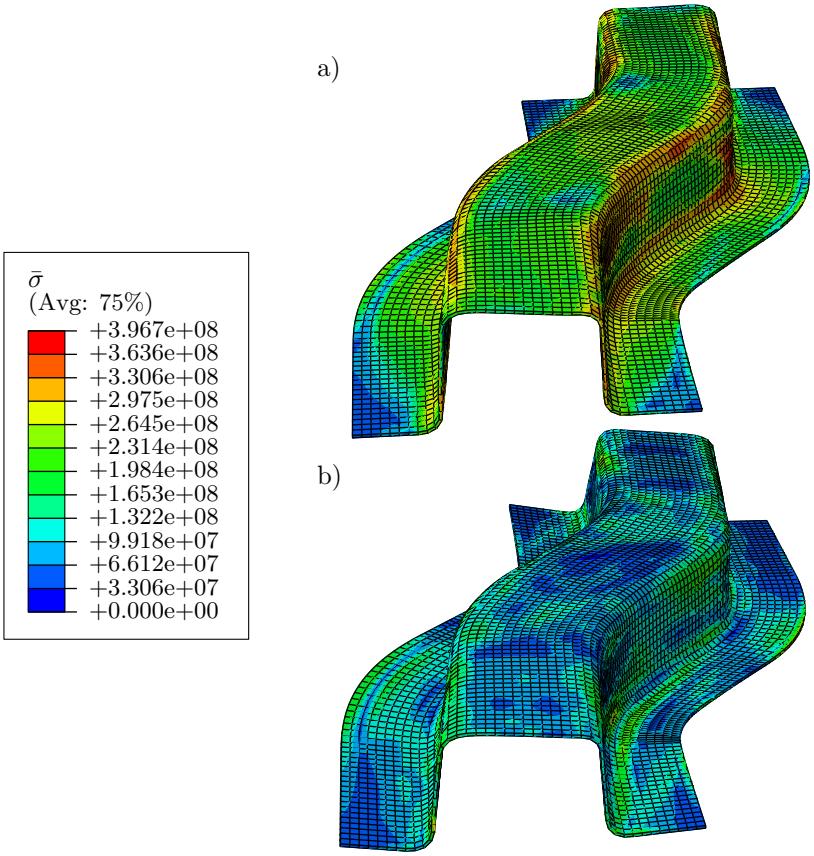

Figure 7.25: S-rail forming - Deformed configurations and distributions of *Yld91* effective stress a) after the forming step and b) after the springback.

The obtained cross-section profiles along the reference lines IE and JD, measured on the top surface of the blank and considering the implemented constitutive models and numerical algorithms, are presented in Fig. 7.26. The obtained results are very similar between each other, regardless the considered constitutive model or the algorithm used to integrate the hypoelastic constitutive equations. The springback of the cross-sections along the reference lines IE and JD, considering the hyperelastic-based model using **R**, is compared with the experimental data (NUMISHEET, 1996) in Fig. 7.27. The obtained results provide a good prediction of the experimentally measured springback, especially in the JD line's case. Fig. 7.28 presents the evolution of the applied punch force with its displacement during

the forming step. The experimental upper (EB2.03) and lower (EB2.01) curves published in the proceedings of the NUMISHEET (1996) conference are also depicted in this figure. The obtained punch force-punch displacement relationships are within the range and follow the evolution trend of the experimental data. Moreover, as for the sectional profiles along the reference lines IE and JD, the obtained results are very similar regardless the constitutive model or integration algorithm considered.

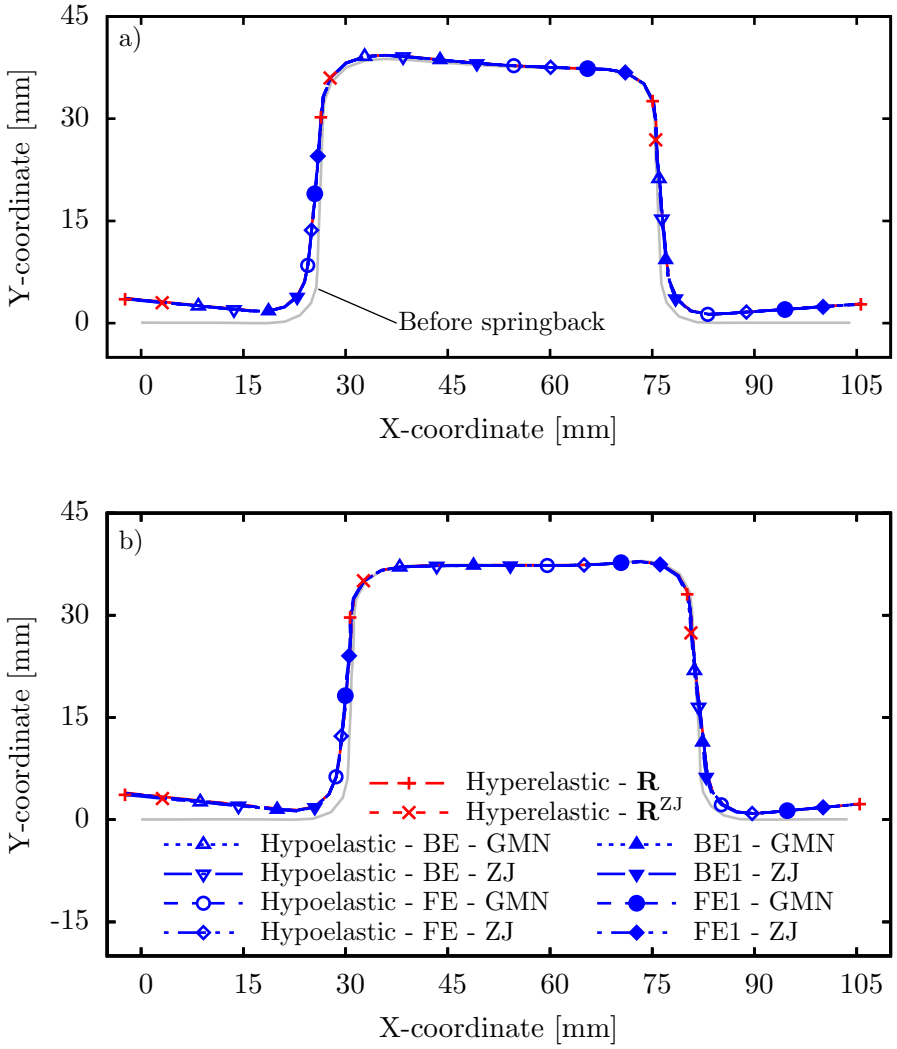

Figure 7.26: S-rail forming - Numerically obtained sectional deformed shapes after springback along a) IE and b) JD lines.

Finally, the number of increments required to numerically simulate this benchmark (only the forming step is taken into account) for each constitutive model with the considered integration algorithms, as well as the corresponding relative times of computation (considering hypoelastic-BE-ZJ as reference) are presented in Table 7.5. Moreover, the predicted springback is quantitatively compared with the experimental results through the angles indicated in Fig. 7.27. In terms of the number of increments to simulate this benchmark, no sig-

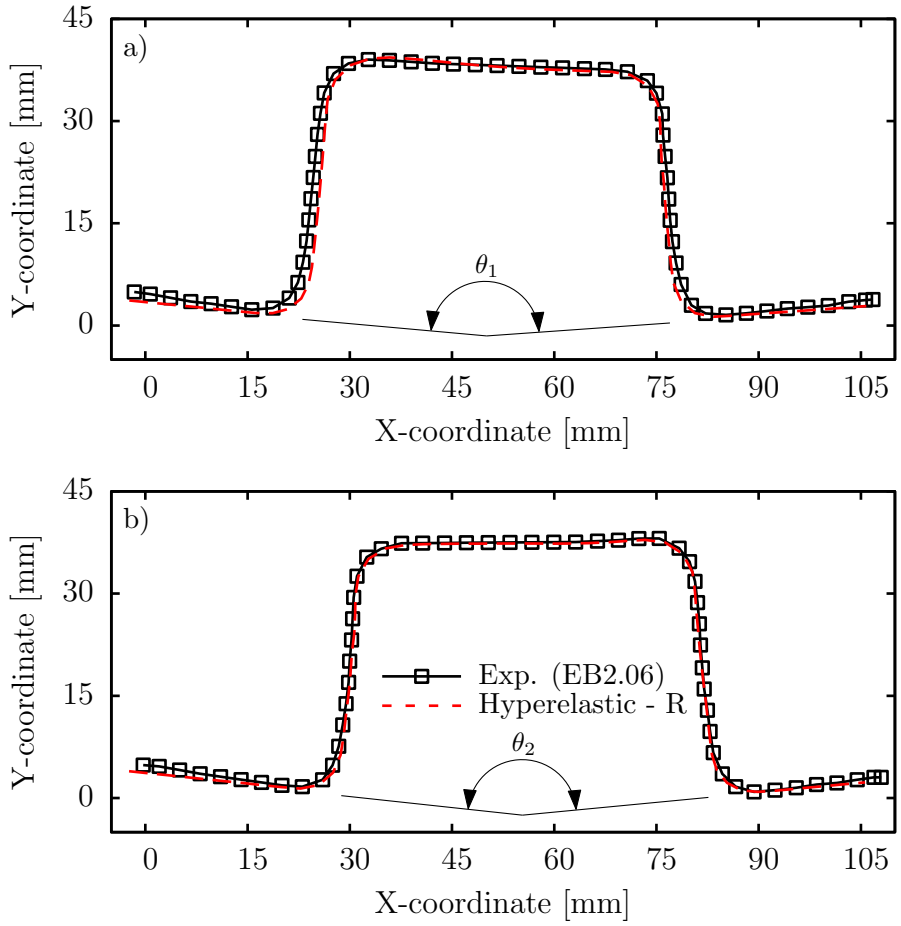

Figure 7.27: S-rail forming - Comparison of the obtained cross-section profiles with the experimental data (NUMISHEET, 1996) after springback along a) IE and b) JD lines.

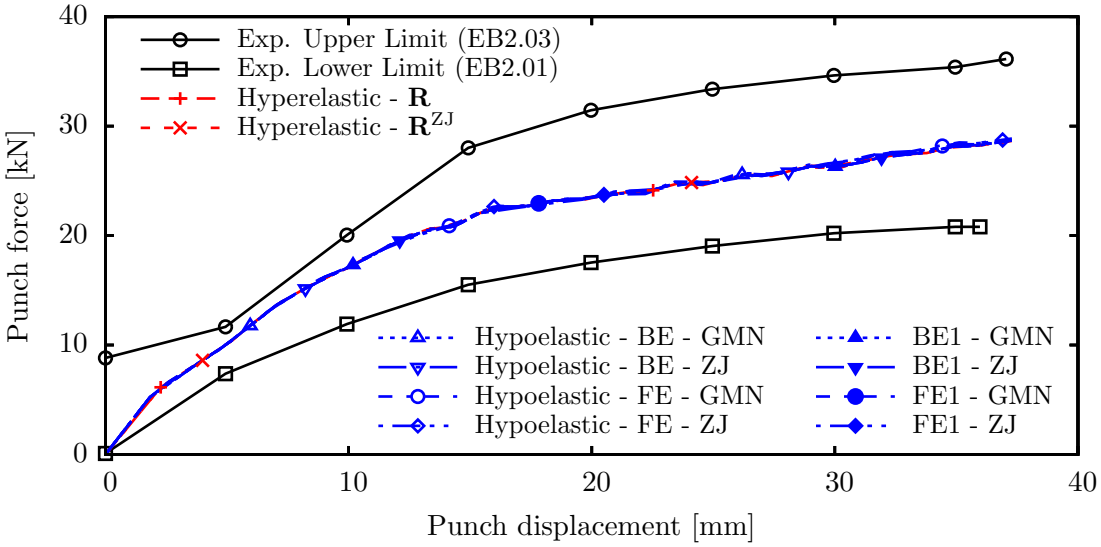

Figure 7.28: S-rail forming - Predicted and experimental (NUMISHEET, 1996) punch force-punch displacement relationships.

nificant differences are seen between the hypoelastic- and hyperelastic-based models. This is due to the fact that, in this example, similarly to the one of Section 7.6, the contact is the main feature (instead of the material model) that delimits the size of the increments during the forming step. This means that, even though the hyperelastic-based model may allow for larger step increments comparatively to the hypoelastic-based one, the size of the step increments are restricted by the contact algorithm. In fact, the step increments in this example are small enough to suppress the advantages of using the multi-stage return mapping procedure, since the number of step increments and the obtained results (see θ_1 and θ_2) are the same. Moreover, looking at the time of computation, one can see that the classical backward-Euler algorithm, BE1, is indeed the more efficient one. The BE algorithm is slightly slower than the BE1 because it performs the return mapping in more than one stage in some step increments, where its small size allows a fast convergence considering only one stage. The forward-Euler algorithm is not so efficient as the backward-Euler regarding either the number of step increments, the computational time, and the obtained results. Here, the use of the sub-incrementation technique improves significantly the performance of the algorithm, specially regarding the number of step increments and the time of computation. Regarding the computational time, the hypoelastic-based model is clearly faster then the hyperelastic-based one, as in the previous numerical example. Comparing the Zaremba-Jaumann and the Green-McInnis-Naghdi rates, one can see that the former allows, in general, for a slightly smaller number of step-increments and thus faster simulations. The obtained angles between the flanges, θ_1 and θ_2, are globally very similar for all simulations. Nevertheless, the results obtained with the hyperelastic-based model are the ones closer to the experimental data.

Table 7.5: S-rail forming - Number of increments and relative times of computation.

Model	Algorithm	Objective rate	# inc.	Rel. time	θ_1 [Deg.]	θ_2 [Deg.]
Hypo-	BE	ZJ	178	1.00 (Ref.)	170.306	168.807
		GMN	179	1.02	170.313	168.835
	BE1	ZJ	178	0.98	170.306	168.807
		GMN	179	1.00	170.313	168.835
	FE	ZJ	183	1.14	170.520	169.038
		GMN	187	1.11	170.522	169.037
	FE1	ZJ	284	1.48	170.674	169.218
		GMN	337	1.64	170.675	169.248
Rotation tensor						
Hyper-		$\mathbf{R}^{\mathrm{ZJ}}$	177	5.07	170.249	168.770
		$\mathbf{R}$	177	5.21	170.240	168.749
Experimental (EB2.06)			—	—	164.78	163.87

7.8 U-channel forming benchmark

The benchmark of the forming of a U-channel was proposed in the NUMISHEET (1993) international conference, also aiming at the study of springback. A scheme of the forming process, as well as the tool dimensions, is represented in Fig. 7.29, and the initial blank size is $350 \times 45 \times 1.2$ [mm]. The process consists of imposing a punch displacement of 70 [mm] and then removing the tools so the blank is allowed to recover elastically. After the two-step simulation, from the final sheet shape, the springback and sidewall curl are assessed using the measuring system represented in Fig. 7.30. As proposed by the NUMISHEET (1993) benchmark committee, three parameters are used to assess the obtained profile, namely the angles between the bottom and the sidewall and between the sidewall and the flange, θ_1 and θ_2 respectively, and the radius of curvature of the sidewall, ρ. A blank holding force of 25.7 [kN] (6.425 [kN] for a quarter section of the blank) is used and a Coulomb's friction coefficient of 0.14 is assumed between the sheet and the tools.

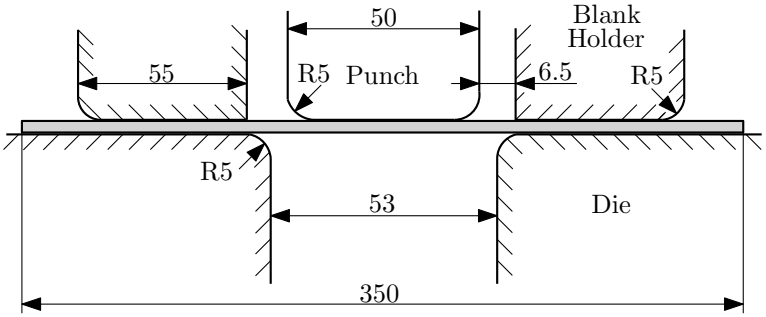

Figure 7.29: U-channel forming - Scheme of the drawing process (units in mm).

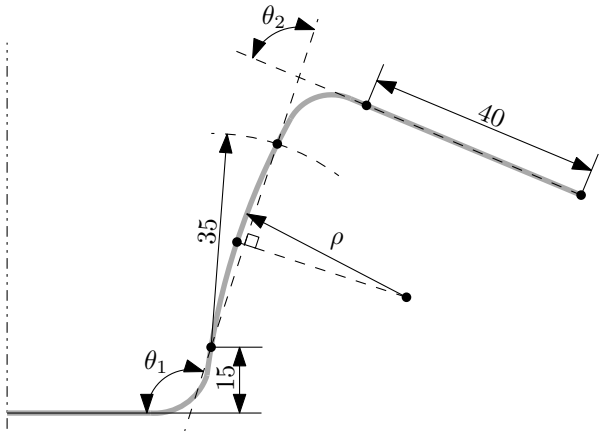

Figure 7.30: U-channel forming - System used to measure the springback and the sidewall curl (units in mm).

The material considered in this numerical example is a DP590 steel, identification of the constitutive parameters of which was presented in Section 6.7. The three hardening models considered in Section 6.7 (namely pure isotropic hardening and pure kinematic hardening with one and two back stress components) are taken into account in this numerical example.

Due to the material's isotropy, only a quarter section of the blank is analysed. The blank is discretized by 18375 8-node trilinear solid elements with reduced integration (C3D8R, in ABAQUS), with dimensions of 1.0×1.5 mm (length $\times$ width). Here, 7 elements along the thickness direction are considered and the tools are modelled as analytical rigid bodies.

The deformed profiles obtained with the constitutive models and algorithms in study are presented in Fig. 7.31. For each hardening model the obtained results are very similar, regardless the constitutive model or the algorithm considered. The differences between the results obtained with each hardening model are only perceptible in the angle between the sidewall and the flange, whereas no differences are observable in the sidewall area. As expected, among the three used models, Model 1 is the one that predicts more springback. This is due to the fact that pure isotropic hardening is not able to describe neither the Bauschinger effect nor the transient behaviour, thus overpredicting the levels of stress. Between Models 2 and 3 slight differences are visible, in a way that Model 2 predicts more springback than Model 3.

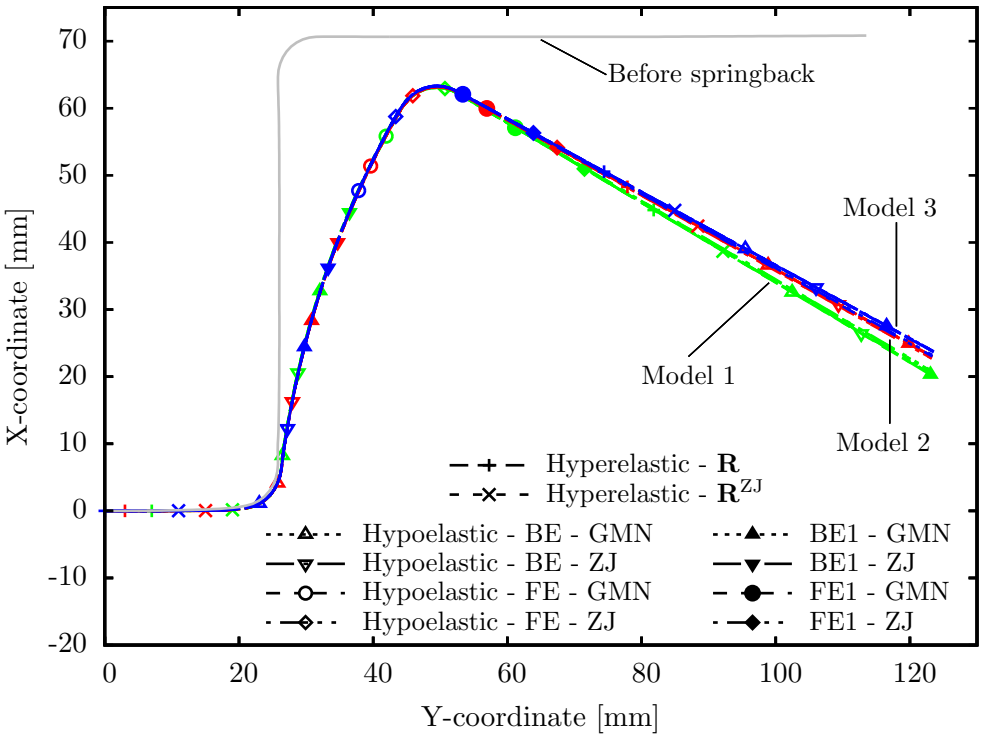

Figure 7.31: U-channel forming - Obtained deformed profiles for Model 1 (green), Model 2 (red), and Model 3 (blue).

The number of increments required to completely form the part (only the forming step is taken into account) and the corresponding relative times of computation (considering the hypoelastic-BE-ZJ for Model 1 as reference), for each constitutive model with the considered integration algorithms, are presented in Table 7.6. In this numerical example, the hyperelastic-based formulation allows for larger step increments, requiring only between about

50% (for Model 1) and 90% (for Model 3) more time of computation comparatively to the hypoelastic-based formulation. Among the algorithms used for the hypoelastic-based model, the standard backward-Euler is generally the more efficient in this numerical example, whereas the advantage of considering the multi-stage return mapping procedure is again suppressed by the use of small increments. Also, the use of an isotropic yield surface and the few changes in the loading direction enable a fast convergence of the iterative procedure, during the plastic corrector phase, with only one stage of return mapping. The forward-Euler algorithms have, in general, a worse efficiency comparatively to the backward-Euler algorithms. Indeed, concerning Model 1, the hyperelastic-based model required less time of computation than the hypoelastic-based model with the standard forward-Euler algorithm. Comparing the computational effort between hardening models, one can see that both the number of increments and the time of computation increase as the complexity of the model grows. This is justified by the increase of the number of state variables, which integrated formulas of evolution equations must converge at the end of the increment.

Table 7.6: U-channel forming - Number of increments and relative times of computation.

Model	Alg.	Obj. rate	Hard. Model 1 # inc.	Hard. Model 1 Rel. time	Hard. Model 2 # inc.	Hard. Model 2 Rel. time	Hard. Model 3 # inc.	Hard. Model 3 Rel. time
Hypo-	BE	ZJ	382	1.000 (Ref.)	468	1.320	487	1.415
		GMN	382	1.011	467	1.274	487	1.427
	BE1	ZJ	382	0.990	488	1.372	487	1.386
		GMN	382	0.996	478	1.301	487	1.393
	FE	ZJ	373	1.525	493	1.993	542	2.096
		GMN	362	1.520	496	2.033	537	2.076
	FE1	ZJ	408	1.555	547	2.213	589	2.353
		GMN	466	1.557	611	2.217	625	2.361
	Rotation tensor							
Hyper-		$\mathbf{R}$	318	1.533	383	2.248	397	2.710
		$\mathbf{R}^{\mathrm{ZJ}}$	318	1.541	383	2.248	397	2.698

The comparison between the obtained deformed profiles, considering hyperelastic-$\mathbf{R}$, after springback with the experimental data, coming from Lee *et al.* (2012b), is presented in Fig. 7.32. Qualitatively speaking, Model 1 overpredicts the experimental springback, whereas the profiles obtained with Models 2 and 3 are in good agreement with the experimental profile. In order to quantitatively assess the obtained results, in Table 7.7 the three parameters defined in Fig. 7.30 are presented regarding the obtained results and the experimental data and numerical results presented by Lee *et al.* (2012b) using the homogeneous anisotropic hardening, HAH, approach. Generally, the obtained results are in excellent agreement with the experimental data, slightly underpredicting the sidewall curl, ρ, and the angle between the sidewall and the flange, θ_2, and marginally overpredicting the angle between the bottom and the sidewall, θ_1. As expected, the use of a kinematic hardening law with two back stress

components (Model 3) allows for better results than Models 1 and 2. One should notice that the better description of the experimental springback is directly related to the better description of the material's hardening behaviour (see Fig. 6.10) provided by this hardening model. Interestingly, Models 2 and 3, that use only 3 and 5 parameters, respectively, provide better predictions of θ_1 and θ_2 than the HAH model, that used 9 parameters.

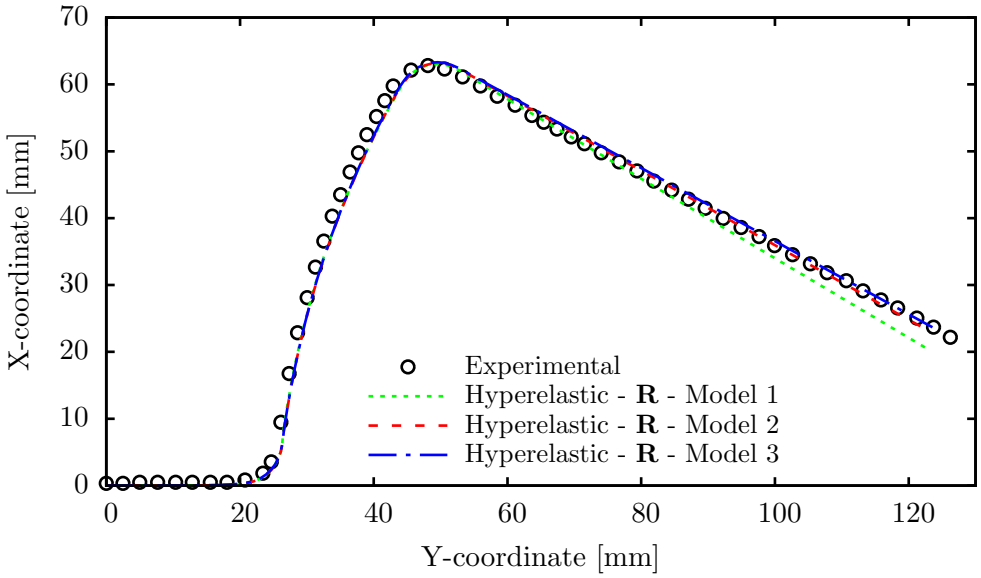

Figure 7.32: U-channel forming - Comparison of the obtained deformed profiles with experimental data (Lee *et al.*, 2012b).

Table 7.7: U-channel forming - Radius of curvature and springback angles.

	Experimental (Lee *et al.*, 2012b)	HAH	Hyperelastic-**R**		
			Model 1	Model 2	Model 3
ρ [mm]	149.5	146.0	140.384	142.038	143.523
θ_1 [Deg.]	107.1	106.3	107.630	107.571	107.494
θ_2 [Deg.]	79.3	77.8	76.884	78.426	78.823

7.9 U-channel forming benchmark with drawbeads

A modification of the previous U-channel benchmark (Section 7.8) has been proposed in the NUMISHEET'05 international conference (as benchmark #3) and considers the use of drawbeads. These drawbeads are located on the die and induce complex cyclic bending/unbending conditions as the material flows into it during the forming process. Moreover, the amount of springback after the tools removal is dependent on the drawbeads' penetration, due to the different straining conditions attained. A scheme of this forming process including the tools dimensions is presented in Fig. 7.33, following Stoughton *et al.* (2005). The process consists

of three steps, firstly, the blank holder is moved downwards up to the point where the kiss blocks contact the die, secondly, a punch displacement of 245 [mm] is imposed, thirdly, the tools are removed and the material is allowed to spring back. Here, two drawbeads' penetrations are considered, namely the shallowest (25%, D_b=2.34 [mm]) and the deepest (100%, D_b=9.09 [mm]). A Coulomb's friction coefficient of 0.15 between the surfaces in contact and a blank holding force of 250 [kN] (62.5 [kN] for a quarter section of the blank) are considered. The kiss blocks are used to maintain a constant distance between the blank holder and the die, i.e., the die contacts the kiss blocks since the end of the blank holder closure until the end of the forming step. The imposed black holder force ensures that the kiss blocks are always in contact with the die.

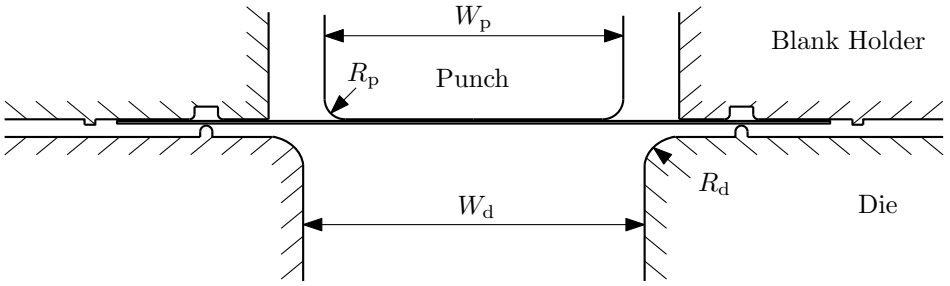

Drawbead and kiss block detail

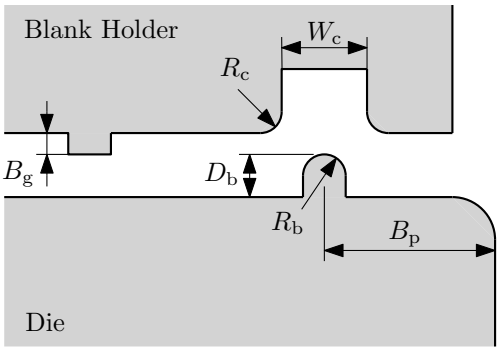

Width of die cavity	$W_d = 319.90$
Radius of die profile	$R_d = 12.00$
Width of punch	$W_p = 224.00$
Radius of punch profile	$R_p = 12.00$
Binder gap	$B_g = 1.42$
Bead position	$B_p = 31.05$
Radius of bead	$R_b = 4.00$
Width of channel	$W_c = 10.80$
Radius of channel	$R_c = 4.00$
Blank width	$B_w = 254.00$
Blank length	$B_l = 1060.00$
Blank thickness	$B_t = 0.991$

[mm]

Figure 7.33: U-channel forming with drawbeads - Scheme of the drawing process.

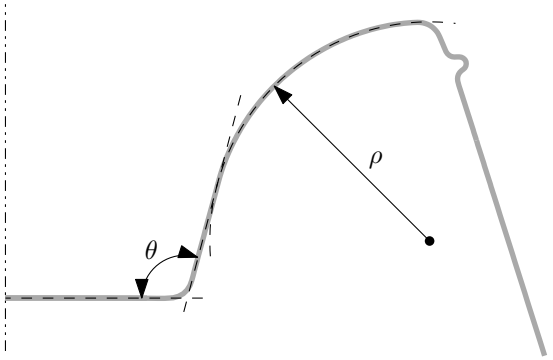

Figure 7.34: U-channel forming with drawbeads - System used to measure the springback and the sidewall curl.

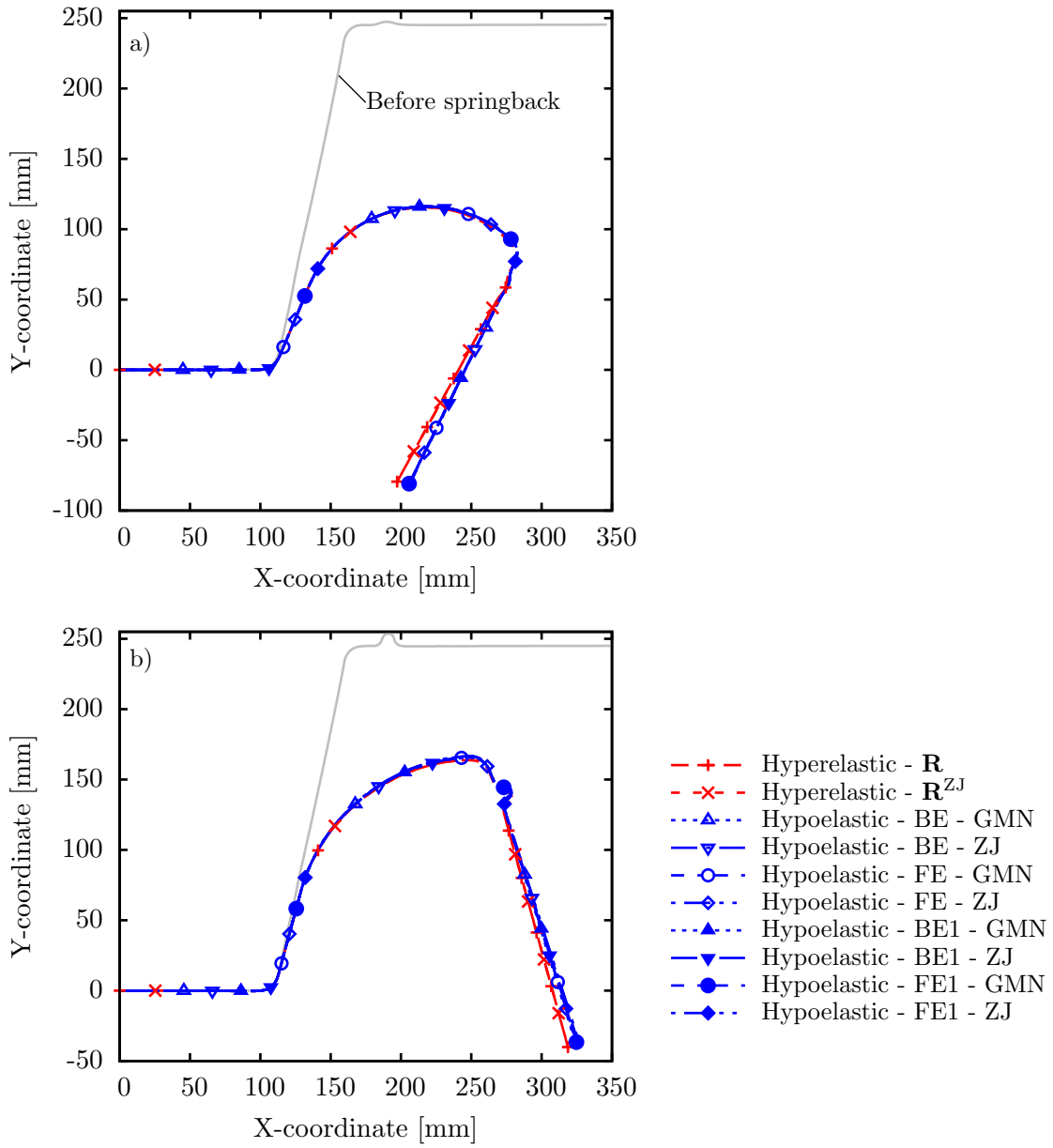

Figure 7.35: U-channel forming with drawbeads - Obtained deformed profiles for a) the shallowest (23%) and b) deepest (100%) penetrations.

The springback in this numerical example is quantitatively compared by means of the measuring system presented in Fig. 7.34, as proposed by Green (2005). Two parameters are used, namely the angle between the bottom and the sidewall, θ, and the radius of curvature of the sidewall, ρ.

The material analysed in this numerical example is the 6022-T43 aluminium alloy, whose hardening parameters' identification was presented in Section 6.6. The anisotropy of the material is described by the *Yld2004-18p* criterion, following the parameters presented in Table 6.3. Only a quarter section of the blank is modelled and analysed due to the orthotropic symmetry of the material, as well as the process symmetry. After a convergence study,

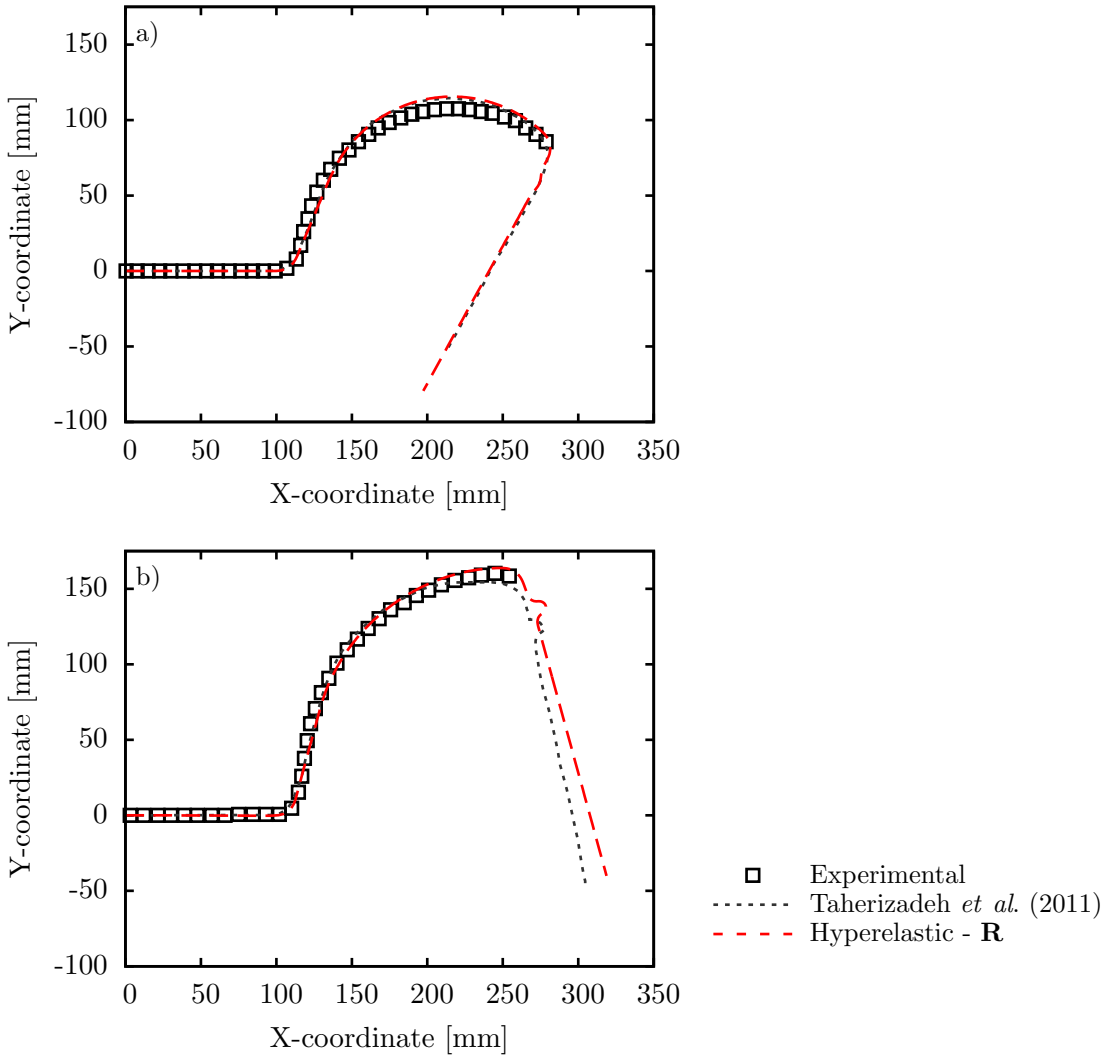

Figure 7.36: U-channel forming with drawbeads - Comparison of the obtained deformed profiles with experimental and numerical data presented by Taherizadeh *et al.* (2011) for a) the shallowest (23%) and b) deepest (100%) penetrations.

the blank is discretized using a mesh of 38400 8-node trilinear finite elements with reduced integration (C3D8R, in ABAQUS), with 5 elements along the thickness direction, whereas the tools are modelled as analytical rigid bodies.

The obtained deformed profiles for the two drawbeads penetrations considering the constitutive models and algorithms in study are presented in Fig. 7.35. A higher amount of springback is predicted for the 25% case and the obtained results are in excellent agreement with each other. Still, differences in the flange's angle are observed between the hyperelastic- and hypoelastic-based models. In Fig. 7.36 the obtained deformed profiles after springback, considering hyperelastic-**R**, are compared with the experimental and numerically obtained profiles presented in the work of Taherizadeh *et al.* (2011). Qualitatively speaking, a good agreement between the obtained profiles and the experimental data is observed, especially

for the 100% case.

The quantitative comparison of the obtained results with the experimental and numerical data presented in Taherizadeh *et al.* (2011) is presented in Table 7.8, by means of the measuring system presented in Fig. 7.34. The differences between the results obtained by the hyperelastic- and hypoelastic-based formulations are mainly on the radius of curvature of the sidewall. In general, the hyperelastic-based formulation predicts more springback than the hypoelastic-based one, in this numerical example. Very small differences are attained between the integration algorithms for the hypoelastic-based formulation, especially between

Table 7.8: U-channel forming with drawbeads - Number of increments and relative times of computation.

25%						
Model	Algorithm	Objective rate	# inc.	Rel. time	θ [Deg.]	ρ [mm]
Hypo-	BE	ZJ	658	1.000 (Ref.)	112.884	89.463
		GMN	658	1.028	112.884	89.459
	BE1	ZJ	658	1.018	112.884	89.463
		GMN	658	1.038	112.884	89.459
	FE	ZJ	822	1.042	112.883	90.256
		GMN	799	1.027	112.869	90.232
	FE1	ZJ	910	1.099	112.862	90.185
		GMN	850	1.060	112.851	90.244
	Rotation tensor					
Hyper-		$\mathbf{R}^{ZJ}$	491	1.337	112.793	87.988
		$\mathbf{R}$	491	1.341	112.793	87.988
Experimental			—	—	106.1	99.6
Taherizadeh *et al.* (2011)			—	—	111.0	86.8
100%						
Model	Algorithm	Objective rate	# inc.	Rel. time	θ [Deg.]	ρ [mm]
Hypo-	BE	ZJ	1058	1.000 (Ref.)	105.077	131.271
		GMN	1054	0.968	105.076	130.880
	BE1	ZJ	1058	1.011	105.077	131.271
		GMN	1054	0.983	105.076	130.880
	FE	ZJ	1467	1.564	105.045	132.304
		GMN	1468	1.519	105.041	132.119
	FE1	ZJ	1777	1.575	105.065	132.404
		GMN	1800	1.562	105.056	132.047
	Rotation tensor					
Hyper-		$\mathbf{R}^{ZJ}$	800	1.506	105.133	127.736
		$\mathbf{R}$	804	1.516	105.129	127.773
Experimental			—	—	100.2	135.9
Taherizadeh *et al.* (2011)			—	—	105.6	104.1

the backward-Euler ones. Globally, the obtained results, characterized by θ and ρ, are in good agreement with the experimental data and provide a better prediction comparatively to the numerical data presented by Taherizadeh *et al.* (2011), which were obtained using combined isotropic-kinematic hardening and the *Yld2000-2D* criterion.

In addition, Table 7.8 also includes the relative times of computation (considering the hypoelastic-BE-ZJ as reference) and the number of step increments required to completely form the part (only the forming step is taken into account). As for the simulations of U-channel forming without drawbeads, in the present numerical example the hyperelastic-based formulation allows for considerably larger step increments comparatively to the hypoelastic-based one. The significantly lower number of required step increments allows for faster computations comparatively to the simulations performed with the forward-Euler algorithms (for the hypoelastic-based formulation). Once more, regarding the computational time the backward-Euler algorithms are the more efficient and the advantage of using the multi-stage return mapping procedure is suppressed by the use of small increments. Is can be seen that the use of the sub-incrementation technique slightly improves the efficiency of the forward-Euler algorithm. Finally, no major differences are obtained in both numerical efficiency and quality of the results, regarding the use of the Zaremba-Jaumann or the Green-McInnis-Naghdi rates.

7.10 Draw/re-draw panel benchmark

In order to assess the performance of the presented constitutive models in situations where several strain path changes occur and both anisotropy and cyclic hardening phenomena have a significant roll in the production of a part, the benchmark #2 proposed in the NUMISHEET'14 international conference in analysed in this section. The main objective of this benchmark is to predict the sprung shape after stamping, restriking and trimming of a metallic sheet panel (Carsley *et al.*, 2013). A scheme of the forming process and the tools dimensions are presented in Fig. 7.37. The initial dimensions of the blank are 300×250×1.1 [mm] (RD×TD×ND). The production of two parts is considered, following different forming steps, namely

Part 1 One forming step with a "larger" tooling radius ($R = 12$ [mm]) to a depth of 51.6 [mm];

Part 2 Two forming steps. The first one with a "larger" tooling radius ($R = 12$ [mm]) to a depth of 51.6 [mm], followed by an additional drawing step with a "smaller" tooling radius ($R = 8$ [mm]) to a greater depth ($u = 53.7$ [mm]).

In the production of both parts, after the forming steps the panels are removed from the tooling, sectioned along a centerline (see Fig. 7.38), and released to allow the measurement of the sprung profile along the trim line (Carsley *et al.*, 2013). In order to prevent wrinkling during the forming steps a blank holder force of 245 [kN] (61.25 [kN] for a quarter section of the blank) is considered.

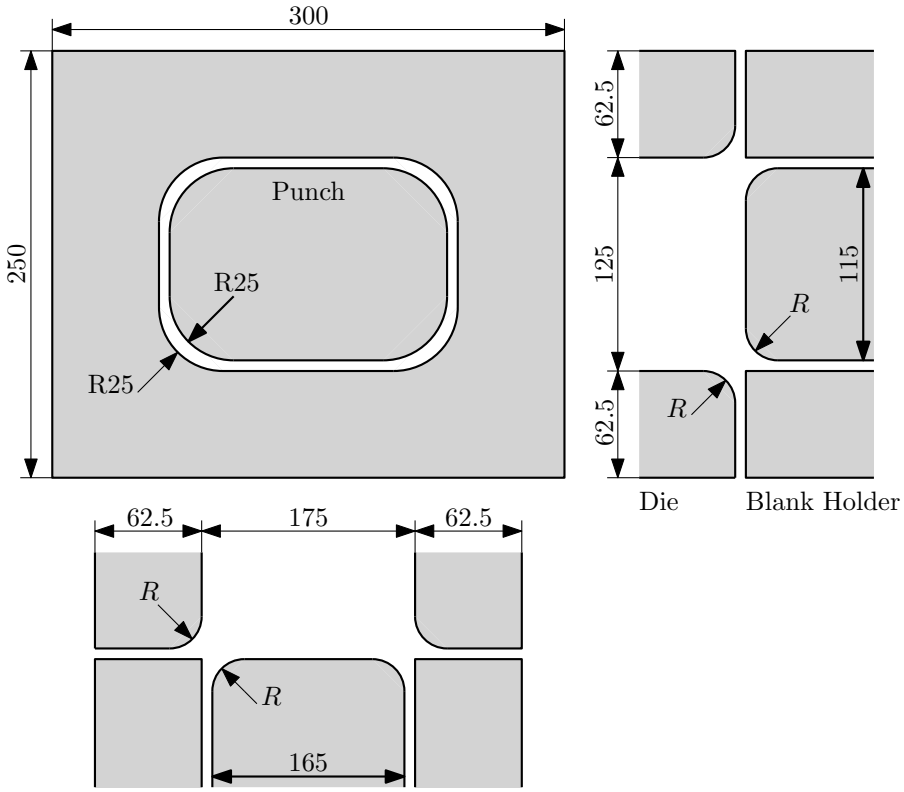

Figure 7.37: Drawing of a panel - Scheme of the drawing process (units in mm).

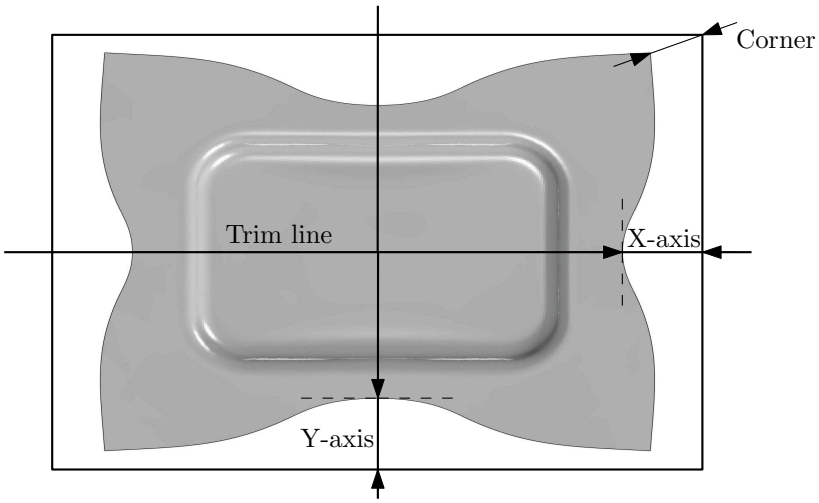

Figure 7.38: Drawing of a panel - Draw-ins measurement and trim line.

In this numerical example the 5182-O aluminium alloy is considered. Both anisotropic *Yld2004-18p* yield function and combined isotropic-kinematic hardening considering two back stress components are taken into account to model the complex mechanical behaviour of the material in study. The constitutive parameters of this material have been identified in Section 6.8. As in some of the previous examples, only a quarter section of the blank is modelled and analysed due to the orthotropic symmetry of the material, as well as the process symmetry. After a convergence study, a mesh constituted by 120700 8-node trilinear

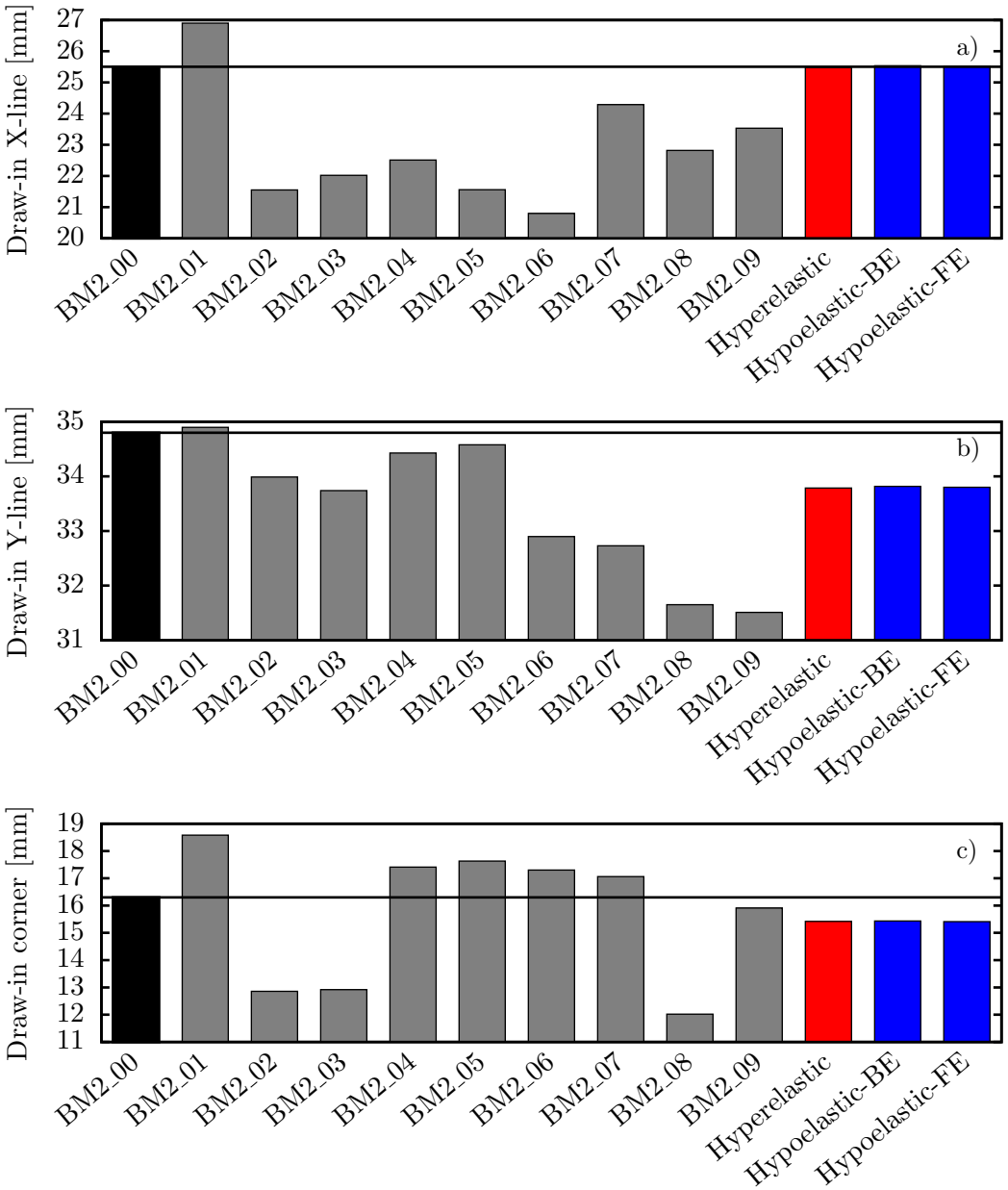

Figure 7.39: Drawing of a panel - Draw-ins after the forming step of Part 1, along a) X-axis, b) Y-axis, and c) corner direction.

finite elements with reduced integration (C3D8R, in ABAQUS) is employed. This way, five elements are considered along the thickness direction and the elements are allocated in the sheet's plane following the distribution 170×142 (length (RD) × width (TD)). The tools are assumed to be rigid bodies modelled by 4-node bilinear quadrilateral rigid elements (R3D4, in ABAQUS). Considering the results obtained in the previous sections, in the numerical simulations performed in this section only Hyperelastic-$\mathbf{R}^{\mathrm{ZJ}}$ and Hypoelastic-ZJ are taken into account.

No coefficient of friction was provided by the benchmark organizers, since the experimental draw-ins (see Fig. 7.38) measured after the forming step of the Part 1 were provided in advance to the participants, so they could calibrate the friction model used in the numerical simulations. Here, the value of the Coulomb's friction coefficient is calibrated in order to fit the numerically obtained draw-in along the X-axis with the experimental one. The choice of the draw-in along the X-axis in detriment of the one along the Y-axis is considered because this is the direction in which the panel is sectioned and the sprung profile is measured. The fitted Coulomb's friction coefficient obtained has the value 0.079. The comparison of the fitted draw-in along the X-axis and the predicted draw-ins along the Y-axis and in the corner with the experimental (BM2_0) draw-ins, and with the ones numerically obtained by the participants of the benchmark, is presented in Fig. 7.39. From this figure, one can see that, in general, and comparing to the results presented by the participants in this benchmark, the obtained results are in good agreement with the experimental draw-ins.

Considering the fitted Coulomb's friction coefficient, the production of the two parts is numerically simulated. Regarding the production of Part 1, the deformed configurations and distributions of the *Yld2004-18p* effective stress after the forming step and after the occurrence of springback are presented in Fig. 7.40. A significant decrease of the *Yld2004-18p* effective stress occurs during the springback step. The deformed configurations, along with the distributions of the accumulated plastic strain, of Part 2, after each forming step and after springback are depicted in Fig. 7.41. As expected, the drawing of the second forming step induces an increase of the accumulated plastic strain. This increase is more pronounced

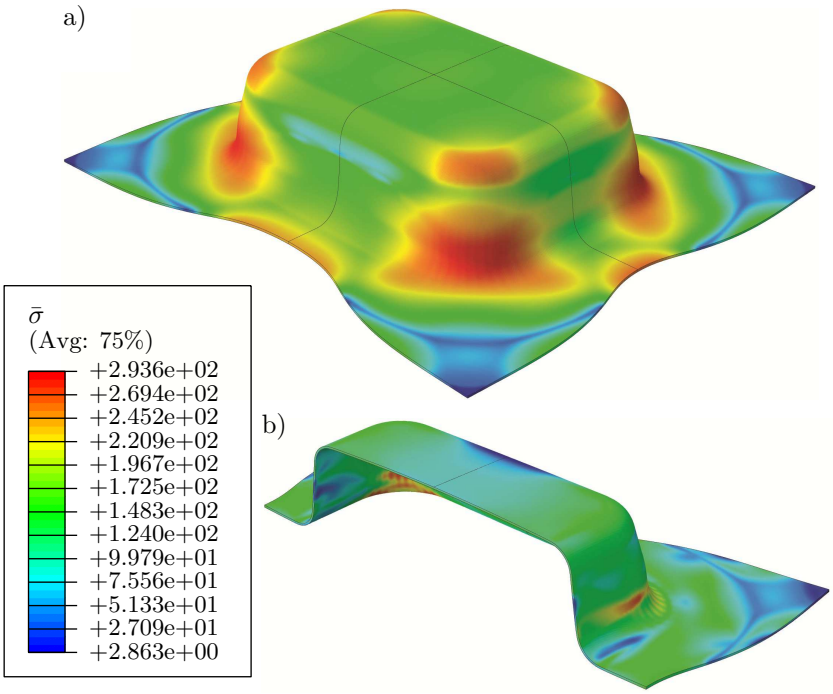

Figure 7.40: Drawing of a panel - Deformed configurations and distributions of *Yld2004-18p* effective stress after the a) forming and b) springback steps of Part 1.

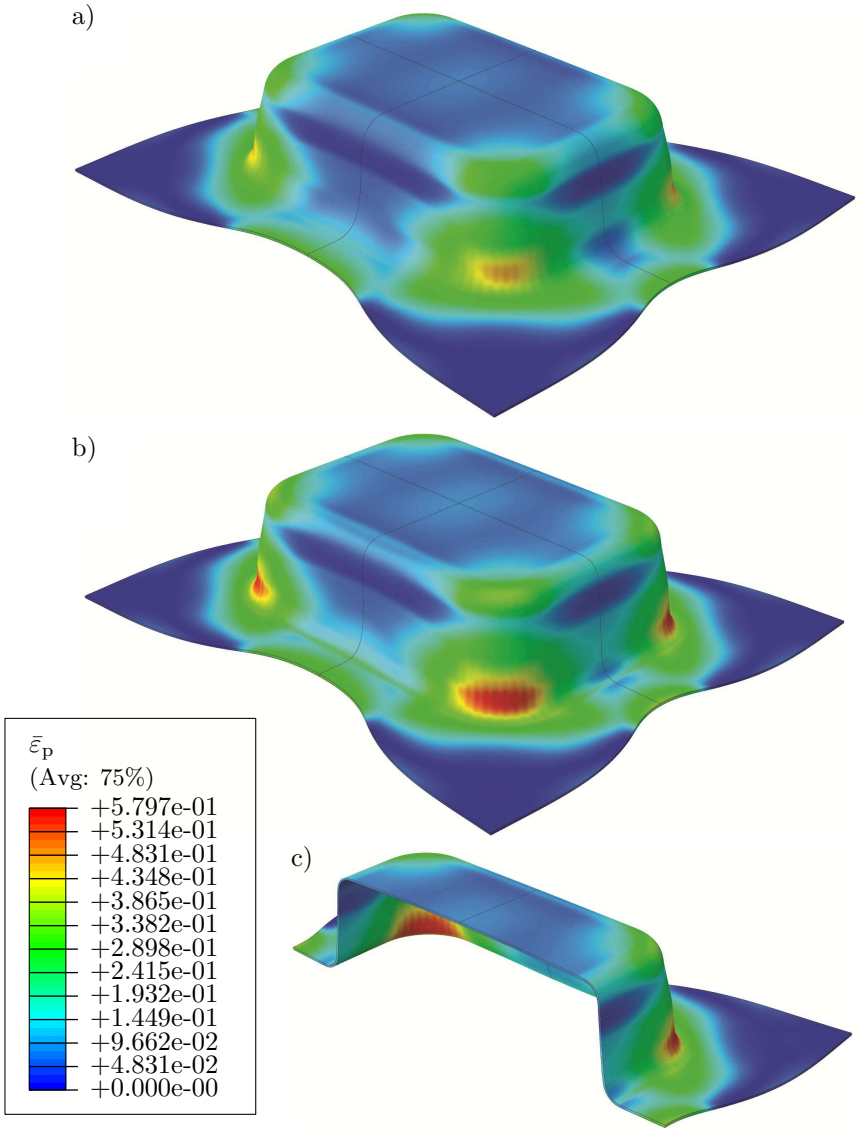

Figure 7.41: Drawing of a panel - Deformed configurations and distributions of accumulated plastic strain after the a) first forming, b) second forming, and c) springback steps of Part 2.

in the bottom corners of the part, meaning that these are the critical locations, in which it is more likely to occur rupture of the material if further drawing is considered.

On the one hand, regarding the production of Part 1, the comparisons of the experimental data and of the results presented by the benchmark's participants with the obtained evolution of the punch force during the forming step and obtained final profile along the trim line after springback are presented in Figs. 7.42 and 7.43, respectively. Similarly to most of the results presented by the benchmark's participants, the predicted punch force-punch displacement relationships overestimate the experimental data. This may be related to the fact that the material does not flow (see draw-ins along Y-axis and in the corner) during the simulation as much as experimentally, meaning that the material offers more resistance to the drawing in the numerical case. The obtained sprung profiles are, in overall, in good agreement with

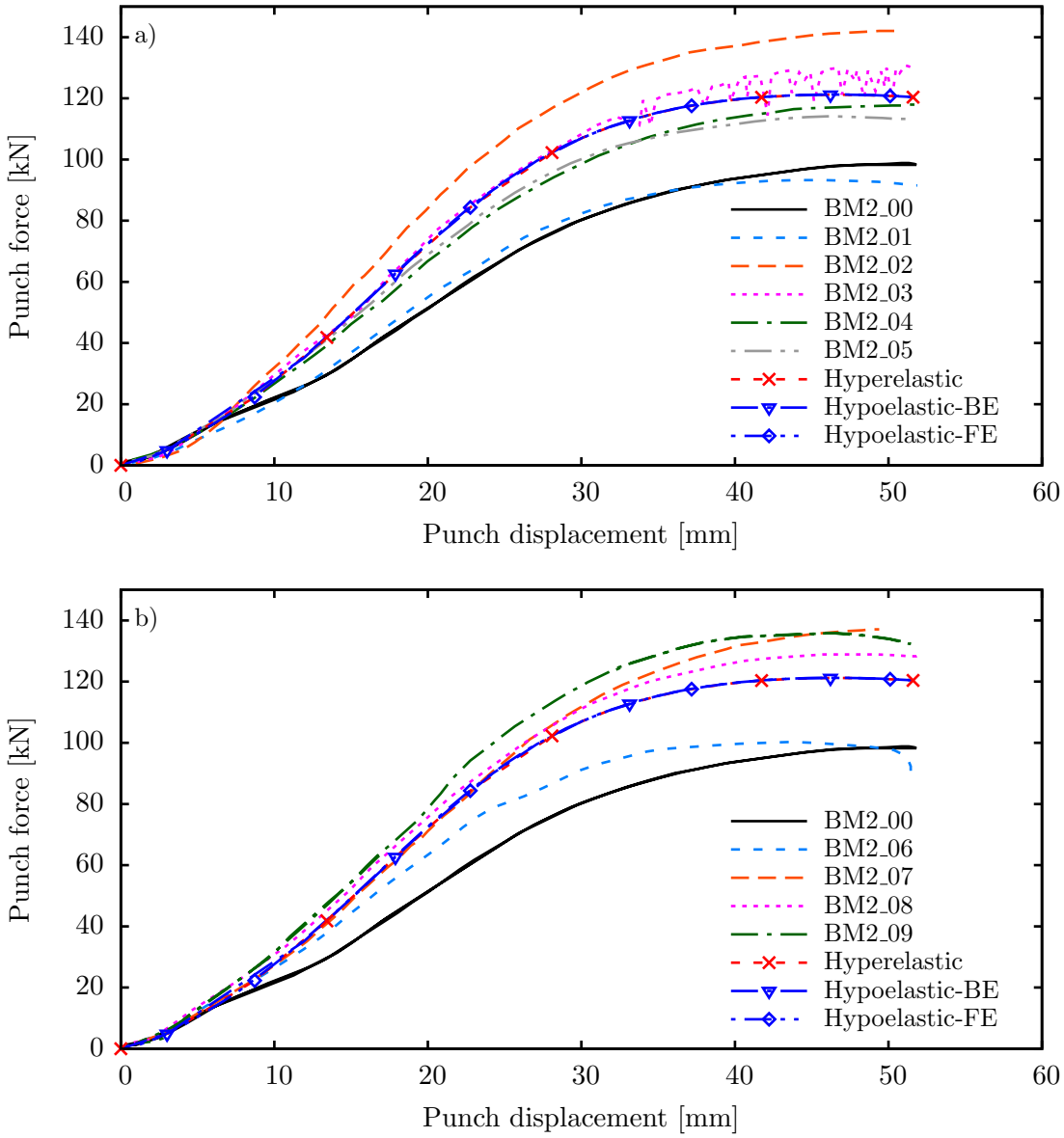

Figure 7.42: Drawing of a panel - Punch force-punch displacement relationships during the forming step of Part 1.

the experimental data and provide a good prediction of the inclination angle of the flange.

Taking the draw-ins, punch force-punch displacement relationships, and sprung profiles into account, the obtained results provide the best reproduction of the experimental data comparatively to the results provided by the benchmark's participants. In fact, the obtained punch force's evolution is not as good as the results provided by some benchmark's participants (e.g., BM2_01 and BM2_06), however they fail in the prediction of the draw-ins and sprung profile.

On the other hand, relatively to the production of Part 2, the obtained results are compared with the experimental data, as well as with the results presented by the benchmark's

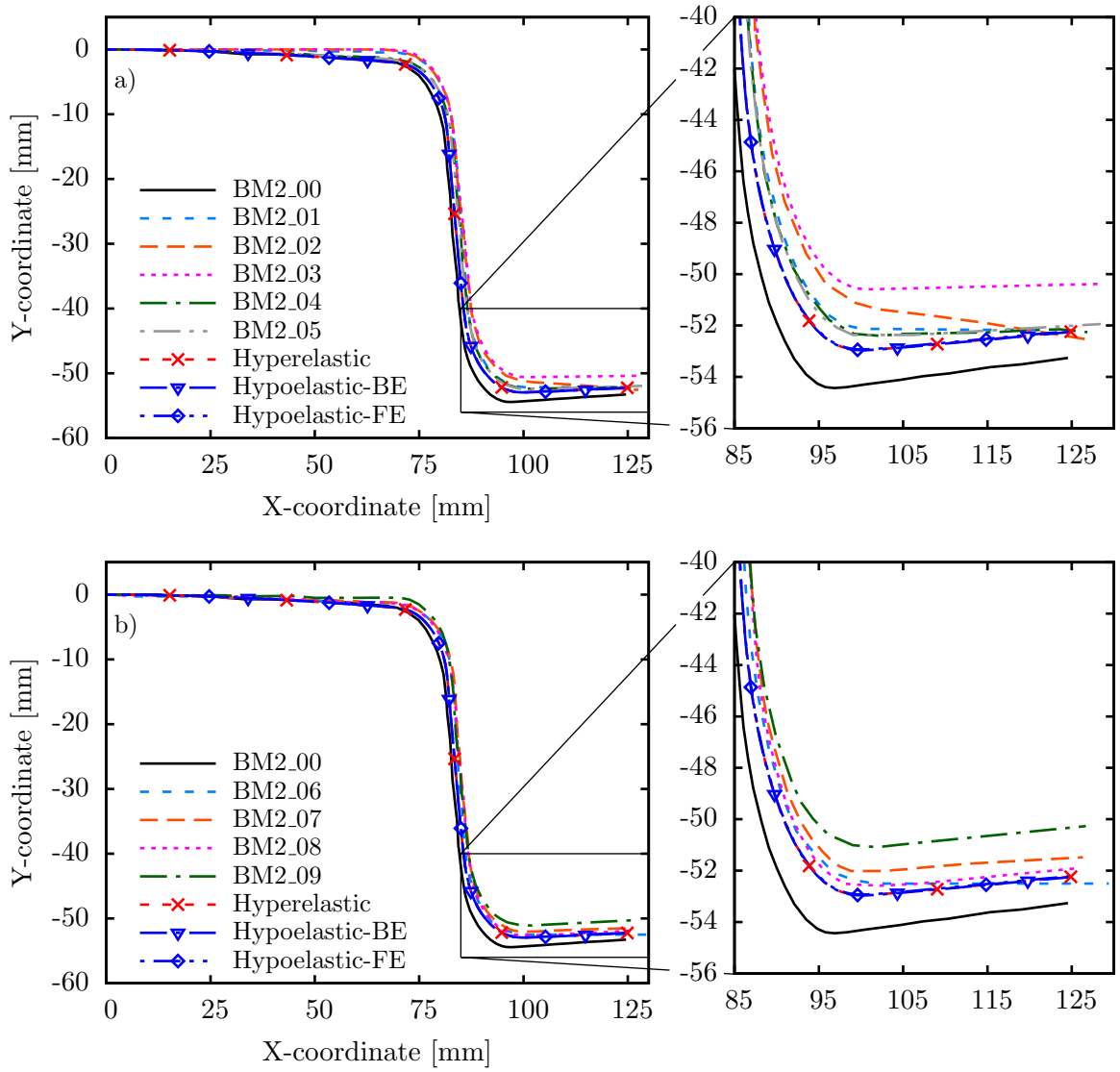

Figure 7.43: Drawing of a panel - Sprung profiles of Part 1 of the center trim line.

participants, in Figs. 7.44-7.46, regarding the draw-ins after the second forming step, punch force's evolution during the second forming step, and sprung profile, respectively. All the draw-ins (with the exception to BM2_00) presented in Fig. 7.44 are predictions, i.e., no additional fitting to adjust the contact model is carried out. The obtained draw-ins are in good agreement with the experimental data. In particular, the ones along the X-axis are an excellent prediction of the experimental ones. This is due to the fact that this direction has been used to calibrate the contact model in the production of Part 1. As during the first forming step, the experimental punch force's evolution is overestimated in the second forming step. Nevertheless, the shape of the obtained curves is similar to the experimental data. Relatively to the sprung profile of Part 2 (Fig. 7.46), the obtained results predict the inclination angle of the flange with excellent accuracy. Comparatively to the springback of Part 1, a higher offset between the experimental and numerical flanges is verified due to the inclination at the

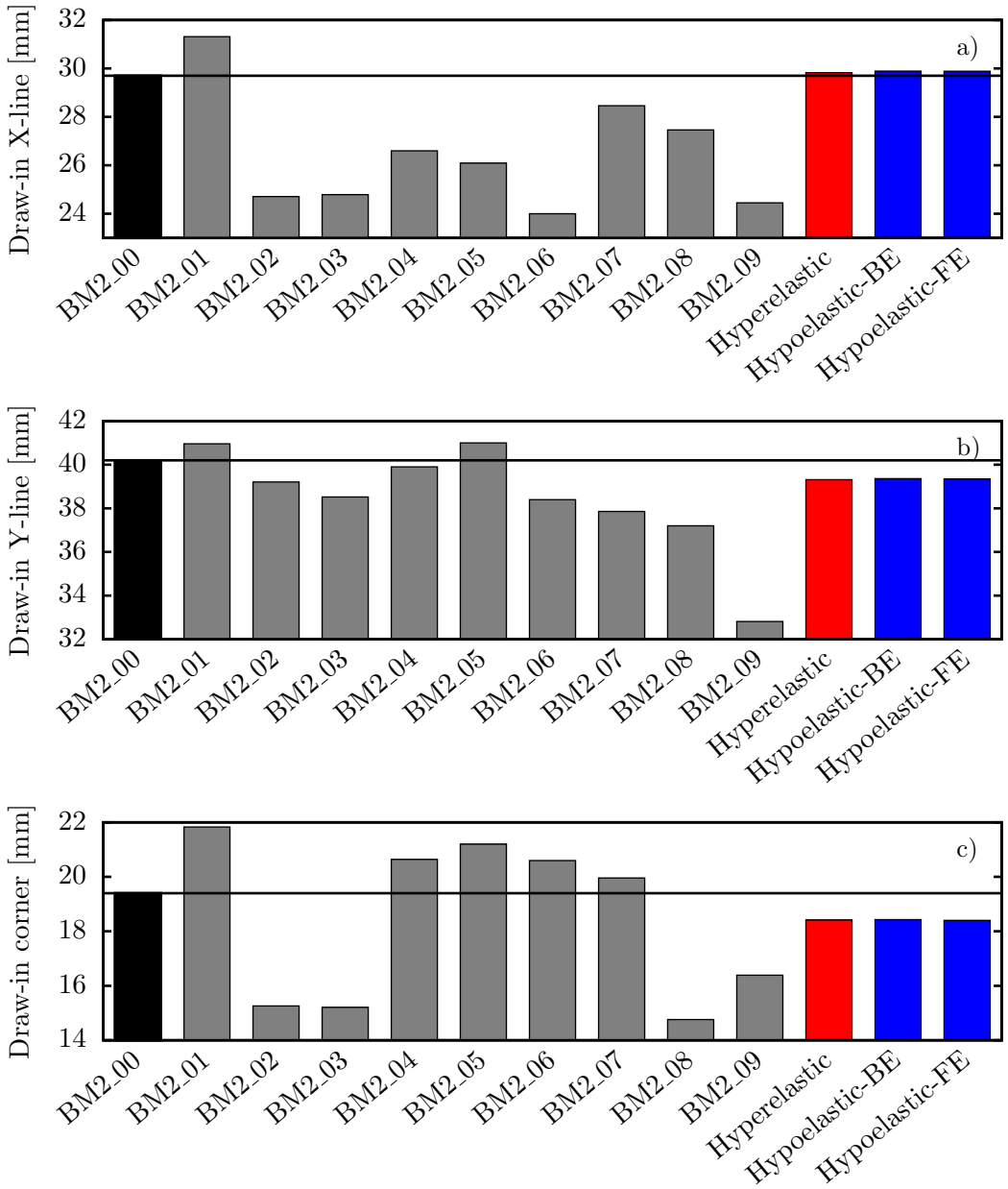

Figure 7.44: Drawing of a panel - Draw-ins after the second forming step of Part 2, along a) X-axis, b) Y-axis, and c) corner direction.

top of the part that occurred experimentally and is not predicted numerically.

As for the Part 1, comparing all the obtained results with the ones presented by the benchmark's participants, one may conclude that the results obtained with the presented constitutive models provide the best reproduction of the experimental data.

When comparing the used constitutive models and numerical algorithms, as in the previous examples, the results obtained with the hyperelastic- and hypoelastic-based models are in excellent agreement with each other. In addition, the algorithms used to integrate the hypoelastic equations provide nearly the same results.

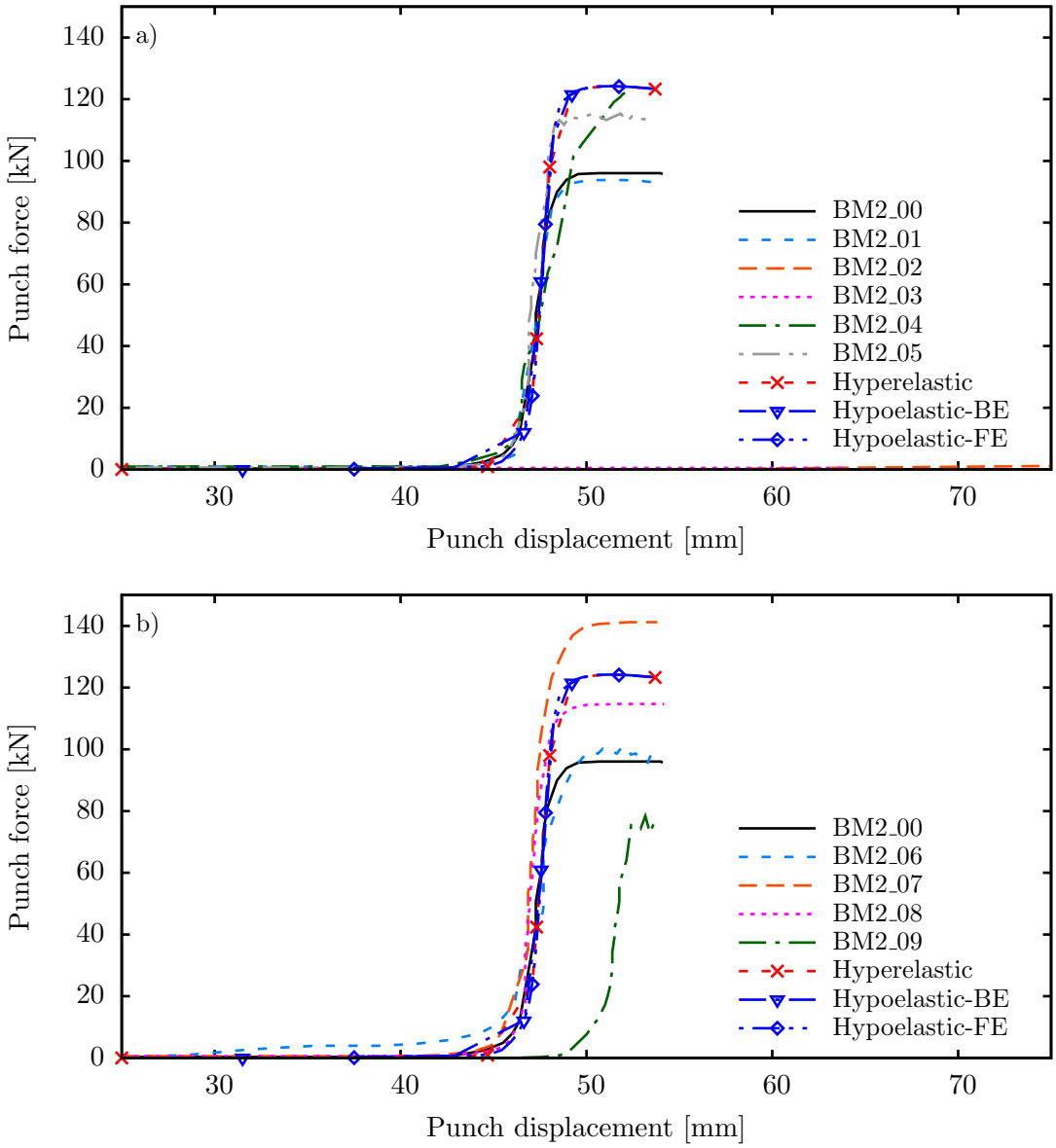

Figure 7.45: Drawing of a panel - Punch force-punch displacement relationships during the second forming step of Part 2.

7.11 Thermoforming

The last numerical example consists of the simulation of the thermoforming process of a polymeric sheet. Among the several methods of processing polymeric materials, thermoforming is one of the oldest and most used, being extensively utilised in the production of a wide range of parts in, e.g., automotive, food, and medical industries. This process is schematically represented in Fig. 7.47. The sheet, in a cold state, is initially clamped and pre-heated up to a specified temperature. Then, it is formed by moving the mould upwards and, subsequently, removing the trapped air by means of a vacuum system. Finally, once the final part is cooled, the mould is moved downwards and a reverse air supply is used to assist the part's

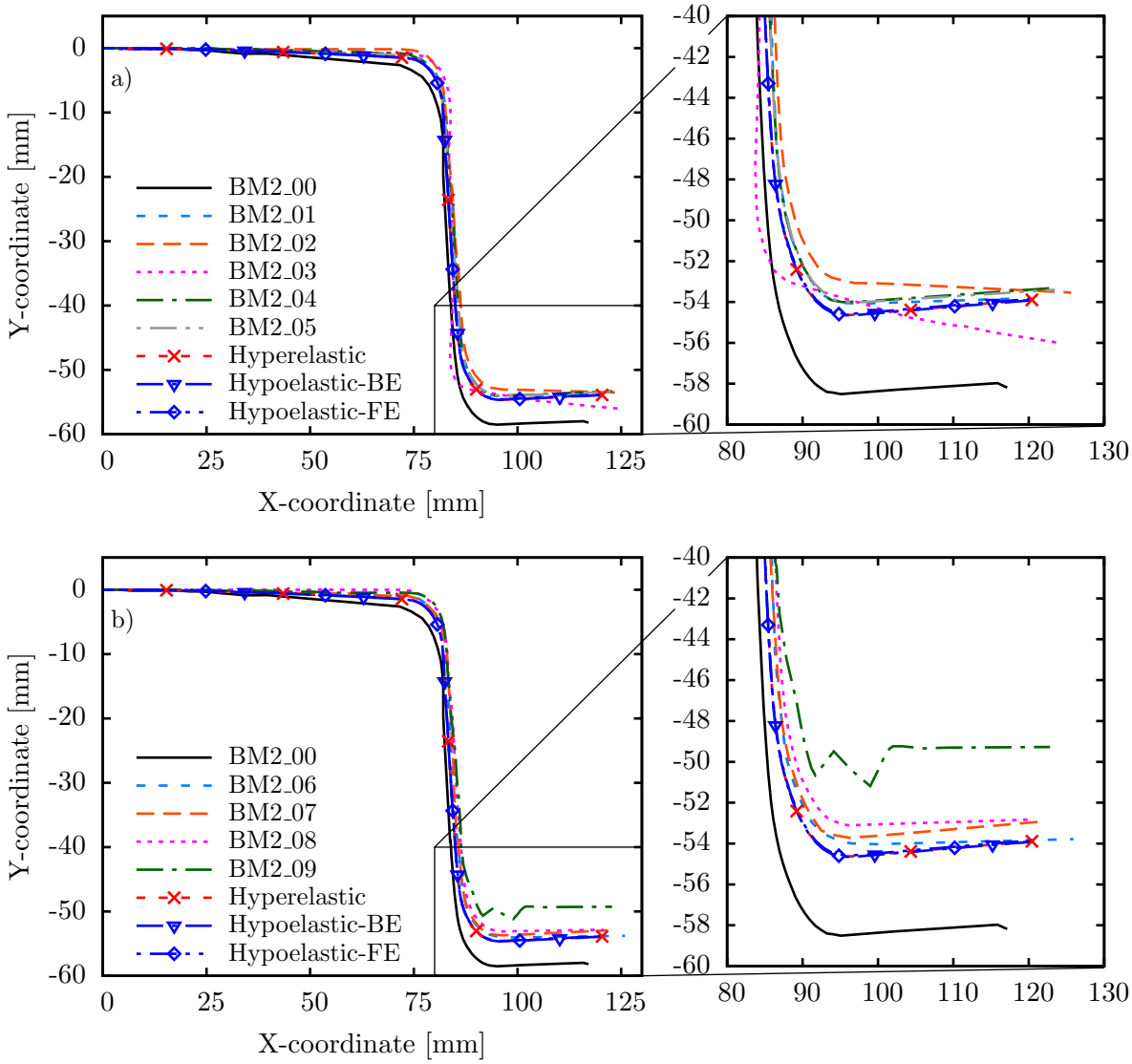

Figure 7.46: Drawing of a panel - Sprung profiles of Part 2 of the center trim line.

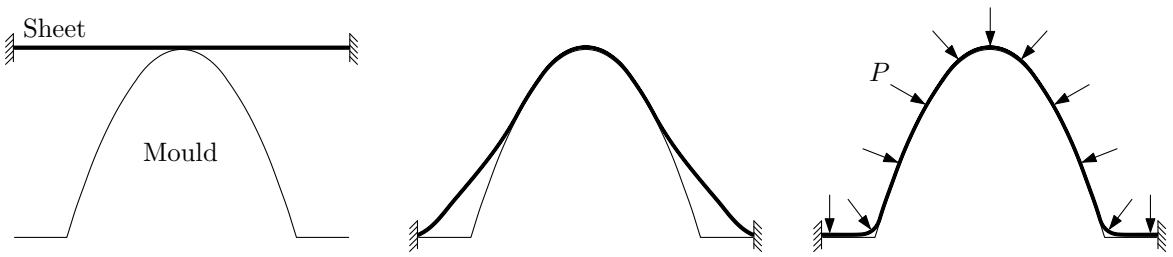

a) Sheet is clamped b) Mould is moved upwards c) Pressure is applied

Figure 7.47: Thermoforming - Scheme of the procedure.

removal from the mould. This example is particularly interesting within the context of the present research work, regarding the comparison of hypoelastic- and hyperelastic-based formulations, due to the considerable amount of elastic deformation that the polymeric material may undergo.

The adopted process parameters, as well as mould and blank dimensions, are the same as the ones used in Brepols *et al.* (2014), along with the material properties, i.e., $E = 7$ [GPa]; $\nu = 0.40$ [-]; linear isotropic hardening following $\sigma_{y_0} - R(\bar{\varepsilon}_p) = 0.7362 + 3.2083\bar{\varepsilon}_p$ [MPa]; no kinematic hardening, i.e., $c = 0.0$ [MPa] and $b = 10^{-8} \approx 0$ [-]; and von Mises yield criterion. Due to the geometrical symmetry of the process, only a quarter section of the flange is analysed in this work. The sheet is discretized by a fine mesh of 12222 (80x126, radial x angular directions) 8-node trilinear finite elements with reduced integration (C3D8R, in ABAQUS), with two elements along the thickness direction. The clamping system is modelled by fixing the nodes of the periphery and the vacuum's effect is simulated through a negative pressure applied to the top surface of the sheet. It is worth noting that the developed constitutive formulations do not take variations of temperature into account, hence a pure mechanical simulation is considered, representing a strong simplification of the real process's conditions. Even so, and as stated before, this example is useful to provide a qualitative comparison between hypoelastic- and hyperelastic-based formulations in the presence of large elastic strains.

Similarly to the numerical example of Section 7.10, and following the same reasoning, only Hyperelastic-$\mathbf{R}^{ZJ}$ and Hypoelastic-BE-ZJ are considered in this section. The deformed configurations and distributions of the accumulated plastic strain after the mould movement and after vacuum, considering Hyperelastic-$\mathbf{R}^{ZJ}$, are presented Fig. 7.48.

The evolution of the stress-strain relationships at the integration point of the element, situated in the upper layer, closer to the sheet' center during the movement of the mould is shown in Fig. 7.49. The transition from elastic to elastoplastic domains is clearly perceptible and, surprisingly, the two constitutive formulations provide very similar results, the curves mainly differing on the maximum strain reached. Whereas in the case of the hypoelastic-based model the maximum strain reached is 54.8%, for the hyperelastic-based model it goes up to 57.9%. The evolution of the mould force with its movement is presented in Fig. 7.50. Once more, the results provided by the two formulations are in excellent agreement with each other.

In Fig. 7.51 the obtained distribution of the effective stress along the radial direction of the sheet after vacuum is depicted. Unlike Figs. 7.49 and 7.50, the distributions of the effective stress predicted by the constitutive formulations differ from each other considerably regarding the stress magnitude, but only negligibly for distances from the sheet's center higher than 120 [mm], whereas the shape of the curves are similar.

In addition to the forming steps (upward movement of the punch and vacuum) analysed in Brepols *et al.* (2014), the springback (removal of vacuum and downward movement of the mould) is also simulated in this work. The procedure considered here to simulate the

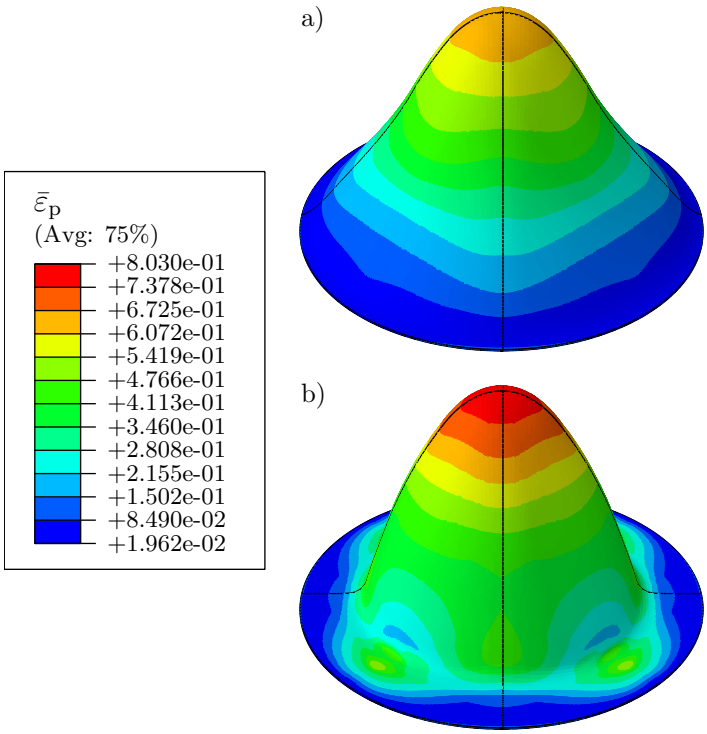

Figure 7.48: Thermoforming - Deformed configurations and distributions of accumulated plastic strain after a) mould movement and b) vacuum.

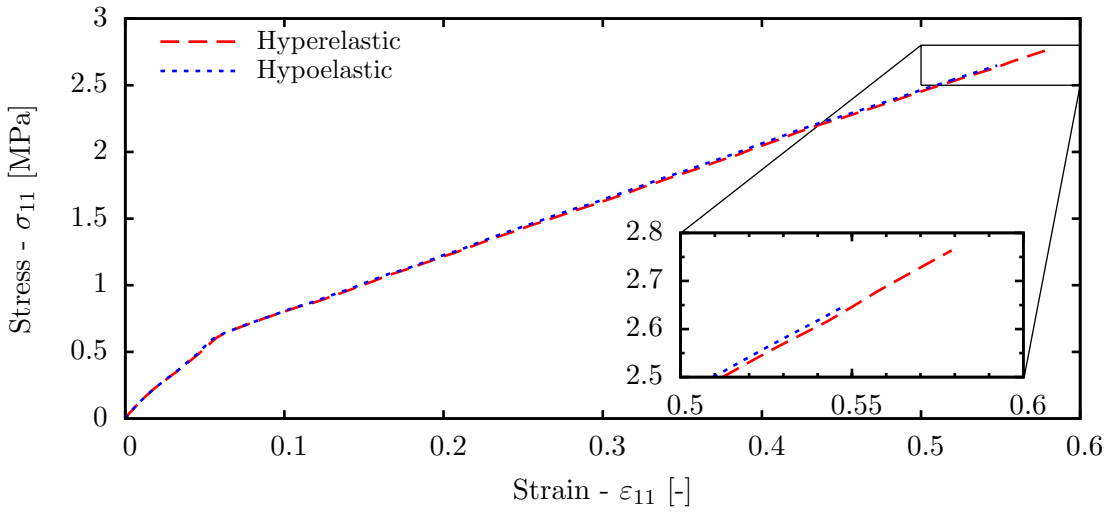

Figure 7.49: Thermoforming - Predicted stress-strain relationships at the integration point, situated in the upper layer of elements, closer to the sheet's center.

springback is clearly nonrealistic regarding the real thermoforming process because a pure mechanical analysis is considered in this work. In real thermoforming processes the part is removed from the mould after cooling, hence reducing considerably the amount of springback due to the change of the mechanical properties of the material during the reduction of temperature. Once more, such a simplification of the process is adopted in order to promote

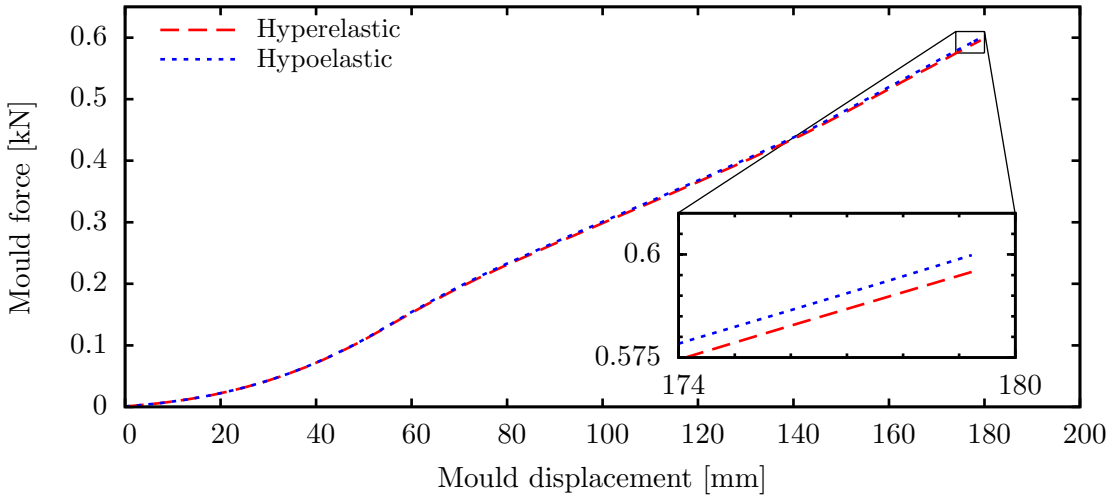

Figure 7.50: Thermoforming - Predicted mould force-mould displacement relationships.

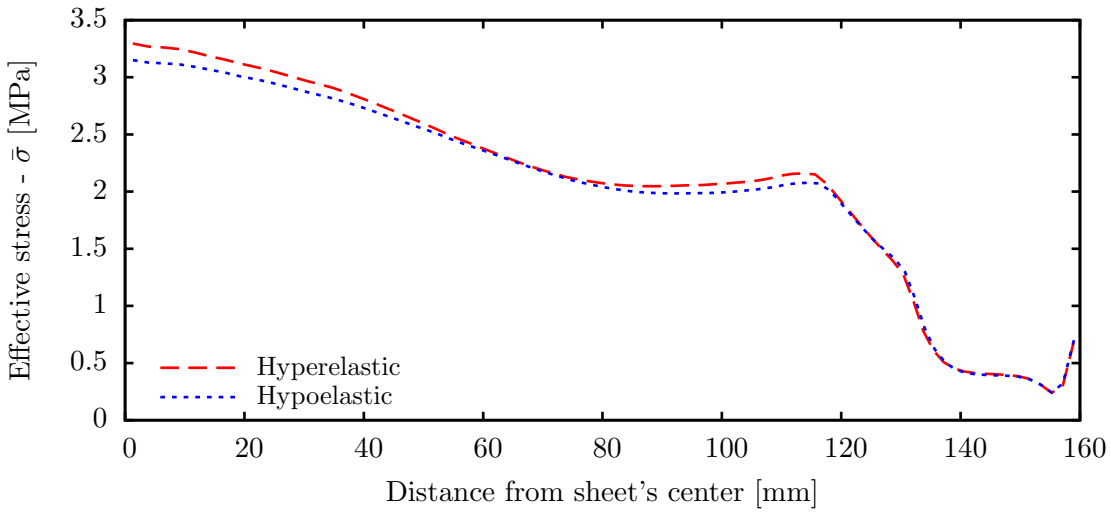

Figure 7.51: Thermoforming - Predicted effective (von Mises) stress distribution along the radial direction after vacuum.

a qualitative comparison between hypoelastic- and hyperelastic-based formulations. As a result, Fig. 7.52 plots the predicted part's profile after springback. The profiles obtained by the two formulations slightly differ from each other (maximum difference of 1.5% at 95 [mm] from the sheet's center), with the hypoelastic-based model predicting less springback than the hyperelastic-based one. This difference is understandable taking into account the lower levels of stress, after vacuum, that is predicted by the hypoelastic-based model.

The differences between hypoelastic- and hyperelastic-based models observed in this numerical example may be due to the elastic constitutive law considered (linear Hooke's law vs. Neo-Hookean law) or the nature of finite strain formulation itself (hypoelastic vs. hyperelastic). On the one hand, the stress-strain responses provided by the two constitutive approaches are similar only at small elastic strains. Fig. 7.53 compares the elastoplastic be-

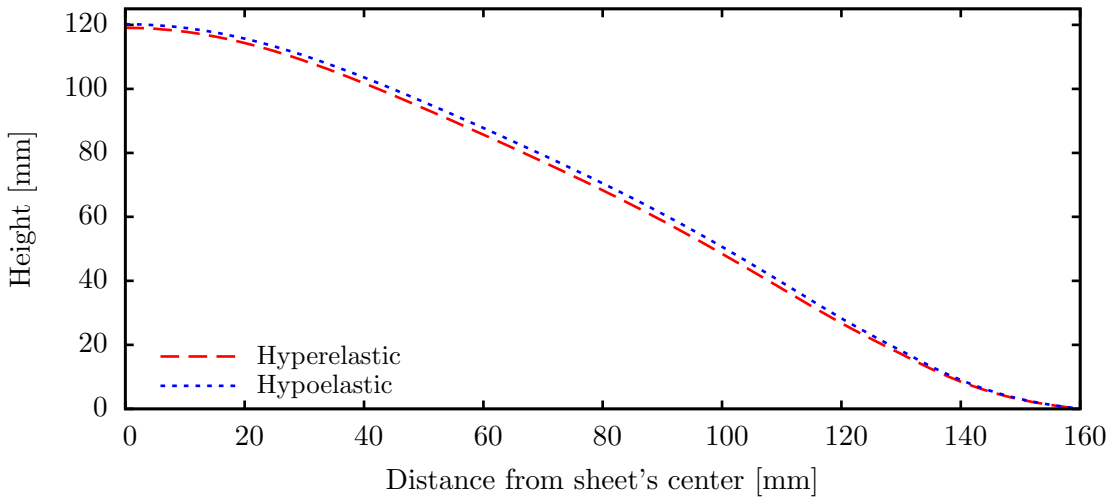

Figure 7.52: Thermoforming - Predicted part's profile after springback.

haviour predicted by the two constitutive approaches for the uniaxial tensile test. In addition, the results of the tensile test considering solely elasticity are also presented. The Neo-Hookean law, used in the hyperelastic-based model, provides a nonlinear stress-strain relation for large elastic strains and higher levels of stress comparatively to the linear Hooke's law, used in the hypoelastic-based model. This may be one of the reasons for the different levels of predicted stress (see Fig. 7.51), and consequently for the different amount of springback (see Fig. 7.52). It is worth noting that one should not do a direct comparison between Figs. 7.49 and 7.53 because of the different stress conditions to which the material is subjected, namely multiaxial (very close to a biaxial stress state) and uniaxial stress states, respectively.

On the other hand, the hypoelastic approach assumes small elastic strains, assumption

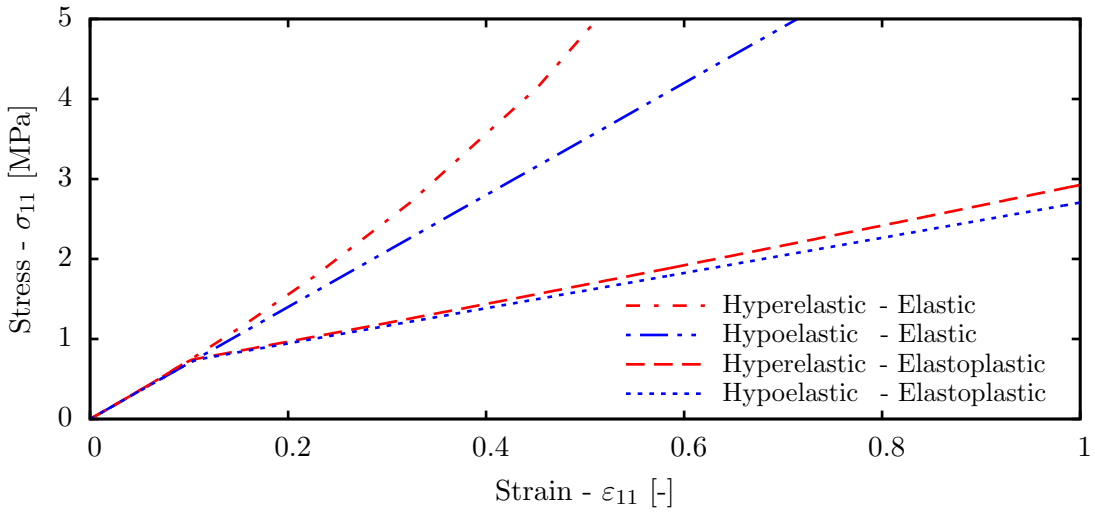

Figure 7.53: Thermoforming - Stress-strain relationships for elasticity and elastoplasticity obtained from the uniaxial tensile test.

that is not verified in this numerical example. In order to confirm the unsuitableness of this approach to simulate the thermoforming process, the process has been simulated considering a fictitious elastic material, i.e., $E = 7$ [GPa]; $\nu = 0.40$ [-]; and no plastic behaviour. The evolution of the effective stress at the integration point, situated in the upper layer of elements, closer to the sheet's center with the position of the mould, during the forming and springback steps, is depicted in Fig. 7.54. The results provided by the two models are in excellent agreement for displacements up to 90 [mm], and then deviate from each other due to the different elastic constitutive laws considered (see Fig. 7.53). The activation and deactivation of the vacuum lead to an abrupt increase and decrease of the effective stress, respectively. The evolutions of the effective stress during the springback for the two models present significant differences. While the hyperelastic-based model predicts a correct decrease of the stress to zero, the hypoelastic-based model predicts a residual stress of 0.71 [MPa] after springback, hence dissipating energy in an elastic deformation path. This dissipation of energy is also verified by looking at the final deformed part after springback (see Fig. 7.55). The dissipation of energy induces residual strains, not allowing the sheet to return to its initial geometry. As expected, the nature of the hyperelastic-based model, namely the use of a strain energy function to describe the elastic behaviour, predicted no dissipation of energy, thus allowing the sheet to exactly return to its initial geometry.

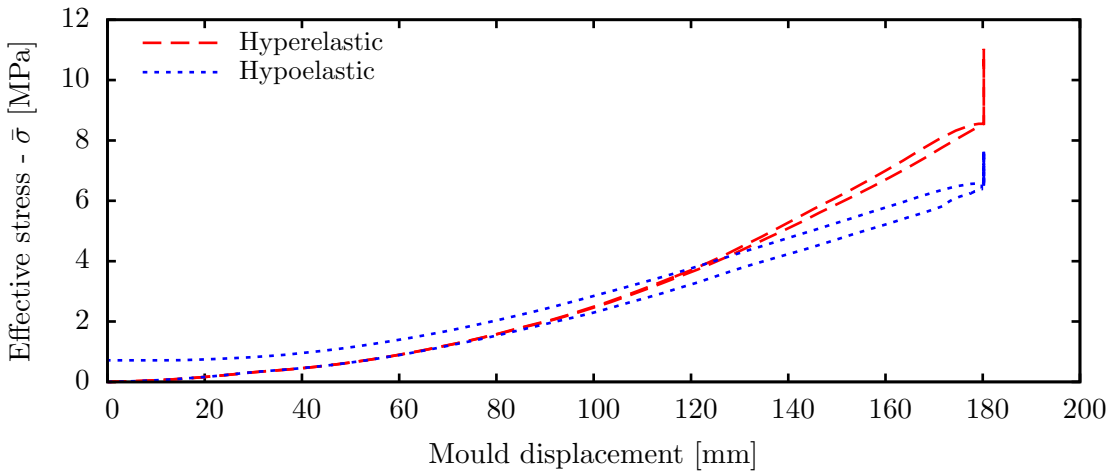

Figure 7.54: Thermoforming - Evolution of the effective stress at the integration point, situated in the upper layer of elements, closer to the sheet's center for the fictitious elastic material.

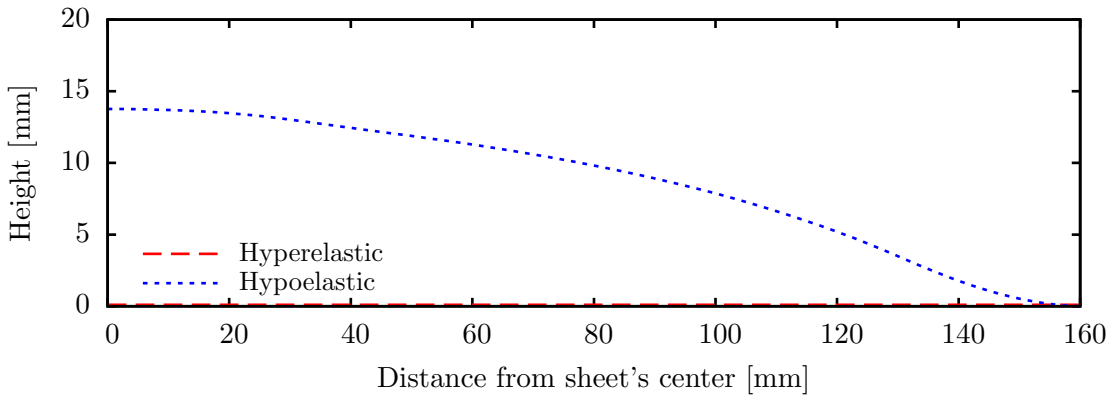

Figure 7.55: Thermoforming - Predicted part's profile after springback for the fictitious elastic material.

Chapter 8

Final remarks

8.1 Conclusions

In this work, advanced elastoplastic constitutive models that provide a reliable representation, at finite strains, of complex plastic behaviours of advanced metallic materials were developed and implemented into Finite Element codes. The motivation for the main objectives of this work was raised by the need of material constitutive models that provide a trustworthy prediction of defects such as earing, thinning, and springback in parts produced by sheet forming. Also, the high industrial competitiveness asks for fast design cycles of complex parts with high performance, thus demanding numerically efficient and robust procedures in, e.g., the implementation of constitutive models into the Finite Element Method.

With this in mind, the developed constitutive models embrace the use of anisotropic yield criteria for the description of plastic anisotropy. The presented constitutive formulations were derived in a general way regarding the yield function, hence allowing the use of any complex quadratic or nonquadratic yield criterion. For an accurate representation of the cyclic hardening phenomena, the developed constitutive formulations include nonlinear kinematic hardening. The studied hardening law consists of the combination of isotropic hardening with nonlinear kinematic hardening following the Armstrong-Frederick law. The approach proposed by Chaboche and Rousselier (1983), in which several back stress components with different evolutions are taken into account, was incorporated in the developed constitutive formulation by means of a modified rheological model of kinematic hardening, hence providing a better reproduction of cyclic hardening phenomena. Bearing in mind that, in the production of real parts the material usually undergoes finite strains and rotations, the constitutive models were derived in the context of hypoelasticity and hyperelasticity.

The rheological model of Armstrong-Frederick kinematic hardening was extended to continuum mechanics considering small strains. A comprehensive study on the algorithmic numerical integration of the constitutive equations of the small strain model was carried out. Both the classical forward- and backward-Euler approaches were adopted. The forward-Euler approach leads to simpler algorithms, easily adaptable to different constitutive models,

when compared to the backward-Euler approach. Nevertheless, backward-Euler algorithms present a higher numerical performance, that leads to more accurate results combined with faster computations. Additionally, particular techniques were employed, namely the sub-incrementation technique and the multi-stage return mapping procedure, in order to enhance the performance of the forward- and backward-Euler algorithms, respectively. The use of the sub-incrementation technique improves the correctness of the integration procedure, thus subsequently providing more accurate results and allowing for larger step increments and faster computations. The main purpose of the multi-stage return mapping procedure is to assist the iterative procedure, inherent to backward-Euler algorithms, when large strain increments occur. The quality of the results is not affected since after the return mapping both backward-Euler algorithms, with and without the multi-stage return mapping procedure, virtually converge to the same value. Due to the small size of the step increments, mainly imposed by contact nonlinearities, in sheet metal forming simulations, the advantage of using this procedure is suppressed, i.e., its effect on the computational time is not significant. Based on the developed small strain model, a finite strain model was formulated following the hypoelastic approach. The algorithmic procedure used in the numerical implementation of the constitutive relations, incorporating objective rates, followed an appropriated objective algorithm. This algorithm, widely used, preserves the structure, and its inherent simplicity, of the numerical algorithms for small strain constitutive models, hence allowing for the direct implementation of the forward- and backward-Euler algorithms developed for small strain elastoplasticity.

A hyperelastic-based constitutive model that describes the considered plastic behaviours was proposed. It has a sounder theoretical background than the hypoelastic model and overcomes its shortcomings. The constitutive relations were directly derived, in a thermodynamically consistent way, from an extension of the rheological model of Armstrong-Frederick kinematic hardening to continuum mechanics. Following a different methodology than the conventional hyperelastic-based elastoplastic models, the constitutive relations are completely expressed in the reference configuration. As a result, the formulation leads to objective tensorial quantities only and the determination of the plastic spin is avoided, leading to solely symmetric tensorial variables. This is advantageous from the computational point of view since it significantly reduces the number of nonlinear relations to be numerically integrated, hence reducing the storage effort and computational time of numerical simulations. In contrast with the majority of the anisotropic hyperelastic-based models present in the literature, the developed formulation is suitable for any quadratic or nonquadratic yield criterion. Moreover, for a correct description of plastic anisotropy in the presence of finite strains and rotations, a new procedure was proposed to ensure that the material's anisotropic axis follow the rigid body motions of the material. For numerical implementation purposes, the evolution equations were numerically integrated by the adaptation of an algorithm that follows a backward-Euler scheme, which is based on the exponential map, to the hyperelastic-based constitutive model in study. The use of the exponential map enables the exact preservation

of the plastic incompressibility, displayed by metallic materials. Moreover, it automatically conserves the symmetry of the internal variables, hence the exponential functions can be exactly determined by employing the spectral decomposition of its tensor-valued arguments.

The developed constitutive models, and algorithms, were implemented in Finite Element codes of numerical simulation by means of material subroutines. These subroutines were structured modularly, enabling the straightforward implementation of different yield criteria and isotropic hardening laws. By carrying out the numerical simulation of several forming processes the performance of the developed constitutive models, and algorithms, was assessed and compared. From the results, it can be seen the significant improvement in the description of cyclic hardening when several back stress components are used and in the modelling of anisotropy with the use of complex nonquadratic yield criteria.

The results provided by the hypoelastic- and hyperelastic-based models are, globally, very similar. Small differences are observed in the description of springback, with the hypoelastic-based model predicting, in general, less springback than the hyperelastic-based one. Two possible reasons for these differences were pointed out, namely the use of different elastic laws and the formulation (hypoelastic vs. hyperelastic) itself. Due to the small elastic strains involved in sheet metal forming processes, these differences are notably small in such processes.

Regarding the time of computation, the hypoelastic-based model is the more efficient one. This is due to the different algorithms used to perform the return mapping. Whereas for hyperelasticity a complex linearization of the residua is carried out, for hypoelasticity the plastic multiplier is computed using a single equation. Nevertheless, the hyperelastic-based model is, in most examples, more efficient than the hypoelastic-based one in terms of the overall convergence of the Finite Element Method, i.e., allowing for larger step increments.

8.2 Future works

Keeping in mind that research is a continuous task and even though the work developed in this Thesis represents an improvement to the state-of-the-art in computational plasticity, further developments in the research fields covered here may be outlined.

Considering the presented work, future guidelines of research should consist of either i) the further improvement of the computational efficiency of the numerical implementation of the developed constitutive models and their use in numerical simulations of different industrial applications and for different materials, or ii) the upgrading of the developed constitutive models aiming at the description of more material behaviours, such as damage, elastic and/or evolving anisotropy, and strain rate and/or temperature dependent plastic behaviour.

The hypoelastic-based model studied in this work considers both Zaremba-Jaumann and Green-McInnis-Naghdi rates, that provide very similar results and computational efficiency in sheet metal forming applications. The implementation of a hypoelastic-based constitutive model using the logarithmic rate could provide an interesting analysis. On the one hand, it

exactly integrates the elastic law, but on the other hand, its computation is more complex. It would be interesting to infer the real benefits of its use in simulation of sheet metal forming processes and its effect on the computational efficiency.

In a global sense, the hyperelastic-based model allows for larger step increments compared to the hypoelastic-based one for the simulation of sheet metal forming applications, requiring though higher times of computation. This means that the hyperelastic-based model has the potential to overcome the numerical efficiency (relatively to the computation time) of the hypoelastic-based one (see Table 7.8). Thus, a thorough study on the improvement of the numerical implementation of the hyperelastic-based model could lead to promising results, such as in the work of Pietryga *et al.* (2014).

In this work, the simulations used to compare the two formulations (hypo- and hyperelastic) considered conventional sheet metal forming and thermoforming processes. On the one hand, it could be interesting to evaluate the performance of the two formulations in, e.g., incremental sheet metal forming applications. In this forming process the material experiences several loading/unloading cycles, hence, considering the dissipation of energy in elastic deformation paths by hypoelastic models, the results provided by the two formulations may present some differences. On the other hand, knowing that the two formulations provide different results when polymeric materials are analysed, the comparison of these results with experimental data to infer the real suitability of hypoelastic-based models to describe the behaviour of such materials could be interesting.

Appendix A

Integration algorithms in small strain theory with several back stresses

The numerical treatment of the constitutive model presented in Section 4.2 for implementation into Finite Element codes is presented here.

The set of differential equations of this constitutive model can be summarized as

$$\dot{\boldsymbol{\sigma}} = \mathbb{D} : (\dot{\boldsymbol{\varepsilon}} - \dot{\lambda}\mathbf{n}), \tag{A.1}$$

$$\dot{\boldsymbol{\alpha}}^j = \dot{\lambda}(c^j\mathbf{n} - b^j\boldsymbol{\alpha}^j) \;\forall\; j = 1\ldots N, \text{ and} \tag{A.2}$$

$$\dot{\bar{\varepsilon}}_{\mathrm{p}} = \dot{\lambda}. \tag{A.3}$$

Employing Equation 4.37 the following integrated formulas are obtained,

$$\boldsymbol{\sigma}_{n+1} = \boldsymbol{\sigma}_n + \mathbb{D} : \Delta\boldsymbol{\varepsilon} - \Delta\lambda\mathbb{D} : \mathbf{n}_{n+\alpha}, \tag{A.4}$$

$$\boldsymbol{\alpha}^j_{n+1} = \boldsymbol{\alpha}^j_n + \Delta\lambda(c^j\mathbf{n}_{n+\alpha} - b^j\boldsymbol{\alpha}^j_{n+\alpha}) \;\forall\; j = 1\ldots N, \text{ and} \tag{A.5}$$

$$\bar{\varepsilon}_{\mathrm{p}_{n+1}} = \bar{\varepsilon}_{\mathrm{p}_n} + \Delta\lambda. \tag{A.6}$$

A.1 Forward-Euler

Following the procedure presented in Section 4.3.3, the incremental consistency condition is represented by

$$\begin{aligned} \Delta\Phi = \mathbf{n}_n : \left(\Delta\boldsymbol{\sigma} - \sum_{j=1}^{N}\Delta\boldsymbol{\alpha}^j\right) - H_n\Delta\bar{\varepsilon}_{\mathrm{p}} = 0 \\ \mathbf{n}_n : \left[\beta_{\boldsymbol{\eta}}\mathbb{D} : \Delta\boldsymbol{\varepsilon} - \Delta\lambda\mathbb{D} : \mathbf{n}_n - \Delta\lambda\sum_{j=1}^{N}(c^j\mathbf{n}_n - b^j\boldsymbol{\alpha}^j_n)\right] - H_n\Delta\lambda = 0. \end{aligned} \tag{A.7}$$

From this equation the increment of the plastic multiplier is obtained as

$$\Delta\lambda = \frac{\mathbf{n}_n : \Delta\boldsymbol{\sigma}^{\text{trial}}}{\mathbf{n}_n : \left[\mathbb{D} : \mathbf{n}_n + \sum_{j=1}^{N}(c^j\mathbf{n}_n - b^j\boldsymbol{\alpha}_n^j)\right] + H_n}. \tag{A.8}$$

The state variables are updated by employing this equation in Equations A.4-A.6. Finally the proportioning procedure is carried out using Equation 4.52 considering that $\boldsymbol{\alpha}_{n+1} = \sum_{j=1}^{N}\boldsymbol{\alpha}_{n+1}^j$. The inclusion of the sub-incrementation technique into this algorithm for this constitutive model can be performed in a straightforward way, following the steps presented in Section 4.3.3.

Consistent elastoplastic tangent modulus Considering the procedure presented in Section 4.3.5, the elastoplastic tangent modulus consistent with the forward-Euler algorithm presented above is given, without derivation, by the expression

$$\mathbb{D}_{\text{ep}}^{\text{alg}} = \frac{\partial(\Delta\boldsymbol{\sigma})}{\partial(\Delta\boldsymbol{\varepsilon})} = \mathbb{D} - \delta\frac{\mathbb{D} : \mathbf{n}\otimes\mathbf{n} : \mathbb{D}}{\mathbf{n} : \left[\mathbb{D} : \mathbf{n} + \sum_{j=1}^{N}(c^j\mathbf{n} - b^j\boldsymbol{\alpha}^j)\right] + H}. \tag{A.9}$$

A.2 Backward-Euler

Adopting the methodology presented in Section 4.3.4 to the constitutive model presented in Section 4.2, the auxiliary residuals are defined as

$$\mathrm{r}_1 = \bar{\eta}(\boldsymbol{\eta}) - [\sigma_{\mathrm{y}_0} - R(\bar{\varepsilon}_{\mathrm{p}_n} + \Delta\lambda)] = 0, \tag{A.10}$$

$$\mathbf{r}_2 = \mathbb{D}^{-1} : \left(\boldsymbol{\sigma} - \boldsymbol{\sigma}^{\text{trial}}\right) + \Delta\lambda\mathbf{n} = \mathbf{0}, \text{ and} \tag{A.11}$$

$$\mathbf{r}_{2+j} = \boldsymbol{\alpha}^j - \boldsymbol{\alpha}_n^j - \Delta\lambda\left(c^j\mathbf{n} - b^j\boldsymbol{\alpha}^j\right) = \mathbf{0} \;\forall\; j = 1\ldots N. \tag{A.12}$$

Applying the Taylor's series expansion on these residuals (considering only the linear terms), for each iteration i the linearised residuals are expressed as

$$\mathrm{r}_1 - H\Delta\Delta\lambda + \mathbf{n} : \Delta\boldsymbol{\sigma} - \sum_{j=1}^{N}\mathbf{n} : \Delta\boldsymbol{\alpha}^j = 0, \tag{A.13}$$

$$\mathbf{r}_2 + \mathbf{n}\Delta\Delta\lambda + \left(\mathbb{D}^{-1} + \Delta\lambda\frac{\partial\mathbf{n}}{\partial\boldsymbol{\eta}}\right) : \Delta\boldsymbol{\sigma} - \Delta\lambda\sum_{j=1}^{N}\frac{\partial\mathbf{n}}{\partial\boldsymbol{\eta}} : \Delta\boldsymbol{\alpha}^j = \mathbf{0}, \text{ and} \tag{A.14}$$

$$\begin{aligned}\mathbf{r}_{2+j} &- \left(c^j\mathbf{n} - b^j\boldsymbol{\alpha}^j\right)\Delta\Delta\lambda - c^j\Delta\lambda\frac{\partial\mathbf{n}}{\partial\boldsymbol{\eta}} : \Delta\boldsymbol{\sigma} + c^j\Delta\lambda\frac{\partial\mathbf{n}}{\partial\boldsymbol{\eta}} : \Delta\boldsymbol{\alpha}^k \\ &+ \left[\left(1 + b^j\Delta\lambda\right)\mathbb{I} + c^j\Delta\lambda\frac{\partial\mathbf{n}}{\partial\boldsymbol{\eta}}\right] : \Delta\boldsymbol{\alpha}^j = \mathbf{0} \;\forall\; j,k = 1\ldots N \;\wedge\; k \neq j.\end{aligned} \tag{A.15}$$

Here and in the following, the superscripts i are omitted for the sake of simplicity. This

system of nonlinear equations can be represented in the matrix form as

$$\mathbf{K_r}\begin{bmatrix}\Delta\Delta\lambda\\ \Delta\boldsymbol{\sigma}\\ \Delta\boldsymbol{\alpha}^1\\ \vdots\\ \Delta\boldsymbol{\alpha}^j\\ \vdots\\ \Delta\boldsymbol{\alpha}^N\end{bmatrix} = -\begin{bmatrix} r_1\\ \mathbf{r}_2\\ \mathbf{r}_3\\ \vdots\\ \mathbf{r}_{2+j}\\ \vdots\\ \mathbf{r}_{2+N}\end{bmatrix}, \tag{A.16}$$

where

$$\mathbf{K_r} = \begin{bmatrix} -H & \mathbf{n} & -\mathbf{n} & \cdots & -\mathbf{n} & \cdots & -\mathbf{n}\\ \mathbf{n} & \mathbb{D}^{-1}+\Delta\lambda\frac{\partial\mathbf{n}}{\partial\boldsymbol{\eta}} & -\Delta\lambda\frac{\partial\mathbf{n}}{\partial\boldsymbol{\eta}} & \cdots & -\Delta\lambda\frac{\partial\mathbf{n}}{\partial\boldsymbol{\eta}} & \cdots & -\Delta\lambda\frac{\partial\mathbf{n}}{\partial\boldsymbol{\eta}}\\ -c^1\mathbf{n}+b^1\boldsymbol{\alpha}^1 & -c^1\Delta\lambda\frac{\partial\mathbf{n}}{\partial\boldsymbol{\eta}} & \frac{\partial\mathbf{r}_3}{\partial\boldsymbol{\alpha}^1} & \cdots & \frac{\partial\mathbf{r}_3}{\partial\boldsymbol{\alpha}^j} & \cdots & \frac{\partial\mathbf{r}_3}{\partial\boldsymbol{\alpha}^N}\\ \vdots & \vdots & \vdots & \ddots & \vdots & & \vdots\\ -c^j\mathbf{n}+b^j\boldsymbol{\alpha}^j & -c^j\Delta\lambda\frac{\partial\mathbf{n}}{\partial\boldsymbol{\eta}} & \frac{\partial\mathbf{r}_{2+j}}{\partial\boldsymbol{\alpha}^1} & \cdots & \frac{\partial\mathbf{r}_{2+j}}{\partial\boldsymbol{\alpha}^j} & \cdots & \frac{\partial\mathbf{r}_{2+j}}{\partial\boldsymbol{\alpha}^N}\\ \vdots & \vdots & \vdots & & \vdots & \ddots & \vdots\\ -c^N\mathbf{n}+b^N\boldsymbol{\alpha}^N & -c^N\Delta\lambda\frac{\partial\mathbf{n}}{\partial\boldsymbol{\eta}} & \frac{\partial\mathbf{r}_{2+N}}{\partial\boldsymbol{\alpha}^1} & \cdots & \frac{\partial\mathbf{r}_{2+N}}{\partial\boldsymbol{\alpha}^j} & \cdots & \frac{\partial\mathbf{r}_{2+N}}{\partial\boldsymbol{\alpha}^N}\end{bmatrix}, \tag{A.17}$$

with

$$\frac{\partial\mathbf{r}_{2+m}}{\partial\boldsymbol{\alpha}^n} = \begin{cases}(1+b^m\Delta\lambda)\,\mathbb{I}+c^m\Delta\lambda\frac{\partial\mathbf{n}}{\partial\boldsymbol{\eta}} & \text{if } m=n\\ c^m\Delta\lambda\frac{\partial\mathbf{n}}{\partial\boldsymbol{\eta}} & \text{if } m\neq n\end{cases} \tag{A.18}$$

The system of equations represented by Equation A.16 may be solved numerically. Here, the analytical closed form solution for the particular model with two back stress components is presented. The adaptation of the presented procedure to a model with a higher number of back stress components may be lengthy but straightforward.

Solving the linearised form of $\mathbf{r}_4$ (see Equation A.15), in order to $\Delta\boldsymbol{\alpha}^2$ yields

$$\Delta\boldsymbol{\alpha}^2 = \frac{\partial(\Delta\boldsymbol{\alpha}^2)}{\partial\mathbf{r}_4}:\mathbf{r}_4+\frac{\partial(\Delta\boldsymbol{\alpha}^2)}{\partial(\Delta\boldsymbol{\alpha}^1)}:\Delta\boldsymbol{\alpha}^1+\frac{\partial(\Delta\boldsymbol{\alpha}^2)}{\partial(\Delta\boldsymbol{\sigma})}:\Delta\boldsymbol{\sigma}+\frac{\partial(\Delta\boldsymbol{\alpha}^2)}{\partial(\Delta\Delta\lambda)}\Delta\Delta\lambda \tag{A.19}$$

where

$$\frac{\partial(\Delta\boldsymbol{\alpha}^2)}{\partial\mathbf{r}_4} = -\mathbb{A}_2^{-1}, \tag{A.20}$$

$$\frac{\partial(\Delta\boldsymbol{\alpha}^2)}{\partial(\Delta\boldsymbol{\alpha}^1)} = -\frac{\partial(\Delta\boldsymbol{\alpha}^2)}{\partial(\Delta\boldsymbol{\sigma})} = -c^2\Delta\lambda\mathbb{A}_2^{-1}:\frac{\partial\mathbf{n}}{\partial\boldsymbol{\eta}}, \text{ and} \tag{A.21}$$

$$\frac{\partial(\Delta\boldsymbol{\alpha}^2)}{\partial(\Delta\Delta\lambda)} = \mathbb{A}_2^{-1} : (c^2\mathbf{n} + b^2\boldsymbol{\alpha}^2), \tag{A.22}$$

with

$$\mathbb{A}_j = \left(1 + b^j\Delta\lambda\right)\mathbb{I} + c^j\Delta\lambda\frac{\partial\mathbf{n}}{\partial\boldsymbol{\eta}} \;\forall\; j = 1, 2. \tag{A.23}$$

Introducing Equation A.19 in the linearised form of $\mathbf{r}_3$ (see Equation A.15) and rearranging it in order to $\Delta\boldsymbol{\alpha}^1$ provides

$$\Delta\boldsymbol{\alpha}^1 = \frac{\partial(\Delta\boldsymbol{\alpha}^1)}{\partial\mathbf{r}_3} : \mathbf{r}_3 + \frac{\partial(\Delta\boldsymbol{\alpha}^1)}{\partial\mathbf{r}_4} : \mathbf{r}_4 + \frac{\partial(\Delta\boldsymbol{\alpha}^1)}{\partial(\Delta\boldsymbol{\sigma})} : \Delta\boldsymbol{\sigma} + \frac{\partial(\Delta\boldsymbol{\alpha}^1)}{\partial(\Delta\Delta\lambda)}\Delta\Delta\lambda, \tag{A.24}$$

where

$$\frac{\partial(\Delta\boldsymbol{\alpha}^1)}{\partial\mathbf{r}_3} = -\mathbb{B}^{-1}, \tag{A.25}$$

$$\frac{\partial(\Delta\boldsymbol{\alpha}^1)}{\partial\mathbf{r}_4} = -c^1\Delta\lambda\mathbb{B}^{-1} : \frac{\partial\mathbf{n}}{\partial\boldsymbol{\eta}} : \frac{\partial(\Delta\boldsymbol{\alpha}^2)}{\partial\mathbf{r}_4}, \tag{A.26}$$

$$\frac{\partial(\Delta\boldsymbol{\alpha}^1)}{\partial(\Delta\boldsymbol{\sigma})} = c^1\Delta\lambda\mathbb{B}^{-1} : \frac{\partial\mathbf{n}}{\partial\boldsymbol{\eta}} : \left[\mathbb{I} - \frac{\partial(\Delta\boldsymbol{\alpha}^2)}{\partial(\Delta\boldsymbol{\sigma})}\right], \text{ and} \tag{A.27}$$

$$\frac{\partial(\Delta\boldsymbol{\alpha}^1)}{\partial(\Delta\Delta\lambda)} = -\mathbb{B}^{-1} : \left[c^1\Delta\lambda\frac{\partial\mathbf{n}}{\partial\boldsymbol{\eta}} : \frac{\partial(\Delta\boldsymbol{\alpha}^2)}{\partial(\Delta\Delta\lambda)} - (c^1\mathbf{n} + b^1\boldsymbol{\alpha}^1)\right], \tag{A.28}$$

with

$$\mathbb{B} = \mathbb{A}_1 + c^1\Delta\lambda\frac{\partial\mathbf{n}}{\partial\boldsymbol{\eta}} : \frac{\partial(\Delta\boldsymbol{\alpha}^2)}{\partial(\Delta\boldsymbol{\alpha}^1)}. \tag{A.29}$$

Considering that $\Delta\boldsymbol{\alpha} = \Delta\boldsymbol{\alpha}^1 + \Delta\boldsymbol{\alpha}^2$, adding Equations A.19 and A.24 yields

$$\Delta\boldsymbol{\alpha} = \frac{\partial(\Delta\boldsymbol{\alpha})}{\partial\mathbf{r}_3} : \mathbf{r}_3 + \frac{\partial(\Delta\boldsymbol{\alpha})}{\partial\mathbf{r}_4} : \mathbf{r}_4 + \frac{\partial(\Delta\boldsymbol{\alpha})}{\partial(\Delta\boldsymbol{\sigma})} : \Delta\boldsymbol{\sigma} + \frac{\partial(\Delta\boldsymbol{\alpha})}{\partial(\Delta\Delta\lambda)}\Delta\Delta\lambda, \tag{A.30}$$

where the auxiliary variables are given by

$$\frac{\partial(\Delta\boldsymbol{\alpha})}{\partial\mathbf{r}_3} = \left[\mathbb{I} + \frac{\partial(\Delta\boldsymbol{\alpha}^2)}{\partial(\Delta\boldsymbol{\alpha}^1)}\right] : \frac{\partial(\Delta\boldsymbol{\alpha}^1)}{\partial\mathbf{r}_3}, \tag{A.31}$$

$$\frac{\partial(\Delta\boldsymbol{\alpha})}{\partial\mathbf{r}_4} = \left[\mathbb{I} + \frac{\partial(\Delta\boldsymbol{\alpha}^2)}{\partial(\Delta\boldsymbol{\alpha}^1)}\right] : \frac{\partial(\Delta\boldsymbol{\alpha}^1)}{\partial\mathbf{r}_4} + \frac{\partial(\Delta\boldsymbol{\alpha}^2)}{\partial\mathbf{r}_4}, \tag{A.32}$$

$$\frac{\partial(\Delta\boldsymbol{\alpha})}{\partial(\Delta\boldsymbol{\sigma})} = \left[\mathbb{I} + \frac{\partial(\Delta\boldsymbol{\alpha}^2)}{\partial(\Delta\boldsymbol{\alpha}^1)}\right] : \frac{\partial(\Delta\boldsymbol{\alpha}^1)}{\partial(\Delta\boldsymbol{\sigma})} + \frac{\partial(\Delta\boldsymbol{\alpha}^2)}{\partial(\Delta\boldsymbol{\sigma})}, \text{ and} \tag{A.33}$$

$$\frac{\partial(\Delta\boldsymbol{\alpha})}{\partial(\Delta\Delta\lambda)} = \left[\mathbb{I} + \frac{\partial(\Delta\boldsymbol{\alpha}^2)}{\partial(\Delta\boldsymbol{\alpha}^1)}\right] : \frac{\partial(\Delta\boldsymbol{\alpha}^1)}{\partial(\Delta\Delta\lambda)} + \frac{\partial(\Delta\boldsymbol{\alpha}^2)}{\partial(\Delta\Delta\lambda)}. \tag{A.34}$$

Introducing Equation A.30 into Equation A.14 and rearranging it in order to $\Delta\boldsymbol{\sigma}$ results

$$\Delta\boldsymbol{\sigma} = \frac{\partial(\Delta\boldsymbol{\sigma})}{\partial\mathbf{r}_2} : \mathbf{r}_2 + \frac{\partial(\Delta\boldsymbol{\sigma})}{\partial\mathbf{r}_3} : \mathbf{r}_3 + \frac{\partial(\Delta\boldsymbol{\sigma})}{\partial\mathbf{r}_4} : \mathbf{r}_4 + \frac{\partial(\Delta\boldsymbol{\sigma})}{\partial(\Delta\Delta\lambda)}\Delta\Delta\lambda, \tag{A.35}$$

employing the following auxiliary variables,

$$\frac{\partial(\Delta\boldsymbol{\sigma})}{\partial\mathbf{r}_2} = -\mathbb{E}^{-1}, \tag{A.36}$$

$$\frac{\partial(\Delta\boldsymbol{\sigma})}{\partial\mathbf{r}_3} = \Delta\lambda\mathbb{E}^{-1} : \frac{\partial\mathbf{n}}{\partial\boldsymbol{\eta}} : \frac{\partial(\Delta\boldsymbol{\alpha})}{\partial\mathbf{r}_3}, \tag{A.37}$$

$$\frac{\partial(\Delta\boldsymbol{\sigma})}{\partial\mathbf{r}_4} = \Delta\lambda\mathbb{E}^{-1} : \frac{\partial\mathbf{n}}{\partial\boldsymbol{\eta}} : \frac{\partial(\Delta\boldsymbol{\alpha})}{\partial\mathbf{r}_4}, \text{ and} \tag{A.38}$$

$$\frac{\partial(\Delta\boldsymbol{\sigma})}{\partial(\Delta\Delta\lambda)} = -\mathbb{E}^{-1} : \left[\mathbf{n} - \Delta\lambda\frac{\partial\mathbf{n}}{\partial\boldsymbol{\eta}} : \frac{\partial(\Delta\boldsymbol{\alpha})}{\partial(\Delta\Delta\lambda)}\right], \tag{A.39}$$

with

$$\mathbb{E} = \mathbb{D}^{-1} + \Delta\lambda\frac{\partial\mathbf{n}}{\partial\boldsymbol{\eta}} : \left[\mathbb{I} - \frac{\partial(\Delta\boldsymbol{\alpha})}{\partial(\Delta\boldsymbol{\sigma})}\right]. \tag{A.40}$$

The expression that establishes the increment of the relative stress tensor, $\Delta\boldsymbol{\eta} = \Delta\boldsymbol{\sigma} - \Delta\boldsymbol{\alpha}$, is then obtained by subtracting Equation A.30 to Equation A.35, resulting in

$$\Delta\boldsymbol{\eta} = \frac{\partial(\Delta\boldsymbol{\eta})}{\partial\mathbf{r}_2} : \mathbf{r}_2 + \frac{\partial(\Delta\boldsymbol{\eta})}{\partial\mathbf{r}_3} : \mathbf{r}_3 + \frac{\partial(\Delta\boldsymbol{\eta})}{\partial\mathbf{r}_4} : \mathbf{r}_4 + \frac{\partial(\Delta\boldsymbol{\eta})}{\partial(\Delta\Delta\lambda)}\Delta\Delta\lambda, \tag{A.41}$$

where

$$\frac{\partial(\Delta\boldsymbol{\eta})}{\partial\mathbf{r}_2} = \left[\mathbb{I} - \frac{\partial(\Delta\boldsymbol{\alpha})}{\partial(\Delta\boldsymbol{\sigma})}\right] : \frac{\partial(\Delta\boldsymbol{\sigma})}{\partial\mathbf{r}_2}, \tag{A.42}$$

$$\frac{\partial(\Delta\boldsymbol{\eta})}{\partial\mathbf{r}_3} = \left[\mathbb{I} - \frac{\partial(\Delta\boldsymbol{\alpha})}{\partial(\Delta\boldsymbol{\sigma})}\right] : \frac{\partial(\Delta\boldsymbol{\alpha})}{\partial\mathbf{r}_3} - \frac{\partial(\Delta\boldsymbol{\alpha})}{\partial\mathbf{r}_3}, \tag{A.43}$$

$$\frac{\partial(\Delta\boldsymbol{\eta})}{\partial\mathbf{r}_4} = \left[\mathbb{I} - \frac{\partial(\Delta\boldsymbol{\alpha})}{\partial(\Delta\boldsymbol{\sigma})}\right] : \frac{\partial(\Delta\boldsymbol{\alpha})}{\partial\mathbf{r}_4} - \frac{\partial(\Delta\boldsymbol{\alpha})}{\partial\mathbf{r}_4}, \text{ and} \tag{A.44}$$

$$\frac{\partial(\Delta\boldsymbol{\eta})}{\partial(\Delta\Delta\lambda)} = \left[\mathbb{I} - \frac{\partial(\Delta\boldsymbol{\alpha})}{\partial(\Delta\boldsymbol{\sigma})}\right] : \frac{\partial(\Delta\boldsymbol{\alpha})}{\partial(\Delta\Delta\lambda)} - \frac{\partial(\Delta\boldsymbol{\alpha})}{\partial(\Delta\Delta\lambda)}. \tag{A.45}$$

Finally, the increment i of the increment of the plastic multiplier is obtained by introducing Equation A.41 into Equation A.13,

$$\Delta\Delta\lambda = \frac{\mathrm{r}_1 + \mathbf{n} : \left[\frac{\partial(\Delta\boldsymbol{\eta})}{\partial\mathbf{r}_2} : \mathbf{r}_2 + \frac{\partial(\Delta\boldsymbol{\eta})}{\partial\mathbf{r}_3} : \mathbf{r}_3 + \frac{\partial(\Delta\boldsymbol{\eta})}{\partial\mathbf{r}_4} : \mathbf{r}_4\right]}{-\mathbf{n} : \frac{\partial(\Delta\boldsymbol{\eta})}{\partial(\Delta\Delta\lambda)} + H}. \tag{A.46}$$

During the iterative procedure, the increment of the plastic multiplier and the stress and back stress tensors are updated, at the end of each iteration i, following Equations 4.77-4.79 and taking Equations A.19, A.24, A.35, and A.46 into account. The employment of the multi-stage return mapping procedure can be done in a straightforward way by applying the steps presented in Section 4.3.4.

Consistent elastoplastic tangent modulus By treating $\boldsymbol{\varepsilon}$ as a variable during the procedure presented above, the elastoplastic tangent modulus consistent with the employed

backward-Euler algorithm can be expressed in closed form, without derivation, by

$$\mathbb{D}_{\mathrm{ep}}^{\mathrm{alg}} = \frac{\partial(\Delta\boldsymbol{\sigma})}{\partial(\Delta\boldsymbol{\varepsilon})} = \mathbb{E}^{-1} + \delta \frac{\frac{\partial(\Delta\boldsymbol{\sigma})}{\partial(\Delta\Delta\lambda)} \otimes \mathbf{n} : \frac{\partial(\Delta\boldsymbol{\eta})}{\partial(\Delta\boldsymbol{\varepsilon})}}{-\mathbf{n} : \frac{\partial(\Delta\boldsymbol{\eta})}{\partial(\Delta\Delta\lambda)} + H}, \tag{A.47}$$

where

$$\frac{\partial(\Delta\boldsymbol{\eta})}{\partial(\Delta\boldsymbol{\varepsilon})} = \left[\mathbb{I} - \frac{\partial(\Delta\boldsymbol{\alpha})}{\partial(\Delta\boldsymbol{\sigma})}\right] : \mathbb{E}^{-1}. \tag{A.48}$$

Appendix B

Linearisation of the residua for the hyperelastoplastic model

The system of nonlinear equations related to the hyperelastoplastic constitutive model with multiple back stress components is constituted by the yield condition and by the integrated formulas for the evolution equations (see Equation 5.174-5.176).

Starting with the flow rule, the residuum associated to its integrated formula is rewritten, for the sake of simplicity, as

$$\mathbf{r}_2 = -\mathbf{C}_{\mathrm{p}_n}^{-1} + \mathbf{U}_{\mathrm{p}}^{-1}\mathbf{Z}\mathbf{U}_{\mathrm{p}}^{-1} = \mathbf{0}, \tag{B.1}$$

where the notation

$$\mathbf{Z} = \exp(\bar{\mathbf{Z}}), \text{ with } \bar{\mathbf{Z}} = \Delta\lambda\mathbf{U}_{\mathrm{p}}^{-1}\mathbf{f}\mathbf{U}_{\mathrm{p}}^{-1}, \tag{B.2}$$

is introduced. The linearisation of Equation B.1 provides

$$\Delta\mathbf{r}_2 = -\underbrace{\Delta\mathbf{C}_{\mathrm{p}_n}^{-1}}_{=0} + \underbrace{\Delta\mathbf{U}_{\mathrm{p}}^{-1}\mathbf{Z}\mathbf{U}_{\mathrm{p}}^{-1} + \mathbf{U}_{\mathrm{p}}^{-1}\mathbf{Z}\Delta\mathbf{U}_{\mathrm{p}}^{-1}}_{{}^{\mathrm{Z}}\mathbb{D} : \Delta\mathbf{U}_{\mathrm{p}}^{-1}} + \mathbf{U}_{\mathrm{p}}^{-1}\Delta\mathbf{Z}\mathbf{U}_{\mathrm{p}}^{-1}, \tag{B.3}$$

where $\Delta\mathbf{C}_{\mathrm{p}_n}^{-1} = \mathbf{0}$ since $\mathbf{C}_{\mathrm{p}_n}$ is a known quantity and kept constant during the iterative procedure and the auxiliary fourth-order tensor ${}^{\mathrm{Z}}\mathbb{D}$ has been introduced,

$${}^{\mathrm{Z}}D_{ijkl} = \delta_{ik}Z_{lm}(U_{\mathrm{p}}^{-1})_{mj} + (U_{\mathrm{p}}^{-1})_{im}Z_{mk}\delta_{lj}. \tag{B.4}$$

Due to the symmetry of $\bar{\mathbf{Z}}$, the exponential tensor function can be represented using the spectral decomposition, resulting on the following linearisation of $\mathbf{Z}$,

$$\Delta\mathbf{Z} = \Delta(\exp\bar{\mathbf{Z}}) = \Delta\left(\sum_{A=1}^{3}\exp(\bar{Z}_A)\boldsymbol{n}_A\otimes\boldsymbol{n}_A\right) = \mathbb{C} : \Delta\bar{\mathbf{Z}}, \tag{B.5}$$

where $\bar{Z}_A$ are the eigenvalues and $\boldsymbol{n}_A$ are the eigenvectors of $\bar{\mathbf{Z}}$. The auxiliary fourth-order

tensor $\mathbb{C}$ is defined by

$$\begin{aligned}\mathbb{C} = \frac{\partial \mathbf{Z}}{\partial \bar{\mathbf{Z}}} = &\sum_{A,B=1}^{3} \exp(\bar{Z}_A)\delta_{AB}\boldsymbol{n}_A \otimes \boldsymbol{n}_A \otimes \boldsymbol{n}_B \otimes \boldsymbol{n}_B \\ &+ \sum_{\substack{A,B=1 \\ A\neq B}}^{3} \frac{1}{2}\frac{\exp(\bar{Z}_B) - \exp(\bar{Z}_A)}{\bar{Z}_B - \bar{Z}_A}(\boldsymbol{n}_A \otimes \boldsymbol{n}_B \otimes \boldsymbol{n}_A \otimes \boldsymbol{n}_B \\ &\qquad + \boldsymbol{n}_A \otimes \boldsymbol{n}_B \otimes \boldsymbol{n}_B \otimes \boldsymbol{n}_A).\end{aligned} \tag{B.6}$$

The linearisation of $\bar{\mathbf{Z}}$ yields

$$\Delta\bar{\mathbf{Z}} = 2\hat{\mathbf{Z}}\Delta\Delta\lambda + 2\Delta\lambda\Delta\hat{\mathbf{Z}}, \tag{B.7}$$

with

$$\hat{\mathbf{Z}} = \mathbf{U}_{\mathrm{p}}^{-1}\frac{\partial\phi}{\partial\mathbf{Y}}\mathbf{U}_{\mathrm{p}}^{-1} \text{ and} \tag{B.8}$$

$$\Delta\hat{\mathbf{Z}} = \underbrace{\Delta\mathbf{U}_{\mathrm{p}}^{-1}\frac{\partial\phi}{\partial\mathbf{Y}}\mathbf{U}_{\mathrm{p}}^{-1} + \mathbf{U}_{\mathrm{p}}^{-1}\frac{\partial\phi}{\partial\mathbf{Y}}\Delta\mathbf{U}_{\mathrm{p}}^{-1}}_{{}^{\mathrm{d}}\mathbb{D} : \Delta\mathbf{U}_{\mathrm{p}}^{-1}} + \mathbf{U}_{\mathrm{p}}^{-1}\Delta\left(\frac{\partial\phi}{\partial\mathbf{Y}}\right)\mathbf{U}_{\mathrm{p}}^{-1}, \tag{B.9}$$

where the auxiliary fourth-order tensor ${}^{\mathrm{d}}\mathbb{D}$ is obtained analogously to ${}^{\mathrm{Z}}\mathbb{D}$ (see Equation B.4). For the sake of particularisation, the *Yld2004-18p* yield function is considered here. Nevertheless, the presented procedure is adaptable to any yield criterion in a straightforward way. Thus, the linearisation of the derivative of the considered yield function is given by

$$\begin{aligned}\Delta\left(\frac{\partial\phi}{\partial\mathbf{Y}}\right) = \Delta\left(\sum_{k=1}^{2}\frac{\partial\phi}{\partial\tilde{\mathbf{s}}^{(k)}} : \bar{\mathbb{L}}^{(k)}\right) &= \sum_{k=1}^{2}\left[\Delta\left(\frac{\partial\phi}{\partial\tilde{\mathbf{s}}^{(k)}}\right) : \bar{\mathbb{L}}^{(k)} + \frac{\partial\phi}{\partial\tilde{\mathbf{s}}^{(k)}} : \Delta\bar{\mathbb{L}}^{(k)}\right] \\ &= \sum_{k=1}^{2}\left[\mathbb{F}_{\mathrm{p}}^{(k)} : \Delta\mathbf{U}_{\mathrm{p}}^{-1} + \sum_{j=1}^{N}\mathbb{F}_{\mathrm{p_i}}^{j(k)} : \Delta(\mathbf{U}_{\mathrm{p_i}}^{j})^{-1}\right],\end{aligned} \tag{B.10}$$

where the relation $\bar{\mathbb{L}}^{(k)} = (\partial\tilde{\mathbf{s}}^{(k)})/(\partial\mathbf{Y})$ is considered and the introduced auxiliary variables are expressed, without derivation, by

$$\mathbb{F}_{\mathrm{p}}^{(k)} = \left[\frac{\partial^2\phi}{\partial(\tilde{\mathbf{s}}^{(k)})^2} : \mathbb{E}_{\mathrm{p}}^{(k)} + \frac{\partial^2\phi}{\partial\tilde{\mathbf{s}}^{(l)}\partial\tilde{\mathbf{s}}^{(k)}} : \mathbb{E}_{\mathrm{p}}^{(l)}\right] : \bar{\mathbb{L}}^{(k)} + \frac{\partial\phi}{\partial\tilde{\mathbf{s}}^{(k)}} : \mathcal{M}^{(k)} \text{ and} \tag{B.11}$$

$$\mathbb{F}_{\mathrm{p_i}}^{j(k)} = \left[\frac{\partial^2\phi}{\partial(\tilde{\mathbf{s}}^{(k)})^2} : \mathbb{E}_{\mathrm{p_i}}^{j(k)} + \frac{\partial^2\phi}{\partial\tilde{\mathbf{s}}^{(l)}\partial\tilde{\mathbf{s}}^{(k)}} : \mathbb{E}_{\mathrm{p_i}}^{j(l)}\right] : \bar{\mathbb{L}}^{(k)} \;\forall\; k,l = 1,2 \;\wedge\; l \neq k, \tag{B.12}$$

where the auxiliary sixth-order auxiliary variables $\mathcal{M}^{(k)}$ are defined by

$$\mathcal{M}^{(k)} = \frac{\partial \bar{\mathbb{L}}^{(k)}}{\partial \mathbf{C}_\mathrm{p}} : \frac{\partial \mathbf{C}_\mathrm{p}}{\partial \mathbf{U}_\mathrm{p}^{-1}}, \text{ with } \left(\frac{\partial \bar{L}^{(k)}}{\partial C_\mathrm{p}}\right)_{ijklxy} = J^{-1}\delta_{kx}F^{-1}_{yn}Q^{\star}_{no}F^{\mathrm{T}}_{ls}Q^{\star}_{sp}L^{(k)}_{ijop}, \quad \left(\frac{\partial C_\mathrm{p}}{\partial U_\mathrm{p}^{-1}}\right)_{ijkl} = -(U_\mathrm{p})_{ik}(C_\mathrm{p})_{lj} - (C_\mathrm{p})_{ik}(U_\mathrm{p})_{lj}. \tag{B.13}$$

In Equation B.10 the relation $\Delta\tilde{\mathbf{s}}^{(k)} = \mathbb{E}_\mathrm{p}^{(k)} : \Delta\mathbf{U}_\mathrm{p}^{-1} + \sum_{j=1}^{N} \mathbb{E}_{\mathrm{p_i}}^{j(k)} : \Delta(\mathbf{U}_{\mathrm{p_i}}^{j})^{-1}$ is assumed, making use of the following auxiliary variables,

$$(E_\mathrm{p}^{(k)})_{ijkl} = \bar{L}^{(k)}_{ijmn}(B_\mathrm{p})_{mnkl} + (M^{(k)})_{ijmnkl}Y_{mn} \tag{B.14}$$

$$\mathbb{E}_{\mathrm{p_i}}^{j(k)} = \bar{\mathbb{L}}^{(k)} : \mathbb{B}_{\mathrm{p_i}}^{j}, \tag{B.15}$$

where

$$\begin{aligned}\Delta\mathbf{Y} &= \Delta\mathbf{C}_\mathrm{p}^{-1}\mathbf{C}\mathbf{S} + \mathbf{C}_\mathrm{p}^{-1}\mathbf{C}\Delta\mathbf{S} - \sum_{j=1}^{N}\Delta\mathbf{X}^{j} \\ &= \mathbb{B}_\mathrm{p} : \Delta\mathbf{U}_\mathrm{p}^{-1} + \sum_{j=1}^{N}\mathbb{B}_{\mathrm{p_i}}^{j} : \Delta(\mathbf{U}_{\mathrm{p_i}}^{j})^{-1},\end{aligned} \tag{B.16}$$

with

$$(B_\mathrm{p})_{ijkl} = \left(\frac{\partial C_\mathrm{p}^{-1}}{\partial U_\mathrm{p}^{-1}}\right)_{imkl} C_{mn}S_{nj} + (C_\mathrm{p}^{-1})_{im}C_{mn}\left(\frac{\partial S}{\partial U_\mathrm{p}^{-1}}\right)_{njkl} - \left(\frac{\partial X}{\partial U_\mathrm{p}^{-1}}\right)_{ijkl} \text{ and} \tag{B.17}$$

$$\mathbb{B}_{\mathrm{p_i}}^{j} = -\frac{\partial \mathbf{X}^{j}}{\partial(\mathbf{U}_{\mathrm{p_i}}^{j})^{-1}}, \tag{B.18}$$

considering the relation $(\partial C_\mathrm{p}^{-1}/\partial U_\mathrm{p}^{-1})_{ijkl} = \delta_{ik}(U_\mathrm{p}^{-1})_{lj} + (U_\mathrm{p}^{-1})_{ik}\delta_{lj}$.

Finally, by introducing Equations B.5, B.7, B.9, and B.10 into the linearisation of $\mathbf{r}_2$ (Equation B.3) yields

$$\Delta\mathbf{r}_2 = \mathbf{K}\Delta\Delta\lambda + (2\Delta\lambda\mathbb{H}_\mathrm{p} + {}^{\mathrm{Z}}\mathbb{D}) : \Delta\mathbf{U}_\mathrm{p}^{-1} + 2\Delta\lambda\sum_{j=1}^{N}\mathbb{H}_{\mathrm{p_i}}^{j} : \Delta(\mathbf{U}_{\mathrm{p_i}}^{j})^{-1}, \tag{B.19}$$

where

$$\mathbf{K} = 2\mathbf{U}_\mathrm{p}^{-1}(\mathbb{C} : \hat{\mathbf{Z}})\mathbf{U}_\mathrm{p}^{-1}, \tag{B.20}$$

$$(H_\mathrm{p})_{ijkl} = (U_\mathrm{p}^{-1})_{im}C_{mnop}({}^{\mathrm{d}}D_{opkl} + (G_\mathrm{p})_{opkl})(U_\mathrm{p}^{-1})_{nj}, \text{ and} \tag{B.21}$$

$$(H_{\mathrm{p_i}}^{j})_{ijkl} = (U_\mathrm{p}^{-1})_{im}C_{mnop}(G_{\mathrm{p_i}}^{j})_{opkl}(U_\mathrm{p}^{-1})_{nj}, \tag{B.22}$$

with

$$(G_{\mathrm{p}})_{ijkl} = (U_{\mathrm{p}}^{-1})_{im}((F_{\mathrm{p}}^{1})_{mnkl} + (F_{\mathrm{p}}^{2})_{mnkl})(U_{\mathrm{p}}^{-1})_{nj} \text{ and} \tag{B.23}$$

$$(G_{\mathrm{p_i}}^{j})_{ijkl} = (U_{\mathrm{p}}^{-1})_{im}((F_{\mathrm{p_i}}^{j(1)})_{mnkl} + (F_{\mathrm{p_i}}^{j(2)})_{mnkl})(U_{\mathrm{p}}^{-1})_{nj}. \tag{B.24}$$

By employing the procedure described above to the residua $\mathbf{r}_{2+j}$ (Equation 5.176) and considering the shorthand notation

$$\mathbf{Z}_{\mathrm{kin}}^{j} = \exp(2\frac{b^j}{c^j}\Delta\lambda\hat{\mathbf{Z}}_{\mathrm{kin}}), \text{ with } \hat{\mathbf{Z}}_{\mathrm{kin}}^{j} = \mathbf{U}_{\mathrm{p_i}}^{-j}\mathbb{P} : (\mathbf{C}_{\mathrm{p_i}}^{j}\mathbf{Y}_{\mathrm{kin}}^{j})\mathbf{C}_{\mathrm{p_i}}^{j}\mathbf{U}_{\mathrm{p_i}}^{-j}, \tag{B.25}$$

and the auxiliary variables

$$\left({}^{\mathrm{Z}}D_{\mathrm{kin}}^{j}\right)_{ijkl} = \delta_{ik}(Z_{\mathrm{kin}}^{j})_{lm}(U_{\mathrm{p_i}}^{-j})_{mj} + (U_{\mathrm{p_i}}^{-j})_{im}(Z_{\mathrm{kin}}^{j})_{mk}\delta_{lj}, \tag{B.26}$$

$$\mathbf{K}_{\mathrm{kin}}^{j} = 2\mathbf{U}_{\mathrm{p_i}}^{-j}(\mathbb{C}_{\mathrm{kin}}^{j} : \hat{\mathbf{Z}}_{\mathrm{kin}}^{j})\mathbf{U}_{\mathrm{p_i}}^{-j}, \tag{B.27}$$

$$(B_{\mathrm{p_{kin}}}^{j})_{ijkl} = (C_{\mathrm{p_i}}^{-j})_{im}\left(\frac{\partial C_{\mathrm{p}}}{\partial U_{\mathrm{p}}^{-1}}\right)_{mnkl} X_{nj}^{j} + (C_{\mathrm{p_i}}^{-j})_{im}(C_{\mathrm{p}})_{mn}\left(\frac{\partial X^j}{\partial U_{\mathrm{p}}^{-1}}\right)_{njkl}, \tag{B.28}$$

$$(B_{\mathrm{p_i kin}}^{j})_{ijkl} = \left(\frac{\partial C_{\mathrm{p_i}}^{-j}}{\partial U_{\mathrm{p_i}}^{-j}}\right)_{imkl}(C_{\mathrm{p}})_{mn}X_{nj}^{j} + (C_{\mathrm{p_i}}^{-j})_{im}(C_{\mathrm{p}})_{mn}\left(\frac{\partial X^j}{\partial U_{\mathrm{p_i}}^{-j}}\right)_{njkl}, \tag{B.29}$$

$$\mathbb{F}_{\mathrm{p_{kin}}}^{j} = \frac{\partial\hat{\mathbf{Z}}_{\mathrm{kin}}^{j}}{\partial\mathbf{U}_{\mathrm{p}}^{-1}} = \frac{\partial\hat{\mathbf{Z}}_{\mathrm{kin}}^{j}}{\partial\mathbf{Y}_{\mathrm{kin}}^{j}} : \mathbb{B}_{\mathrm{p_{kin}}}^{j}, \tag{B.30}$$

$$\mathbb{F}_{\mathrm{p_i kin}}^{j} = \frac{\partial\hat{\mathbf{Z}}_{\mathrm{kin}}^{j}}{\partial\mathbf{U}_{\mathrm{p_i}}^{-j}} = \frac{\partial\hat{\mathbf{Z}}_{\mathrm{kin}}^{j}}{\partial\mathbf{Y}_{\mathrm{kin}}^{j}} : \mathbb{B}_{\mathrm{p_i kin}}^{j} + \frac{\partial\hat{\mathbf{Z}}_{\mathrm{kin}}^{j}}{\partial\mathbf{U}_{\mathrm{p_i}}^{-j}}, \tag{B.31}$$

$$(H_{\mathrm{p_{kin}}}^{j})_{ijkl} = (U_{\mathrm{p_i}}^{-j})_{im}(C_{\mathrm{kin}})_{mnop}(F_{\mathrm{p_{kin}}}^{j})_{opkl}(U_{\mathrm{p_i}}^{-j})_{nj}, \text{ and} \tag{B.32}$$

$$(H_{\mathrm{p_i kin}}^{j})_{ijkl} = (U_{\mathrm{p_i}}^{-j})_{im}(C_{\mathrm{kin}})_{mnop}(F_{\mathrm{p_i kin}}^{j})_{opkl}(U_{\mathrm{p_i}}^{-1})_{nj}, \tag{B.33}$$

the residua related to the kinematic hardening ($\mathbf{r}_{2+j}$) are linearised, without derivation, according to

$$\Delta\mathbf{r}_{2+j} = \frac{b^j}{c^j}\mathbf{K}_{\mathrm{kin}}^{j}\Delta\Delta\lambda + 2\frac{b^j}{c^j}\Delta\lambda\mathbb{H}_{\mathrm{p_{kin}}}^{j} : \Delta\mathbf{U}_{\mathrm{p}}^{-1} + \left(2\frac{b^j}{c^j}\Delta\lambda\mathbb{H}_{\mathrm{p_i kin}}^{j} + {}^{\mathrm{Z}}\mathbb{D}_{\mathrm{kin}}^{j}\right) : \Delta(\mathbf{U}_{\mathrm{p_i}}^{j})^{-1}. \tag{B.34}$$

The residuum r_1 is linearised as follows

$$\begin{aligned}\Delta r_1 = \Delta\Phi(\mathbf{Y}) &= \frac{\partial\Phi}{\Delta\lambda} : \Delta\Delta\lambda + \sum_{k=1}^{2}\frac{\partial\phi}{\partial\tilde{\mathbf{s}}^{(k)}} : \Delta\tilde{\mathbf{s}}^{(k)} \\ &= -H\Delta\Delta\lambda + \sum_{k=1}^{2}\frac{\partial\phi}{\partial\tilde{\mathbf{s}}^{(k)}} : \mathbb{E}_{\mathrm{p}}^{(k)} : \Delta\mathbf{U}_{\mathrm{p}}^{-1} + \sum_{j=1}^{N}\left(\sum_{k=1}^{2}\frac{\partial\phi}{\partial\tilde{\mathbf{s}}^{(k)}} : \mathbb{E}_{\mathrm{p_i}}^{j(k)} : \Delta\mathbf{U}_{\mathrm{p_i}}^{-j}\right),\end{aligned} \tag{B.35}$$

where H is given by Equation 4.24.

In Equations B.25-B.29 and B.32-B.35 the short hand notation $(U_{\mathrm{p_i}}^{-j})_{ij} = [(U_{\mathrm{p_i}}^{j})^{-1}]_{ij}$ is

employed for the sake of simplicity.

As a resume, if the Newton-Raphson method is used to solve the system of equations, the increments, at each iteration i, of the state variables are obtained from

$$\begin{bmatrix} \Delta\Delta\lambda \\ \Delta\mathbf{U}_{\mathrm{p}}^{-1} \\ \Delta(\mathbf{U}_{\mathrm{p_i}}^{1})^{-1} \\ \vdots \\ \Delta(\mathbf{U}_{\mathrm{p_i}}^{j})^{-1} \\ \vdots \\ \Delta(\mathbf{U}_{\mathrm{p_i}}^{N})^{-1} \end{bmatrix} = - \begin{bmatrix} r_1 \\ \mathbf{r}_2 \\ \mathbf{r}_3 \\ \vdots \\ \mathbf{r}_{2+j} \\ \vdots \\ \mathbf{r}_{2+N} \end{bmatrix} \begin{bmatrix} \frac{\partial r_1}{\partial(\Delta\lambda)} & \frac{\partial r_1}{\partial\mathbf{U}_{\mathrm{p}}^{-1}} & \frac{\partial r_1}{\partial(\mathbf{U}_{\mathrm{p_i}}^{1})^{-1}} & \cdots & \frac{\partial r_1}{\partial(\mathbf{U}_{\mathrm{p_i}}^{j})^{-1}} & \cdots & \frac{\partial r_1}{\partial(\mathbf{U}_{\mathrm{p_i}}^{N})^{-1}} \\ \frac{\partial \mathbf{r}_2}{\partial(\Delta\lambda)} & \frac{\partial \mathbf{r}_2}{\partial\mathbf{U}_{\mathrm{p}}^{-1}} & \frac{\partial \mathbf{r}_2}{\partial(\mathbf{U}_{\mathrm{p_i}}^{1})^{-1}} & \cdots & \frac{\partial \mathbf{r}_2}{\partial(\mathbf{U}_{\mathrm{p_i}}^{j})^{-1}} & \cdots & \frac{\partial \mathbf{r}_2}{\partial(\mathbf{U}_{\mathrm{p_i}}^{N})^{-1}} \\ \frac{\partial \mathbf{r}_3}{\partial(\Delta\lambda)} & \frac{\partial \mathbf{r}_3}{\partial\mathbf{U}_{\mathrm{p}}^{-1}} & \frac{\partial \mathbf{r}_3}{\partial(\mathbf{U}_{\mathrm{p_i}}^{1})^{-1}} & \cdots & \mathbb{O} & \cdots & \mathbb{O} \\ \vdots & \vdots & \vdots & \ddots & \vdots & & \vdots \\ \frac{\partial \mathbf{r}_{2+j}}{\partial(\Delta\lambda)} & \frac{\partial \mathbf{r}_{2+j}}{\partial\mathbf{U}_{\mathrm{p}}^{-1}} & \mathbb{O} & \cdots & \frac{\partial \mathbf{r}_{2+j}}{\partial(\mathbf{U}_{\mathrm{p_i}}^{j})^{-1}} & \cdots & \mathbb{O} \\ \vdots & \vdots & \vdots & & \vdots & \ddots & \vdots \\ \frac{\partial \mathbf{r}_{2+N}}{\partial(\Delta\lambda)} & \frac{\partial \mathbf{r}_{2+N}}{\partial\mathbf{U}_{\mathrm{p}}^{-1}} & \mathbb{O} & \cdots & \mathbb{O} & \cdots & \frac{\partial \mathbf{r}_{2+N}}{\partial(\mathbf{U}_{\mathrm{p_i}}^{N})^{-1}} \end{bmatrix}^{-1}, \tag{B.36}$$

where the auxiliary derivatives are summarised as

$$\begin{aligned} &\frac{\partial r_1}{\partial\Delta\lambda} = -H, && \frac{\partial r_1}{\partial\mathbf{U}_{\mathrm{p}}^{-1}} = \sum_{k=1}^{2} \frac{\partial\phi}{\partial\tilde{\mathbf{s}}^{(k)}} : \mathbb{E}_{\mathrm{p}}^{(k)}, && \frac{\partial r_1}{\partial(\mathbf{U}_{\mathrm{p_i}}^{j})^{-1}} = \sum_{k=1}^{2} \frac{\partial\phi}{\partial\tilde{\mathbf{s}}^{(k)}} : \mathbb{E}_{\mathrm{p_i}}^{j(k)}, \\ &\frac{\partial \mathbf{r}_2}{\partial\Delta\lambda} = \mathbf{K}, && \frac{\partial \mathbf{r}_2}{\partial\mathbf{U}_{\mathrm{p}}^{-1}} = 2\Delta\lambda\mathbb{H}_{\mathrm{p}} + {}^{\mathrm{Z}}\mathbb{D}, && \frac{\partial \mathbf{r}_2}{\partial(\mathbf{U}_{\mathrm{p_i}}^{j})^{-1}} = 2\Delta\lambda\mathbb{H}_{\mathrm{p_i}}^{j}, \\ &\frac{\partial \mathbf{r}_{2+j}}{\partial\Delta\lambda} = \frac{b^j}{c^j}\mathbf{K}_{\mathrm{kin}}^{j}, && \frac{\partial \mathbf{r}_{2+j}}{\partial\mathbf{U}_{\mathrm{p}}^{-1}} = 2\frac{b^j}{c^j}\Delta\lambda\mathbb{H}_{\mathrm{p_{kin}}}^{j}, && \frac{\partial \mathbf{r}_{2+j}}{\partial(\mathbf{U}_{\mathrm{p_i}}^{j})^{-1}} = 2\frac{b^j}{c^j}\Delta\lambda\mathbb{H}_{\mathrm{p_{i_{kin}}}}^{j} + {}^{\mathrm{Z}}\mathbb{D}_{kin}^{j}, \end{aligned} \tag{B.37}$$

and the fourth-order tensor $\mathbb{O}$ is defined by $O_{ijkl} = 0$.

Appendix C

Numerical computation of the consistent elastoplastic tangent modulus

Here, the numerical procedure presented by Miehe (1996b) is adapted to the hyperelastic-based constitutive model presented in Section 5.3. The increments of the right Cauchy-Green deformation tensor are related to the second Piola-Kirchhoff stress tensor according to

$$\Delta \mathbf{S} = \bar{\mathbb{D}}^{\text{alg}}_{\text{ep}} : \Delta \mathbf{E}^{(2)} = \bar{\mathbb{D}}^{\text{alg}}_{\text{ep}} : \frac{1}{2} \Delta \mathbf{C}, \tag{C.1}$$

where the fourth-order consistent elastoplastic tangent modulus tensor is numerically computed following the forward difference approximation,

$$(\bar{D}^{\text{alg}}_{\text{ep}})_{ijkl} \approx \frac{2}{\epsilon} \left[S_{ij}({}^{kl}\mathbf{C}^{\epsilon}_{n+1}) - S_{ij}(\mathbf{C}_{n+1}) \right], \tag{C.2}$$

where ϵ is a perturbation parameter, which value of $\epsilon = 10^{-8}$ is a reasonable choice for most applications according to the work of Miehe (1996b) and ${}^{kl}\mathbf{C}^{\epsilon}_{n+1}$ is the perturbed right Cauchy-Green deformation tensor, that is assumed to be expressed as

$${}^{kl}\mathbf{C}^{\epsilon}_{n+1} = \mathbf{C}_{n+1} + \epsilon (\boldsymbol{e}_k \otimes \boldsymbol{e}_l) \mathbf{C}_{n+1}, \tag{C.3}$$

where $\boldsymbol{e}_i$, with $i = 1 \ldots 3$, is the set of basis vectors.

Note that due to the history dependence of the elastoplastic response, the current (perturbed) stress $\mathbf{S}({}^{kl}\mathbf{C}^{\epsilon}_{n+1})$ has to be computed using a integration algorithm. This way, the integration procedure presented in Section 5.3.9.2 is carried out for each set (kl), by keeping the variables at t_n frozen and replacing $\mathbf{C}_{n+1}$ by ${}^{kl}\mathbf{C}^{\epsilon}_{n+1}$. It is worth to mention that due to the symmetry of the variables of the constitutive model only the computation of the set of indices $(kl) = (11),\ (22),\ (33),\ (12),\ (13)$, and (23) is required.

Appendix D

Determination of the analytical Lankford r-values

Regarding the directional r_θ-value obtained from an in-plane uniaxial tensile test with orientation θ relatively to the rolling direction, one must consider that in such loading conditions, the components of the stress tensor $\boldsymbol{\sigma}^\theta$ expressed in the material coordinate system are given by

$$\sigma_{11}^\theta = \sigma_{\mathrm{y}}^\theta \cos^2\theta, \tag{D.1}$$

$$\sigma_{22}^\theta = \sigma_{\mathrm{y}}^\theta \sin^2\theta, \tag{D.2}$$

$$\sigma_{12}^\theta = \sigma_{21}^\theta = \sigma_{\mathrm{y}}^\theta \cos\theta \sin\theta, \text{ and} \tag{D.3}$$

$$\sigma_{33}^\theta = \sigma_{13}^\theta = \sigma_{31}^\theta = \sigma_{23}^\theta = \sigma_{32}^\theta = 0, \tag{D.4}$$

where $\sigma_{\mathrm{y}}^\theta$ is the yield stress in the corresponding direction. Considering this stress tensor, the r-value associated with the orientation angle θ can be obtained from

$$r_\theta = -\frac{\sin^2\theta(\partial\bar{\sigma}/\partial\sigma_{11}^\theta) - \sin 2\theta(\partial\bar{\sigma}/\partial\sigma_{12}^\theta) + \cos^2\theta(\partial\bar{\sigma}/\partial\sigma_{22}^\theta)}{(\partial\bar{\sigma}/\partial\sigma_{11}^\theta) + (\partial\bar{\sigma}/\partial\sigma_{22}^\theta)} \tag{D.5}$$

(see e.g., Aretz (2004)). Taking into account that the stress tensor $\boldsymbol{\sigma}^\theta$ can be represented as $\boldsymbol{\sigma}^\theta = \sigma_{\mathrm{y}}^\theta \bar{\boldsymbol{\sigma}}^\theta$, and that this work considers only positively homogeneous functions of degree 1 (i.e., $f(c\mathbf{x}) = cf(\mathbf{x})$), $\sigma_{\mathrm{y}}^\theta$ can be determined from the yield criterion following

$$\begin{aligned} \bar{\sigma}(\sigma_{\mathrm{y}}^\theta \bar{\boldsymbol{\sigma}}^\theta) - \sigma_{\mathrm{y}} &= 0 \\ \sigma_{\mathrm{y}}^\theta \bar{\sigma}(\bar{\boldsymbol{\sigma}}^\theta) - \sigma_{\mathrm{y}} &= 0 \\ \sigma_{\mathrm{y}}^\theta &= \frac{\sigma_{\mathrm{y}}}{\bar{\sigma}(\bar{\boldsymbol{\sigma}}^\theta)}. \end{aligned} \tag{D.6}$$

Moreover, from the property $\partial\bar{\sigma}/\partial(\sigma_{\mathrm{y}}^\theta \bar{\boldsymbol{\sigma}}^\theta) = \sigma_{\mathrm{y}}^\theta(\partial\bar{\sigma}/\partial(\bar{\boldsymbol{\sigma}}^\theta))$, the directional r_θ value can be

expressed, independently to $\sigma_{\mathrm{y}}^{\theta}$, by

$$r_{\theta} = -\frac{\sin^2\theta(\partial\bar{\sigma}/\partial\bar{\sigma}_{11}^{\theta}) - \sin 2\theta(\partial\bar{\sigma}/\partial\bar{\sigma}_{12}^{\theta}) + \cos^2\theta(\partial\bar{\sigma}/\partial\bar{\sigma}_{22}^{\theta})}{(\partial\bar{\sigma}/\partial\bar{\sigma}_{11}^{\theta}) + (\partial\bar{\sigma}/\partial\bar{\sigma}_{22}^{\theta})}. \tag{D.7}$$

Concerning the biaxial r_{b}-value obtained from, e.g., the in-plane balanced biaxial test, the components of the stress tensor $\boldsymbol{\sigma}^{\mathrm{b}}$ expressed in the material coordinate system are given by

$$\sigma_{11}^{\mathrm{b}} = \sigma_{22}^{\mathrm{b}} = \sigma_{y}^{\mathrm{b}} \tag{D.8}$$

$$\sigma_{33}^{\mathrm{b}} = \sigma_{12}^{\mathrm{b}} = \sigma_{21}^{\mathrm{b}} = \sigma_{13}^{\mathrm{b}} = \sigma_{31}^{\mathrm{b}} = \sigma_{23}^{\mathrm{b}} = \sigma_{32}^{\mathrm{b}} = 0, \tag{D.9}$$

where the biaxial yield stress is denoted by $\sigma_{\mathrm{y}}^{\mathrm{b}}$ and obtained from $\sigma_{\mathrm{y}}^{\mathrm{b}} = \sigma_{\mathrm{y}}/\bar{\sigma}(\bar{\boldsymbol{\sigma}}^{\mathrm{b}})$. Finally, the biaxial r_{b}-value is attained from

$$r_{\mathrm{b}} = \frac{\partial\bar{\sigma}/\partial\sigma_{22}^{\mathrm{b}}}{\partial\bar{\sigma}/\partial\sigma_{11}^{\mathrm{b}}} = \frac{\partial\bar{\sigma}/\partial\bar{\sigma}_{22}^{\mathrm{b}}}{\partial\bar{\sigma}/\partial\bar{\sigma}_{11}^{\mathrm{b}}}. \tag{D.10}$$

Bibliography

Abdel-Karim, M., Ohno, N., 2000. Kinematic hardening model suitable for ratchetting with steady-state. Int. J. Plasticity 16, 225–240.

Abedrabbo, N., Pourboghrat, F., Carsley, J., 2007. Forming of AA5182-O and AA5754-O at elevated temperatures using coupled thermo-mechanical finite element models. Int. J. Plasticity 23, 841–875.

Alves, J. L. C. M., 2003. Simulação numérica do processo de estampagem de chapas metálicas - modelação mecânica e métodos numéricos. Ph.D. thesis, *in Portuguese*.

Alves de Sousa, R. J., Yoon, J. W., Cardoso, R. P. R., Valente, R. A. F., Grácio, J. J., 2007. On the use of a reduced enhanced solid-shell (RESS) element for sheet forming simulations. Int. J. Plasticity 23, 490–515.

Andrade-Campos, A., de Carvalho, R., Valente, R. A. F., 2012. Novel criteria for determination of material model parameters. Int. J. Mech. Sci. 54, 294–305.

Andrade-Campos, A., Thuillier, S., Pilvin, P., Teixeira-Dias, F., 2007. On the determination of material parameters for internal variable thermoelastic-viscoplastic constitutive models. Int. J. Plasticity 23, 1349–1379.

Aravas, N., 1992. Finite elastoplastic transformations of transversely isotropic metals. Int. J. Solids Struct. 29, 2137–2157.

Aretz, H., 2004. Applications of a new plane stress yield function to orthotropic steel and aluminium sheet metals. Model. Simul. Mater. Sci. Eng. 12, 491–509.

Aretz, H., 2008. A simple isotropic-distortional hardening model and its application in elastic-plastic analysis of localized necking in orthotropic sheet metals. Int. J. Plasticity 24, 1457–1480.

Aretz, H., Aegerter, J., Engler, O., 2010. Analysis of earing in deep drawn cups. AIP Conf. Proc. 1252, 417–424.

Aretz, H., Barlat, F., 2013. New convex yield functions for orthotropic metal plasticity. Int. J. Nonlin. Mech. 51, 97–111.

Arghavani, J., Auricchio, F., Naghdabadi, R., 2011. A finite strain kinematic hardening constitutive model based on Hencky strain: General framework, solution algorithm and application to shape memory alloys. Int. J. Plasticity 27, 940–961.

Argyris, J. H., Kleiber, M., 1977. Incremental formulation in nonlinear mechanics and large strain elasto-plasticity - natural approach. Part 1. Comput. Methods Appl. Mech. Engrg. 11, 215–247.

Armstrong, P. J., Frederick, C. O., 1966. A mathematical representation of the multiaxial bauschinger effect. Central Electricity Generating Board Report, Berkeley Nuclear Laboratories, RD/B/N 731.

Artioli, E., Auricchio, F., Beirão da Veiga, L., 2006. A novel "optimal" exponential-based integration algorithm for von-Mises plasticity with linear hardening: Theoretical analysis on yield consistency, accuracy, convergence and numerical investigations. Int. J. Numer. Meth. Engng. 67, 449–498.

Artioli, E., Auricchio, F., Beirão da Veiga, L., 2007. Second-order accurate integration algorithms for von-mises plasticity with a nonlinear kinematic hardening mechanism. Comput. Methods Appl. Mech. Engrg. 196, 1827–1846.

Asaro, R. J., 1983. Crystal plasticity. J. Appl. Mech. 50, 921–934.

Badreddine, H., Saanouni, K., Dogui, A., 2010. On non-associative anisotropic finite plasticity fully coupled with isotropic damage for metal forming. Int. J. Plasticity 26, 1541–1575.

Banabic, D., 2010. Sheet metal forming Processes - Constitutive modelling and numerical simulation. Springer.

Banabic, D., Aretz, H., Comsa, D. S., Paraianu, L., 2005. An improved analytical description of orthotropy in metallic sheets. Int. J. Plasticity 21, 493–512.

Banabic, D., Balan, T., Comsa, D. S., 2000. A new yield criterion for orthotropic sheet metals under plane-stress conditions. In: Banabic, D. (Ed.), Proc. 7th Cold Metal Forming Conference, Cluj

Napoca, 217–224.

Banabic, D., Comsa, D. S., Sester, M., Selig, M., Kubli, W., Mattiasson, K., Sigvant, M., 2008. Influence of constitutive equations on the accuracy of prediction in sheet metal forming simulation. In: Hora, P. (Ed.), Proc. Numisheet 2008, Interlaken, 37–42.

Bargmann, S., Reddy, B. D., Klusemann, B., 2014. A computational study of a model of single-crystal strain-gradient viscoplasticity with an interactive hardening relation. Int. J. Solids Struct. 51, 2754–2764.

Bargmann, S., Svendsen, B., Ekh, M., 2011. An extended crystal plasticity model for latent hardening in polycrystal. Comput. Mech. 48, 631–645.

Barlat, F., Aretz, H., Yoon, J. W., Karabin, M. E., Brem, J. C., Dick, R. E., 2005. Linear transformation-based anisotropic yield functions. Int. J. Plasticity 21, 1009–1039.

Barlat, F., Becker, R. C., Hayashida, Y., Maeda, Y., Yanagawa, M., Chung, K., Brem, J. C., Lege, D. J., Matsui, K., Murtha, S. J., Hattori, S., 1997a. Yielding description for solution strengthened aluminum alloys. Int. J. Plasticity 13, 385–401.

Barlat, F., Brem, J. C., Yoon, J. W., Chung, K., Dick, R. E., Lege, D. J., Pourboghrat, F., Choi, S. H., Chu, E., 2003. Plane stress yield function for aluminum alloy sheets. Part 1: theory. Int. J. Plasticity 19, 1297–1319.

Barlat, F., Chung, K., 1993. Anisotropic potentials for plastically deformation metals. Model. Simul. Mater. Sci. Eng. 1, 403–416.

Barlat, F., Chung, K., 2005. Anisotropic strain rate potential for aluminum alloy plasticity. In: Banabic, D. (Ed.), Proc. 8th ESAFORM Conference on Material Forming. The Publishing House of the Romanian Academy, Cluj-Napoca, 415–418.

Barlat, F., Grácio, J. J., Lee, M.-G., Rauch, E., Vincze, G., 2011. An alternative to kinematic hardening in classical plasticity. Int. J. Plasticity 27, 1309–1327.

Barlat, F., Ha, J., Grácio, J., Lee, M.-G., Rauch, E., Vincze, G., 2012. Extension of homogeneous anisotropic hardening model to cross-loading with latent effects. Int. J. Plasticity 46, 130–142.

Barlat, F., Ha, J., Grácio, J. J., Lee, M.-G., Rauch, E., Vincze, G., 2013. Extension of homogeneous anisotropic hardening model to cross-loading with latent effects. Int. J. Plasticity 46, 130–142.

Barlat, F., Lege, D. J., Brem, J. C., 1991. A six-component yield function for anisotropic materials. Int. J. Plasticity 7, 693–712.

Barlat, F., Lian, J., 1989. Plastic behavior and stretchability of sheet metals. Part I: yield function for orthotropic sheets under plane stress conditions. Int. J. Plasticity 5, 51–66.

Barlat, F., Maeda, Y., Chung, K., Yanagawa, M., Brem, J. C., Hayashida, Y., Lege, D. J., Matsui, K., Murtha, S. J., Hattori, S., Becker, R. C., Makosey, S., 1997b. Yield function development for aluminum alloy sheets. J. Mech. Phys. Solids 45, 1727–1763.

Barlat, F., Richmond, O., 1987. Prediction of tricomponent plane stress yield surfaces and associated flow and failure behavior of strongly textured f.c.c. polycrystaline sheets. Mat. Sci. Eng. 95, 15–29.

Barlat, F., Vincze, G., Grácio, J. J., Lee, M.-G., Rauch, E. F. Tomé, C. N., 2014. Enhancements of homogeneous anisotropic hardening model and application to mild and dual-phase steels. Int. J. Plasticity 58, 201–218.

Beaudoin, A. J., Dawson, P. R., Mathur, K. K., Kocks, U. F., Korzekwa, D. A., 1994. Application of polycrystal plasticity to sheet forming. Comput. Methods Appl. Mech. Engrg. 117, 49–70.

Bertram, A., 1998. An alternative approach to finite plasticity based on material isomorphisms. Int. J. Plasticity 52, 353–374.

Boehler, J.-P., 1979. A simple derivation of representations for non-polynomial constitutive equations in some cases of anisotropy. Zeitschrift fr Angewandte Mathematik und Mechanik 59, 157–167.

Böhlke, T., Risy, G., Bertram, A., 2006. Finite element simulation of metal forming operation with texture based material models. Modelling Simul. Mater. Sci. Eng. 14, 365–387.

Brepols, T., Vladimirov, I. N., Reese, S., 2014. Numerical comparison of isotropic hypo- and hyperelastic-based plasticity models with application to industrial forming processes. Int. J. Plasticity 63, 18–48.

Bron, F., Besson, J., 2003. A yield function for anisotropic materials. Application to aluminum alloys. Int. J. Plasticity 20, 937–963.

Bruhns, O. T., Xiao, H., Meyers, A., 1999. Self-consistent eulerian rate type elasto-plasticity models based upon the logarithmic stress rate. Int. J. Plasticity 15, 479–520.

Brünig, M., Chyra, O., Albrecht, D., Driemeier, L., Alves, M., 2008. A ductile damage criterion at various stress triaxilities. Int. J. Plasticity 24, 1731–1755.

Caminero, M. Á., Montás, F. J., Bathe, K.-J., 2011. Modeling large strain anisotropic elasto-plasticity with logarithmic strain and stress measures. Comput. Struct. 89, 826–843.

Cao, J., Lin, J., 2008. A study on formulation of objective functions for determining material models. Int. J. Mech. Sci. 50, 193–204.

Cardoso, R. P. R., Yoon, J. W., 2009. Stress integration method for a nonlinear kinematic/isotropic hardening model and its characterization based on polycrytal plasticity. Int. J. Plasticity 25, 1684–1710.

Carsley, J. E., Xia, C., Yang, L., Stoughton, T. B., Xu, S., Hartfield-Wünsch, S. E., Li, J., Chen, Z., 2013. Benchmark 2 - springback of a draw / re-draw panel: Part A: Benchmark description. AIP Conf. Proc. 1567, 177–182.

Cazacu, O., Barlat, F., 2001. Generalization of drucker's yield criterion to orthotropy. Math. Mech. Solids 6, 613–630.

Cazacu, O., Barlat, F., 2004. A criterion for description of anisotropy and yield differential effects in pressure-insensitive metals. Int. J. Plasticity 20, 2027–2045.

Cazacu, O., Ionescu, I. R., Yoon, J. W., 2010. Orthotropic strain rate potential for the description of anisotropy in tension and compression of metals. Int. J. Plasticity 26, 887–904.

Cazacu, O., Plunkett, B., Barlat, F., 2006. Orthotropic yield criterion for hexagonal closed packed metals. Int. J. Plasticity 22, 1171–1194.

Chaboche, J. L., 1991. On some modification of kinematic hardening to improve the description of ratcheting effects. Int. J. Plasticity 7, 661–678.

Chaboche, J. L., 1994. Modelling of ratcheting: evaluation of various approaches. Eur. J. Mech. A-Solid. 13, 501–518.

Chaboche, J. L., 2008. A review of some plasticity and viscoplasticity constitutive theories. Int. J. Plasticity 24, 1642–1693.

Chaboche, J. L., Rousselier, G., 1983. On the plastic and viscoplastic constitutive equations - part i: rules development with internal variable concept. J. Press. Vess. Technol. 105, 153–158.

Chatti, S., 2010. Effect of the elasticity formulation in finite strain on springback prediction. Comput. Struct. 88, 796–805.

Chen, X., Jiao, R., Kim, K. S., 2005. On the Ohno-Wang kinematic hardening rules for multiaxial ratcheting modeling of medium carbon steel. Int. J. Plasticity 21, 161–184.

Chen, Y. P., Lee, W. B., To, S., 2007. Influence of initial texture on formability of aluminum sheet metal by crystal plasticity fe simulation. J. Mater. Process. Technol. 192-193, 397–403.

Choi, Y., Han, C.-S., Lee, J. K., Wagoner, R. H., 2006. Modeling multi-axial deformation of planar anisotropic elasto-plastic materials, part II: Applications. Int. J. Plasticity 22, 1765–1783.

Chu, E., 1995. Genealization of Hill's 1979 anisotropic yield criteria. J. Mater. Process. Technol. 50, 207–215.

Chung, K., Kim, D., Park, T., 2011. Analytical derivation of earing in circular cup drawing based on simple tension properties. Eur. J. Mech. A-Solid. 30, 275–280.

Chung, K., Lee, M.-G., Kim, D., Kim, C., Wenner, M. L., Barlat, F., 2005. Spring-back evaluation of automotive sheets based on isotropic-kinematic hardening laws and non-quadratic anisotropic yield functions Part I: theory and formulation. Int. J. Plasticity 21, 861–882.

Cleja-Ţigoiu, S., 2000. Nonlinear elasto-plastic deformations of transversely isotropic material and plastic spin. Int. J. Eng. Sci. 38, 737–763.

Comsa, D. S., Banabic, D., 2008. Plane-stress yield criterion for highly-anisotropic sheet metals. In: Hora, P. (Ed.) Proc. Numisheet 2008, Interlaken, 43–48.

Dafalias, Y. F., 1985. The plastic spin. ASME J. Appl. Mech. Rev. 52, 865–871.

Dafalias, Y. F., Popov, E. P., 1976. Plastic internal variables formalism of cyclic plasticity. J. Appl. Mech. 43, 645–651.

Darbandi, P., Pourboghrat, F., 2011. An evolutionary yield function based on Barlat 2000 yield function for the superconducting niobium sheet. AIP Conf. Proc. 1383, 210–217.

Dashner, P. A., 1986. Invariance considerations in large strain elasto-plasticity. J. Appl. Mech. 53, 55–60.

Dettmer, W., Reese, S., 2004. On the theoretical and numerical modelling of Armstrong-Frederick kinematic hardening in the finite strain regime. Comput. Methods Appl. Mech. Engrg. 193, 87–116.

Dienes, J. K., 1979. On the analysis of rotation and stress rate in deforming bodies. Acta Mechanica 32, 217–232.

Drucker, D. C., 1949. Relation of experiments to mathematical theories of plasticity. J. Appl. Mech.

16, 349–357.

Eidel, B., Gruttmann, F., 2003. Elastoplastic orthotropy at finite strains: multiplicative formulation and numerical implementation. Comput. Mater. Sci. 28, 732–742.

Feigenbaum, H. P., Dafalias, Y. F., 2007. Directional distortional hardening in metal plasticity within thermodynamics. Int. J. Solids Struct. 44, 7526–7542.

Feigenbaum, H. P., Dafalias, Y. F., 2014. Directional distortional hardening in large plastic deformations. Int. J. Solids Struct. 51, 3904–3918.

Freund, M., Shutov, A. V., Ihlemann, J., 2012. Simulation of distortional hardening by generalizing a uniaxial model of finite strain viscoplasticity. Int. J. Plasticity 36, 113–129.

Furukawa, T., Yagawa, G., 1997. Inelastic constitutive parameter identification using an evolutionary algorithm with constinuous individuals. Int. J. Numer. Meth. Engng. 40, 1071–1090.

Gao, X., Zhang, T., Zhou, J., Graham, M., Hayden, M., Roe, C., 2011. On stress-state dependent plasticity modeling: Significance of the hydrostatic stress, the third invariant of stress deviator and the non-associated flow rule. Int. J. Plasticity 27, 217–231.

Geng, L., Shen, Y., Wagoner, R. H., 2002. Anisotropic hardening equations derived from reverse-bend testing. Int. J. Plasticity 18, 743–767.

Geng, L., Wagoner, R. H., 2002. Role of plastic anisotropy and its evolution on springback. Int. J. Mech. Sci. 44, 123–148.

Gotoh, M., 1977. A theory of plastic anisotropy based on a yield function of fourth order (plane stress state) - I. Int. J. Mech. Sci. 19, 505–512.

Green, A. E., Naghdi, P., 1965. A general theory of an elasto-plastic continuum. Arch. Rational Mech. Anal. 18, 251–281.

Green, D. E., 2005. Description of Numisheet 2005 Benchmark #3 Stage-1: Channel Draw with 75% drawbead penetration. In: Cao, J., Shi, M. F., Stoughton, T. B., Wang, C. T., Zhang, L. (Eds.), Proc. Numisheet 05, CP778, vol. B. American Institute of Physics, 894–904.

Guo, C., Kang, G., Zhang, J., 2011. Meso-mechanical constitutive model for ratchetting of particle-reinforced metal matrix composites. Int. J. Plasticity 27, 1896–1915.

Haddadi, H., Belhabib, S., 2012. Improving the characterization of a hardening law using digital image correlation over an enhanced heterogeneous tensile test. Int. J. Mech. Sci. 62, 47–56.

Haddag, B., Abdel-Karim, M., Balan, T., 2009. Strain localization analysis using a large deformation anisotropic elastic-plastic model coupled with damage. Int. J. Plasticity 25, 1970–1996.

Håkansson, P., Wallin, M., Ristinmaa, M., 2005. Comparison of isotropic hardening and kinematic hardening in thermoplasticity. Int. J. Plasticity 21, 1435–1460.

Han, C.-S., Chung, K., Wagoner, R. H., Oh, S.-I., 2003. A multiplicative finite elasto-plastic formulation with anisotropic yield functions. Int. J. Plasticity 19, 197–211.

He, W. J., Zhang, S. H., Song, H. W., 2013. An extended homogenous yield function based anisotropic hardening model for description of anisotropic hardening behaviour of materials. Int. J. Mech. Sci. 77, 343–355.

Helm, D., 2006. Stress computation in finite thermoviscoplasticity. Int. J. Plasticity 22, 1699–1727.

Henann, D. L., Anand, L., 2009. A large deformation theory for rate-dependent elastic-plastic materials with combined isotropic and kinematic hardening. Int. J. Plasticity 25, 1833–1878.

Hershey, A. V., 1954. The plasticity of an isotropic aggregate of anisotropic face centered cubic crystals. J. Appl. Mech. 21, 241–249.

Hibbitt, H. D., Marcal, P. V., Rice, J. R., 1970. A finite element formulation for problems of large strain and large displacement. Int. J. Solids Struct. 6, 1069–1086.

Hill, R., 1948. A theory of the yielding and plastic flow of anisotropic metals. Proc. R. Soc. Lond. A 193, 281–297.

Hill, R., 1978. Aspects of invariance in solid mechanics. Adv. Appl. Mech. 18, 1–75.

Hill, R., 1979. Theoretical plasticity of textured aggregates. Math. Proc. Camb. Philos. Soc. 85, 179–191.

Hill, R., 1990. Constitutive modelling of orthotropic plasticity in sheet metals. J. Mech. Phys. Solids 38, 405–417.

Hill, R., 1993. A user-friendly theory of orthotropic plasticity in sheet metals. Int. J. Mech. Sci. 35, 19–25.

Hinton, E., 1992. Introduction to nonlinear finite element analysis. NAFEMS Publications.

Hollomon, J. H., 1945. Tensile deformation. Trans. AIME 162, 268–290.

Hosford, W. F., 1966. Texture strengthening. Metals Eng. Quarterly 6, 13–19.

Hosford, W. F., 1972. A generalised isotropic yield criterion. J. Appl. Mech. Trans. ASME 39, 607–609.

Hosford, W. F., 1979. On yield loci of anisotropic cubic metals. In: Proc. 7th North American Metalworking Conference, SME, Dearborn, 191–197.

Hu, W., 2007. Constitutive modeling of orthotropic sheet metals by presenting hardening-induced anisotropy. Int. J. Plasticity 23, 620–639.

Hughes, T. J. R., Winget, J., 1980. Finite rotation effects in numerical integration of rate constitutive equations arising in large-deformation analysis. Int. J. Numer. Meth. Engng. 15, 1862–1867.

Itskov, M., 2004. On the application of the additive decomposition of generalized strain measures in large strain plasticity. Mech. Res. Commun. 31, 507–517.

Itskov, M., Aksel, N., 2004. A constitutive model for orthotropic elasto-plasticity at large strains. Arch. Appl. Mech. 75, 75–91.

Jiang, Y., Sehitoglu, H., 1996. Modelling of cyclic ratchetting plasticity, Part I: development of constitutive relations. J. Appl. Mech. 63, 720–725.

Johansson, G., 2008. On the non-oscillation criterion for multiplicative anisotropic plasticity at large simple shear deformation. Int. J. Plasticity 24, 1190–1204.

Kang, G., 2004. A visco-plastic constitutive model for ratcheting of cyclically stable materials and its finite element implementation. Mech. Mater. 36, 299–312.

Kang, G., Ohno, N., Nebu, A., 2003. Constitutive modeling of strain range dependent cyclic hardening. Int. J. Plasticity 19, 1801–1819.

Karafillis, A. P., Boyce, M. C., 1993. A general anisotropic yield criterion using bounds and a transformation weighting tensor. J. Mech. Phys. Solids 41, 1859–1886.

Khan, A. S., Pandey, A., Stoughton, T. B., 2010. Evolution of subsequent yield surfaces and elastic constants with finite plastic deformation. Part-II: A very high work hardening aluminum alloy (annealed 1100Al). Int. J. Plasticity 26, 1421–1431.

Kim, D., Barlat, F., Bouvier, S., Rabahallah, M., Balan, T., Chung, K., 2007. Non-quadratic anisotropic potentials based on linear transformation of plastic strain rate. Int. J. Plasticity 23, 1380–1399.

Kim, D., Dargush, G. F., Basaran, C., 2013. A cyclic two-surface thermoplastic damage model with application to metallic plate dampers. Eng. Struct. 52, 608–620.

Kim, J. H., Lee, M., Barlat, F., Wagoner, R. H., Chung, K., 2008. An elasto-plastic constitutive model with plastic strain rate potentials for anisotropic cubic metals. Int. J. Plasticity 24, 2298–2334.

Krieg, R. D., 1975. A pratical two surface plasticity theory. J. Appl. Mech. 42, 641–646.

Kröner, E., 1960. Allgemeine Kontinuumstheorie der Versetzungen und Eingespannungen. Arch. Rational Mech. Anal. 4, 273–334.

Leacock, A. G., 2006. A mathematical description of orthotropy in sheet metals. J. Mech. Phys. Solids 54, 425–444.

Lee, E. H., 1969. Elastic-plastic deformation at finite strains. J. Appl. Mech. 36, 1–6.

Lee, J., Lee, J.-Y., Barlat, F., Wagoner, R. H., Chung, K., Lee, M.-G., 2013a. Extension of quasi-plastic-elastic approach to incorporate complex plastic flow behavior - application to springback of advanced high-strength steels. Int. J. Plasticity 45, 140–159.

Lee, J., Lee, M.-G., Barlat, F., Kim, J. H., 2012a. Stress integration schemes for novel homogeneous anisotropic hardening model. Comput. Methods Appl. Mech. Engrg. 247-248, 73–92.

Lee, J.-W., Lee, M.-G., Barlat, F., 2012b. Finite element modeling using homogeneous anisotropic hardening and application to spring-back prediction. Int. J. Plasticity 29, 13–41.

Lee, M. G., Lee, J. W., Grácio, J. J., Vincze, G., Rauch, E. F., Barlat, F., 2013b. A dislocation-based hardening model incorporated into an anisotropic hardening approach. Comput. Mater. Sci. 79, 570–583.

Lehmann, T., 1972. Anisotrope plastische formnderungen. Romanian J. Techn. Sci. Appl. Mech. 17, 1077–1086.

Levenberg, K., 1944. A method for the solution of certain problems in least squares. Quart. Appl. Math. 2, 164–168.

Lin, S. B., Ding, J. L., 1996. A modified form of Hill's orientation-dependent yield criterion for orthotropic sheet metals. J. Mech. Phys. Solids 44, 1739–1764.

Lion, A., 2000. Constitutive modelling in finite thermoviscoplasticity: a physical approach based on nonlinear rheological models. Int. J. Plasticity 16, 469–494.

Liu, C., Huang, Y., Stout, M. G., 1997. On the asymmetric yield surface of plastically orthotropic materials: a phenomenological study. Acta. Metall. 45, 2397–2406.

Liu, C.-S., Hong, H.-K., 1999. Non-oscillation criteria for hypoelastic models under simple shear deformation. J. Elasticity 57, 201–241.

Löblein, J., Schröder, J., Gruttmann, F., 2003. Application of generalized measures to an orthotropic finite elasto-plasticity model. Comput. Mater. Sci. 28, 696–703.

Lou, Y., Huh, H., Yoon, J. W., 2013. Consideration of strength differential effect in sheet metals with symmetric yield functions. Int. J. Mech. Sci. 66, 214–223.

Ludwigson, D. C., 1971. Modified stress-strain relation for FCC metals and alloys. Metall. Trans. 2, 2825–2828.

Lührs, G., Hartmann, S., Haupt, P., 1997. On the numerical treatment of finite deformations in elastoviscoplasticity. Comput. Methods Appl. Mech. Engrg. 144, 1–21.

Marquardt, D. W., 1963. An algorithm for least-squares estimation of nonlinear parameters. J. Soc. Indust. Appl. Math. 11, 431–441.

McDowell, D. L., 1995. Stress state dependence of cyclic ratchetting behaviour of two rail steels. Int. J. Plasticity 11, 397–421.

McMeeking, R. M., Rice, J. R., 1975. Finite-element formulations for problems of large elasto-plastic deformation. Int. J. Solids Struct. 11, 601–616.

Menzel, A., Ekh, M., Runesson, K., Steinmann, P., 2005. A framework for multiplicative elastoplasticity with kinematic hardening coupled to anisotropic damage. Int. J. Plasticity 21, 397–434.

Menzel, A., Steinmann, P., 2003. On the spatial formulation of anisotropic multiplicative elastoplasticity. Comput. Methods Appl. Mech. Engrg. 192, 3431–3470.

Metzger, M., Selfert, T., 2013. On the exploitation of Armstrong-Frederick type nonlinear kinematic hardening in the numerical integration and finite-element implementation of pressure dependent plasticity models. Comput. Mech. 52, 515–524.

Miehe, C., 1996a. Exponential map algorithm for stress updates in anisotropic multiplicative elastoplasticity for single crystals. Int. J. Numer. Meth. Engng. 39, 3367–3390.

Miehe, C., 1996b. Numerical computation of algorithmic (consistent) tangent moduli in large-strain computational inelasticity. Comput. Methods Appl. Mech. Engrg. 134, 223–240.

Miehe, C., Apel, N., 2004. Anisotropic elastic-plastic analysis of shells at large strains. a comparison of multiplicative and additive approaches to enhanced finite element design and constitutive modelling. Int. J. Numer. Meth. Engng. 61, 2067–2113.

Miehe, C., Apel, N., Lambrecht, M., 2002. Anisotropic additive plasticity in the logarithmic strain space: modular kinematic formulation and implementation based on incremental minimization principles for standard materials. Comput. Methods Appl. Mech. Engrg. 191, 5383–5425.

Montheillet, F., Jonas, J. J., Benferrah, M., 1991. Development of anisotropy during the cold rolling of aluminium sheet. Int. J. Mech. Sci. 33, 197–209.

Moon, Y. H., Kim, D. W., Van Tyne, C. J., 2008. Analytical model for prediction of sidewall curl during stretch-bend sheet metal forming. Int. J. Mech. Sci. 50, 666–675.

Mroz, Z., 1967. On the description of anisotropic work hardening. J. Mech. Phys. Solids 15, 163–175.

Nakamachi, E., Xie, C. L., Harimoto, M., 2001. Drawability assessment of bcc steel sheet by using elastic/crystalline viscoplastic finite element analyses. Int. J. Mech. Sci. 43, 631–652.

Nemat-Nasser, S., 1982. On finite deformation elasto-plasticity. Int. J. Solids Struct. 18, 857–872.

Nixon, M. E., Cazacu, O., Lebensohn, R. A., 2010. Anisotropic response of high-purity α-titanium: Experimental characterization and constitutive modeling. Int. J. Plasticity 26, 516–532.

Noman, M., Clausmeyer, T., Barthel, C., Svendsen, B., Huétink, J., van Riel, M., 2010. Experimental characterization and modeling of the hardening bahaviour of the sheet steel LH800. Mat. Sci. Eng. A 527, 2515–2526.

NUMISHEET, 1993. Numisheet'93 benchmark problem. In: Makinouchi, A., Nakamachi, E., Onate, E., Wagoner, R.H. (Eds.), Proc. 2nd International Conference on Numerical Simulation of 3D Sheet Metal Forming Processes - Verification of Simulation with Experiment, Isehara, Japan.

NUMISHEET, 1996. Numisheet'96 benchmark problem. In: Lee, J. K., Kinzel, G. L., Wagoner, R. H. (Eds.), Proc. 3rd International Conference on Numerical Simulation of 3D Sheet Metal Forming Processes, Dearborn, USA.

Ohno, N., Wang, J.-D., 1993. Kinematic hardening rules with critical state of dynamic recovery, part I: formulation and basic features for ratcheting behaviour. Int. J. Plasticity 9, 375–390.

Ortiz, M., Pinsky, P. M., 1981. Global analysis methods for the solution of elastoplastic and viscoplastic dynamic problems. Report UCB/SESM 81/08, Dept. Civil Eng. University of California, Berkley, EUA.

Ortiz, M., Pinsky, P. M., Taylor, R. L., 1983. Operator split methods for the numerical solution of the elastoplastic dynamic problem. Comput. Methods Appl. Mech. Engrg. 39, 137–157.

Ortiz, M., Simo, J. C., 1986. An analysis of a new class of integration algorithms for elastoplastic relations. Int. J. Numer. Meth. Engng. 23, 253–366.

Owen, D. R. J., Hinton, E., 1980. Finite elements in plasticity: theory and practice. Pineridge Press Limited, Swansea, United Kingdom.

Papadopoulos, P., Lu, J., 1998. A general framework for the numerical solution of problems in finite elasto-plasticity. Comput. Methods Appl. Mech. Engrg. 159, 1–18.

Papadopoulos, P., Lu, J., 2001. On the formulation and numerical solution of problems in anisotropic finite plasticity. Comput. Methods Appl. Mech. Engrg. 190, 4889–4910.

Paraianu, L., Comsa, D. S., Cosovici, G., Jurco, P., Banabic, D., 2003. An improvement of the BBC2000 yield criterion. In: Brucato, V. (Ed.), Proc. 6th ESAFORM2003 Conference on Metal forming, Nuova Ipsa, Salermo, 215–219.

Pearce, R., 1968. Some aspects of anisotropic plasticity in sheet metals. Int. J. Mech. Sci. 10, 995–1004.

Peters, P., Manopulo, N., Lange, C., Hora, P., 2014. A strain rate dependent anisotropic hardening model and its validation through deep drawing experiments. Int. J. Mater. Form. 7, 447–457.

Pietryga, M. P., Vladimirov, I. N., Reese, S., 2012. A finite deformation model for evolving flow anisotropy with distortional hardening including experimental validation. Mech. Mater. 44, 163–173.

Pietryga, M. P., Vladimirov, I. N., Reese, S., 2014. On the use of explicit and implicit exponential map algorithms of finite strain combined hardening plasticity in the simulation of draw bending. Key Eng. Mat. 611-612, 1796–1806.

Plunkett, B., Cazacu, O., Barlat, F., 2008. Orthotropic yield criteria for description of the anisotropy in tension and compression of sheet metals. Int. J. Plasticity 24, 847–866.

Plunkett, B., Lebensohn, R. A., Cazacu, O., Barlat, F., 2006. Anisotropic yield function of hexagonal materials taking into account texture development and anisotropic hardening. Acta Materialia 54, 4159–4169.

Pöhlandt, K., Banabic, D., Lange, K., 2002. Equi-biaxial anisotropy coefficient used to describe the plastic behavior of sheet metal. Proc. ESAFORM conference, Krakow, 723–727.

Prager, W., 1956. A new method of analyzing stresses and strains in work-hardening plastic solids. J. Appl. Mech. 23, 493–496.

Raabe, D., Roters, F., 2004. Using texture components in cystal plasticity element simulations. Int. J. Plasticity 20, 339–361.

Raabe, D., Wang, Y., Roters, F., 2005. Crystal plasticity simulation study on the influence of texture on earing in steel. Comput. Mater. Sci. 34, 221–234.

Rabahallah, M., Bouvier, S., Balan, T., Bacroix, B., 2009. Numerical simulation of sheet metal forming using anisotropic strain-rate potentials. Mat. Sci. Eng. A-Struct. 517, 261–275.

Reese, S., 2003. Meso-macro modelling of fibre-reinforced rubber-like composites exhibiting large elastoplastic deformation. Int. J. Solids Struct. 40, 951–980.

Reese, S., Govindjee, S., 1998. A theory of finite viscoelasticity and numerical aspects. Int. J. Solids Struct. 35, 3455–3482.

Reina, C., Conti, S., 2014. Kinematic description of crystal plasticity in the finite kinematic framework: A micromechanical understanding of $\mathbf{f} = \mathbf{f}^e\mathbf{f}^p$. J. Mech. Phys. Solids 67, 40–61.

Rice, J. R., 1971. Inelastic constitutive relations for solids: an internal-variable theory and its application to metal plasticity. J. Mech. Phys. Solids 19, 433–455.

Rodas, C. O., Zaïri, F., Naït-Abdelaziz, M., 2014. A finite strain thermo-viscoelastic constitutive model to describe the self-heating in elastomeric materials during low-cycle fatigue. J. Mech. Phys. Solids 64, 396–410.

Roters, F., Eisenlohr, P., Hantcherli, L., Tjahjanto, D. D., Bieler, T. R., Raabe, D., 2010. Overview of constitutive laws, kinematics, homogenization and multiscale methods in crystal plasticity finite-element modeling: Theory, experiments, applications. Acta Materialia 58, 1152–1211.

Sansour, C., Karšaj, I., Sorić, J., 2006a. A formulation of anisotropic continuum elastoplasticity at finite strains. Part I: Modelling. Int. J. Plasticity 22, 2346–2365.

Sansour, C., Karšaj, I., Sorić, J., 2006b. On free energy-based formulations for kinematic hardening and the decomposition $\mathbf{f} = \mathbf{f}_p\mathbf{f}_e$. Int. J. Solids Struct. 43, 7534–7552.

Sansour, C., Karšaj, I., Sorić, J., 2007. On anisotropic flow rules in multiplicative elastoplasticity at finite strains. Comput. Methods Appl. Mech. Engrg. 196, 1294–1309.

Sansour, C., Karšaj, I., Sorić, J., 2008. On a numerical implementation of a formulation of anisotropic continuum elastoplasticity at finite strains. J. Comput. Phys. 227, 7643–7663.

Schmidt, I., 2005. Some comments on formulations of anisotropic plasticity. Comput. Mater. Sci. 32, 518–523.

Schröder, J., Gruttmann, F., Löblein, J., 2002. A simple orthotropic finite elasto-plasticity model based on generalized stress-strain measures. Comput. Mech. 30, 48–64.

Seth, B. R., 1962. Generalized strain measure with applications to physical problems. In: Proc. IUTAM symposium on second order effects in elasticity, plasticity and fluid mechanics, Haifa.

Shi, B., Bartels, A., Mosler, J., 2014. On the thermodynamically consistent modeling of distortional hardening: A novel generalized framework. Int. J. Plasticity 63, 170–182.

Shi, B., Mosler, J., 2013. On the macroscopic description of the yield surface evolution by means of distortional hardening models: Application to magnesium. Int. J. Plasticity 44, 1–22.

Shutov, A. V., Ihlemann, J., 2014. Analysis of some basic approaches to finite strain elasto-plasticity in view of reference change. Int. J. Plasticity 63, 183–197.

Shutov, A. V., Kreißig, R., 2008. Finite strain viscoplasticity with nonlinear kinematic hardening. Phenomenological modeling and time integration. Comput. Methods Appl. Mech. Engrg. 197, 2015–2029.

Simo, J. C., 1985. On the computational significance of the intermediate configuration and hyperelastic stress relations in finite deformation elastoplasticity. Mech. Mater. 4, 439–451.

Simo, J. C., 1992. Algorithms for static and dynamic multiplicative plasticity that preserve the classical return mapping schemes of the infinitesimal theory. Comput. Methods Appl. Mech. Engrg. 99, 61–112.

Simo, J. C., Hughes, T. J. R., 1998. Computational Inelasticity. Springer.

Simo, J. C., Ortiz, M., 1985. A unified approach to finite deformation elastoplastic analysis based on the use of hyperelastic constitutive equations. Comput. Methods Appl. Mech. Engrg. 49, 221–245.

Simo, J. C., Pister, K. S., 1984. Remarks on rate constitutive equations for finite deformation problems: computational implications. Comput. Methods Appl. Mech. Engrg. 46, 201–215.

Soare, S., Barlat, F., 2010. Convex polynomial yield functions. J. Mech. Phys. Solids 58, 1804–1818.

Soare, S., Yoon, J. W., Cazacu, O., 2008. On the use of homogeneous polynomials to develop anisotropic yield functions with applications to sheet forming. Int. J. Plasticity 24, 915–944.

Souza Neto, E. A., 2001. The exact derivative of the exponential of an unsymmetric tensor. Comput. Methods Appl. Mech. Engrg. 190, 2377–2383.

Souza Neto, E. A., Perić, D., Owen, D. R. J., 2008. Computational Methods for Plasticity: Theory and Applications. John Wiley and Sons, Ltd.

Spencer, A. J. M., 1971. Continuum Physics, Vol. I. Editor: A. C. Eringen, Academic Press, Ch. Theory of invariants, pp. 239–353.

Spitzig, W. A., Sober, R. J., Richmond, O., 1975. Pressure dependence of yielding and associated volume expansion in tempered martensite. Acta Metall. 23, 885–893.

Stoughton, T. B., 2002. A non-associated flow rule for sheet metal forming. Int. J. Plasticity 18, 687–714.

Stoughton, T. B., Green, D. E., Iadicola, M., 2005. Specification for BM3: two-stage channel/cup draw. In: Cao, J., Shi, M. F., Stoughton, T. B., Wang, C. T., Zhang, L. (Eds.), Proc. Numisheet 05, CP778, vol. B. American Institute of Physics, 1157–1172.

Stoughton, T. B., Shi, M. F., Huang, G., Yoon, J. W., 2013. Material characterizations for benchmark 1 and benchmark 2. AIP Conf. Proc. 1567, 9–14.

Stoughton, T. B., Yoon, J. W., 2004. A pressure-sensitive yield criterion under a non-associated flow rule for sheet metal forming. Int. J. Plasticity 20, 705–731.

Sun, L., Wagoner, R. H., 2011. Complex unloading behavior: Nature of the deformation and its constitutive representation. Int. J. Plasticity 27, 1126–1144.

Sung, J. H., Kim, J. H., Wagoner, R. H., 2010. A plastic constitutive equation incorporating strain, strain-rate, and temperature. Int. J. Plasticity 26, 1746–1771.

Svendsen, B., 2001. On the modelling of anisotropic elastic and inelastic material behaviour at large deformation. Int. J. Solids Struct. 38, 9579–9599.

Svendsen, B., Arndt, S., Klingbeil, D., Sievert, R., 1998. Hyperelastic models for elastoplasticity with non-linear isotropic and kinematic hardening at large deformation. Int. J. Solids Struct. 35, 3363–3389.

Svendsen, B., Levkovitch, V., Wang, J., Reusch, F., Reese, S., 2006. Application of the concept of evolving structure tensors to the modeling of initial and induced anisotropy at large deformation.

Comp. Struct. 84, 1077–1085.

Swift, H. W., 1952. Plastic instability under plane stress. J. Mech. Phys. Solids 1, 1–18.

Taherizadeh, A., Green, D. E., Ghaei, A., Yoon, J. W., 2010. A non-associated constitutive model with mixed iso-kinematic hardening for finite element simulation of sheet metal forming. Int. J. Plasticity 26, 288–309.

Taherizadeh, A., Green, D. E., Yoon, J. W., 2011. Evaluation of advanced anisotropic models with mixed hardening for general associated and non-associated flow metal plasticity. Int. J. Plasticity 27, 1781–1802.

Thuillier, S., Manach, P. Y., Menezes, L. F., 2010. Occurence of strain path changes in a two-stage deep drawing process. J. Mater. Process. Technol. 210, 226–232.

Tikhovskiy, I., Raabe, D., Roters, F., 2007. Simulation of earing during deep drawing of an Al-3% Mg alloy (AA 5754) using a texture component crystal plasticity FEM. J. Mater. Process. Technol. 183, 169–175.

Tresca, H., 1864. On the yield of solids at high pressures (*in french*). Comptes Rendus Academie des Sciences, Paris 59, 754.

Tsakmakis, C., 1996. Kinematic hardening rules in finite plasticity. Part I: A constitutive approach. Continuum Mech. Thermodyn. 8, 215–231.

Tsakmakis, C., Willuweit, A., 2004. A comparative study of kinematic hardening rules at finite deformations. Int. J. Nonlin. Mech. 39, 539–554.

Tuninetti, V., Gilles, G., Milis, O., Pardoen, T., Habraken, A. M., 2015. Anisotropic and tension-compression asymmetry modeling of the room temperature plastic response of Ti-6Al-4V. Int. J. Plasticity 67, 53–68.

Ulz, M. H., 2009. A Green-Naghdi approach to finite anisotropic rate-independent and rate-dependent thermo-plasticity in logarithmic Lagrangean strain-entropy space. Comput. Methods Appl. Mech. Engrg. 198, 3262–3277.

Van Houtte, P., Gaward, J., Eyckens, P., Van Bael, B., Samaey, G., Roose, D., 2012. Multi-scale modelling of the development of heterogeneous distributions of stress, strain, deformation texture and anisotropy in sheet metal forming. Procedia IUTAM 3, 67–75.

Vegter, H., Drent, P., Huétink, J., 1995. A planar isotropic yield criterion based on mechanical testing at multi-axial stress states. In: Shen, S.-F., Dawson, P. R. (Eds.), Simulation of Materials Processing: Theory, Methods and Applications. Balkema, Rotterdam, 345–350.

Vegter, H., van den Boogaard, A. H., 2006. A plane stress function for anisotropic sheet material by interpolation of biaxial stress states. Int. J. Plasticity 22, 557–580.

Vladimirov, I. N., Pietryga, M. P., Kiliclar, Y., Tini, V., Reese, S., 2014. Failure modelling in metal forming by means of an anisotropic hyperelastic-plasticity model with damage. Int. J. Damage Mech., doi:10.1177/1056789513518953.

Vladimirov, I. N., Pietryga, M. P., Reese, S., 2008. On the modelling of non-linear kinematic hardening at finite strains with application to springback - Comparison of time integration algorithms. Int. J. Numer. Meth. Engng. 75, 1–28.

Vladimirov, I. N., Pietryga, M. P., Reese, S., 2010. Anisotropic finite elastoplasticity with nonlinear kinematic and isotropic hardening and application to sheet metal forming. Int. J. Plasticity 26, 659–687.

Vladimirov, I. N., Pietryga, M. P., Reese, S., 2011. On the influence of kinematic hardening on plastic anisotropy in the context of finite strain plasticity. Int. J. Mater. Form. 4, 255–267.

Voce, E., 1948. The relationship between stress and strain for homogeneous deformation. J. Inst. Met. 74, 537–562.

von Mises, R. V., 1913. Mechanik der fasten korper in plastisch deformablen zustand (*in german*). In: Gottinger Nachrichten, Germany, 582–592.

Vrh, M., Halilovič, M., Starman, B., Štok, B., Comsa, D. S., Banabic, D., 2014. Capability of the BBC2008 yield criterion in predicting the earing profile in cup deep drawing simulations. Eur. J. Mech. A-Solid. 45, 59–74.

Vrh, M., Halilovič, M., Štok, B., 2010. Improved explicit integration in plasticity. Int. J. Numer. Meth. Engng. 81, 910–928.

Wagoner, R. H., Lim, H., Lee, M.-G., 2013. Advanced issues in springback. Int. J. Plasticity 45, 3–20.

Wallin, M., Ristinmaa, M., 2005. Deformation gradient based kinematic hardening model. Int. J. Pl 21, 2025–2050.

Wallin, M., Ristinmaa, M., Ottosen, N. S., 2003. Kinematic hardening in large strain plasticity. Eur.

J. Mech. A-Solid. 22, 341–356.

Weber, G., Anand, L., 1990. Finite deformation constitutive equations and a time integration procedure for isotropic, hyperelastic-viscoplastic solids. Comput. Methods Appl. Mech. Engrg. 79, 173–202.

Wilkins, M. L., 1963. Calculation of elastic-plastic flow. In. Methods of Comp. Physics, vol. 3. Academic Press. Livermore, California.

Xiao, H., Bruhns, O. T., Meyers, A., 1997. Logarithmic strain, logarithmic spin and logarithmic rate. Acta Mechanica 124, 89–105.

Xiao, H., Bruhns, O. T., Meyers, A., 2006. Elastoplasticity beyond small deformations. Acta Mechanica 182, 31–111.

Yoon, J.-H., Cazacu, O., Yoon, J. W., Dick, R. E., 2010. Earing predictions for strongly textured aluminum sheets. Int. J. Mech. Sci. 52, 1563–1578.

Yoon, J. W., Barlat, F., Chung, K., Pourboghrat, F., Yang, D., 2000. Earing predictions based on symmetric nonquadratic yield function. Int. J. Plasticity 16, 1075–1104.

Yoon, J. W., Barlat, F., Dick, R. E., Karabin, M. E., 2006. Prediction of six or eight ears in a drawn cup based on a new anisotropic yield function. Int. J. Plasticity 22, 174–193.

Yoon, J. W., Lou, Y., Yoon, J., Glazoff, M. V., 2014. Asymmetric yield function based on the stress invariants for pressure sensitive metals. Int. J. Plasticity 56, 184–202.

Yoon, J. W., Yang, D. Y., Chung, K., 1999. Elasto-plastic finite element method based on incremental deformation theory and continuum based shell elements for planar anisotropic sheet materials. Comput. Methods Appl. Mech. Engrg. 174, 23–56.

Yoshida, F., Hamasaki, H., Uemori, T., 2013. A user-friendly 3D yield function to describe anisotropy of steel sheets. Int. J. Plasticity 45, 119–139.

Yoshida, F., Uemori, T., 2002. A model of large-strain cyclic plasticity describing the Bauschinger effect and workhardening stagnation. Int. J. Plasticity 18, 661–686.

Yoshida, F., Uemori, T., 2003. A model of large-strain cyclic plasticity and its application to springback simulation. Int. J. Mech. Sci. 45, 1687–1702.

Zang, S. L., Liang, J., Guo, C., 2007. A constitutive model for spring-back prediction in which the change of Young's modulus with plastic deformation is considered. Int. J. Mach. Tool Manu. 47, 1791–1797.

Zhou, W., 1990. A new non-quadratic orthotropic yield criterion. Int. J. Mech. Sci. 32, 513–520.

Zhu, Y., Kang, G., Kan, Q., Bruhns, O. T., 2014. Logarithmic stress rate based constitutive model for cyclic loading in finite plasticity. Int. J. Plasticity 54, 34–55.

Ziegler, H., 1959. A modification of Prager's hardening rule. Quart. Appl. Math. 17, 55–65.

Ziegler, H., 1977. An introduction to thermodynamics. North-Holland, Amsterdam.